UC San Diego

UC San Diego Electronic Theses and Dissertations

Title

Optical signatures of exciton condensate dynamics studied by broadband terahertz spectroscopy

Permalink

https://escholarship.org/uc/item/68s0f1vv

Author

Haque, Sheikh Rubaiat Ul

Publication Date

2023

Peer reviewed|Thesis/dissertation

eScholarship.org Powered by the California Digital Library
University of California

UNIVERSITY OF CALIFORNIA SAN DIEGO

Optical Signatures of Exciton Condensate Dynamics Studied by Broadband Terahertz Spectroscopy

A Dissertation submitted in partial satisfaction of the requirements
for the degree Doctor of Philosophy

in

Physics

by

Sheikh Rubaiat Ul Haque

Committee in charge:

Professor Richard D. Averitt, Chair
Professor Yeshaiahu (Shaya) Fainman
Professor Michael M. Fogler
Professor Alex Fraño
Professor Wei Xiong

2023

Copyright

Sheikh Rubaiat Ul Haque, 2023

All rights reserved.

The Dissertation of Sheikh Rubaiat Ul Haque is approved, and it is acceptable in quality and form for publication on microfilm and electronically.

University of California San Diego

2023

Dedication

To my family who have given unconditional love and support throughout my life. And to my lovely wife who has filled my life with happiness and keeps me motivated even during the hardest of times.

Epigraph

فَإِنَّ مَعَ ٱلْعُسْرِ يُسْرًا

So, verily, with hardship comes ease.

إِنَّ مَعَ ٱلْعُسْرِ يُسْرًا

Verily, with hardship comes ease.

The Quran (94:5-6)

Table of Contents

List of Figures

List of Tables

List of Abbreviations

DOF	Degree of freedom
GL	Ginzberg-Landau
GS	Ground state
DFT	Density Functional Theory
DMFT	Dynamic Mean Field Theory
LDA	Local Density Approximation
FTIR	Fourier transform infrared spectroscopy
ARPES	Angle-resolved photoemission spectroscopy
tr-	Time-resolved
STM	Scanning tunnelling microscopy
NMR	Nuclear magnetic resonance
IXS	Inelastic X-ray scattering
RIXS	Resonant inelastic X-ray scattering
XRD	X-ray diffraction
RF	Radio frequency
THz	Terahertz
IR	Infrared
MIR	Mid-infrared
NIR	Near-infrared
UV	Ultraviolet
ps	Picosecond
fs	Femtosecond

EI	Excitonic insulator
TNS	Ta_2NiSe_5
BEC	Bose-Einstein condensate
BCS	Bardeen-Cooper-Schrieffer
CDW	Charge density wave
PDW	Pair density wave
CO	Charge order
SC	Superconductor
AFM	Antiferromagnet
FM	Ferromagnet
PM	Paramagnet
IMT	Insulator-metal transition
PIPT	Photoinduced phase transition
HT	High temperature
LT	Low temperature
CB	Conduction band
VB	Valence band
CT	Charge transfer
BZ	Brillouin zone
DOS	Density of states
2DEG	2-dimensional electron gas
QP	Quasiparticle
RT	Rothwarf-Taylor

KS	Kindt-Schmuttenmaer
KK	Kramers-Kronig
FH	Fundamental harmonic
SHG	Second harmonic generation
THG	Third harmonic generation
SFG	Sum frequency generation
DFG	Difference frequency generation
FWM	Four-wave mixing
EO	Electro-optic
LNO	$LiNbO_3$
TDS	Time-domain scan
OPTP	Optical pump – THz probe
WP	Wollaston prism
WGP	Wire grid polarizer
BS	Beam splitter
PBS	Pellicle beam splitter
BPD	Balanced photodetector
FWP	Full waveplate
HWP	Half waveplate
QWP	Quarter waveplate
OAP	Off-axis parabolic mirror
OPA	Optical parametric amplifier
DWP	Dual wave plate

BBO	β-Barium Borate
DAQ	Data acquisition
TTL	Transistor-transistor-logic
FFT	Fast Fourier transform
FWHM	Full width half maximum
s	Signal
id	Idler
PBE	Perdew-Burke-Ernzerhof
VASP	Vienna *ab intito* Simulation Package

Acknowledgements

First, I want to thank my advisor, Professor Richard Averitt. He is a top-level physicist whose knowledge in condensed matter physics and ultrafast science never ceases to amaze me. I admire how he approaches a new problem by asking the right questions and his uncanny ability to see the bigger picture has always been helpful to get the most solid but interesting explanation for the experimental observations. Rick's attention to minute details and the effort he puts in perfecting a manuscript has been one of the biggest takeaways for me. He gave me freedom to lead the research projects he entrusted me with, and his hands-off approach helped me flourish into an independent scientist. I am also grateful how he has been promoting my works in invited talks, seminars and how he helped me get a footing in the physics community.

Notwithstanding the COVID-19 pandemic, I had a productive time at the Averitt group. In particular, there are two Averitt group alumni I would like to express my gratitude to: Jingdi and Gu-Feng. My first mentor, Jingdi, is probably one of the best experimentalists I have met. He has kindly taught me all the ins and outs of THz spectroscopy and I always cherish the memories of working long hours with him at MH 4545. We built the upstairs lab from scratch and the joy of building a new experiment, working at the forefront of physics research kept us tirelessly motivated. Gu-Feng was my second mentor and like Jingdi, he is another big brother to me as well. His experimental prowess will surprise anyone and his ability to design and build new experiments has made him a powerhouse. Without his suggestions, the optical pump – broadband THz probe setup I built would not be in its current shape.

Another person I want to give special thanks to is Yuan, a talented younger grad student who I had the privilege to mentor in his early years in PhD. He quickly learned all the skills and

eventually helped me in taking the final data for both the Ta_2NiSe_5 and InAs metamaterial projects. Without his help, none of these works would have been possible. I also thank Varun, another talented grad student I mentored, for learning everything with utmost patience. Passing the baton to Yuan and Varun makes me believe that MH 4545 is in very safe hands who will produce top quality results in the years to come.

In the UCSD physics department, I thank Brad Hanson for the machine shop training, Lester Brooks for the HVAC management, and Susan Marshall for helping us regarding travel reimbursements. I also thank Kevin (Smith), Sharmila, Jasmyn, Erin, Anne, Catherine, Saixious and Dawn for making the grad students' life much easier by taking care of all the logistics. I am also grateful to Misha Fogler, Dan Arovas, Tarun Grover, John McGreevy, Jorge Hirsch, Max di Ventra, Ken Intriligator, Dan Dubin, and Tom Murphy for all the enjoyable physics courses they taught. I would also like to express gratitude to the professors I was TA with: Kaixuan Ni, Elizabeth Jenkins, Avi Yagil and Phil Tsai for being very accommodating. I thank Alex Fraño for all the research discussions and career advice. I would like to express thanks to the amazing people I met at school: Sridip, Ahanjit, Shouvik, Rourav, Meng, Mac (Lee), Ben, Kevin (Cremin), Anamika, Gautam, Shruti, Shijun, Shubham, Connie, Avaneesh, Kelson, Peter (Lu), Peter (Kissin), Peter (Kim), Ghita, Aravind, Karthik, Ahmed (Akhtar), Max, Jonathan, Wang, Chao, Balaji, Dylan, Jacob and Dawei for their support in different capacities.

I particularly thank my theoretical collaborators Marios Michael and Eugene Demler for the first principles theoretical calculation and simulations of the results on Ta_2NiSe_5 (TNS). Without their tremendous effort, the manuscript would not be complete. I am proud to be part of their team that developed Fresenel-Floquet theory, a novel and elegant formalism to explain generalized photoexcited dynamics in quantum materials.

I also express my gratitude to Lukas Windgätter, Simone Latini and Angel Rubio for the DFT calculations that provided the last missing piece of the puzzle and gave the TNS manuscript a much more solid story. Also, Angel spent a lot of time editing the manuscript and his corrections only made the manuscript better. Further, I would like to mention the career advice and help I received from Eugene and Angel which I will remain forever grateful for.

An experiment without a sample is no experiment at all. TNS is extremely difficult to grow and making rigid stable TNS samples with good surface quality is an incredible feat. Hence, I acknowledge Junbo Zhu, Josh Wakefield and Joe Checkelsky for providing us with top quality TNS single crystals.

Plasmonic InAs metamaterials comprised a substantial part of my PhD studies which eventually led to a beautiful paper. I thank Xiaoguang Zhao and Xin Zhang for providing excellent samples, and Fu Deng for the simulations.

In the last phase of my PhD, Rick and I have separately given multiple talks on my results on TNS, a putative excitonic insulator at various seminars and colloquiums at other schools and conferences. During this time, we have received questions/suggestions/comments from many ultrafast experts which has helped us improve our manuscript. I want to thank Anshul Kogar, Mengkun Liu, David Hsieh, Andrew Millis, Prineha Narang, Alfred Zong, Michael Zürch, Tony Heinz, Aaron Lindenberg, Patrick Kirchmann, Jonathan Sobota, Alessandra Lanzara, Edoardo Baldini, Andrea Cavalleri, Daniele Fausti, Ryo Shimano, Takashi Oka, Patrick Kirchmann, Jonathan Sobota, Liuyan Zhao, Fahad Mahmood, Dante Kennes, Michael Schüler, and Aditya Sood. I also thank my friends in ultrafast community: Zhuquan Zhang, Batyr Ilyas, Honglie Ning, Xinwei Li, Alex von Hoegen, Emre Ergeçen, Yi Lin, Carina Belvin, Omar Mehio, Hugo Wang, Hari Padmanabhan, Jonathan Curtis, and Rishi Bhandia for

fruitful discussions. In particular, I am grateful to Zhuquang for helping me address some important questions in the manuscript. I thank Ki-Yong Kim for his valuable advice regarding broadband THz generation using the two-color laser plasma scheme which helped me to add polarization control capabilities to our setup. Furthermore, I would like to thank Alfred Zong, Vladimir Stoica, and Alon Ron for valuable career advice.

Life without friends would be a boring one. Moral support from my close friends has been crucial during the pandemic. I express my gratitude to Ahmed (Naguib), Rudy, Totti (Yueqi) and Yuqi. Having friends like them makes my life a meaningful one. Ahmed and Rudy were extremely kind roommates to me, and never made me feel that I was far away from home. I also thank my other roommate Abdoulie for being so kind to me and for being such a good friend. I would like to thank Yiheng, Mac (Huang), Natalie, Sau Yee, Kazuki, Haik and Talin for being there for me and never losing faith in me. And special thanks to Shishimanu (Mueed) for his constant motivation and insight of experimental physics. I thank my other friends, much of whom I met through UCSD MSA or Islamic Center of San Diego: Feroze uncle, Hammad, Shaikh, Zahid, Galib, Mehrab, Raihan, Gajanan, Oni, Siam, Iftekhar, Adib, Ahmed (Taha), Eslam, Ahmed (Ismail), and Amer.

In every chapter of my life, my family has provided me with constant love and support. Without them, I would not be here, and no word can describe my gratitude. I want to thank my parents Ferdousi and Jahur for raising me and giving me the values and attributes needed to prosper in life. I want to thank my sister Sadia and brother-in-law Arif for always supporting me in my endeavors, encouraging me to never give up, and for being my role models. I also thank my nieces Arisha and Elif for being bundles of joy and for always bringing a smile to my face. I also thank my parents-in-law for treating me like their son. I am grateful to my siblings-

in-law: Badrul, Sidra, Qamrul and Mehreen for welcoming me into their beautiful family. Owing to their love and kindness, Michigan has become another home to me.

And finally, my lovely wife, Mobashira. She is the best thing that has happened to my life and without her support, not a single letter of this thesis would have been written. If I ever feel dejected and hopeless, her kind words would rejuvenate me. She can bring a smile on my face even during the hardest times. She is my constant companion, the best of my best friends, the sunshine of my life. She has been with me throughout the arduous process of manuscript writing, submission, review process, rebuttal and kept motivating me to remain calm and never give up. It is beyond description how much she has helped me get through the tedious writing process while herself going through pregnancy. A life without her would be an empty one. She has brought all the good things into my life. And hence, I dedicate this thesis to her.

Chapter 4, in part, is currently under review for publication of the material. Sheikh Rubaiat Ul Haque, Marios H. Michael, Junbo Zhu, Yuan Zhang, Lukas Windgätter, Simone Latini, Joshua P. Wakefield, Gu-Feng Zhang, Jingdi Zhang, Angel Rubio, Joseph G. Checkelsky, Eugene Demler, and Richard D. Averitt. The dissertation author was the primary researcher and author of this material.

Chapter 5, in part, is currently under review for publication of the material. Marios H. Michael, Sheikh Rubaiat Ul Haque, Lukas Windgätter, Simone Latini, Yuan Zhang, Angel Rubio, Richard D. Averitt, Eugene Demler, and Richard D. Averitt. The dissertation author was the primary researcher and author of this material. The remaining part is a reprint of work published in *Physical Review B* **105**, 174301 (2022). In both cases, the thesis author is the coauthor of this material.

Vita

2017 Bachelor of Engineering in Applied Physics, The University of Tokyo

2021 Master of Science in Physics, University of California San Diego

2023 Doctor of Philosophy in Physics, University of California San Diego

Publications

'†' defines equal contribution.

1. **Haque, S. R. U.**, Michael, M. H., Zhao, J., Zhang, Y, Windgätter, L, Latini, S., J. P Wakefield, J. P., Zhang, G.-F., Zhang, J., Rubio, A., Checkelsky, J. G., Demler, E. & Averitt, R. D., Terahertz parametric amplification as a reporter of exciton condensate dynamics in Ta_2NiSe_5. *Under review* (2022).

2. Michael, M. H., **Haque, S. R. U.**, Windgätter, L., Latini, S., Zhang, Y., Rubio, A., Averitt, R. D. & Demler, E., THz amplification of optical reflection after electron photoexcitation in Ta_2NiSe_5. *Under review* (2022).

3. Michael, M. H., Först, M., Nicoletti, D., **Haque, S. R. U.**, Zhang, Y., Cavalleri, A., Averitt, R. D., Podolsky, D. & Demler, E., Generalized Fresnel-Floquet equations in driven quantum materials. *Physical Review B* **105**, 174301 (2022).

4. Zhang, J†, **Haque, S. R. U.**†, Zhao, X.†, Deng, F.†, Zhang, G.-F., Zhang, Y., March, S. D., Maddox, S. J., Bank, S. R., Zhang, X. & Averitt, R. D., Ultrafast octave tuning of phonon-augmented terahertz surface plasmon. *To be submitted* (2023).

5. Huang, Y., Kaj, K., Chen, C., Yang, Z., **Haque, S. R. U.**, Zhang, Y., Zhao, X., Averitt, R. D. & Zhang, X., Broadband terahertz silicon membrane metasurface absorber. *ACS Photonics* **9**, 1150-1156 (2022).

6. Keiser, G. R., Karl, N., **Haque, S. R. U.**, Brener. I., Mittleman, D. M. & Averitt, R. D., "Structurally tunable nonlinear THz metamaterials using broadside-coupled split-ring resonators" *AIP Advances* **11**, 095103 (2021).

7. Island, J. O., Kissin, P., Schalch, J., Cui, X., **Haque, S. R. U.**, Potts, A., Taniguchi, T., Watanabe, K., Averitt, R. D. & Young, A. F., Chip-scale terahertz emission and modulation with integrated graphene junctions. *Applied Physics Letters* **116**, 161104 (2020).

8. Zhang, J., Stoica, V., Gu, K., Teitelbaum, S., Zhang, G.-F., **Haque, S. R. U.**, Ofori-Okai, B., McLeod, A. S., McChesney, J., Rodolakis, F., Basov, D. N., Reis, D. A., Rondinelli, Freeland, J. W. & Averitt, R. D., Photoinduced homogeneous metastable states by single-shot control of charge order and exchange interaction in manganite thin films. *In preparation.*

9. Deng, F., **Haque, S. R. U.**, Zhang, G.-F., Averitt, R. D & Zhang, J., Observation of temporal Gouy phase. *In preparation.*

10. Deng, F., **Haque, S. R. U.**, Zhao, X., Zhang, Y., March, S. D., Maddox, S. J., Bank, S. R., Zhang, J. & Averitt, R. D., J. Zhang, Ultrafast optical tuning of an absorption mode in GaAs-InAs interface. *In preparation.*

Field of Study

Time-resolved pump-probe and THz spectroscopy, nonlinear optics, light-matter interactions, light-induced states, optical tuning of quantum materials, Fresnel-Floquet theory, nonequilibrium dynamics, excitonic insulators, charge density wave, plasmonic and 2D materials etc.

Abstract of the Dissertation

Optical Signatures of Exciton Condensate Dynamics Studied by Broadband Terahertz Spectroscopy

by

Sheikh Rubaiat Ul Haque

Doctor of Philosophy in Physics

University of California San Diego, 2023

Professor Richard D. Averitt, Chair

Condensates are a hallmark of emergence in quantum materials with superconductors and charge density waves as prominent examples. Excitonic insulators (EI) present an intriguing addition to this library, exhibiting spontaneous condensation of electron-hole pairs in the vicinity of an insulator-semiconductor phase transition. Across this library, canonical condensate observables can be obscured through parasitic coupling to various degrees of freedom. Broadband terahertz (THz) spectroscopy can disentangle such obscurants through temperature and fluence dependent measurements of the quantum dynamics. We target Ta_2NiSe_5 (TNS) a putative room-temperature EI where electron-lattice coupling complicates

the identification of excitonic correlations. The first three chapters cover a concise background of strongly correlated materials, the power of ultrafast spectroscopy as a tool to unveil novel physics of condensed matter systems, properties of TNS as an EI, experimental techniques built and developed by myself. In the following chapter, I report the optical signatures of exciton condensate dynamics in TNS where a pronounced increase in the THz reflectivity manifests following photoexcitation showing a BEC-like temperature dependence. This occurs well below the structural transition temperature (326K), suggesting a novel approach to monitor exciton condensate dynamics stripped of residual static interactions. Nonetheless, dynamic condensate-phonon coupling remains as evidenced by peaks in the enhanced reflectivity spectrum at select infrared active phonon frequencies. Indeed, the origin of the parametric reflectivity enhancement arises from phonon squeezing upon condensate perturbation, validated using Fresnel-Floquet theory and DFT calculations. Our results highlight that coherent order parameter dynamics can, in the presence of signal photons, drive parametric stimulated emission with concomitant possibilities that includes novel entangled photon sources at terahertz frequencies.

Chapter 1 Strongly Correlated Materials & Ultrafast Optical Spectroscopy

1.1 Strongly correlated materials

One of the most recurring themes in modern condensed matter physics is the study of strongly correlated materials. These materials do not exhibit any dominant energy scales and different degrees of freedom, i.e., charge, lattice, orbital and spin interact with each other. This multifaceted interaction between different DOFs eventually leads to an extremely rich energy landscape and interesting collective properties.

1.1.1 Interplay between degrees of freedom

From a perspective of materials science, correlated materials provide a very fertile ground of novel properties not manifested in weakly-correlated materials where single-particle behavior dominates the physics. In this case, simpler theoretical formalism and band theory can well explain all the electronic properties. However, the presence of d and f orbitals make it impossible for band theory to give a clear idea of the microscopic picture. In the complex band structure, a lot of peaks caused by multi-particle correlation occur and thus, one must take into account this correlation effect for both theoretical and experimental interrogation of these materials.

Figure 1.1 shows us a schematic picture of the interplay between charge, orbital, lattice and spin. These are the four key ingredients of strongly correlated materials. When no interaction is present, it is relatively simple to describe the physical phenomena of the materials in terms of individual DOFs. In addition, the electronic behavior can be described by a simple Hamiltonian. On the contrary, for strongly correlated materials, these DOFs interact with each other, conspiring together to demonstrate new quantum phases. This leads to an extremely complicated phase

diagram as well as a high level of susceptibility to external excitation [1]. Furthermore, a free-electron Hamiltonian description is no longer valid and more complicated Hubbard model Hamiltonian is the starting point to delve into the electronic and structural properties of the system.

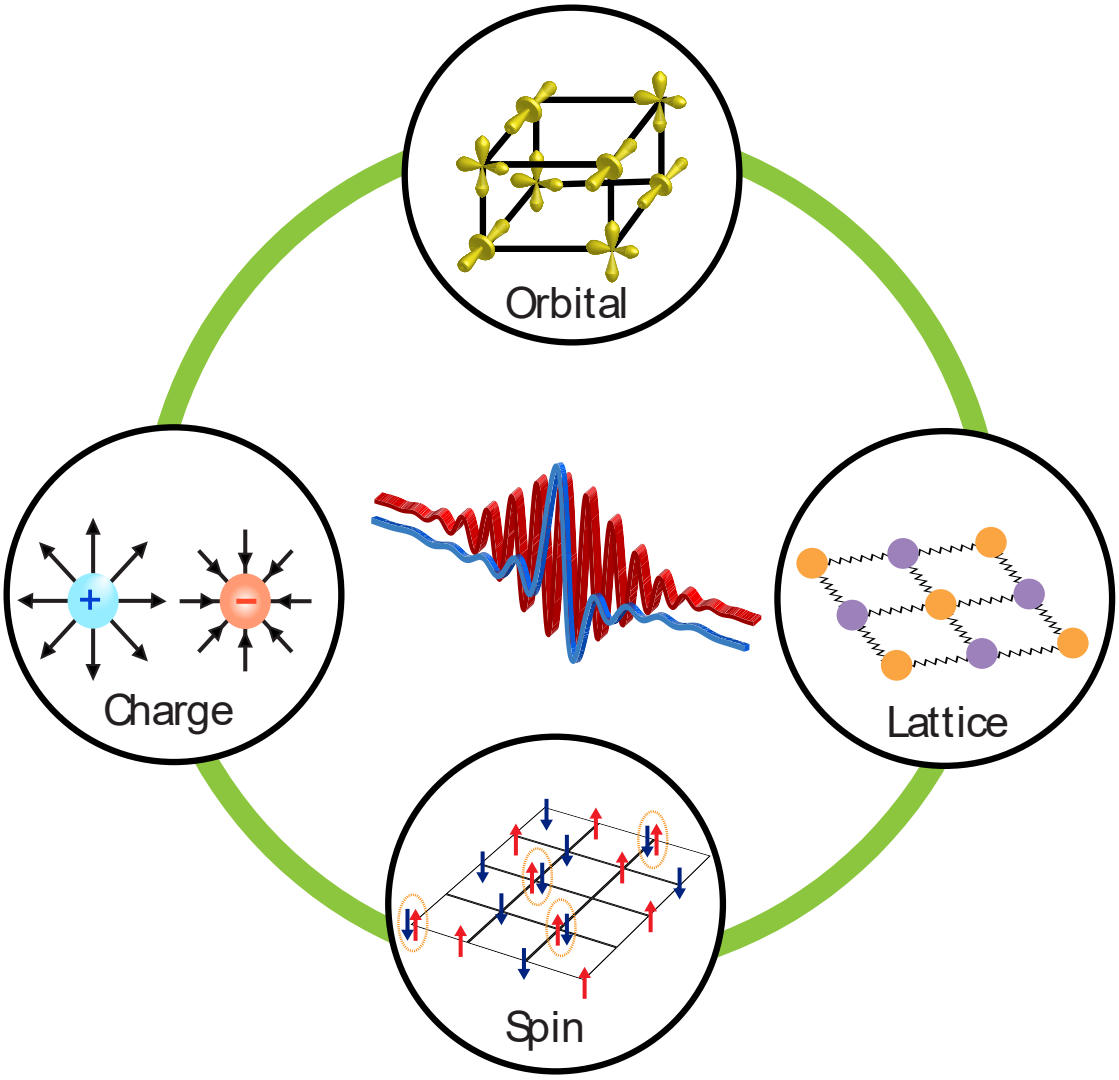

Figure 1.1: A schematic of different DOFs: charge, orbital, lattice and spin. When they interact together, novel quantum phases arise, leading to a rich phase diagram and energy landscape. Conventional band theory is not effective to describe the correlated properties and new approaches are needed to investigate the electronic and structural properties of the materials.

1.1.2 Spontaneous symmetry breaking

Along with the complex interplay leading to exotic quantum phases, one other aspect of correlated materials is spontaneous breaking of symmetry. Theoretically speaking, a spontaneous symmetry breaking is accompanied by a phase transition. That is, the different quantum phases in strongly correlated materials also indicate the possibility of transitioning from one phase to another concomitant with symmetry breaking incidents. Some good examples of correlated materials are superconductors (SC), charge density waves (CDW), excitonic insulators (EI), ferromagnets (FM), antiferromagnets (AFM) and Mott insulators. In superconductors, a $U(1)$ symmetry breaking causes the cooper pairs to form below a certain temperature which is known as the transition temperature T_C [2]. This opens up the SC gap Δ in accordance with Anderson-Higgs mechanism [3]. The gap functions as the complex order parameter of superconductivity. Above T_C, the symmetry is recovered and hence, the gap vanishes. The material is not superconducting anymore then and it behaves as a normal metal.

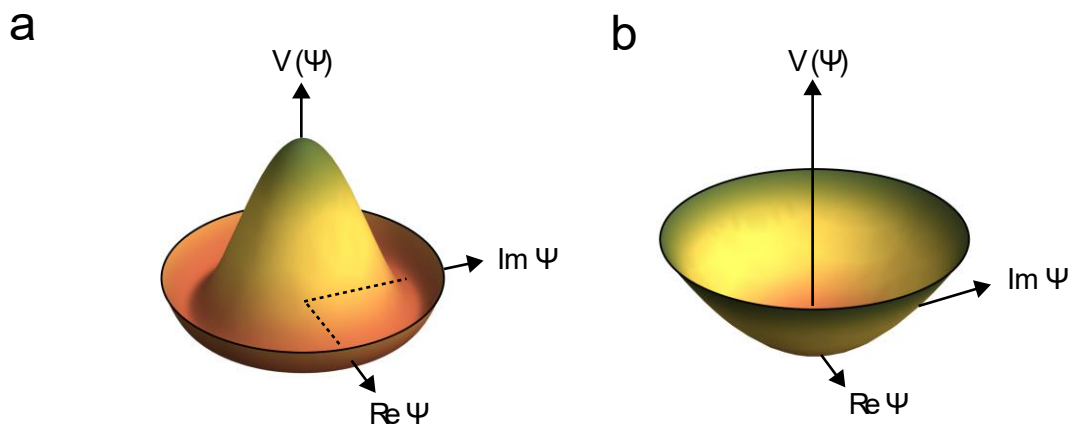

Figure 1.2: Spontaneous symmetry breaking in terms of GL theory. **a**, below T_c the symmetry is broken, and the potential energy surface resembles a Mexican hat with infinite number of solutions for the real and imaginary parts of the complex order parameter Ψ. **b**, Above T_c, where the real and imaginary parts of the order parameter are both zero.

Similarly, for CDW, a translation symmetry is broken below T_C, resulting in the electrons and holes aligning themselves in a way that the spatial distribution of the charge density looks like a wave followed by a gap opening due to the electron-hole interaction [4, 5]. Moreover, when a continuous symmetry is broken, gapless modes can arise as Goldstone modes [6]. This can well be captured by a Ginzberg-Landau free energy description as shown in Fig. 1.2 which plots the potential energy $V(\Psi)$ as a function of the complex order parameter Ψ.

Below T_C, the symmetry is broken and thus, the potential energy surface looks like a Mexican hat (Fig. 1.2a). Here, there are numerous solutions for the ground state with the minimum energy. However, above T_C, the symmetry is not broken anymore, and the energy surface looks like a paraboloid. For the GS, the real and imaginary parts of the order parameter are zero. This GL description gives us a glimpse into the correlation-induced complex energy landscape and phase space. Further, these phases can compete or cooperate with each other, for example, in YBCO superconductors, superconductivity and charge density wave compete with each other [7]. Another example is that electrons from FeSe and phonons from $SrTiO_3$ cooperate to enhance superconductivity in $FeSe/SrTiO_3$ [8].

It is evident from this description that with the complexity brought by the electron correlation and with myriad phases cooperating or competing with each other, it is difficult to investigate correlated materials both theoretically and experimentally. Density Functional Theory (DFT) can only be used for GS calculation. Local Density Approximation (LDA) computes the exchange-correlation energy functional from a uniform electron gas model and gives band structure information for non-interacting systems while electron correlation is not explained. Dynamic Mean Field Theory (DMFT) describes the correlation effects and combining DMFT and

LDA can be effective in interpreting the strongly correlated system given their complementary nature and versatility [9].

1.1.3 Experimental Interrogation

A variety of experimental techniques can be used to study strongly correlated materials. This includes electronic transport, specific heat measurements, scanning tunneling microscopy (STM), magnetic susceptibility measurement, nuclear magnetic resonance (NMR), angle-resolved photoemission spectroscopy (ARPES), tr-ARPES, Fourier transform infrared spectroscopy (FTIR) and various types of optical spectroscopy covering terahertz (THz), IR, visible and UV and several X-ray scattering methods such as Inelastic X-ray scattering (IXS), Resonant inelastic X-ray scattering (RIXS) and X-ray diffraction (XRD). These techniques can give us a whole picture of the structural, electronic, magnetic and optical properties of materials. Of particular interest is optical spectroscopy which also is a central focus in this thesis.

Optical spectroscopy has proven to be a versatile role in studying correlated materials since several correlated phenomena and their intrinsic timescales happen to be in the optical frequency region [1]. Therefore, optical probes can study the interacting DOFs as well as the coupling between them that gives rise to the diverse quantum phases on a very fast timescale (ps or fs scale). In the following section, we will describe the versatility of ultrafast optical spectroscopy and their prospect in unraveling the novel phases in correlated solids.

1.2 Ultrafast Optical spectroscopy

With the advent of coherent photon sources and revolutionary discoveries in the field of laser technology, light has brought itself at the forefront of experimental condensed matter physics and materials science. According to special theory of relativity, light moves faster than anything

in any reference frame, hereby making it an immensely powerful tool to acquire information about physical phenomena that occur at very short time scales. The whole electromagnetic spectrum covers a broad range of frequencies from RF and THz to UV with their corresponding wavelength ranging from nanometer to millimeter scale. This enables us to access physics at the atomic/molecular level and gives us a vivid microscopic picture of the interplay of different DOFs in strongly correlated materials [10-12].

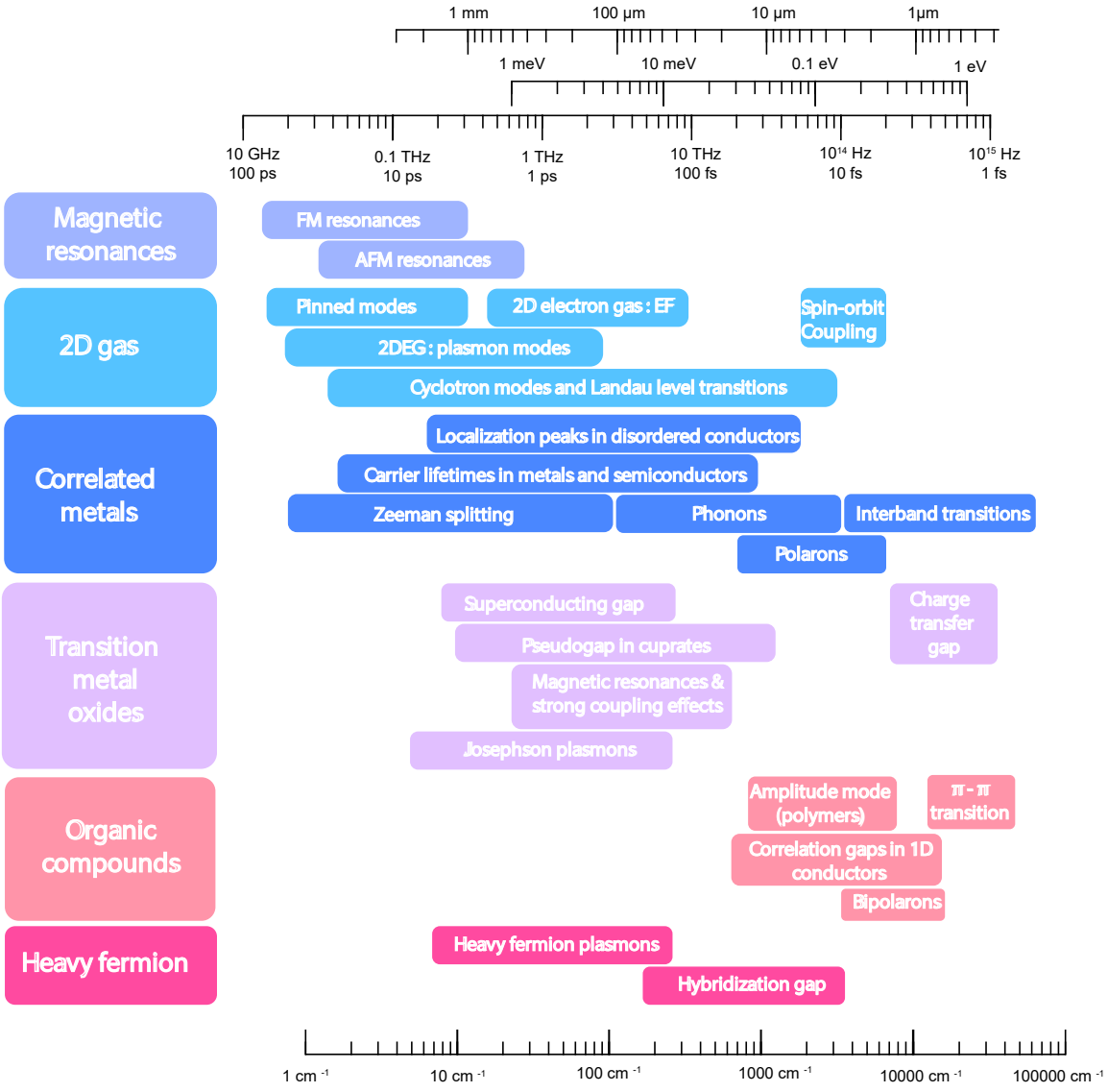

Figure 1.3: Pictorial representation of characteristic energy and time scales in correlated electron systems. Adapted from ref. [1].

1.2.1 Fast timescale & fast changes due to perturbations

Figure 1.3 displays the schematics of the energy and timescales of a wide range of correlated electron systems. As shown in the figure, numerous correlated phenomena and elementary excitations occur in the THz and IR regime and the timescales corresponding to ps and fs regime. Consequently, optical spectroscopy can spectrally access these excitations since the timescale of low energy electromagnetic spectrum matches with the intrinsic timescales of these excitations. Moreover, collective excitations arise from the interaction between individual DOFs whose spectral fingerprints can be monitored via optical spectroscopic measurements. Also, peaks in the optical reflection or absorption spectrum or optical conductivity can help us identify specific features such as phonon, gap, quasiparticle peak etc.

Additionally, changes in the optical properties with small perturbation can be quite large owing to correlated materials' higher susceptibility to external drives. Therefore, ultrafast optical spectroscopy can investigate nonequilibrium dynamics of the correlated electron systems on a ps timescale following a perturbation with current, voltage bias or photoexcitation. Strongly correlated materials host numerous quantum phases and it is imperative not only to study these phases, but also the transition pathways between them. This is where optical spectroscopy comes in handy thanks to its spectral access the fundamental time dynamics and can monitor relevant energy excitation such as coherent Drude response in transition metal oxides or gapped phenomena in superconductors [1-3].

1.2.2 Time-integrated (static) & time-domain spectroscopy

For most spectroscopic experiments, either reflection or transmission of the optical beam from the sample is measured, in order to determine the real and imaginary part of the complex

refractive index n and κ. The relation between real and imaginary parts complex dielectric constant $\varepsilon(\omega) = \varepsilon_1(\omega) + i\varepsilon_2(\omega)$ and refractive index is given in the following.

$$\varepsilon_1 = n^2 - \kappa^2. \tag{1.1}$$

$$\varepsilon_2 = 2\, n\, \kappa. \tag{1.2}$$

The starting point to extract complex optical parameter is the Maxwell's equation and Ohm's law from which frequency-dependent complex optical conductivity $\sigma(\omega) = \sigma_1(\omega) + i\sigma_2(\omega)$ can be determined. The real and imaginary parts of $\sigma(\omega)$ can be written as,

$$\varepsilon(\omega) = \varepsilon_\infty + \frac{i\sigma(\omega)}{\omega}, \tag{1.3}$$

$$\sigma_1(\omega) = \omega\, \varepsilon_2(\omega), \tag{1.4}$$

$$\sigma_2(\omega) = \omega[\varepsilon_\infty - \varepsilon_1(\omega)], \tag{1.5}$$

where ε_∞ is the high frequency dielectric function that arises from inter-band transitions. By knowing one optical parameter, one can calculate other quantities. The optical parameters can be measured by reflectivity/transmittance, ellipsometry and time-domain spectroscopy. In reflectivity measurements, for normal incidence the reflectivity R is given by the following equation,

$$R(\omega) = \left|\frac{\tilde{n}(\omega) - 1}{\tilde{n}(\omega) + 1}\right|^2, \tag{1.6}$$

where $\tilde{n}(\omega) = n(\omega) + i\kappa(\omega) = \tilde{n}(\varepsilon_1, \varepsilon_2)$. Using the Kramers-Kronig (KK) transformation from causality we obtain,

$$\varepsilon_1(\omega) = \frac{1}{\pi} p \int_{-\infty}^{+\infty} \frac{\varepsilon_2(\omega')}{\omega' - \omega}\, d\omega'. \tag{1.7}$$

$$\varepsilon_2(\omega) = \frac{1}{\pi} p \int_{-\infty}^{+\infty} \frac{\varepsilon_1(\omega')}{\omega' - \omega}\, d\omega'. \tag{1.8}$$

Using (1.1) — (1.7) and then performing the KK transform, we can assign values for both real and imaginary parts of dielectric constants. However, this method has some serious drawbacks

since it lacks information throughout the whole frequency region. As a result, KK transform can yield erroneous results owing to the fact that KK integral requires $-\infty$ and $+\infty$ as lower and upper bounds respectively, which is not experimentally feasible.

To resolve this problem, time-domain experiments have been instrumental in extracting the optical parameters as a function of time. In a time-domain setup, the electric field waveform $E(t)$ of a laser pulse is directly measured. Let $E_{ref}(t)$ be the time-domain electric field signal from a reference and $E_{sample}(t)$ be the signal from the sample. Fast Fourier transform (FFT) enables us to calculate $E_{ref}(\omega)$ and $E_{sample}(\omega)$, the FFT signals in frequency domain. Note that, $E(\omega)$ is a complex quantity and depicts a complex spectrum in frequency domain ω. Thus, it contains both amplitude and phase since any complex number z can be written in the form $z = z_0 e^{i\phi}$, where z_0 and ϕ are the amplitude and phase, respectively.

Dividing $E_{sample}(\omega)$ by $E_{ref}(\omega)$, one can extract the absolute amplitude and phase change due to the sample, with which the complex refractive index can be calculated without using KK transform. It is an excellent technique in transmission measurements, without any artificial phase shift and can be well adapted to reflectivity experiments with phase correction. However, since time-domain spectroscopy uses another much shorter optical pulse (gate beam) to convolute with the target pulse, it is always crucial to make sure that gate pulse is approximately a Dirac delta function, in comparison with the target pulse length. As a consequence, the current limit of ultrashort pulse generation (< 10 fs) restricts the spectral range (30 THz), beyond which a precise measurement of electric field waveform cannot be done with electro-optic (EO) sampling method [13-16]. Nevertheless, 1 – 30 THz is a very broad spectral range, enabling us to probe a huge number of correlated phenomena and collective modes.

1.2.3 Time-resolved spectroscopy of correlated materials

Time-domain spectroscopy enables us to measure the optical constants without any phase artifacts, thereby offering insight into the GS band structures and collective modes (phonon, magnon, CDW, SDW, SC gap, pseudogap) and free carrier response [1, 11, 17]. In contrast, time-resolve spectroscopy provides information about the optical parameters under nonequilibrium conditions. In materials with strongly interacting DOFs, ultrafast time-resolved spectroscopy can monitor the time evolution of the coupling between DOFs at a very fast timescale in the presence of an external photoexcitation drive and can provide enlightening insight in understanding light-matter interaction.

With the development of femtosecond laser technology, ultrafast spectroscopy can enable to multiple nonequilibrium processes such as generation of a nonequilibrium distribution of electrons, electron-electron thermalization, electron-phonon coupling, ballistic transport, pair breaking and recovery in superconductors [18]. This is shown in Fig. 1.4 where sub 100 fs pump excitation from an 800 nm NIR pulse generated form a Ti:sapphire laser results in an inhomogeneous distribution of electrons. The photoinduced changes in reflection $\Delta R/R$ (or transmission $\Delta T/T$)can be written as,

$$\frac{\Delta R}{R} = \frac{\partial lnR}{\partial \varepsilon_1}\Delta\varepsilon_1 + \frac{\partial lnR}{\partial \varepsilon_2}\Delta\varepsilon_2, \tag{1.9}$$

where $\Delta\varepsilon_1$ and $\Delta\varepsilon_2$ are the photoinduced changes in the real and imaginary parts of the dielectric function. Prior to photoexcitation, the electron and lattice temperature are the same, that is, $T_e = T_L$. Following photoexcitation, nonthermal electron distribution thermalizes to a hot Fermi distribution. The large difference between the electronic and lattice specific heat ($C_e \ll C_L$) allows for the preferential excitation of the electron gas by absorption of the laser pulse. As a result, electron-electron thermalization occur and electrons reach a much higher temperature than the

lattice, leading to the rise in $\Delta R/R$. Afterwards, electrons go back to the equilibrium distribution and reach thermal equilibrium through electron-phonon coupling. During this stage, $\Delta R/R$ exponentially decays back to equilibrium, electron gas loses its energy and thermalizes with the lattice. After a few ps, a local equilibrium will be reached, and electrons and phonons return to the initial equilibrium temperature (See Fig. 1.5).

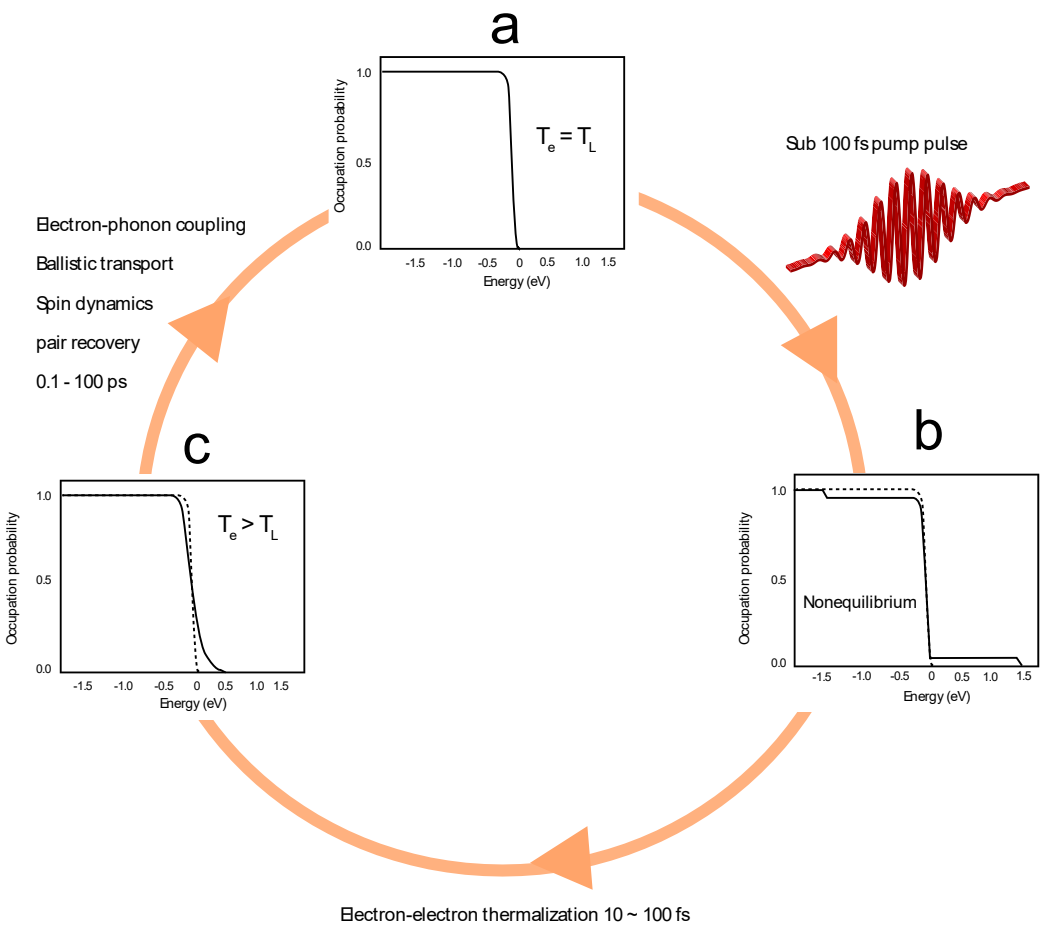

Figure 1.4: Schematic depiction of ultrafast dynamics in correlated materials with femtosecond spectroscopy. **a**, Electrons, lattice and spins are in thermal equilibrium before photoexcitation, **b**, a photoexcited nonthermal electron distribution followed by electron-electron thermalization. **c**, Relaxation to thermal distribution with excess energy transferred to other DOFs. Adapted from ref. [10].

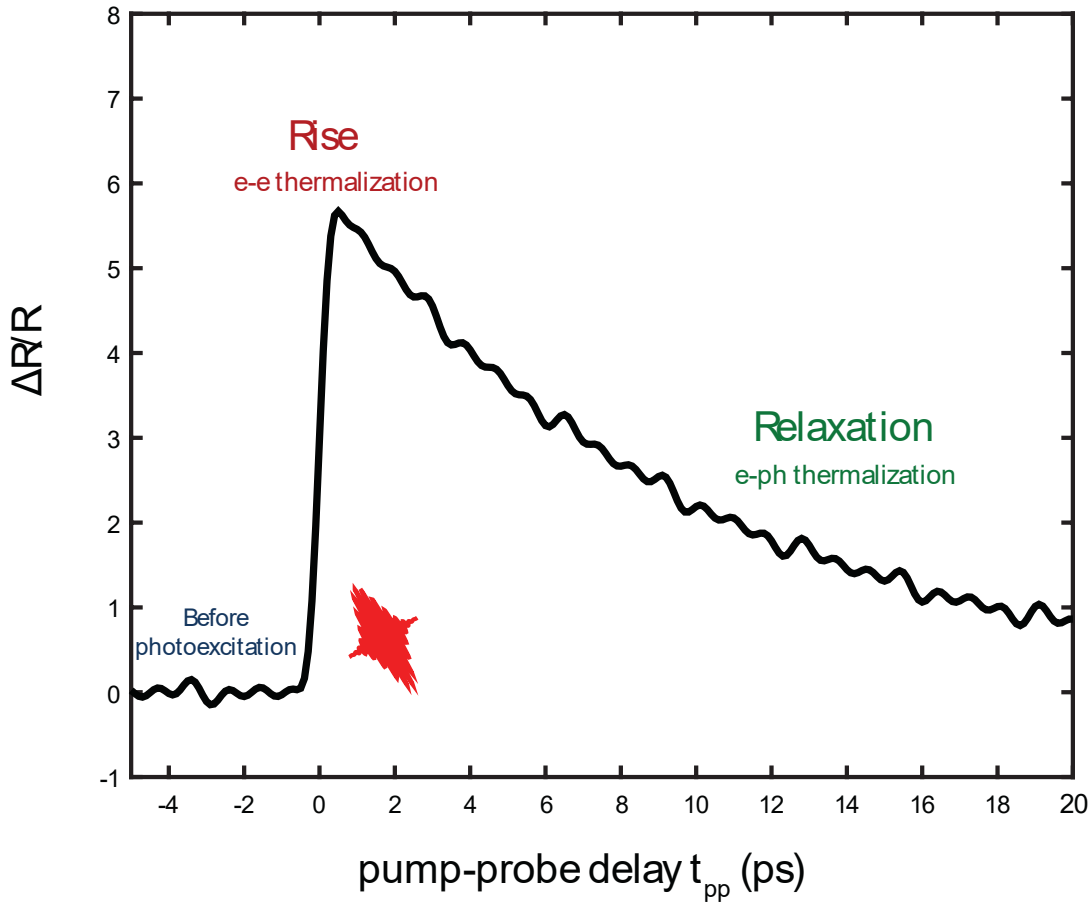

Figure 1.5: Illustration of a typical pump-induced process. $\Delta R/R$ stands for the transient change in reflectivity due to photoexcitation. Before $t_{pp} = 0$, pump has not arrived yet and so the system is in thermal equilibrium. At $t_{pp} = 0$, photoexcitation takes place and $\Delta R/R$ reaches peak due to electron-electron thermalization. After this, the system returns to thermal equilibrium in an exponential decay fashion.

A typical ultrafast spectroscopy employs an excitation pulse (pump) to drive the system out of equilibrium state, another much weaker laser pulse (probe) to probe the induced nonequilibrium dynamics as a function of the time delay between pump and probe. This time delay is labeled as t_{pp}, which is practically the difference between arrival time of pump and probe. When

pump and probe arrive the sample at the same time, $t_{pp} = 0$. On the occasion when probe arrives before probe, $t_{pp} < 0$, and $t_{pp} > 0$ when probe arrives after pump.

Figure 1.6 shows the schematic of an ultrafast pump-probe spectroscopy experiment. A strong pump pulse (red) arrives at the sample and excites it out of its equilibrium state. Following the photoexcitation, a probe pulse (blue) arrives at the sample. The orange arrows indicate the time delay t_{pp}. The detector plots the time trace of the dynamics measured by the probe pulse.

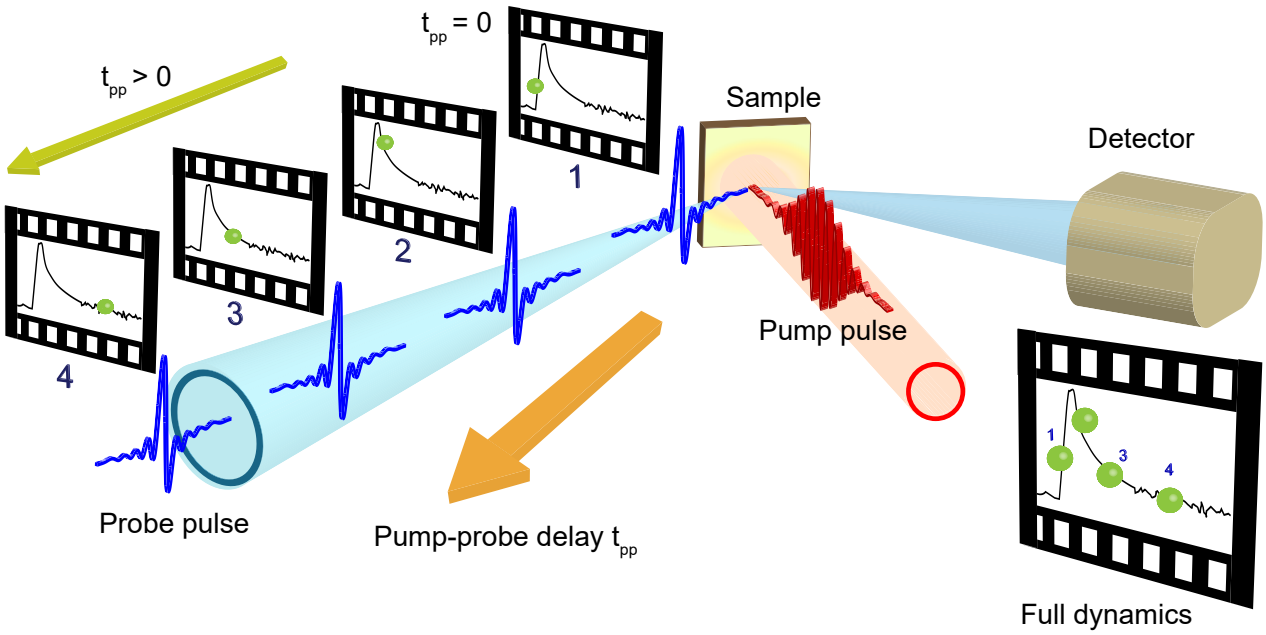

Figure 1.6: Schematic of the ultrafast pump probe spectroscopy. First a pump pulse (red) drives the sample out of equilibrium, followed by a weaker probe pulse (blue). The probe pulse traces the photoinduced dynamics as a function of time delay t_{pp}.

In other words, the probe pulse measures the transient changes in optical parameters which have been perturbed by the pump pulse. Thus, the probe pulse captures the whole photoinduced dynamics in the sample as a function of t_{pp}. The relaxation dynamics are shown in Fig. 1.5 as a cartoon. One thing to be noted is that the relaxation dynamics looks like an exponential decay, in

conjunction with (1.9) and Fig. 1.5. This is how pump-probe spectroscopy enables us to take the "snapshots" of the photoinduced transient states, leading to a clear understanding of the temporal evolution of the nonequilibrium state. Furthermore, it can disentangle the coupled DOFs and offers valuable insight into the fundamental timescale of the electronic and atomic motion, formation or destruction of a CDW or SC condensate and photoinduced phase transition (PIPT).

1.2.4 Access to transient metastable states & photoinduced phases

A new aspect of ultrafast spectroscopy is observation and optical control of novel quantum phases which can pave the way towards revolutionary ultrafast switches and devices based on strongly correlated materials. One such prospective direction is PIPT where photons are used to drive a material far from equilibrium, leading to hidden metastable states. These are often referred to as hidden order state. This hidden order states can have new lattice structure and electronic order that are not accessible by static tuning parameters (temperature, current, voltage bias). Photoexcitation with optical pulses provides a new route to reach the metastable states, allowing one to investigate the dynamic phase transition as well as the relevant order parameter and symmetry-breaking involved in the process.

A prominent example is the discovery photoinduced metastable phase in strained $La_{0.67}Ca_{0.33}MnO_3$ (LCMO) thin film. Unstrained LCMO is an FM metal at low temperature. However, strained LCMO undergoes a paramagnetic (PM) insulator to AFM insulator phase transition with $T_N = 260$ K. In equilibrium, an AFM insulator to PM insulator phase transition can be achieved by tuning the temperature. An AFM insulator – FM metal or a PM insulator – FM metal phase transition is not viable. Nevertheless, single shot 800 nm pulses on strained LCMO can drive the AFM insulator to an FM metal (see Fig. 1.7). This phase transition leads to a long-lived metastable state lasting several hundred picoseconds.

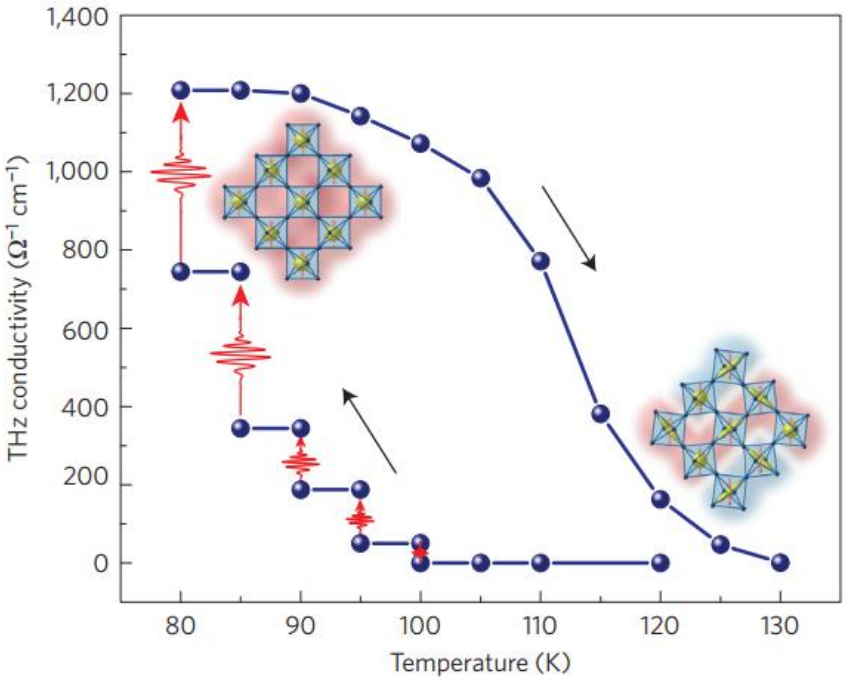

Figure 1.7: Unstrained LCMO film is an FM metal while strained LCMO is an AFM insulator. Starting from the AFM insulator phase, single shot photoexcitation with a 800 nm pulse, followed by cooling can manifest into the FM metal phase. Adapted from ref. [21].

Another important example is photoinduced superconductivity [22, 23] where mid-IR (MIR) femtosecond pulses can ostensibly induce a transient superconductivity above T_C. Fig. 1.8 depicts the transient superconductivity phenomenon in organic superconductor K_3C_{60} ($T_C = 20$ K). In the equilibrium condition below T_C, the real part of optical conductivity $\sigma_1(\omega)$ shows a gap feature and imaginary part of optical conductivity shows a $1/\omega$ divergence, indicative of a superconducting state. Above T_C these features are absent, and the material is in its normal metal state. However, following a MIR pump, $\sigma_1(\omega)$ develops a gap feature and imaginary part of optical conductivity exhibits a $1/\omega$ divergence, much above T_C (25 K and 100 K). Excitation of molecular vibrations is the main driver of this mechanism which, if photoexcited can coherently drive a transition from the HT metallic state into a nonequilibrium transient SC phase.

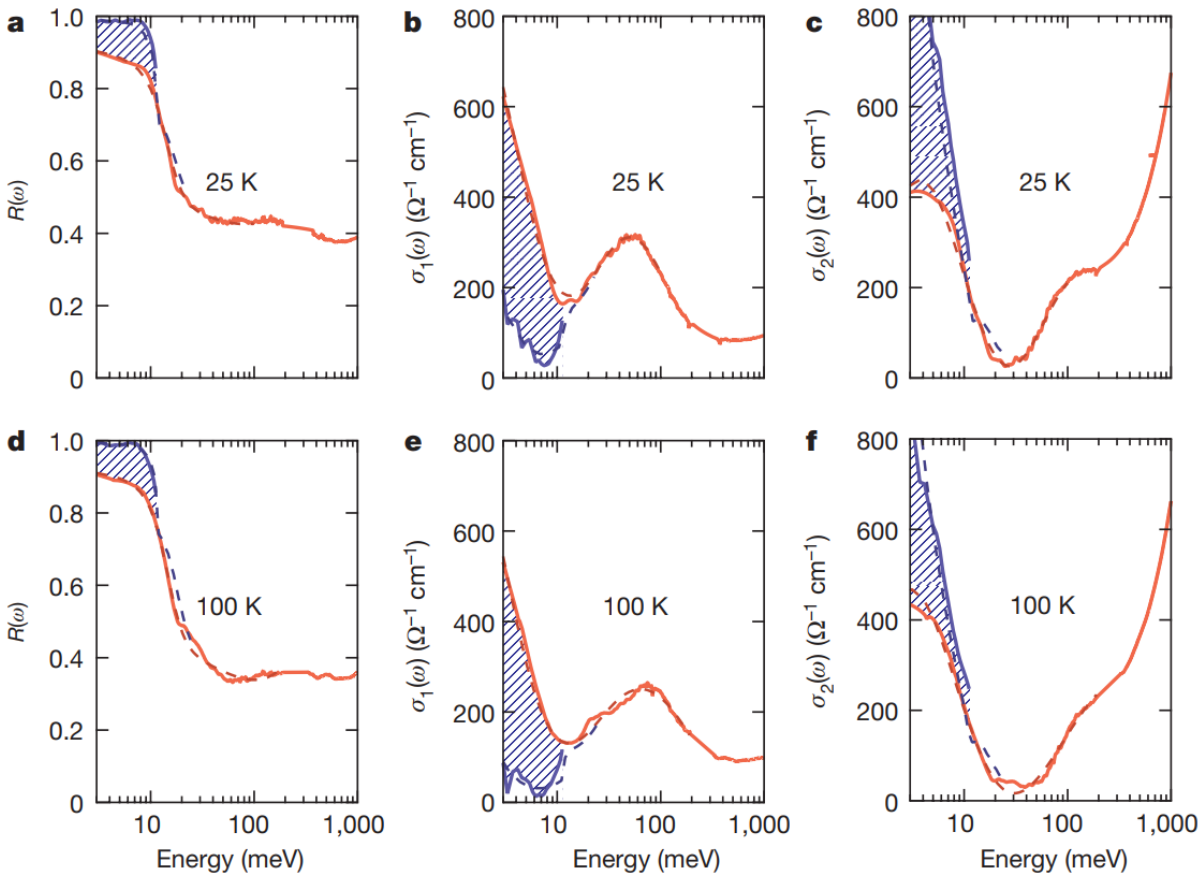

Figure 1.8: Transient superconductivity in K_3C_{60} following a MIR pump. Above T_C, $\sigma_1(\omega)$ and $\sigma_2(\omega)$ displaying gap feature and $1/\omega$ divergence, respectively. Adapted from ref. [23].

1.3 Thesis outline

From this chapter, we can have a grasp of the versatility and power of ultrafast optical spectroscopy as a highly effective tool to look into the photoinduced collective modes, various nonequilibrium phases and light-induced transient states of strongly correlated materials. In the next chapter we will emphasize on the physics of excitonic insulator (EI) and Ta_2NiSe_5 (TNS), a candidate EI material that has recently caught interest of the physicist due to its possibility to host a room temperature excitonic Bose-Einstein condensate (BEC).

In Chapter 3, I will describe the aspects of THz spectroscopy as an important experimental technique to unveil various collective modes and emergent phenomena in correlated materials. Various THz generation techniques will also be discussed along with the optical pump – broadband THz probe spectroscopy system that I designed and built to investigate TNS. This chapter will also cover the data acquisition and data analysis method.

Chapter 4 will focus on the optical pump – broadband THz probe study of TNS. Subsequently, we will describe our results and show that transient reflectivity enhancement at select IR-active phonon frequencies exhibit a BEC-like temperature behavior. We will also show that this parametric effect is the first spectral fingerprint of an exciton condensate dynamics.

In Chapter 5, using the new Fresnel-Floquet theory and phonon squeezing mechanism with support from DFT calculations, we will thoroughly prove that the transient reflectivity enhancement is a parametric process and will establish this as a novel method to track exciton condensation.

In Chapter 6, I will mainly discuss the broader impacts of our results and mention how phonon squeezing can lead to parametric amplification and how it can impact thinking in the field of THz photon sources and nonlinear optics.

Chapter 2 Physics of Excitonic Insulators & Ta_2NiSe_5

2.1 Excitonic insulators

In the previous chapter we provided a detailed account of the strongly correlated electron materials that has attracted the interest of condensed matter physicists over the last few decades. In this chapter we will focus on excitonic insulators (EI). Therefore, we will discuss the basic properties of an exciton as a starting point, and then discuss excitonic insulators and the importance of EIs as a source of Bose condensation at relatively higher temperatures.

2.1.1 Physics of excitons

An exciton is a bound state of an electron and a hole attracted to each other by the Coulomb force. It occurs in insulators and semiconductors and is charge neutral. As a result, it is an elementary excitation that can transport energy without carrying the electric charge.

An exciton can form when a valence band (VB) electron transitions across the band gap to the conduction band (CB). This transition can occur as a result of a photoexcitation with energy higher than the optical band gap. The VB electron absorbs the excitation photon and jumps to the CB, leaving behind a hole. The binding energy between this electron and hole pair is the exciton binding energy E_B and this bound electron-hole pair is called the exciton [24]. Fig. 2.1 shows a very simplistic picture of the formation of exciton from the perspective of a direct band gap semiconductor band structure and a formation of excitation between an electron (orange) and hole (gray).

The bound electron-hole pair in an exciton is analogous to a hydrogen atom. However, there are subtle differences between the two. The electron in the CB is less attracted to the VB hole because of screening. As a consequence, the binding energy of an exciton is less than the hydrogen

atom binding energy and the exciton's size is larger than hydrogen atom. The potential of creating an exciton via light makes it an intriguing candidate in the field of optics and numerous studies have confirmed exciton as an important main mechanism behind optical resonances in solids [25, 26], leaving open the possibilities of optical manipulation of light matter interactions.

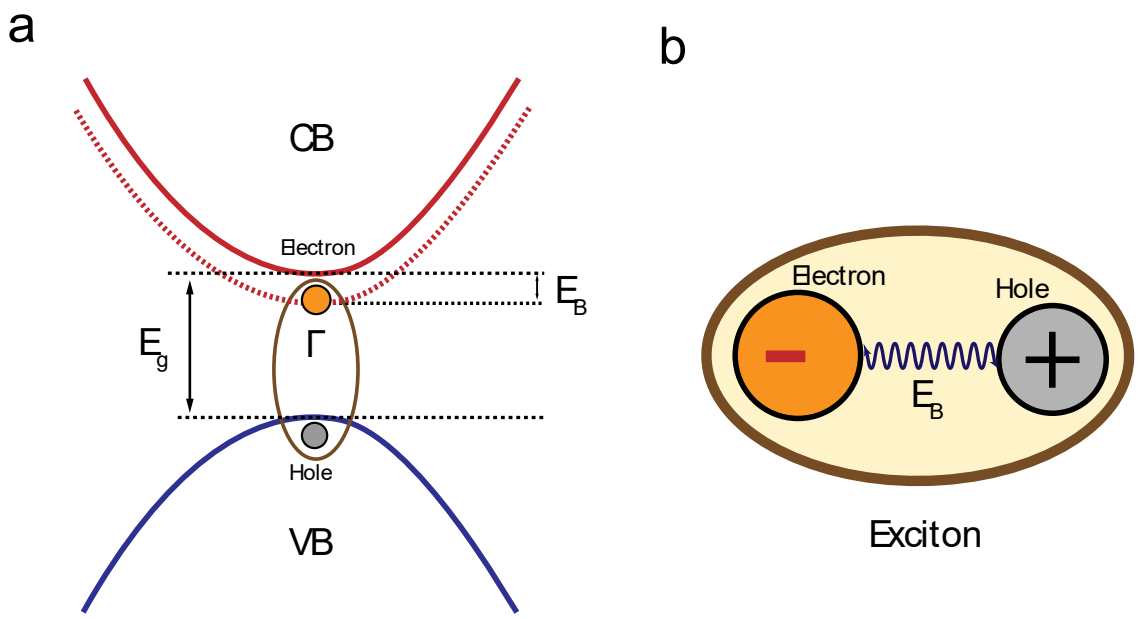

Figure 2.1: a, Schematic of an exciton where an electron (orange) moves to CB, leaving a hole (gray) in VB, the brown ellipse is a guide to the eye and shows the bound pair (band gap E_g). **b**, Exciton binding energy E_B.

There are two types of excitons: (1) Frenkel excitons, and (2) Wannier-Mott excitons. In a Frenkel exciton, bound electron and hole are localized and E_B is relatively large (one the order of 0.1 – 1 eV). It occurs in semiconductors with small dielectric constants, resulting in a higher binding energy [27]. Some examples are alkali halides and organic semiconductors. In contrast to this, a Wannier-Mott exciton is observed in semiconductors with large dielectric constants [28], paving way for the dielectric screening to be dominant over Coulomb attraction between electron

and hole. For this reason, the binding energy E_B is smaller and the exciton radius is larger than the lattice constant. Also, because of the smaller Coulomb attraction and smaller mass, the binding energy is much smaller than the hydrogen atom GS energy (on the order of 0.01 eV). The energy and radius of the n-th quantum level of the exciton particle is given below.

$$E(n) = -\frac{\mu}{m_0 \varepsilon_r^2} \frac{Ry}{n^2}, \tag{2.1}$$

$$r_n = \frac{m_0 \varepsilon_r a_H}{\mu} n^2. \tag{2.2}$$

Here, μ is the reduced mass, Ry is the Rydberg constant, m_0 is the stationary mass of electron, ε_r is the permittivity and a_H is the Bohr radius. In a Wannier exciton, the bound electron-hole pair is not localized at a certain location and can diffuse through the whole crystal lattice as seen in Fig. 2.1b. The red arrow indicates the exciton diffusion direction.

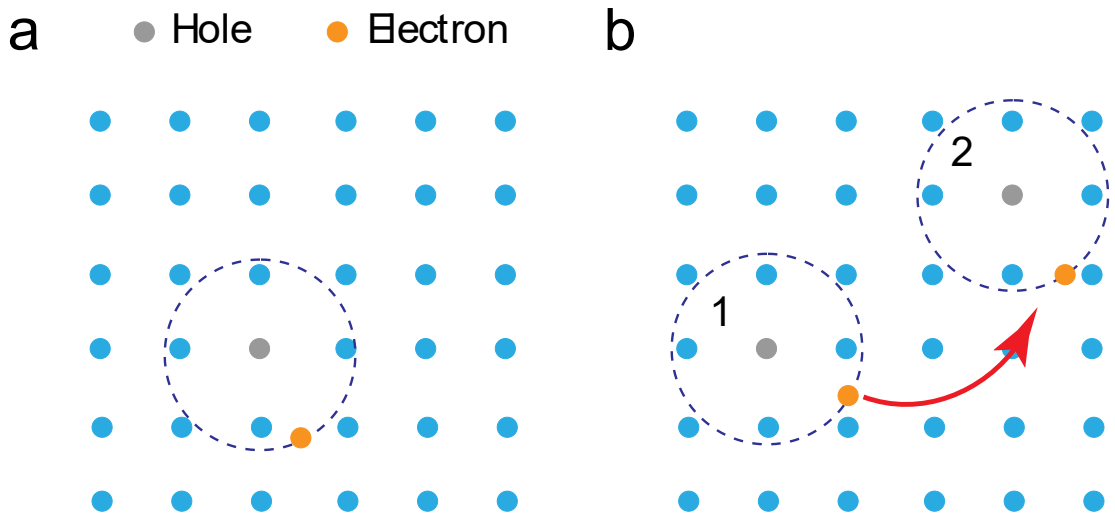

Figure 2.2: a, Frenkel exciton where the bound electron-hole pair is localized in the crystal. **b**, Wannier exciton with the exciton delocalized and moving to different crystal location (from position 1 to 2).

2.1.2 Introduction to Excitonic Insulators

In the previous section, we discussed the basic properties of an exciton and its binding energy from the perspective of band structure. In this section, we will discuss the physical properties of an excitonic insulator (EI). As we have seen from the earlier discussion, when excitons form following the absorption of a photon in a semiconductor with band gap E_g, due to the dielectric screening being stronger compared to the Coulomb attraction, the exciton binding energy becomes smaller than the band gap. This is illustrated in Fig. 2.3a where $E_B < E_g$.

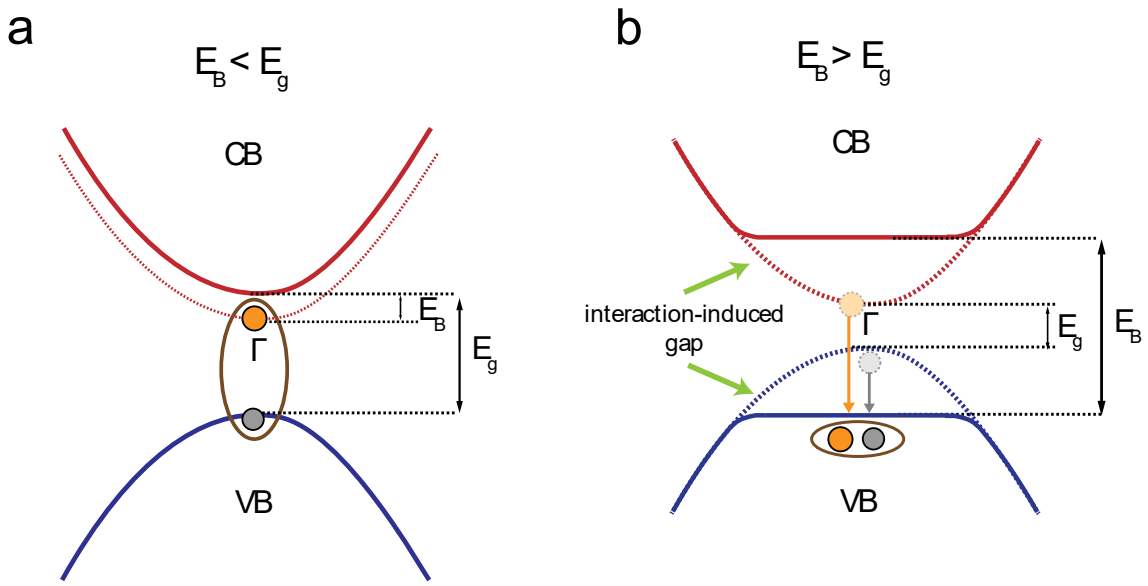

Figure 2.3: a, Exciton formation when $E_B < E_g$. **b**, When $E_B > E_g$, the coulomb interaction develops excitonic instability and a gap opens alongside the bound-electron hole pair formation.

Now let us consider the case of a small or zero band gap semiconductor or a band-overlap semimetal. A very low carrier concentration leads to a weakly screened Coulomb attraction between an electron and a hole. This is how the exciton pair formation occurs. However, if the exciton binding energy E_B is larger than the band gap E_g, then the semiconducting or semimetallic

GS becomes unstable against the coherent exciton formation and the system attains a new GS which is called an excitonic insulator (EI) [29]. The Coulomb interaction favors pair formation and lays the foundation for an interaction-induced insulating gap. In Fig. 2.3b, it is shown that while the semiconductor band gap is E_g, Coulomb interaction between the electron-hole pair creates a renormalization of the gap, and a subsequent gap opening. This new gap equals the exciton binding energy E_B.

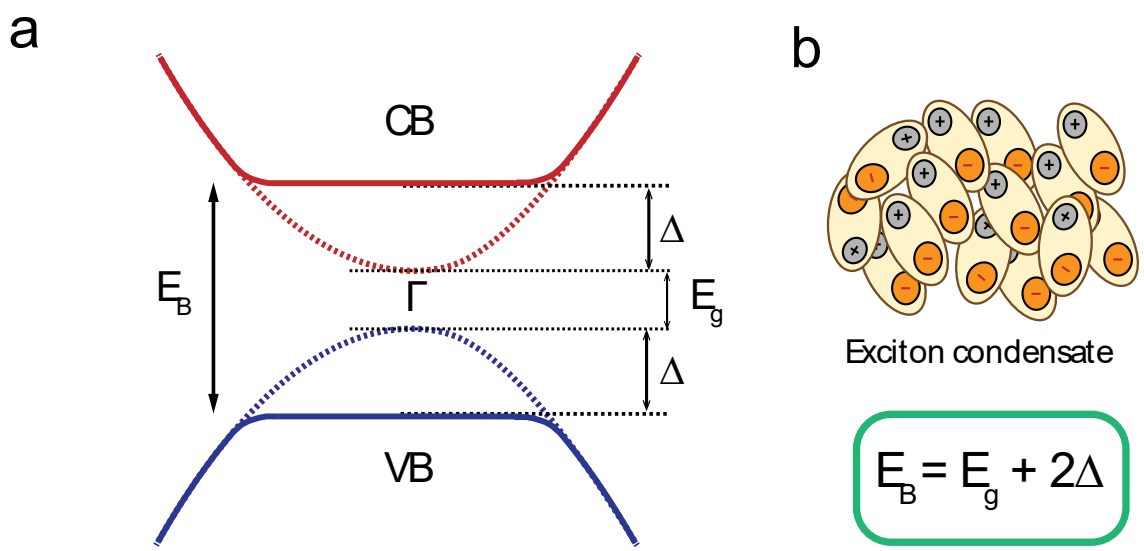

Figure 2.4: a, Exciton formation when $E_B > E_g$, pairing correlation leads to a gap opening. **b**, Exciton condense into a Bose condensate below T_C.

Another hallmark of an EI phase is the formation of an exciton condensate [29]. With the emergence of the EI phase, the excitons tend to arrange themselves in the lowest possible quantum state, which is a signature of a Bose condensate where a large number of Bosons condense into the lowest energy single-particle quantum state. Since exciton condensation involves a phase transition, it has a transition temperature T_C and the pair formation causes an insulating gap to

open. As seen in Fig. 2.4a-b, the binding energy E_B is larger than the optical gap E_g and the new GS has the gap $E_B = E_g + 2\Delta$. Here, 2Δ is the magnitude of the gap opening. From now on, we will use the symbol $\Delta_E = E_B = E_g + 2\Delta$, which stands for the total band gap due to exciton condensate formation [30].

In the vicinity of an insulator-semiconductor phase transition, when an EI phase arises, it leads the excitons to form a Bose-Einstein condensate (BEC) and an interaction-induced insulating gap formation also occurs [31, 32]. On the other hand, excitons may form a BCS-like condensate while undergoing an insulator-semimetal phase transition (see Fig. 2.5 for details).

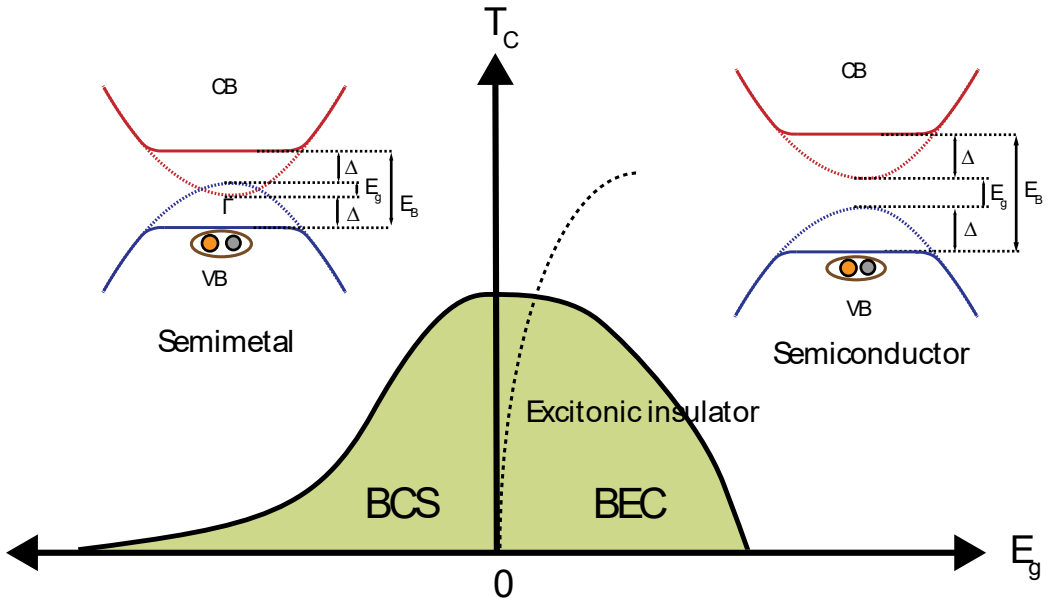

Figure 2.5: Conditions of an EI phase as a function of band gap E_g. For a semimetal case ($E_g < 0$), excitons undergo a BCS-like phase transition and for the semiconductor case, a BEC is formed.

Owing to the small mass and high binding energy of exciton, an exciton condensate is stable at relatively high temperatures, unlike superconductivity in which cooper pairs form mainly

at low temperatures. Hence, the study of exciton condensates can unravel pair formation mechanisms, offering insights about long-standing problems, such as high-T_C superconductivity.

While exciton condensates have been observed in quantum Hall bilayers [33] and semiconductor quantum wells [34], a pure EI remains difficult to find. Electron-lattice interactions are instrumental both in disrupting the purity of an EI state and in hiding observable consequences of exciton condensation. For example, charge density modulation can arise from exciton condensation as recently shown in indirect-gap transition metal dichalcogenides [35, 36]. As shown in Fig. 2.6, when an exciton forms between an electron CB and hole in VB separated by the wavevector q_0, charges align themselves as a CDW with wavelength $2\pi/q_0$. This CDW modulation coexists with the exciton condensate, thereby making the identification of the exciton condensate extremely arduous. To find the signatures of exciton condensation and the EI phase, the first and foremost challenge is to disentangle the CDW and EI order parameters.

Due to the parasitic couplings to the lattice that obstruct the identification of exciton condensate, tracking the spectral fingerprints of an exciton condensate is extremely difficult. Due to exciton's charge neutrality and thereby no coupling to light, it's difficult to optically detect exciton condensate in static limit, as opposed to the Josephson plasmon resonance (JPR) in cuprates, which is a direct reporter of superconductivity [37]. As such, optical signatures of an exciton condensate have been elusive and the possibility of time-resolved novel optical techniques in solving this puzzle remains open [38]. It is imperative, therefore, to delineate the full ramifications of electron-phonon coupling which includes dynamical attributes.

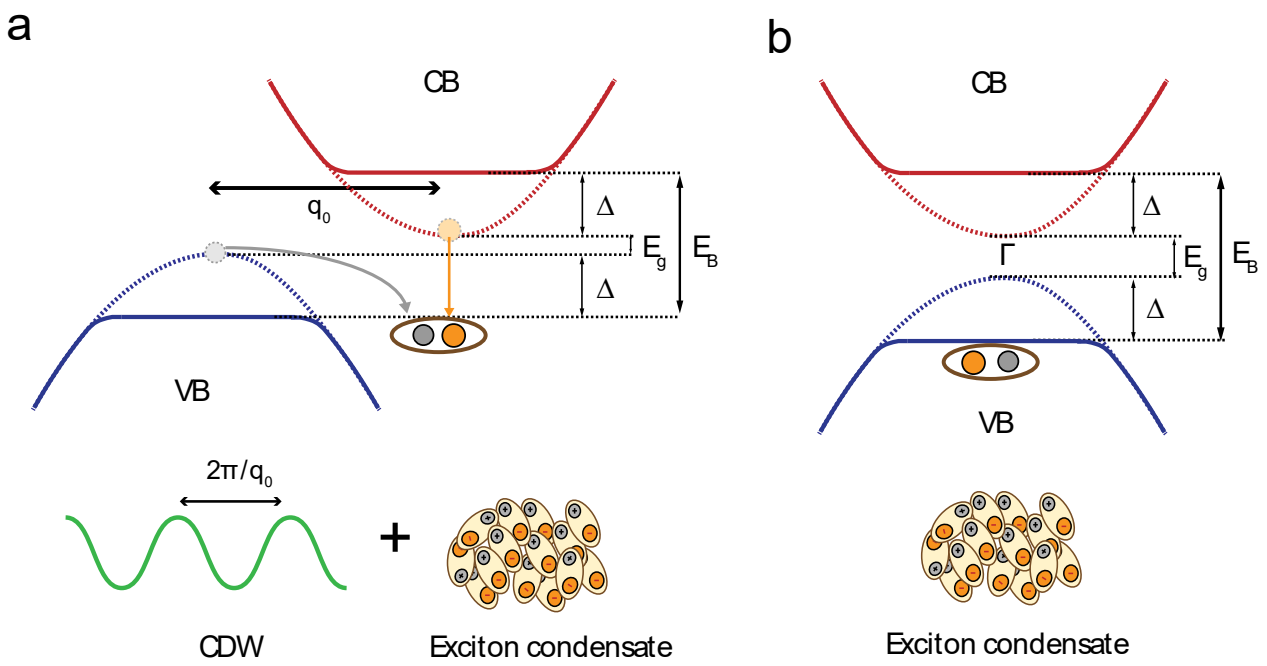

Figure 2.6: a, for an indirect gap EI, the electron-hole separation by the wavevector q_0 results in a CDW modulation, concomitant with EI phase. **b**, For a direct band gap, no CDW is formed.

2.2 Ta_2NiSe_5 : a putative EI

We have described the physical properties of EIs and their potential to host an exciton condensate. In the following section, we will discuss about Ta_2NiSe_5 (TNS), a popular EI candidate. After expounding the structural properties of TNS, we will concentrate on the electronic properties and the possibility of exciton condensation at near room temperature. Further, in Chapters 4 and 5 a full accounting of optical pump – broadband THz probe spectroscopy studies of TNS will be given which will shed light on the nonlinear optical properties of TNS at THz frequencies, a key ingredient to confirm the existence of a BEC in TNS.

2.2.1 A quasi-1D layered semiconductor

The layered quasi-1D direct-gap semiconductor TNS has drawn considerable interest as a potential EI material. Fig. 2.7 shows a schematic of the TNS crystal structure in which alternating Ta and Ni chains run along the a axis. In the Ni $3d$ band, there are 2 electrons, while there are no electrons in the Ta $5d$ band. Therefore, an electron from Ni chain hops onto the Ta chain, thereby creating an extra electron in Ta chain and leaving Ni chain one electron short (hole). If we consider the band structure perspective, Ta $5d$ orbitals form the CB while Ni $3d$ orbitals form the VB. From the electron exchange between Ta and Ni chain, an exciton is formed between the Ni chain hole and Ta chain electron. As such, the excitons in TNS are of charge transfer (CT) character. The energy cost for this CT process is equal to the exciton binding energy E_B which we term as the excitonic correlation gap Δ_E [39].

This gap formation is accompanied by a LT monoclinic – HT orthorhombic phase transition at $T_C = 326$ K. Below this transition temperature, the EI phase emerges and Δ_E is considered as the condensate gap or the order parameter. For the ARPES and optical conductivity measurements, the gap is found to be 160 meV. From optical conductivity measurements, it has been observed that a gap develops below 326 K with resistivity and specific heat displaying kink features [40].

2.2.2 EI phase in TNS

The possibility of above room temperature EI phase and exciton condensate makes TNS a very intriguing EI candidate. Moreover, understanding the mechanism of EI in TNS can pave the way towards designing more efficient materials with exciton condensate at higher temperatures and can offer valuable insight into understanding quantum many-body effects and ordered phases.

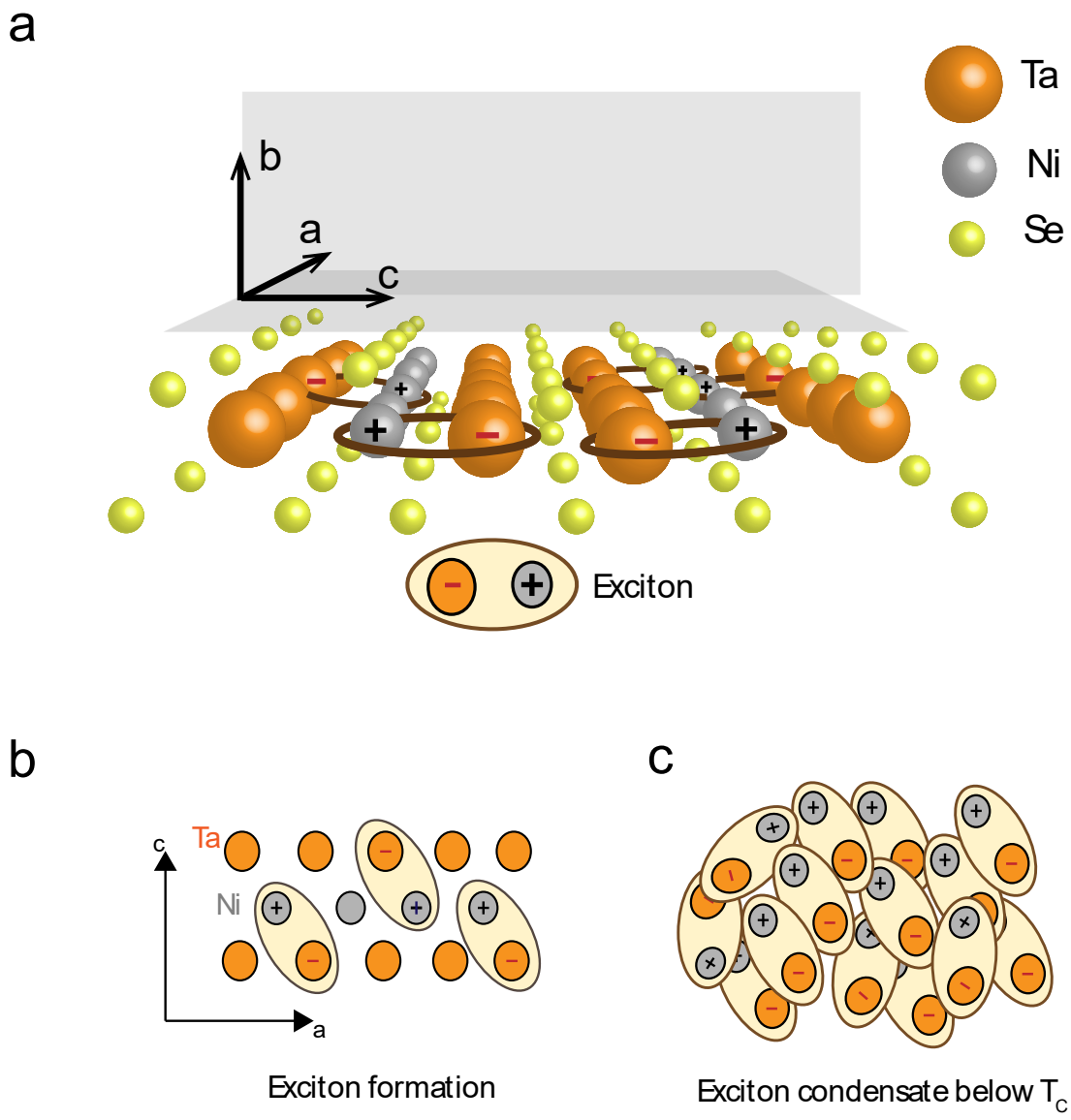

Figure 2.7: a, Ta_2NiSe_5 (TNS) structure with alternating Ta and Ni chains running along a axis. **b**, An electron transfer from Ni to Ta chain creates an exciton, c, the excitons condensing below $T_C = 326$ K.

There have been numerous studies to investigate the origin of the EI phase in TNS. The first question that must be answered is whether TNS is an EI. The second question is what the mechanism of exciton condensation in TNS is. Does TNS host a BEC or a BCS-like exciton

condensate? In this section, we will establish TNS as an EI in the light of previous studies. Alongside, we will also discuss the results that contradict the assumption that TNS is an EI.

According to ARPES results and supporting theoretical analysis, existence of a BEC has been demonstrated where a large number of excitons are preformed above T_C. In this case, excitons exist above T_C but condense only below T_C, as opposed to the BCS case where condensation and exciton formation take place simultaneously below T_C. Here, the excitonic gap Δ_E equals the binding energy for the exciton and is temperature independent. The reason is that excitons exist below and above T_C; excitons exist as exciton condensate below T_C, and as preformed excitons above T_C. For a BEC, the system above the transition is not a semimetal, but a small band gap semiconductor ($E_g > 0$).

Nonzero band gap and flat VB top was observed above T_C, suggesting the preformed exciton binding energy in ARPES results as seen in Fig. 2.8 [41, 42]. This preformed exciton picture is closely related to the results seen in underdoped cuprates where preformed cooper pairs form much above T_C, but form a condensate only below T_C [43, 44]. This supports the existence of an exciton BEC. However, BEC cannot be solved by MFT and warrants for variational cluster approximation on extended Falicov-Kimball model to explain ARPES data. In this line of thought, 3-chain Hubbard model analysis has shown spontaneous formation of BEC consisting of bound electron-hole pairs which cooperatively induces phonon instability at $q \to 0$ [45].

In another ARPES experiment, hybridization between the VB and CB was evident below T_C. However, no hybridization was seen above T_C, and bandgap always remained nonzero at all temperatures [46]. Further, a photoemission feature above T_C was recorded which was attributed to single exciton. In contrast, there was no photoemission below T_C. The most plausible explanation is that a condensate exists below T_C and as such no single exciton is present, resulting

in a lack of photoemission feature. This also confirms the preformed exciton and BEC picture. Exciton condensation is highly sensitive to electron-hole concentration and screened Coulomb interaction, and semiconducting TNS is not a normal state but an exciton preparing state [47]. This also hints at a BEC-like phase transition. Nevertheless, doping control can enable continuous transition from semiconductor—insulator—semimetal phases.

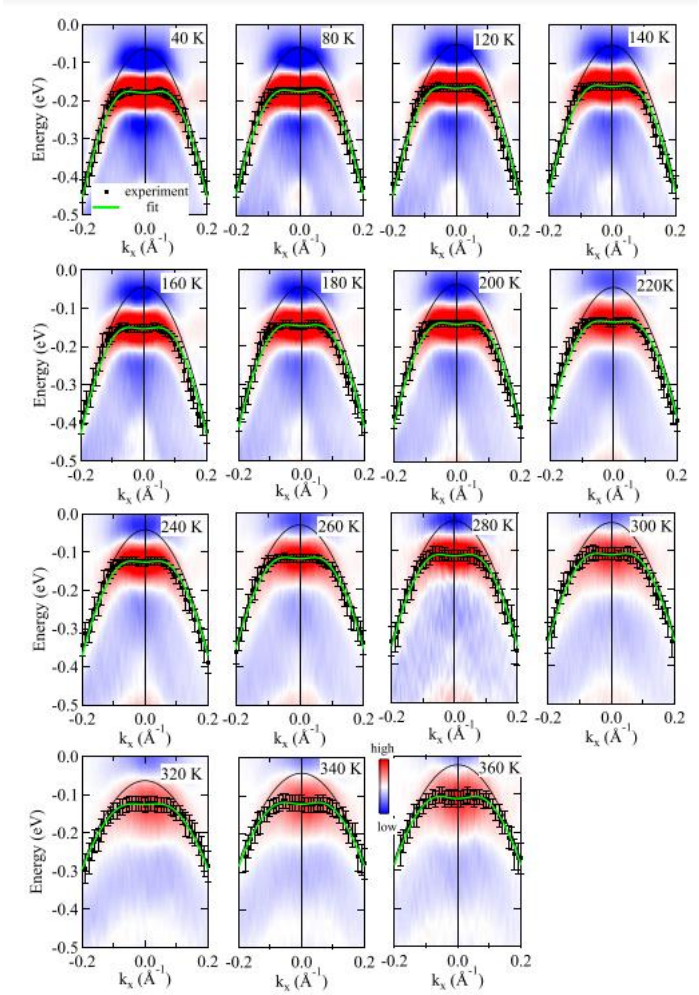

Figure 2.8: ARPES energy map on TNS over a wide temperature range. The red color is showing a band gap evident at all temperature, indicative of a BEC-like exciton condensate with preformed exciton above T_C. Adapted from ref. [41].

There is also a lot of controversy as to whether the EI phase in TNS is of structural and electronic origin. Raman spectroscopy also suggests that TNS is in the BEC-BCS crossover regime with an electronic phase transition. Two discrete mirror symmetries near the Brillouin zone (BZ) center result in finite energy gap as opposed to $U(1)$ symmetry breaking. Two bands closest to Fermi surface are quasi-1D and originate from Ta $5d$ and Ni $3d$ bands. Band hybridization is the order parameter induced by condensate of interband excitons [48, 49]. The inverse Raman susceptibility has shown a discontinuity at 161 K which means that without the lattice coupling, the electronic phase transition temperature is $T_C^{el} = 161$ K. And due to electron-phonon coupling, the transition temperature increases to $T_C^{el} = 237$ K. Moreover, a B_{2g} strain also plays a vital role in enhancing the T_C to 326 K. In IXS measurements, a B_{2g} mode softening was observed, indicating strong electron-phonon coupling driving the structural transition [50]. Similarly, other Raman measurements reveal a Curie-Weiss temperature of $T_w = 240$ K, as a signature of electronic phase transition preempting the structural transition. That is, if there was no monoclinic – orthorhombic transition, the real T_C of TNS would be 240 K, stipulating the direct observation of excitonic instability [51].

Rather than solely electron-hole interactions, electron-phonon coupling can also explain phonon-coupled states of the exciton condensate, in concert with first principles DFT and electron-phonon Hamiltonian analysis which reveals a semiconductor – insulator transition [52]. In addition, earlier studies have reported scattering of photoexcited electrons with the condensate as the origin of the phase transition, where a phase transition upon photoexcitation was observed with the gap closing on a faster timescale than phonon oscillations [53]. However, this is contradictory with previous MIR reports of lattice distortion by photoexcitation [54, 55]. The monoclinic phase favors excitonic coupling and causes gap narrowing below a critical fluence. Also, no nonthermal

structural change was noted, and above a critical fluence, a transient modulation of the condensate density and widening of the gap were reported. This is explained by the Hartree-Fock calculation where an excitonic condensate exists and the critical photoexcitation density is related to different resonance channels which cause band narrowing/widening by renormalizing the exciton condensate density, confirming an EI phase in TNS. Besides, in STM measurements, a band renormalization and Ta $5d$ and Ni $3d$ orbital inversion at the band edges provides evidence of TNS as an EI, with the condensate close to BCS regime [56].

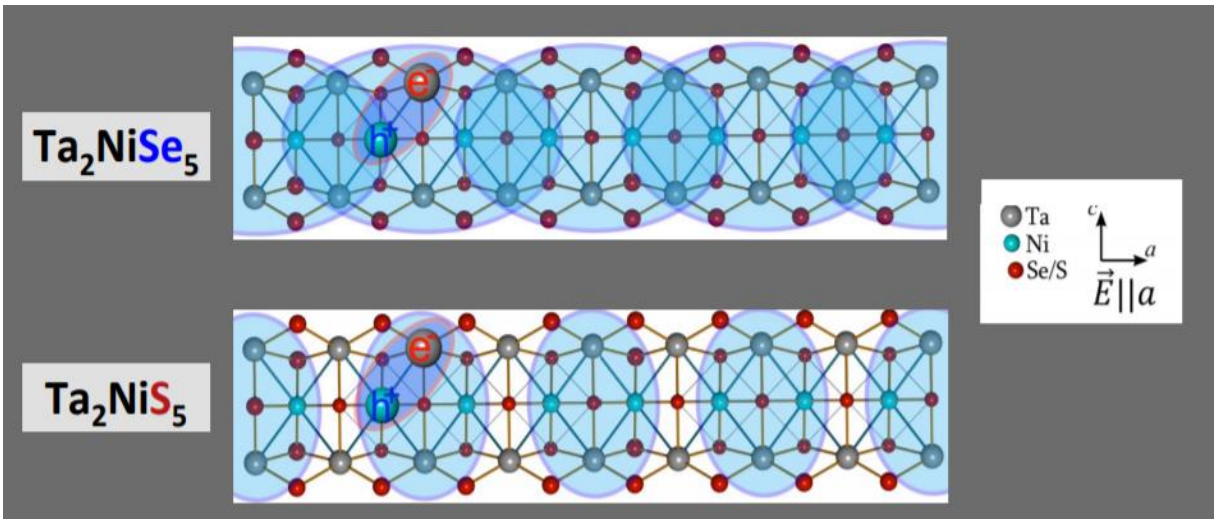

Figure 2.9: Bound states of excitons in Ta_2NiSe_5 (TNS) and its parent compound Ta_2NiS_5. Although excitonic correlations exist in the parent compound, it does not extend spatially and thus cannot show long-range order. On the contrary, thanks to the exciton condensate-phonon coupling, the bound states extend spatially, leading to giant Fano spectral weight. Adapted from ref. [58].

Ellipsometry and FTIR measurements have reported a giant Fano resonance feature in the optical conductivity that signifies a broad excitonic continuum. The Fano resonance occurs due to exciton-phonon bound states where the holes localize at Ni sites because of interaction with a breathing phonon. A self-trapped excitonic bound state appears on a free electron-hole pair

background, leading to a high susceptibility to distortion [57, 58]. This data was compared with the parent compound Ta_2NiS_5, an isoelectric semiconductor with no phase transition. Compared to the parent compound, TNS displays a giant Fano spectral weight which can be attributed to exciton-phonon bound states that are absent in Ta_2NiS_5. Although, excitons can form in Ta_2NiS_5, due to the smaller size of S atoms and larger Ta - S binding energy, there are no spatially extended bound states in it. In other words, $E_B^{Ta_2NiSe_5} < E_B^{Ta_2NiSe_5}$, and thus, $r_{trap}^{Ta_2NiSe_5} > r_{trap}^{Ta_2NiSe_5}$, resulting in long range order of exciton bound states and a large Fano resonance in TNS, implying the EI phase (see Fig. 2.9 for details).

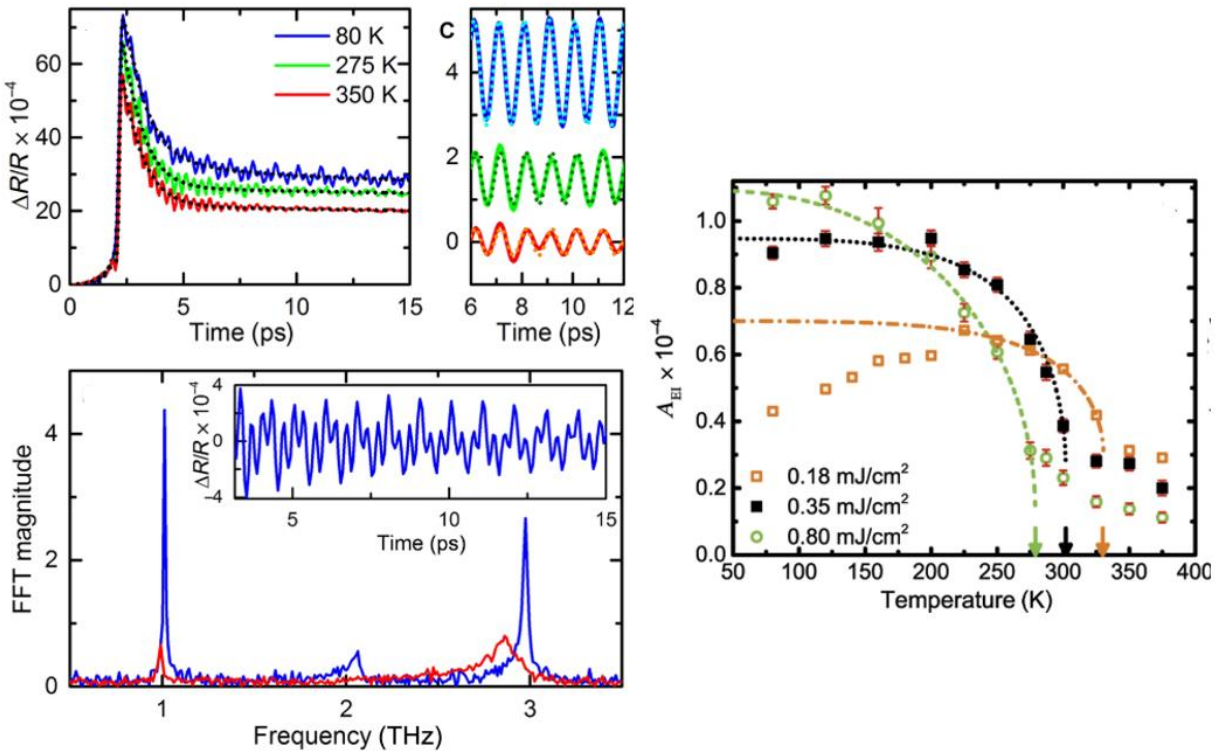

Figure 2.10: Optical pump-probe measurement on TNS showing different Raman oscillation in transient reflectivity change $\Delta R/R$ (top left). Bottom left panel depicts the FFT, revealing oscillations at 1, 2 and 3 THz. Right panel shows the temperature roll-off of the amplitude of the 1 THz oscillation that shows an order-parameter like fashion, touted as Higgs mode feature. Adapted from ref. [59].

Previous optical pump-probe measurements Ultrafast NIR pump-probe experiments have reported the transient reflectivity amplitude showing an order parameter-like temperature dependence. This was termed as the first Higgs mode fingerprint in TNS as shown in the temperature behavior of a 1 THz Raman-active oscillation which is coupled to the Higgs mode (see Fig. 2.10). In the nonequilibrium condition (upon perturbing the condensate with light), the condensate can be tracked through its coupling to the 1 THz phonon [59]. The electronic background of the signal also shows a BEC-like phase transition, consistent with the preformed exciton and temperature independent gap scenario. However, there are some indications of partial closing of the gap below T_C which suggest that there are still some temperature dependences of the gap. These results also stipulate that TNS is an EI at the BEC-BCS crossover [60].

Ultrafast spectroscopic techniques have further revealed many key ingredients responsible for the EI phase in TNS. An NIR pump-probe study unveiled hallmarks of preformed excitons above T_C and directionality of the condensate along the chain. NIR pump excites quasiparticles (QP) across the gap and transient reflectivity change shows carrier multiplication process. Afterwards, QPs recombine to create bound electron-hole pairs by emitting Higgs mode of the condensate at ~ 2 ps after the pumping. This short-lived dynamics is different from the bottleneck effect in superconductors where Cooper pairs rebreak and QPs have longer lifetime due to Anderson-Higgs mechanism [61]. This indicates that the phase transition is mainly electronic, although there is also strong electron-phonon coupling and it is necessary to thoroughly investigate the role of phonon in the structural transition as well as the exciton condensation.

Another dichotomy regarding the EI character of TNS is the nature of the condensate. If the condensate occurred as a result of continuous $U(1)$ symmetry breaking, the charges in VB and CB would be separately conserved and an amplitude mode and a gapless Goldstone mode would

arise. However, in TNS, two discrete mirror symmetries are broken as a consequence of electron-phonon coupling and band hybridization [62, 63]. If the transition is entirely by electron-phonon coupling, the gapless phase mode will not be visible, and the EI phase will not be supported. However, for an entirely electronic transition, the gapless phase mode exists, and the continuous symmetry is largely conserved, and EI phase is present in the system. Ultrafast pump-probe microscopy demonstrates the propagation of the condensate's phase mode at close to the electron velocity [64]. This can be accounted for by electron-phonon coupling which leads to the hybridization of phase mode with phonons, creating excitations of both electronic and phononic nature that can ballistically propagate.

Nonetheless, the predominant mechanism of symmetry breaking as well as the phase transition still remains controversial. Recent trARPES reports have revealed the ultrafast phase transition is purely electronic and the LT gap is a result of strong electron-hole coupling [65]. Other studies have shown that electron-electron interaction plays a bigger role than electron-phonon coupling [66]. However, a recent Raman study has demonstrated that the phase transition is neither purely electronic nor purely phononic and the excitonic transition coexists with the structural transition which involves a linear coupling of electronic and lattice order parameters. Further, an unstable B_{2g} optical phonon softening occurs as the temperature approaches T_C from above, and an electronic background with highest weight at T_C was observed which provides a good argument in favor of electron-phonon coupling as an integral part of the phase transition [67-70].

Hence, electron-phonon coupling has proved to be instrumental in the phase transition as evidenced by the unusual temperature dependence and interpretation of electron-phonon coupling can envision the correct mechanism of the EI phase. It is therefore essential to map out the role of

electron-phonon coupling in phase transition in TNS in order to obtain a clear picture of the origin and nature of the EI phase.

In an EI, optical fingerprints are very hard to detect by means of equilibrium spectroscopy since the optical sum rule is violated in an EI, contrary to SC. In an SC, the real part of the optical conductivity displays a Dirac delta function-like feature at zero frequency which accounts for the missing spectral weight at finite frequency that is present in the normal state. This large value of DC conductivity is consistent with the fact that an SC exhibits a very large conductivity at the DC limit. Since the spectral weight remains constant, the optical sum rule is conserved. However, in an EI, there is no conductivity in DC limit which means that there is always missing spectral weight in an EI (see Fig. 2.11), pointing to optical sum rule violation [71].

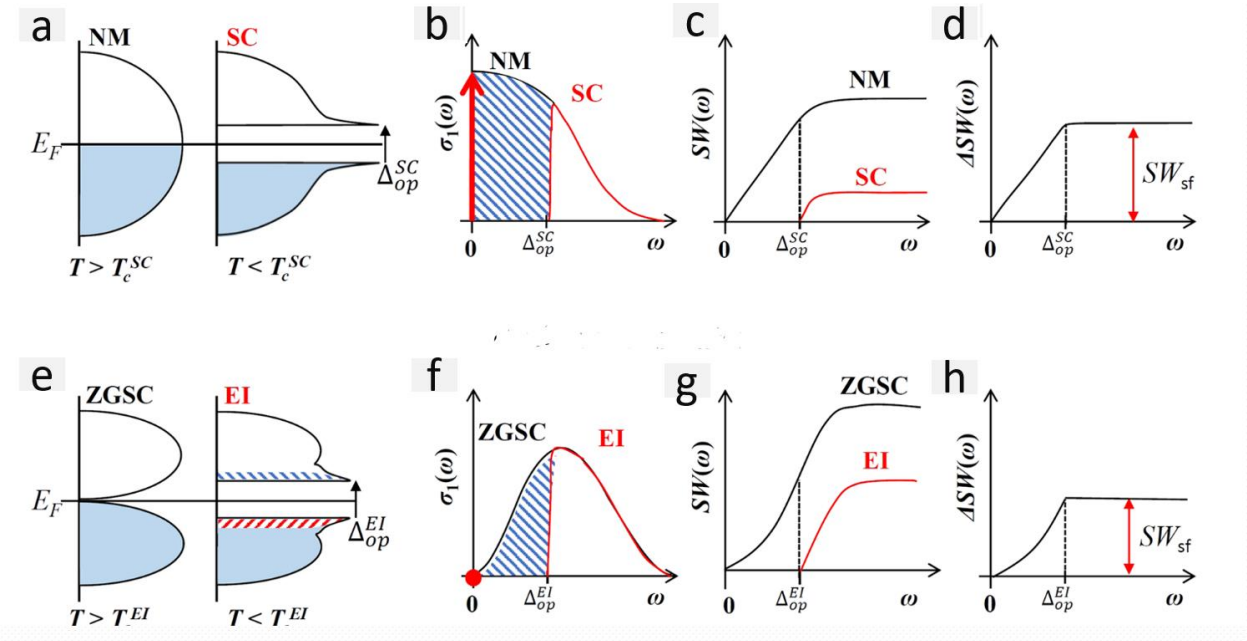

Figure 2.11: DOS and gap opening, optical conductivity, spectral weight and change in spectral weight with respect to normal state for SC (**a—d**), and for EI (**e—f**). Note that for SC, there is a δ function feature in optical frequency at the dc limit which accounts for the extra spectral weight that is present in normal metal state. In contrast, EI has missing spectral weight at zero frequency. Adapted from ref. [71].

As a result, considering the technical challenges, instead of steady-state optical spectroscopy, nonequilibrium spectroscopy can be an effective method to push the material far from equilibrium and study the relaxation dynamics and the corresponding changes in the spectrum. This can also provide us with immense insight into the timescales of the elementary excitations.

From the discussion in this chapter, we have learned the physics of TNS, its potential as an EI, the nature of its condensate as well as the controversy regarding the origin of its phase transition. Nonetheless, the above-room temperature T_c, TNS is a direct bandgap ($q \rightarrow 0$) material there is no CDW formation which make TNS an intriguing EI candidate. In the next chapter, we will discuss the power of time-resolved THz spectroscopy as a unique tool to probe condensate dynamics and utilize it to study the exciton condensate signatures in TNS single crystals.

Chapter 3 Optical Pump – Broadband THz Probe Spectroscopy

3.1 Introduction to THz spectroscopy

In Chapter 1, we discussed the power of ultrafast spectroscopic technique to explore the electromagnetic properties of novel materials. In this chapter, we will narrow our discussion of time-domain spectroscopic technique to THz spectroscopy, since it is the most relevant technique for this thesis.

3.1.1 THz regime of the electromagnetic spectrum

The usage of THz spectroscopy in condensed matter physics has opened new possibilities to investigate elementary excitations in materials on a picosecond scale. THz spectroscopy is uniquely suited to probe the low energy end of the electromagnetic spectrum, otherwise inaccessible by conventional optical spectroscopic methods. The coherent generation and detection of ultrafast THz pulses allows for extraction of complex material parameters, facilitating the study of complex materials at very low energy scale. Thus, the study of THz wave has flourished into a rich area of physics, attracting the interests of many physicists and engineers.

THz radiation spans the frequency range from approximately 100 GHz to 10 THz. From the spectroscopic point of view, THz radiation covers wavelengths from approximately 30 μm to 3 mm which corresponds to the energy window from 0.4 meV to 40 meV (1 THz ~ 4.1 meV).

As mentioned above, 1 THz corresponds to a photon of 4 meV energy. This is an energy scale that is less than the energy difference between orbitals or the vibrational modes of most materials. This makes it quite challenging to develop a coherent light source that directly emits THz photons. The same problem exists regarding the detection of THz pulses. Semiconductor

detectors do not work at THz frequencies, since such small photon energy at meV regime cannot excite electrons across the band gap to generate an electric signal. The lack of efficient generation and detection techniques of THz was termed as “THz gap” by the optics community. One of the growing topics in the field of nonlinear optics is the search for new schemes to generate coherent THz waves and bridge this “THz gap”, and numerous efforts by physicists and engineers have resulted in seminal discoveries of various novel nonlinear optical techniques of THz generation and detection.

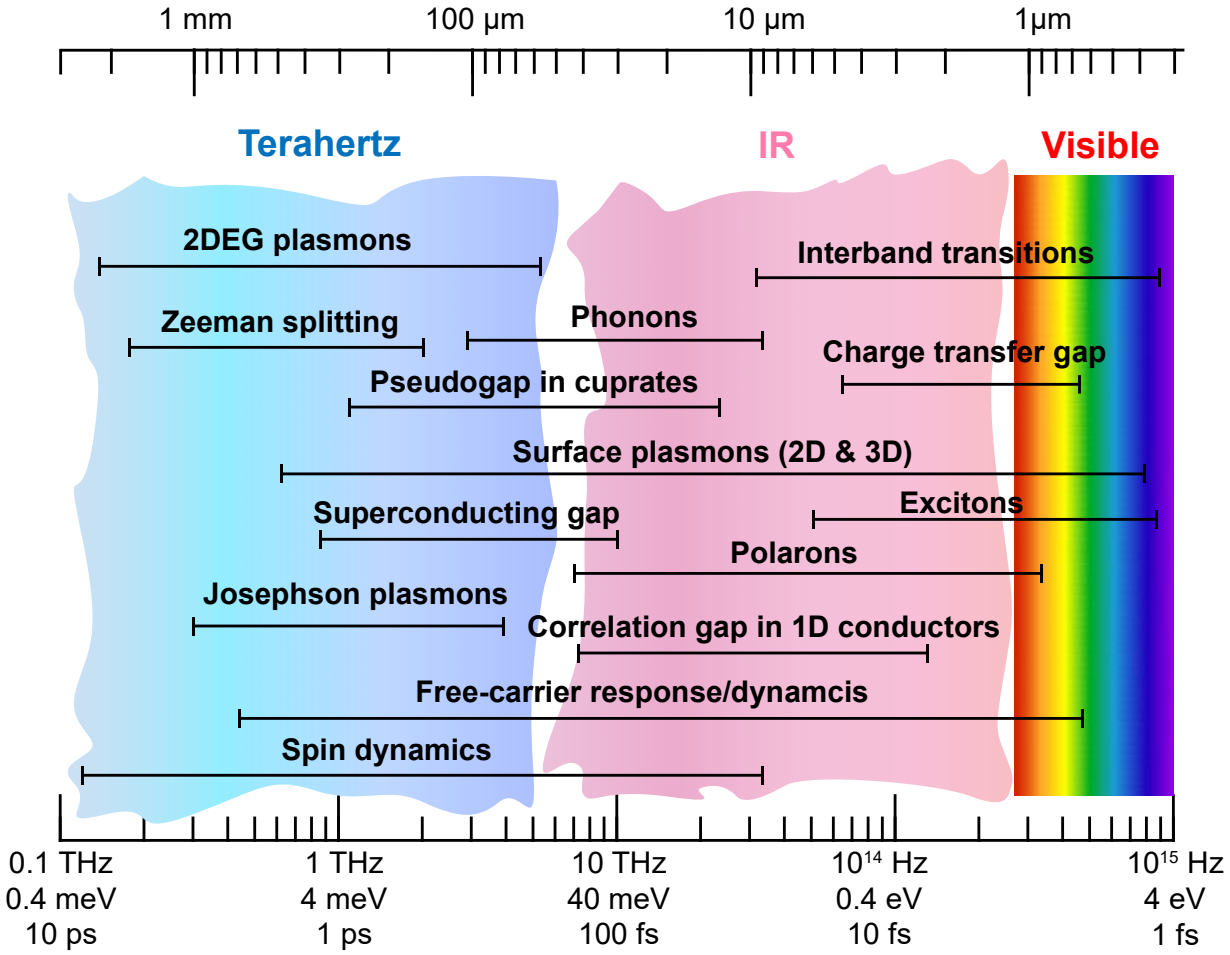

Figure 3.1: The electromagnetic spectrum covering THz, IR and visible spectrum. Elementary excitations with their relevant energy scales.

3.1.2 A versatile tool to probe quantum dynamics

In condensed matter systems, THz spectroscopy is of great importance as THz photons are resonant with numerous elementary excitations and collective modes. Figure 3.1 shows a schematic of the electromagnetic spectrum covering the THz, IR, and visible spectral regions. The selection of the wavelength of electromagnetic field depends on the energy of the elementary excitation that is of interest. From Fig. 3.1, it is evident that many elementary excitations such as superconducting gap, pseudogap in cuprates, Josephson plasmon resonance (JPR), plasmons in a 2-dimentional electron gas (2DEG), and optical phonons share the same timescale as THz waves. Hence, THz wavelengths provide direct access to these phenomena.

Development in THz science and technology has enabled researchers to fill up the "THz gap" gradually during the past three decades. This served as the motivation to new sources of THz generation leading to study of lattice vibration, collective modes [72, 73] and carrier dynamics [74]. Using THz radiation as a probe in combination with optical photoexcitation, it allows for insight into phenomena, such as electron-electron interactions, phase transitions [75] and nonequilibrium dynamics.

Besides this, THz spectroscopy can be used to observe or control dynamics of the excited states. One such example is the enhancement and suppression of coherent spin waves by varying the time delay between two pump pulses [76]. As shown in Fig. 3.2, a strong THz pump drives magnon oscillations in AFM NiO, which is captured by the probe that records the Faraday rotation following photoexcitation. By varying the time delay of an additional THz pump, one can realize the enhancement/suppression of the coherent magnons.

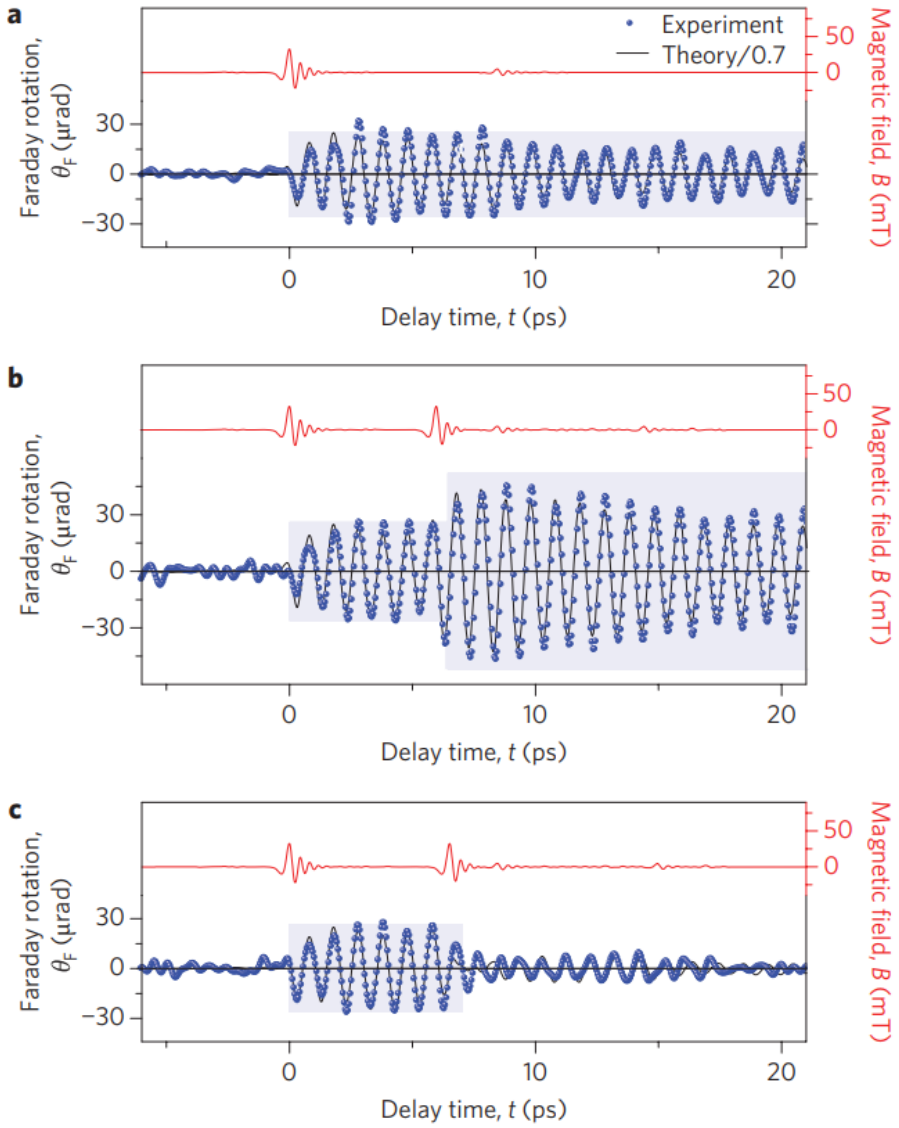

Figure 3.2: **a**, Coherent magnon oscillations on AFM NiO using femtosecond THz pump-Faraday rotation probe. **b**, Enhancement of magnon oscillation after excitation by two THz pump pulses with time separation of 6 ps. **c**, suppression of magnon after excitation by two THz pump pulses separated by 6.5 ps. Adapted from ref. [76].

In this thesis, we utilize time-resolved terahertz (THz) spectroscopy as this technique is uniquely suited to probe condensate dynamics with discriminatory power arising from the temporal response coupled with broadband spectral access of the low energy electrodynamics. Groundbreaking developments in THz spectroscopy have been instrumental in studying order

parameter dynamics in materials, i.e., pair density wave studies in striped cuprates exhibit a third harmonic generation (THG) of the JPR when probed by a nonlinear THz field. Another prominent example is the Higgs mode in superconductors where a THz pump with frequency close to the BCS gap introduces order parameter oscillations at twice the pump frequency [77].

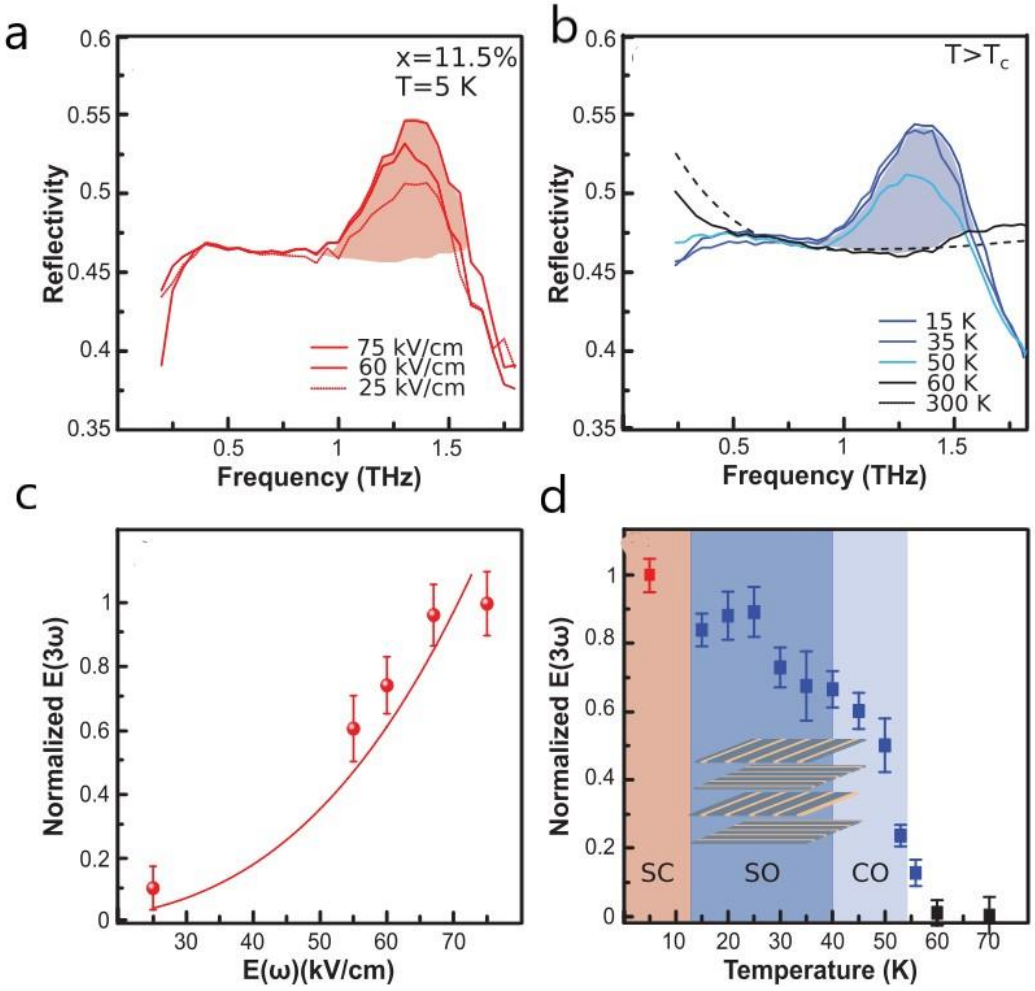

Figure 3.3: Pair density wave studies in striped cuprate $La_{1.885}Ba_{0.115}CuO_4$ **a**, A third harmonic of the JPR is observed when probed in the nonlinear regime. **b**, The THG persists above T_C. **c**, Field strength and **d**, dependence of the THG, showing an order parameter behavior that scales with the stripe order. Adapted from ref. [77].

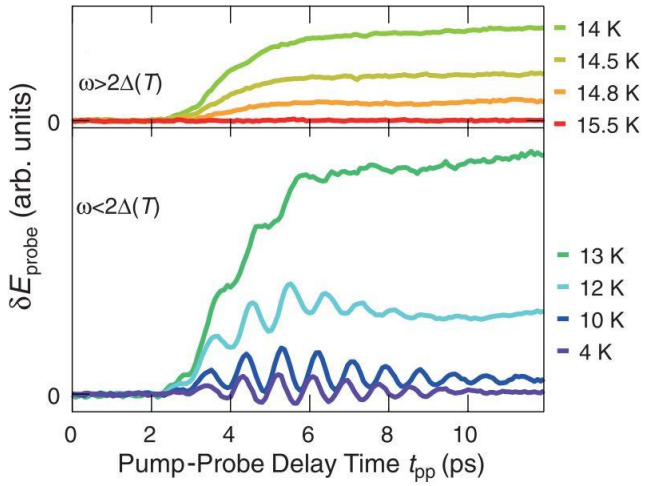

Figure 3.4: Higgs mode studies in NbN thin films. A high-field THz pump introduces no oscillation when the pump frequency ω is greater than the superconducting gap 2Δ (top panel). However, for $\omega < 2\Delta$, the differential probe electric field δE_{probe} oscillates at frequency 2ω (bottom panel). Adapted from ref. [78].

From these examples, it can be noted that THz experiments can access nonlinear optical phenomena that do not manifest in the linear response and can open new pathways to detect and control collective modes in correlated materials. Extending this approach to the detection of an exciton condensate in the putative excitonic insulator TNS is a central theme of this thesis. In the following sections, we will delineate the ins and outs of THz generation and detection as well as the optical pump – broadband THz probe system I built to investigate the exciton condensate dynamics in TNS.

3.2 THz generation and detection techniques

A plethora of condensed matter phenomena show up in the THz frequency regime including Drude response, JPR, phonons, magnons, gap phenomena etc. Since the frequency range covers the low energy Drude response that converges to the DC conductivity $\sigma(\omega = 0) = \sigma_{DC} =$

σ_0, THz time-domain spectroscopy can be treated as a non-contact method to measure the quasistatic conductivity of a material. The Drude conductivity can be written as,

$$\sigma(\omega) = \frac{\sigma_0}{1 - i\omega\tau}, \tag{3.1}$$

where $\sigma_0 = ne^2\tau/m$ is the DC conductivity, and τ and n are the scattering time and carrier density, respectively.

The main idea of THz time-domain spectroscopy is to use a NIR femtosecond pulse to generate a single or multi-cycle THz pulse. The second part is the detection of this THz pulse with an optical gating pulse much shorter than the THz pulse. This gate pulse arrives at the detector at a specific time delay with respect to the THz pulse and records the electric field profile of the THz pulse as a function of the varying delay between the THz and the gate pulses.

The temporal electric field profile of the THz pulse is then Fourier transformed in order to obtain the frequency-resolved spectrum. This spectrum contains information about the characteristic dispersion and absorption of the sample and thus allows for investigation of the optical properties of the materials.

Another important advantage of THz spectroscopy over other static optical techniques is that the direct measurement of the time-domain electric field contains both amplitude and phase information rather than just intensity as seen in FTIR spectroscopy. As a result, no KK transformation is needed to extract the real and imaginary parts of the optical constants.

There are various methods to generate THz waves. In the following section, I will describe the methods I implemented to generate THz pulses in our lab: (1) optical rectification, (2) tilted pulse front and, (3) 2-color laser plasma method. I will also describe THz detection using the electro-optic (EO) sampling method.

3.2.1 Optical rectification

A popular source of THz generation is the generation via nonlinear optical processes in crystals. In the process of optical rectification, the incident NIR multi-cycle femtosecond laser pulse is converted into a nearly single-cycle THz pulse. More precisely, THz generation using optical pulse is difference frequency generation (DFG) over the bandwidth of the generating optical pulse. This can be understood within the framework of nonlinear optics. In a nonlinear crystal, the second-order optical susceptibility is large and so, the polarization *P* changes not only with the driving electric field, but also has a quadratic component that scales with E^2. The polarization can be written as,

$$P(t) = \varepsilon_0 \chi^{(1)} E(t) + \varepsilon_0 \chi^{(2)} E^2(t) + \cdots, \tag{3.2}$$

where χ is the optical susceptibility of the material. The polarization can be written as a sum of linear and nonlinear components, $P(t) = P_L(t) + P_{NL}(t)$, where $P_{NL}(t) = \varepsilon_0 \chi^{(2)} E^2(t)$. For simplicity, we are only considering the quadratic part. For a crystal with space inversion symmetry,

$$P_{NL}(-E) = -P_{NL}(E), \tag{3.3}$$

$$\varepsilon_0 \chi^{(2)} (-E(t))^2 = -\varepsilon_0 \chi^{(2)} E^2(t), \tag{3.4}$$

$$\varepsilon_0 \chi^{(2)} E^2(t) = 0, \tag{3.5}$$

$$P_{NL}(t) = 0. \tag{3.6}$$

We can see that for an optically nonlinear crystal with large nonlinear optical susceptibility, the inversion symmetry must be broken. Let us consider two electric fields $E_1 = E_0 \, cos\omega_1 t$ and $E_2 = E_0 \, cos\omega_2 t$. In this case the second-order polarization can be written as,

$$P_{NL}(t) = P^{(2)}(t) = \varepsilon_0 \chi^{(2)} E_0^2 \, (cos\omega_1 t + cos\omega_2 t)^2, \tag{3.7}$$

$$P^{(2)}(t) = \varepsilon_0 \chi^{(2)} E_0^2 [1 + \frac{1}{2}\cos(2\omega_1 t) + \frac{1}{2}\cos(2\omega_2 t) + \cos(\omega_1 + \omega_2)t + \cos(\omega_1 - \omega_2)t]. \tag{3.8}$$

On the right side of (3.8), there are five terms. The first term does not have any oscillatory component, it functions like a DC field. The second the third terms are called second harmonic generation (SHG) terms since their frequencies are twice the fundamental harmonics (FH). The fourth term is called sum frequency generation (SFG). The last term is called the DFG term, and this term describes the optical rectification process.

The generation pulse we used in our experiment is the 35 fs 800 nm beam from a regenerative amplifier (Spectra Physics Spitfire Pro) with bandwidth of 50 nm, which is broad enough to generate DFG $\omega_1 - \omega_2$ light in the THz regime.

3.2.2 THz detection with electro-optic sampling

To detect a THz waveform, the most used method is called electro-optic (EO) sampling. The THz detection scheme is shown in Fig. 3.5. An ultrashort optical sampling (gate) pulse overlaps with the THz pulse on the detection crystal. Due to the Pockel's effect, the change of birefringence of the detection crystal is proportional to the THz electric field. The transient THz electric field experienced by the detection crystal is quasistatic at a given time delay, which can be read out through the polarization change of the sampling pulse. The initial polarization of the optical sampling pulse is linear.

Without the THz pulse, when the gate pulse goes through the quarter wave plate (QWP), the polarization changes into circular. Then this circularly polarized light goes through a Wollaston prism (WP). The WP decomposes the circularly polarized light into a s-polarized (vertical: V) and a p-polarized (horizontal: H) component. For a circularly polarized light, the V and H components have equal magnitude and thus when they reach the balanced photodiode (BPD), a null signal is obtained.

On the other hand, when the THz is present, the gate pulse interacts with it at the detection crystal and becomes elliptically polarized after QWP. Then the difference between the V and H components can be read out in the BPD. As a function of delay time, the gate pulse interacts at different points of the THz pulse. As such, the BPD records a time trace of the THz signal as a function of the gate-THz delay time and the measured signal is proportional to the THz field.

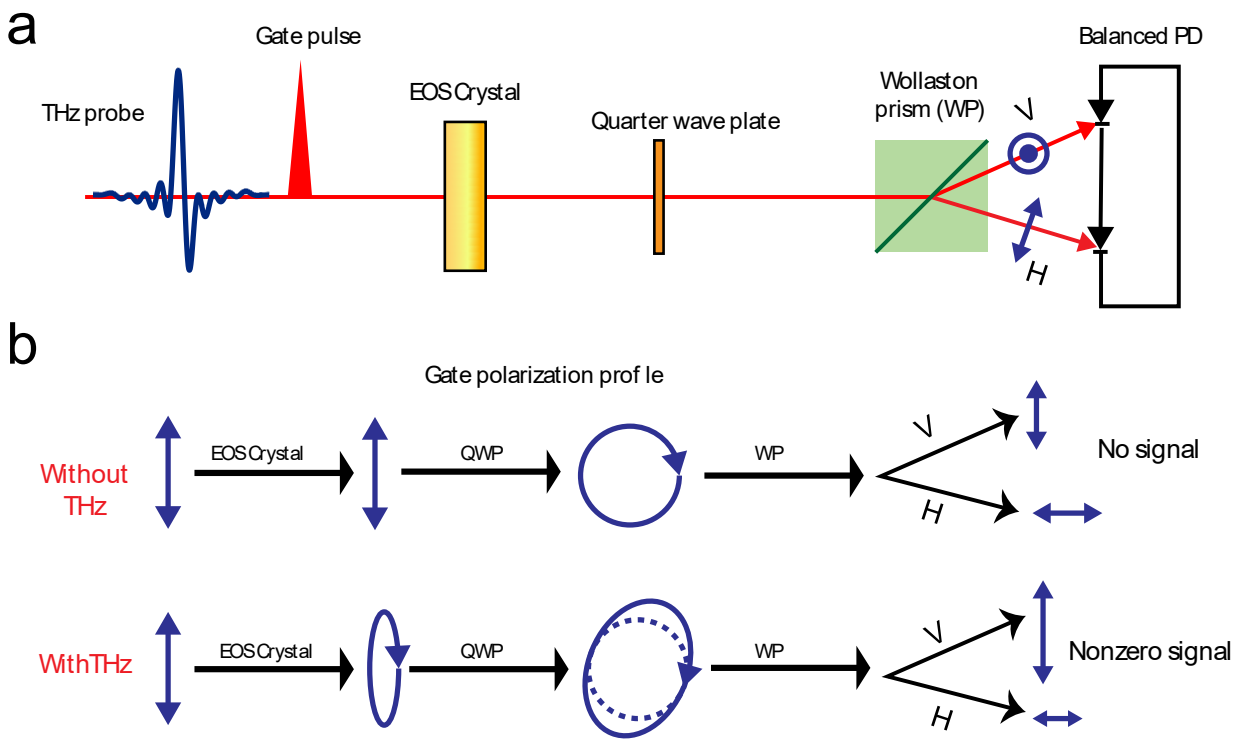

Figure 3.5: a, Schematics of EO sampling. **b**, Gate pulse polarization profile to read out THz electric field by measuring the birefringence change.

It is crucial that the pulse duration of the optical sampling pulse needs to be much shorter than the THz pulse. The selection of the EO sampling crystal depends on the detection frequency range and sensitivity. As shown in Table 3.1, ZnTe and GaP cannot be used to detect THz frequency higher than their lowest optical phonons (5.4 THz and 10. 96 THz), while ZnTe has

much better detection sensitivity thanks to its higher electro-optic constant. On the other hand, GaSe is used to detect THz at frequencies above 7.1 THz [79-81].

Table 3.1: Physical properties of some commonly used THz generation and detection crystals

Material	Lowest optical phonon (THz)	Electro-optic coefficient (pm/V)
ZnTe	5.4	3.9
GaP	10.96	0.97
GaSe	7.1	14.4

3.2.3 High-sensitivity THz generation from ZnTe crystal

To generate THz waves using the DFG scheme, it is a prerequisite to make sure that the refractive index of the fundamental frequency and the generated THz wave must have the same value inside the nonlinear medium so that frequency-mixed wave is always in phase with the generated THz wave to avoid destructive interference. This is called phase matching. In symmetry broken nonlinear crystals such as ZnTe, GaP etc., the optical group velocity and the THz phase velocity are the same. In terms of nonlinear optics, we express the optical rectification as,

$$P_i^{(2)}(\Omega_{THz}) = \sum_{j,k} \varepsilon_0 \chi_{ijk}^{(2)}(\Omega_{THz}, \omega_1, -\omega_2) E_j(\omega_1) E_k^*(-\omega_2)\,, \tag{3.9}$$

where Ω_{THz} denotes the THz frequency; i, j and k are the vector/tensor field components, $\chi_{ijk}^{(2)}(\Omega_{THz}, \omega_1, -\omega_2)$ denotes the second-order nonlinear susceptibility that involves the DFG for THz radiation. In this scheme, the fundamental optical beam impinges on the nonlinear crystal and the frequency components in its bandwidth mix with each other, thereby generating a THz wave via the DFG ($\omega_1 - \omega_2 = \Omega_{THz}$) process.

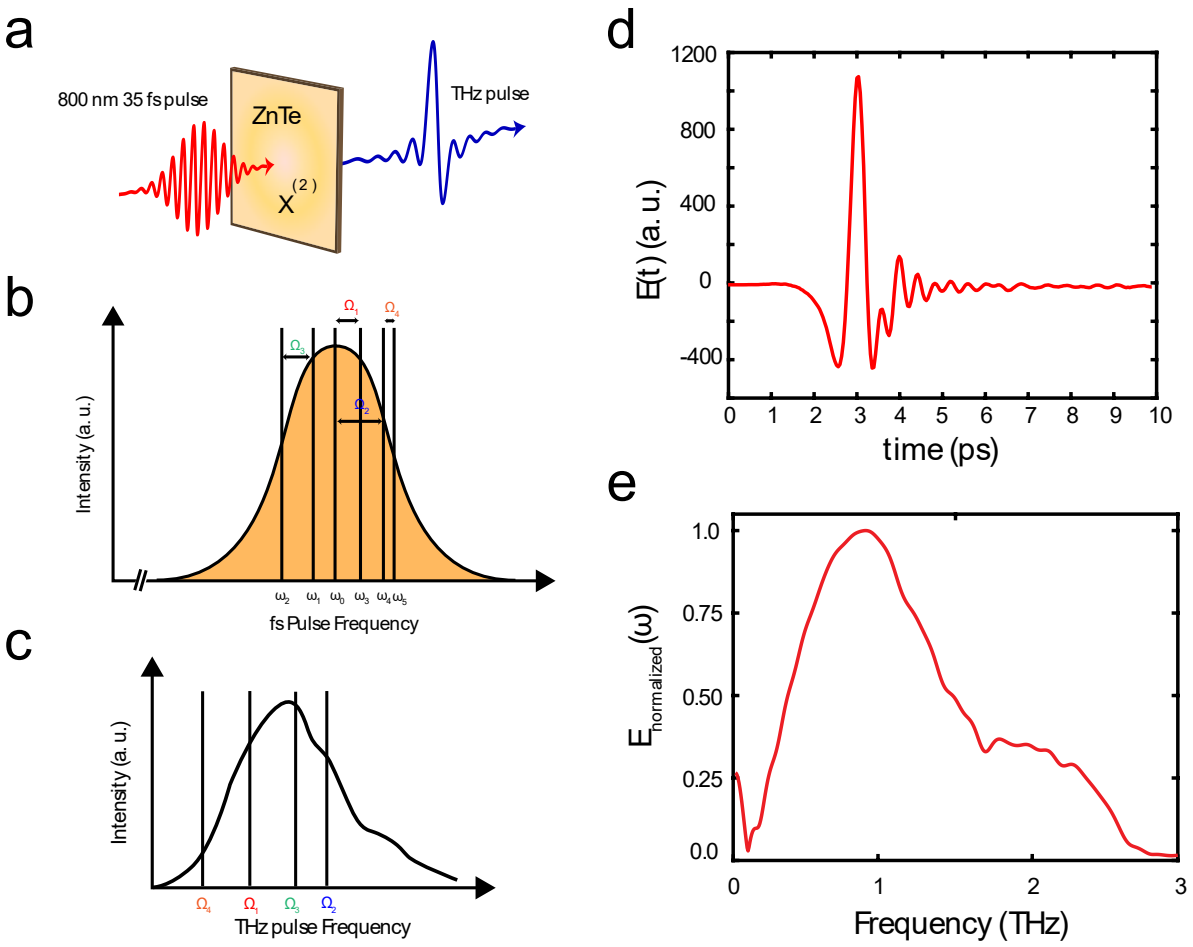

Figure 3.6: a, A 800 nm 35 fs pulse generating THz from a ZnTe crystal. **b**, 800 nm beam bandwidth with different frequency components ω_1, ω_2, ω_3 etc. **c**, Frequency mixings among different ω components in its spectrum giving rise to the THz spectrum with difference frequency spectrum Ω. **d**, A THz time-domain scan (TDS) and **e**, corresponding spectrum from ZnTe crystal.

Figure 3.6 captures the generation of THz through the DFG process. Here an 800 nm beam is incidence on ZnTe crystal. The frequency components of the 800 nm beam mix with each other and the DFG spectrum is the corresponding THz spectrum. Another important thing is that the phase matching in this scheme is very straightforward and THz generation takes place in collinear geometry. Fig. 3.7 depicts an optical pump —THz probe system in transmission geometry I built

in the lab which uses ZnTe as the generation and the EO sampling crystal. NIR pulses with a central frequency of 800 nm and pulse width of 35 fs, are generated from a Spitfire regenerative amplifier with repetition rate of 1 kHz. The THz is generated after the ZnTe crystal and is focused onto the sample using an off-axis parabolic mirror (OAP). The THz beam size is 1 mm FWHM. After transmitting through the sample, THz beam is collimated and refocused on the EO sampling ZnTe crystal, overlapping with the optical gate beam (sampling pulse). The THz signal at a certain THz-gate time delay can be further read out by the EO sampling process. Figure 3.6c depicts a time-trace of a THz scan with its corresponding spectrum in Fig. 3.6d. The spectrum ranges from 0.1 THz to 2.6 THz with detection signal to noise ratio of 10000.

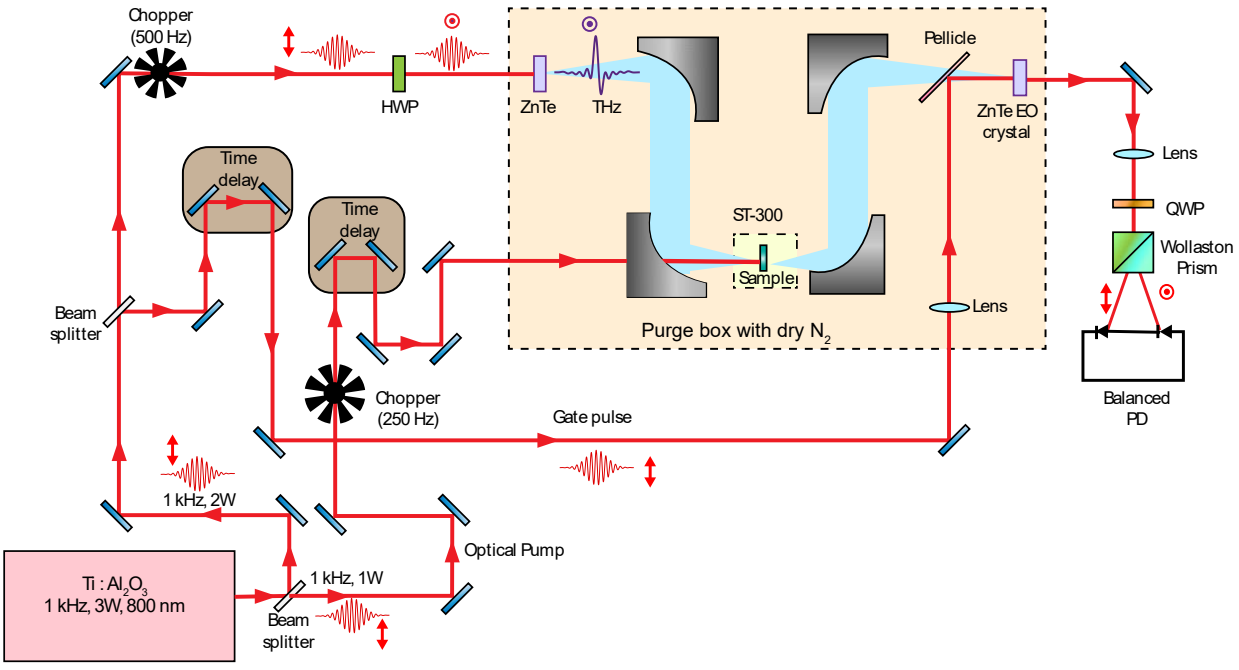

Figure 3.7: Schematic of the high-sensitivity optical pump – THz probe system in transmission geometry. THz is generated and detected using ZnTe crystal.

3.2.4 High-field THz generation with tilted pulse front scheme

Another prominent method to generate extremely high-field single-cycle THz pulses is called the tilted pulse front method. This is accomplished using a $LiNbO_3$ (LNO) crystal. In the previous section, we mentioned that in ZnTe or GaP crystals that generate THz pulses via DFG, the phase matching condition, $\boldsymbol{k}(\Omega_{THz}) = \boldsymbol{k}(\omega_1) - \boldsymbol{k}(-\omega_2)$ is satisfied because the 800 nm group velocity is equal to the THz phase velocity. As a result, a simple collinear geometry is used to generate THz. However, it is difficult to generate intense THz pulses in ZnTe since it is prone to two-photon absorption leading to free carrier absorption of THz pulse within the crystal when the fluence is high.

In light of this, LNO crystal is better suited to generate intense high-field THz pulses, since it has a higher damage threshold and is not prone to two-photon absorption, allowing higher pump fluences. However, because of large refractive index mismatch, LNO has a large mismatch between the optical group velocity and THz phase velocity. This results in a short coherence length and poor conversion efficiency in a collinear geometry. To overcome this, a tilted pulse front method was developed [82, 83] where the pump pulse continuously generates THz radiation in phase along the direction of THz output while propagating through the crystal. To fulfill the phase matching condition, the pump and THz pulse's propagation directions inside the crystal should make an angle γ such that, $v_{800\,nm}^{gr} cos\gamma = v_{THz}^{ph}$ and thus,

$$\gamma = \cos^{-1}\left(\frac{n_{800\,nm}^{gr}}{n_{THz}^{ph}}\right). \tag{3.10}$$

Using $n_{800\,nm}^{gr} = 2.27$ and $n_{THz}^{ph} = 4.96$, we obtain $\gamma = 63°$. We see a cartoon of the THz generation with tilted pulse method in Fig. 3.8. When the LNO crystal is cut in the angle of $63°$,

the THz pulse front generated upon entering LNO remains in phase with THz produced as the pump pulse travels further.

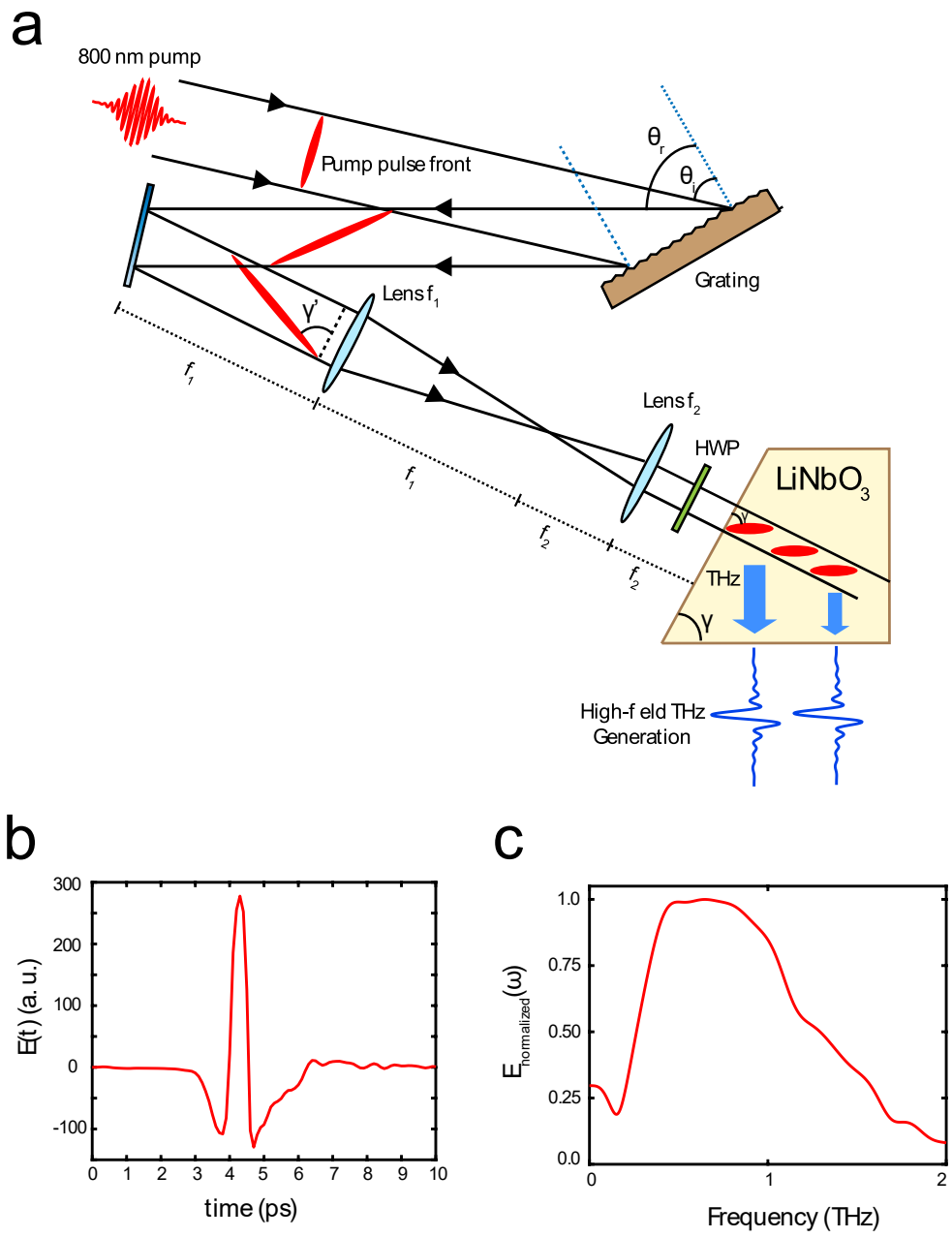

Figure 3.8: a, High field THz generation with tilted pulse front method. It shows the internal geometry of the pump pulse propagating through the LNO crystal with and angle of $\gamma = 63°$ with respect to the direction of travel. **b**, A THz time-domain signal and **c**, its spectrum.

In Fig. 3.8a, the 800 nm pump pulse is incident on the diffraction grating at an angle θ_i and is diffracted at the angle θ_r. The pulse front tilt angle in the air is γ' which can be expressed as,

$$tan\gamma' = \frac{sin\theta_i + sin\theta_r}{\cos\theta_r} = \frac{m\lambda p}{cos\theta_r}. \tag{3.11}$$

Here p is the groove density of the grating and $\lambda = 800$ nm. Therefore, by adjusting the diffraction angle and choosing a grating with proper groove density, one can control the tilt angle of the wave front in free space. However, just tilting the wave front does not guarantee generation efficiency because the beam after the grating is dispersed and spatially chirped after the grating which reduces the efficiency. This can be resolved by adding a pair of cylindrical lenses that form a telescope in $4f$ configuration. On the image plane of the telescope, the spatially dispersed beam is focused spatially and temporally, yielding the shortest possible pulse duration. To achieve the optimal THz output, we need to match the image of the grating and the tilt angle of the wave front so that the phase matching condition and shortest pulse duration are simultaneously satisfied. For $\theta_r = 60°$ and $\theta_i = 47°$, $\gamma' = 78°$.

Figure 3.8b shows the THz TDS off an LNO crystal and Fig. 3.8c depict its FFT spectrum. It is noted that the THz pulses generated in this method have very high electric field, and in our system, it was measured to be 400 kV/cm.

3.2.5 Broadband THz generation with 2-color laser plasma

We have discussed the THz generation via optical rectification and tilted pulse front method. Although the THz generated from these schemes have robustness, high sensitivity (ZnTe), high electric field (LNO), the bandwidth is limited to 3 THz. Hence, the search for a broadband THz source remains an open problem.

The development of two-color laser-induced gas plasma fills this gap. It can be used as a versatile tool for both intense and broadband THz generation [84-85]. The bandwidth depends on the pulse duration of the generation and detection. For a 35 fs 800 nm pulse used for generation, the bandwidth is 0.1 – 23 THz. Such a broadband spectrum allows for the time-domain measurement of numerous intriguing phenomena (phonons magnons, gaps and plasma edge). In the same way, the THz electric field from the plasma can be tens to hundreds of kV/cm., making it convenient for nonlinear THz spectroscopy, remote THz sensing etc. [86, 87].

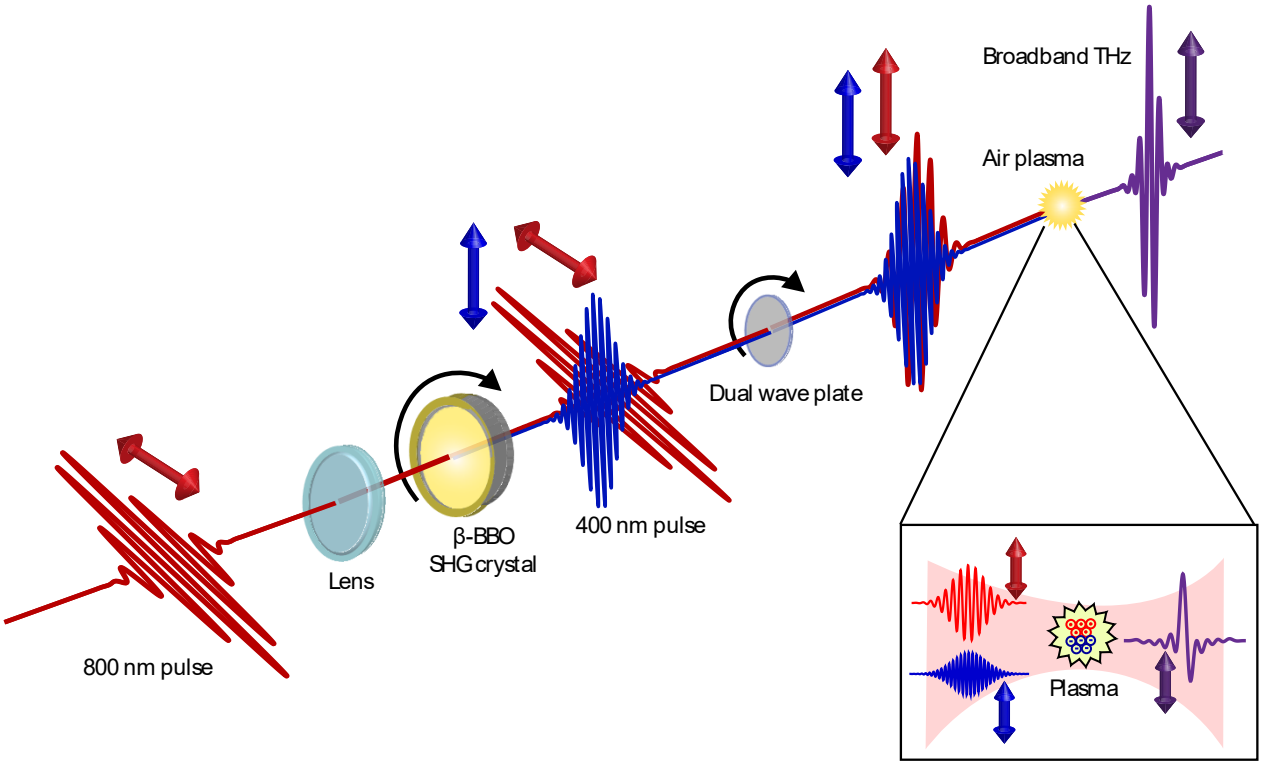

Figure 3.9: Horizontally polarized 800 nm pulses generate vertically polarized 400 nm pulses after passing through the BBO crystal. The DWP rotates the 800 nm polarization from horizontal to vertical. Both beams are focused into the air and create an air plasma which radiates broadband THz waves. Arrows indicate the polarization directions. Inset shows a detailed schematic of the THz generation process from the air plasma.

The most common way to generate the gas plasma is by focusing an 800 nm fundamental pulse (ω: FH) with its second harmonic (2ω: SH) into gas molecules. The polarization and power of the generated THz are determined by the relative phase difference ϕ between the FH and the SH beams, their polarization, and the plasma filament length [88, 89]. If both FH and SH are linearly polarized but are perpendicular, the THz intensity follows a sinusoidal relation with respect to ϕ and the resultant THz is radially polarized. If both FH and SH are circularly polarized, the THz polarization rotates with change of ϕ while keeping the intensity the same [90, 91]. When FH is circularly polarized but SH is linearly polarized, the THz polarization is elliptical and can be controlled tuning ϕ and the plasma filament length.

In this scheme, relative phase ϕ between FH and SH needs to be controlled to tune the intensity and polarization of the beam. Fig. 3.9 shows a cartoon of the THz generation. A p-polarized 800 nm beam goes through a β −Barium Borate (BBO) SHG crystal and generates s-polarized 400 nm pulses. As mentioned earlier, the 800 nm and 400 nm polarizations are perpendicular and hence, when they are tightly focused on the gas plasma, the resultant THz pulses will be radially polarized. To solve this problem, a 40 μm-thick dual wave plate (DWP) is used. A DWP works as a FWP with respect to 400 nm beam and rotates its polarization by 180°. However, it works as a HWP with respect to the 800 nm beam and its polarization is rotated by 90°. As a result, although the polarization of the 400 nm remains intact (s-polarized), the 800 nm polarization changes from p-polarized to s-polarized, and both beams become parallelly polarized. The THz generated in this case will be s-polarized (see inset of Fig. 3.9).

To have higher generation efficiency, one can add a wedge pair to control the relative delay between the 800 nm and 400 nm so that the beams reach the plasma at the same time. In our

system, we found that the DWP induces a phase delay to compensate for the lag between 800 nm and 400 nm beams, and both beams reach the plasma nearly at the same time.

The generated THz can be detected by THz field-induced second harmonic (TFISH) [92], air-biased coherent detection (ABCD) with the addition of heterodyning detection [93] or EO sampling. In our setup, we chose the EO sampling method, using GaP crystal to detect 0.4 – 7.5 THz and GaSe for 7.5 – 22.5 THz.

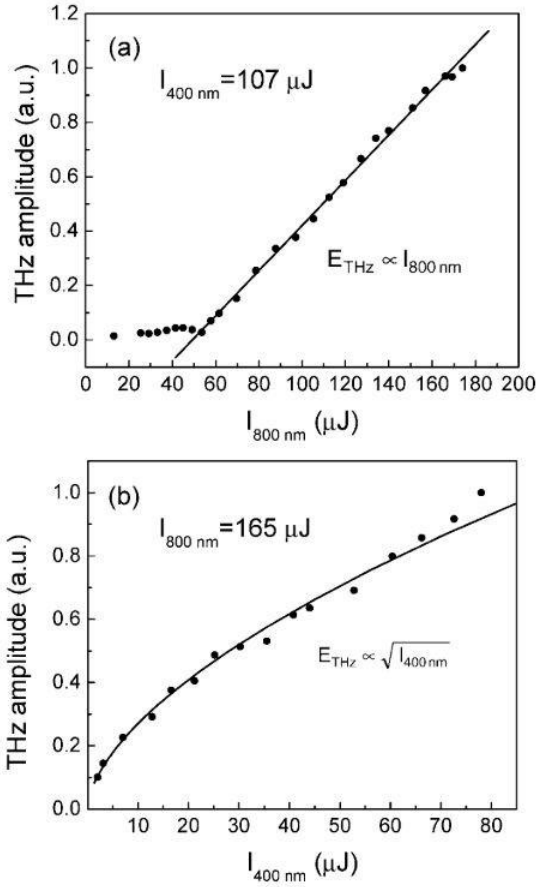

Figure 3.10: Power scaling of the generated THz wave with that of 800 nm and 400 nm. Adapted from ref. [94].

The generation mechanism of broadband THz from plasma filament has been under debate for a long time. The most commonly proposed scenario is the optical rectification by the four-wave mixing (FWM) [84]:

$$E_{THz} \propto \chi^{(3)} E_{2\omega}(t) E_{\omega}^{*}(t) E_{\omega}^{*}(t) \cos\phi\,, \tag{3.12}$$

where ϕ is the relative phase between the FH and SH beams. The THz frequency is determined by difference frequency $\Omega_{THz} = \Omega_{2\omega} - 2\Omega_{\omega}$ (Ω represents a frequency band), and its power scales with $P_{THz} \propto P_{2\omega} P_{\omega}^{2}$, as confirmed by previous reports [94] (see Fig. 3.10). Other reports indicate that the third order nonlinearity $\chi^{(3)}$ either from thermal or pondermotive effect is too small to explain the strong THz field strength [95].

Besides common laser frequency ratios ($\omega_1 : \omega_2 = 1:2$), THz can also be generated effectively from other ratios ($\omega_1 : \omega_2 = 1:4$, $2:3$ and $3:4$) [96, 97]. The THz field strength shows similar scaling behavior with different frequency ratios, confirming the FWM mechanism [98]. A plasma current model (field ionization) was proposed. In this process, a net current is formed from field ionization, shorter than laser pulse duration which is expressed as

$$\boldsymbol{J}_0 = -e n_e \boldsymbol{v}_0 = \frac{e^2 n_e \boldsymbol{A}_L(\Psi_0)}{m_e c}, \tag{3.13}$$

where $\boldsymbol{v}_0 = -e\boldsymbol{A}_L(\Psi_0)/m_e c$ is the elctron velocity, $\boldsymbol{A}_L$ is the laser vector potential and Ψ_0 is the electron creation position. The second step is radiation generation while current is modified by the plasma,

$$\left(\nabla^2 - \frac{1}{c^2}\frac{\partial^2}{\partial t^2} - \frac{\omega_p^2}{c^2}\right)\boldsymbol{A}_{THz} = -\frac{4\pi \boldsymbol{J}_0}{c}. \tag{3.14}$$

Here, $\omega_p = \sqrt{4\pi e^2 n_e / m_e}$ is the plasma frequency and $\boldsymbol{A}_{THz}$ is the THz vector potential. It has also been shown that THz generation efficiency decreases with the increasing laser frequency and scales linearly with laser wavelength, i.e., the THz generation efficiency from two-color laser plasma for 1800 nm is 30 times stronger than that for 800 nm [98].

3.3 Optical pump – broadband THz probe spectroscopy

In this section, we will discuss the experimental layout of the optical pump – broadband THz probe experiment that I built in the lab.

3.3.1 Experimental scheme

Figure 3.11 shows a schematic of our experiment. For our near-infrared optical pump – broadband THz probe experiment, we used a regenerative amplified Ti:sapphire laser system with pulse energy of 3 mJ, pulse duration of 35 fs, 1 kHz repetition rate and 800 nm central wavelength as the main light source.

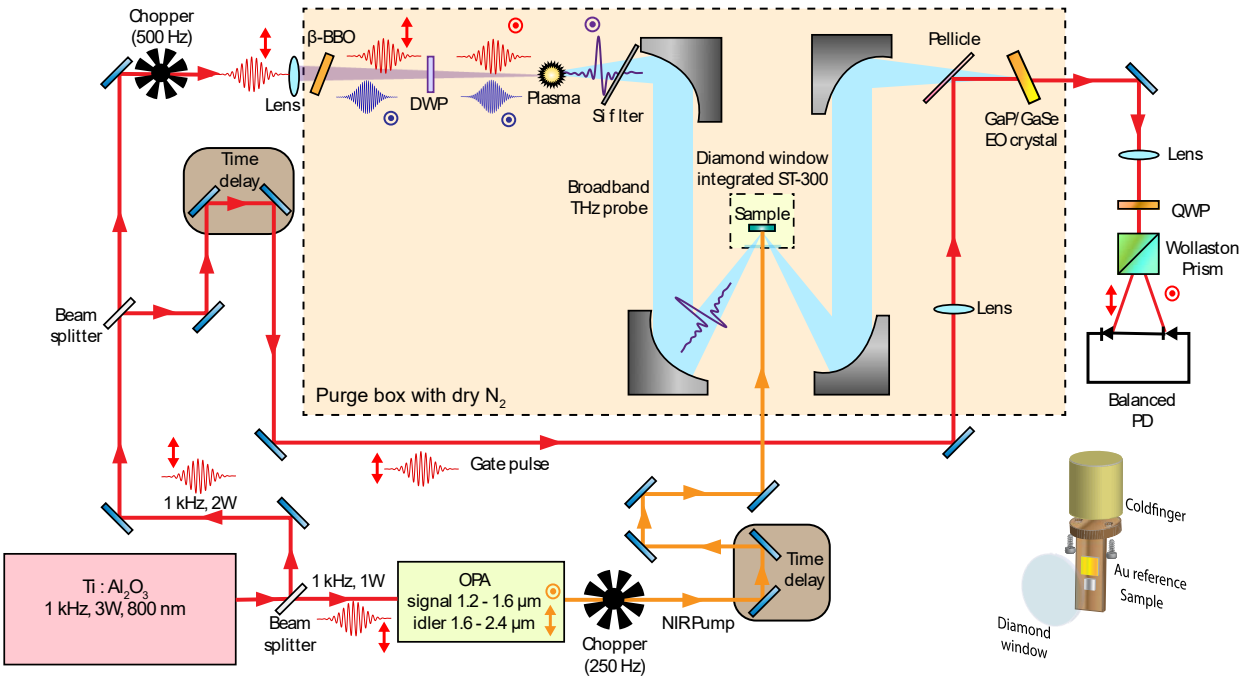

Figure 3.11: Experimental setup for near-infrared pump – broadband THz probe spectroscopy. DWP: dual wave plate, OPA: optical parametric amplifier, BBO: β-Barium Borate, QWP: quarter wave plate, PD: photodiode. 2.4 μm pump beams are generated as idler beams from the OPA while broadband THz probe pulses are generated from a two-color laser-induced air plasma. GaP/GaSe crystals are utilized as the EO sampling crystal.

The light source is split into three ways: one beam for the pump pulse and two beams for the generation and detection of the THz pulse. The OPA can generate signal beams with wavelengths from1.2 μm – 1.6 μm, and weaker idler beams with wavelengths from 1.6 μm – 2.4 μm. We choose 2.4 μm idler beam as the pump in our experiment with TNS. Horizontally polarized 2.4 μm pump pulses were generated after 1mJ 800 nm laser pulse was injected into a commercial TOPAS-C optical parametric amplifier (OPA). The beam diameter was 3 mm FWHM. The pulse width out of the OPA, 2 mirrors before the sample, was measured to be 45 fs.

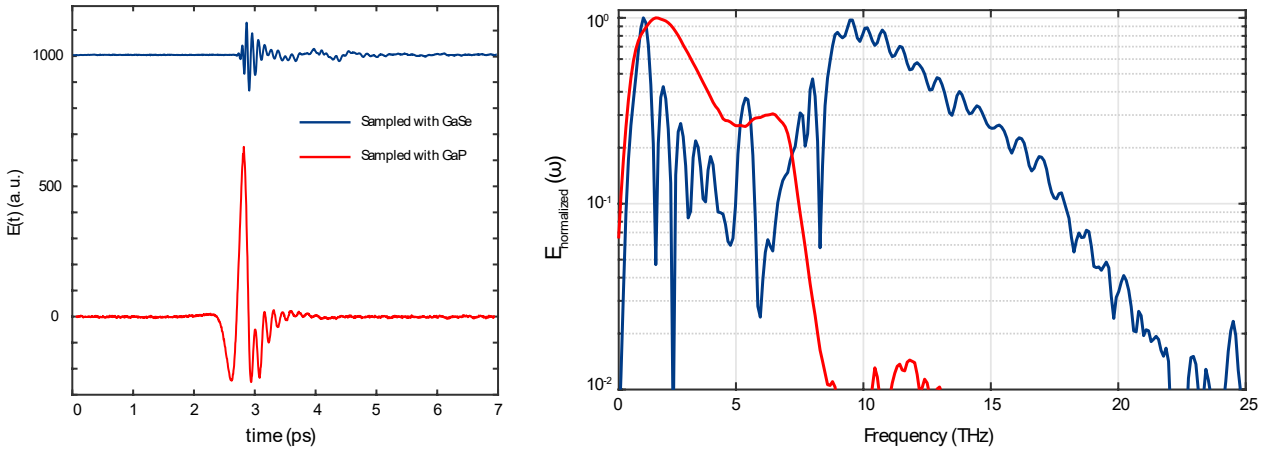

Figure 3.12: a, THz TDS signal from a gold reference when EO sampled with GaP (red) and with GaSe (blue). **b**, The normalized FFT spectrum, it is noted that GaP can give access to 0.4 – 7.5 THz while GaSe resolves 7.5 – 22.5 THz.

For the broadband THz generation, 800 nm pulses go through a 100 μm type-I BBO crystal which generates vertically polarized SH (400 nm) waves. Then the FH and the SH signals are passed through a 40 μm-thick dual wave plate (DWP) which rotates the polarization of the 800 nm and 400 nm waves by 90° and 180° respectively. DWP behaves as a quarter wave plate (QWP) and half wave plate (HWP) with respect to 800 nm and 400 nm wavelengths, respectively. As

such, both 800 nm and 400 nm waves become vertically polarized. Then both beams are focused into air by a 6-inch lens to generate an air-plasma that radiates vertically polarized THz waves. The setup is enclosed in a nitrogen purged box. A silicon wafer is placed to block the residual 800 nm and 400 nm beams.

The THz beam is collimated using a 4-inch focal length OAP. It is then focused on the sample using another OAP with 3-inch focal length. The incident angle for the THz probe on the sample is $30°$ and the beam diameter is ~ 1 mm. To detect the THz beam, we employed electro-optic sampling (EOS). For this purpose, we used a 300 μm-thick $\langle 110 \rangle$ GaP detection crystal that enabled spectral measurements from 0.5 – 7.5 THz and a 90 μm z-cut GaSe for 7.5 – 22.5 THz detection. We also show THz TDS from a gold mirror used as a reference and the corresponding Fourier transform amplitude (Fig. 3.12).

3.3.2 Diamond window for broadband LT measurements

The TNS and gold reference samples were mounted inside a Janis ST-300 cryostat with a 36 mm-diameter, 600 μm-thick diamond window custom-made by Diamond Materials GmbH®. In most cryostats, the window used is made of quartz. However, quartz has a narrow bandwidth and cannot resolve the frequencies beyond 3 THz. On the contrary, in our optical pump – broadband THz probe setup, the frequency range is 0.4 – 22.5 THz. As such, a quartz window cannot enable us to investigate material properties at lower temperatures at high frequency regime owing to the lower transmission of quartz. Integrating the diamond window to the cryostat gave us access to the broad THz spectrum at low temperatures thanks to the broadband transmission properties of diamond (see Fig. 3.13 and Fig. 3.14 for details).

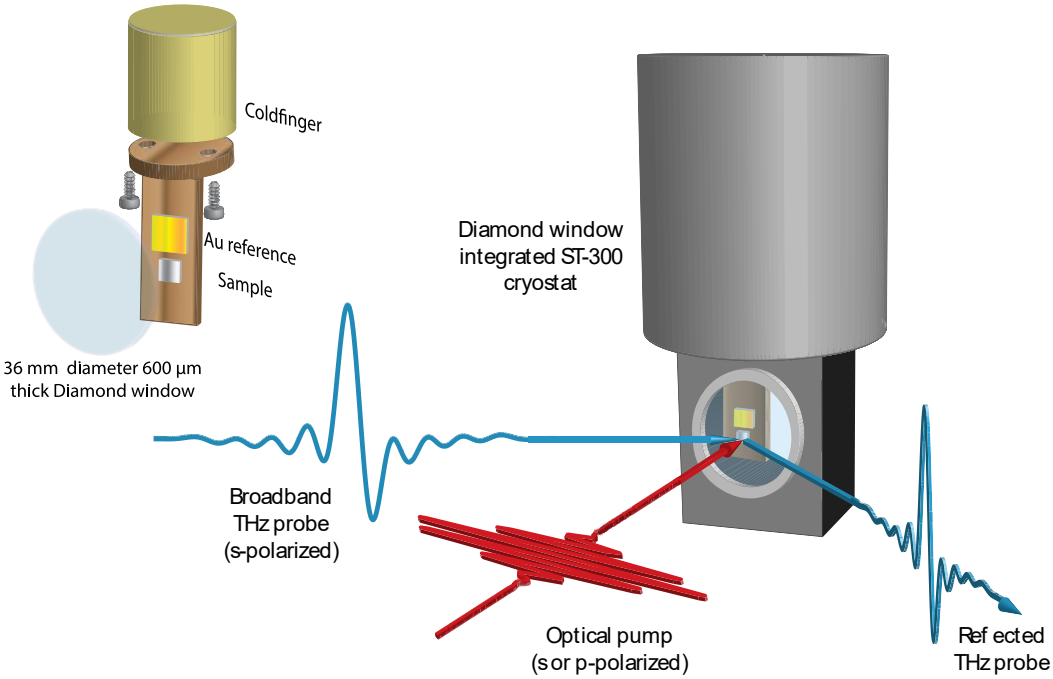

Figure 3.13: Incorporation of a diamond window in the cryostat to enable measurements at higher frequencies.

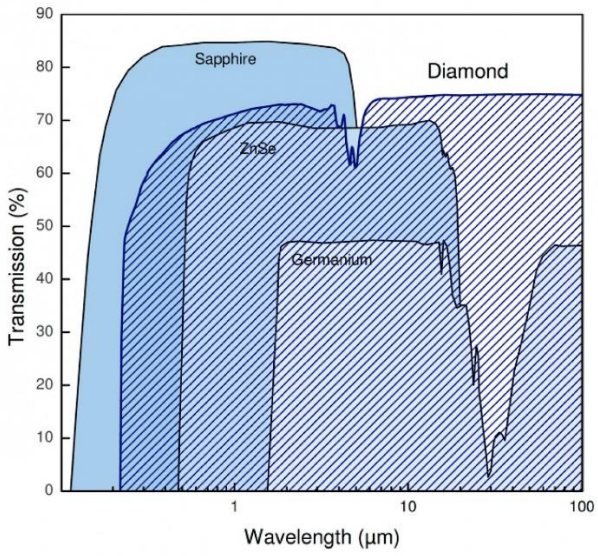

Figure 3.14: Diamond transmission, revealing a higher transmission rate in the regime suitable for our measurements.

3.3.3 Polarization check of the broadband THz

Previously we mentioned that, when the 800 nm FH and 400 nm SH are both s-polarized, the THz generated will be s-polarized as well. To perform this, we used a DWP that changes the originally p-polarized FH to s-polarized and keep the SH polarization same (s-polarized). In principle, the generated broadband THz pulse from the two-color laser plasma will be s-polarized as well.

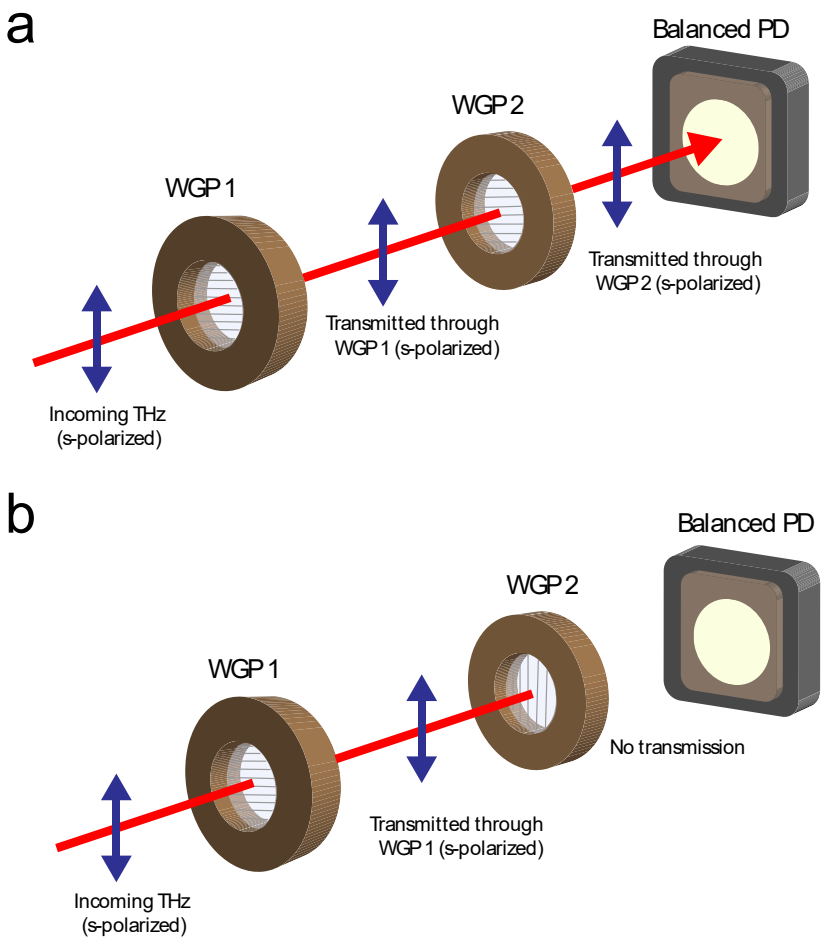

Figure 3.15: a, configuration 1 with both WGP horizontally polarized and **b**, cross polarized configuration.

In order to confirm this, we used two wire grid polarizers (WGP). If a WGP is polarized horizontally (vertically), s-polarized light will be transmitted (reflected) while p-polarized light will be reflected (transmitted). We used two configurations: (1) both WGPs horizontally polarized (Fig. 3.15a), and (2) WGP 1 is horizontally polarized but WGP 2 is vertically polarized (cross polarized, Fig 3.15b).

In configuration 1, WGP 1 is horizontally (p) polarized and therefore, s-polarized THz beam will be transmitted. Since WGP 2 is also horizontally polarized, the THz beam will be transmitted through it and will reach the balanced photodiode (BPD), resulting in a finite signal. In contrast, in configuration 2, WGP 2 is vertically polarized and as such, the s-polarized THz beam will not be able to reach the BPD, leading to a zero signal.

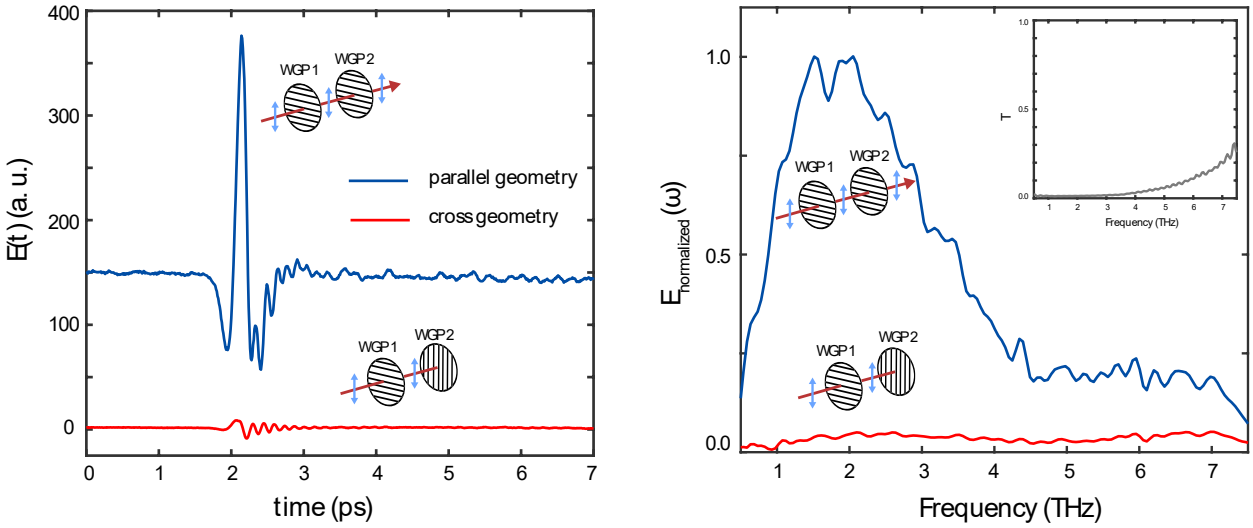

Figure 3.16: a, THz TDS of a gold reference mirror with two WGPs horizontally polarized (blue), and cross polarized (red). **b**, Corresponding FFT spectrum, showing a large signal for parallel configuration and very small signal for cross polarized configuration, inset shows the relative transmission of the cross polarization scheme referenced with the parallel polarization scheme.

Figure 3.16 shows the data of the THz profile (TDS and FFT) in both parallel polarization and cross polarization scheme. In the parallel configuration (blue), both WGPs are horizontally polarized, and the s-polarized THz wave will transmit through both WGPS to reach the BPD. This is manifested in a large signal in BPD, with same magnitude as the signal with no WGPs. On the other hand, for the cross-polarization scheme, the signal in the BPD is very small or negligible. Fig. 3.16a and 3.16b show a clear difference between both configurations, with parallel polarization of WGPs leading to a very large signal compared to the cross-polarization scheme.

The inset of Fig. 3.16b shows the transmission spectrum of the cross-polarization signal when it was referenced with the parallel polarization signal. It is revealed from the data that the transmission is very low at lower frequencies, verifying that the THz is s-polarized and cannot transmit through WGP 2. However, there is a small transmission at higher frequencies which may be leakage of high-frequency s-polarized components through the vertically polarized WGP 2 in the cross polarized scheme.

3.4 Data acquisition (DAQ)

The extraction of very weak pump-probe signals is challenging. Lock-in amplifier has been the standard equipment since the 1930's to extract signal from noisy backgrounds by locking the detection frequency to the modulation frequency of the signal. However, pulsed lasers experience shot-to-shot noise and long-term drift during the measurement, making the signal analysis more complicated. A more straightforward way to overcome this is to record each pulse by the data acquisition (DAQ) system. The DAQ system digitizes all the signals from the photodiode pulse by pulse, allowing real time noise reduction, and it has competitive signal to noise performance as the lock-in amplifier [99].

We implemented the DAQ on our 1kHz regenerative amplifier laser system. The DAQ card is PXIe-5122 from National Instrument with 100 MHz maximum sampling rate, 100 MHz bandwidth, and 14-bit analog digitization. The sampling rate is enough to digitize the signal on most of the photodiodes with bandwidth smaller than ~ 10 MHz. We mainly focus on the THz-TDS and pump-THz-probe experiments using 1 MHz bandwidth Newport 2307 balanced photodiodes.

3.4.1 DAQ scheme for THz TDS setup

In this section, we will discuss the data acquisition scheme for a THz time-domain setup. A typical temporal sequence of data taking for THz-TDS experiments is shown in Fig. 3.17. The repetition rate of the gate pulse is 1 kHz, and the THz pulse is chopped at 500 Hz, which means the gate beam sees the THz on the detection crystal every other millisecond (ms). The DAQ is triggered by a 500 Hz transistor-transistor-logic (TTL) signal. This is accomplished by using a frequency divider which takes in the 1 kHz laser TTL signal as input and produces the 500 Hz trigger signal. The reason to use the TTL signal from the frequency divider, and not the signal from the 500 Hz chopper is that the signal from chopper is not stable enough to trigger the DAQ.

The signal on the balanced photodetector for each pulse is fully digitized by the DAQ, which enables further analysis of the signal pulse by pulse. In Fig. 3.17, The first row shows the gate pulses at 1 kHz repetition rate, arriving every 1 ms. The second row depicts THz TDS chopped at 500 Hz, arriving every 2 ms. At $t = 1$ ms, both the gate and THz beams are on the detection crystal. The signal on the balanced photodiode is proportional to the instantaneous THz electric field plus some background signal.

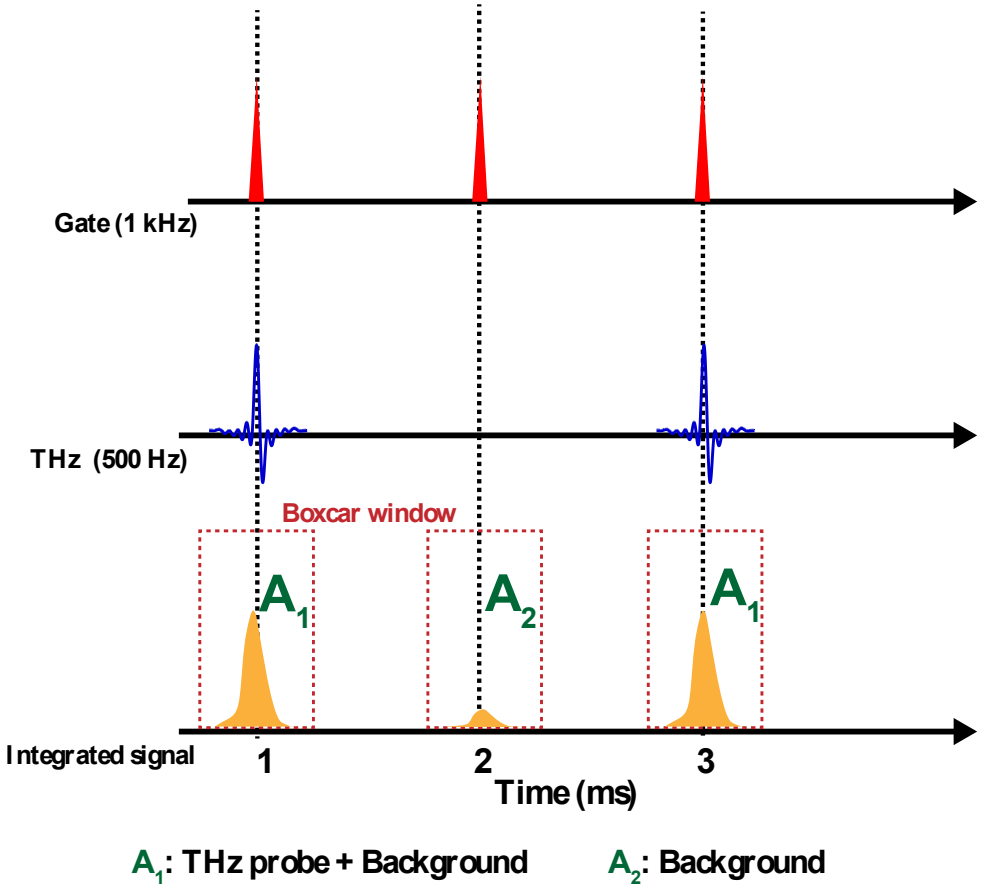

Figure 3.17: Temporal sequence of data acquisition for THz TDS using DAQ. Gate pulse (red) is arriving at the detection crystal at a 1 kHz repetition rate. The THz pulse (blue) is chopped at 500 Hz, enabling a beam to reach the detection crystal every other millisecond. The red dotted rectangle is the boxcar integration time window and yellow region show the integrated signal, where A_1 = THz signal and A_2 = background.

We select a boxcar integration time window (red dotted rectangle) that covers only the signal to obtain the integrated signal without adding the noise tail. In the third row, the yellow region is the boxcar integration of both THz and gate pulses. The integrated signal is computed by summing over all the data points in the selected time window. At the $t = 2$ ms, the THz is blocked by the chopper. Thus, only the gate beam on the detection crystal is present which yields an output.

The integrated signal is thus a background (very small yellow region). The THz signal from the first two milliseconds is calculated by,

$$E_{THz} = A_1 - A_2, \tag{3.15}$$

where A_1 and A_2 are the integrated signals at $t = 1$ ms and $t = 2$ ms, respectively. Fig. 3.18 displays the DAQ connection diagram for a THz TDS setup. The 1 kHz TTL signal decomposed into a 500 Hz trigger signal which goes to the DAQ Channel 0. The 500 Hz TTL signal is also used to chop the THz probe at 500 Hz frequency. In the experiment, the THz pulse reaches the BPD which is connected to the DAQ through Channel 1. DAQ processes the signal, and the output is shown in a computer using LabVIEW software.

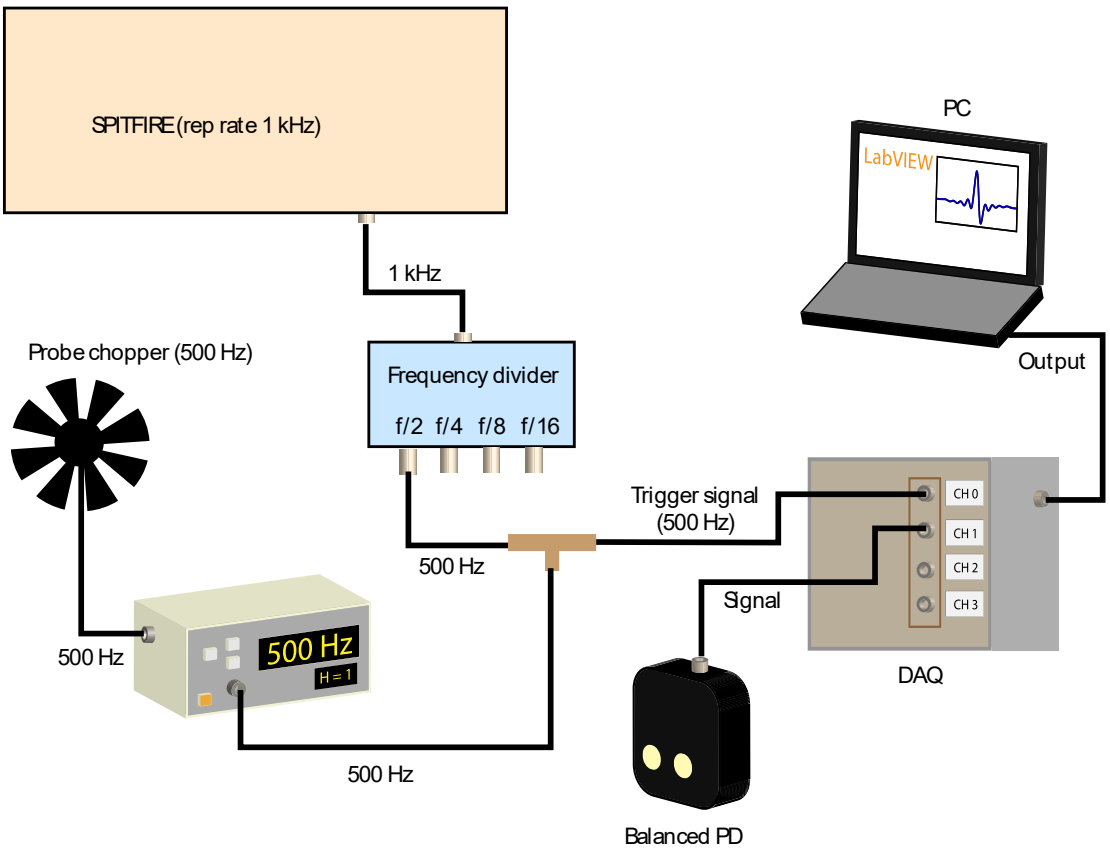

Figure 3.18: THz TDs setup connection for DAQ.

3.4.2 DAQ scheme for Pump-probe setup

By adding an appropriate pump beam into the THz-TDS set-up, we can perform a pump-THz probe experiment. In this case, we use the differential chopping technique where the THz and pump beams are chopped by 500 Hz and 250 Hz, respectively. Since the THz is chopped at 500 Hz, pulses will arrive at the detection crystal every other millisecond. On the contrary, 250 Hz chopped pump means that first two pulses will be allowed in the first two milliseconds and next two pulses will be blocked in the next two milliseconds. The gate pulse repetition is 1 kHz, same as the THz TDS setup discussed earlier. The temporal sequence is shown in Fig. 3.19. The DAQ treats four milliseconds as a period since it's triggered by 250 Hz. We consider four boxcar integration time windows defined by the red dotted rectangles in Fig. 3.19:

At $t = 1$ ms, Gate, THz probe and pump beams reach the detection crystal. The signal on the balanced signal consists of the pumped THz probe signal $E_{THz\ probe\ with\ pump}$, background E_{bkg}, and pump scattering signal δE_{pump}. The integrated signal is $A_1 = E_{THz\ probe\ with\ pump} + E_{bkg} + \delta E_{pump}$. As evident in Fig. 3.19, it results in a large integrated signal (yellow region).

At $t = 2$ ms, the THz probe is blocked by the optical chopper and only the pump pulse and the gate pulse are present in the detection crystal. The signal consists of the pump scattering and background: $A_2 = E_{bkg} + \delta E_{pump}$, resulting in a smaller integrated signal.

At $t = 3$ ms, the pump beam is blocked by the optical chopper. The signal consists of the unpumped THz probe and background. Integrated signal $A_3 = E_{THz\ probe\ without\ pump} + E_{bkg}$.

At $t = 4$ ms, both the THz probe and pump beams are blocked. The signal is the balanced output from the photodetector. Integrated signal $A_4 = E_{bkg}$. This will be a negligible signal predominantly containing background noise.

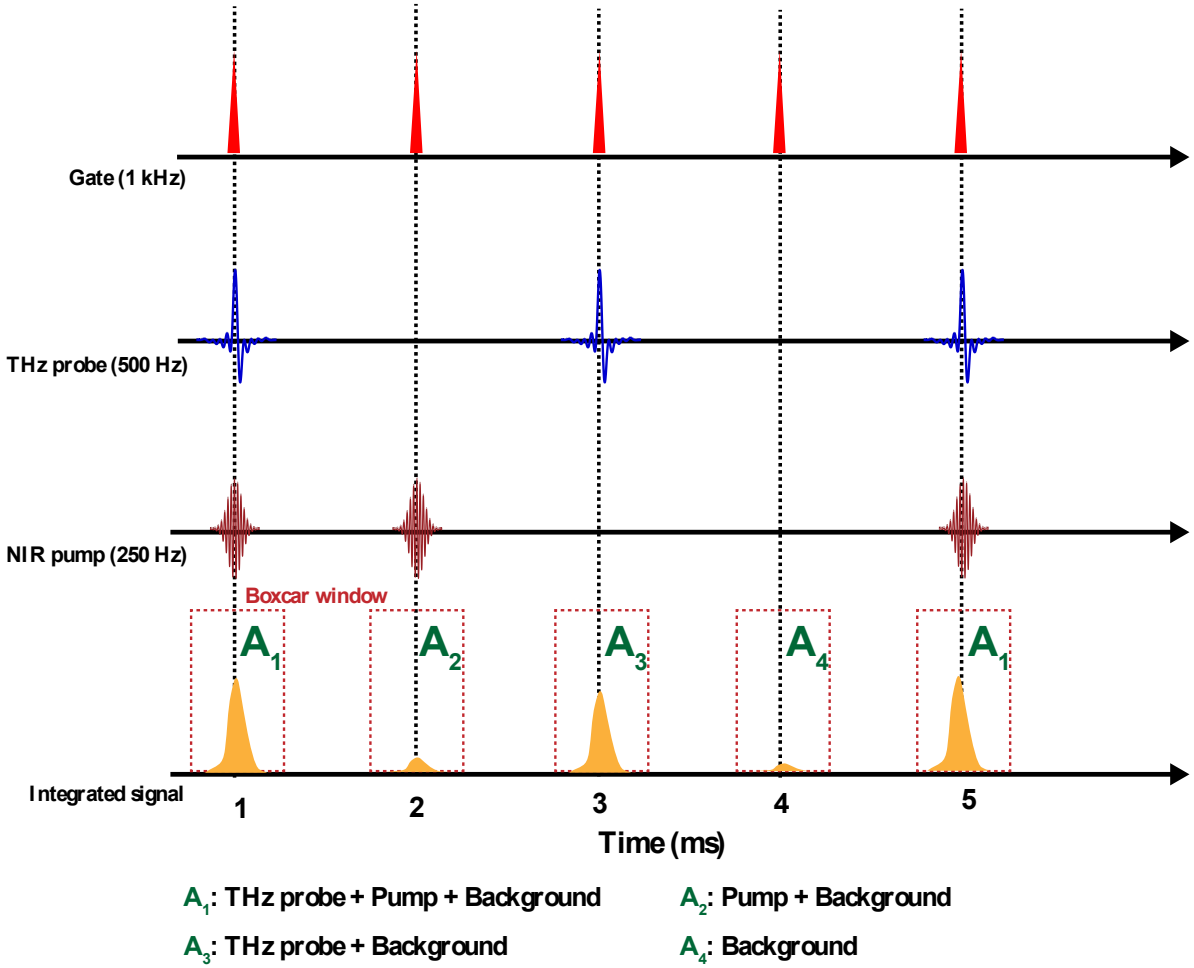

Figure 3.19: Temporal sequence of data acquisition for THz TDS using DAQ. Gate pulse (red) is arriving at the detection crystal at a 1 kHz repetition rate. The THz pulse (blue) is chopped at 500 Hz, enabling a beam to reach the detection crystal every other millisecond. The pump beam (maroon) is chopped at 250 THz, resulting in two consecutive pulses in the first two milliseconds and no pulses in the next two milliseconds. The red dotted rectangle is the boxcar integration time window and yellow region show the integrated signal, where A_1 = THz + pump, A_2 = pump only, A_3 = THz only, and A_4 = background.

We can obtain all the information for the pump-probe measurement by doing simple algebra of the four integrated signals. The unpumped THz probe signal is written as,

$$E_{THz\ probe\ without\ pump} = A_3 - A_4, \tag{3.16}$$

while the pumped-THz signal is,

$$E_{THz\ probe\ with\ pump} = A_1 - A_2. \tag{3.17}$$

Thus, we write the pump induced change of the THz probe as,

$$dE_{pump-probe} = E_{THz\ probe\ with\ pump} - E_{THz\ probe\ without\ pump} = A_1 - A_2 - A_3 + A_4, \tag{3.18}$$

and the pump-probe signal is expressed as,

$$\frac{dE_{pump-probe}}{E_{probe}} = \frac{A_1 - A_2 - A_3 + A_4}{A_3 - A_4}. \tag{3.19}$$

The DAQ has the advantage over a single lock-in amplifier in that pulse-by-pulse pump-probe signal is recorded. Any short- or long-term drift of the signal will be corrected. For THz pump – THz probe experiment, intense THz pump scattered into the EOS crystal can overwhelm the THz probe. With the help of DAQ and differential chopping, a weak THz probe signal can be extracted as shown in (3.19).

The connection diagram of DAQ for pump-THz probe is shown in Fig. 3.20. The 1 kHz TTL signal decomposed into a 250 Hz trigger signal using the frequency divider. Using a T-connector, one part of this signal can reach the pump chopper to chop the pump at 250 Hz frequency.

Another part of the 250 Hz trigger signal goes to the probe chopper. Using a second T-connector, this signal is divided into two components. The first component goes to the probe chopper. Although this is a 250 Hz trigger signal, the probe chopper is set into the second harmonic ($H = 2$) mode and hence, the probe will be chopped at 500 Hz. The remaining component of the 250 Hz TTL signal is connected to the Channel 0 of DAQ from the other side of the T-connector. This is the signal that will trigger DAQ. The pump-probe signal reaches the BPD which is connected to the DAQ through Channel 1. DAQ processes the signal, and the output is shown in a computer using LabVIEW software.

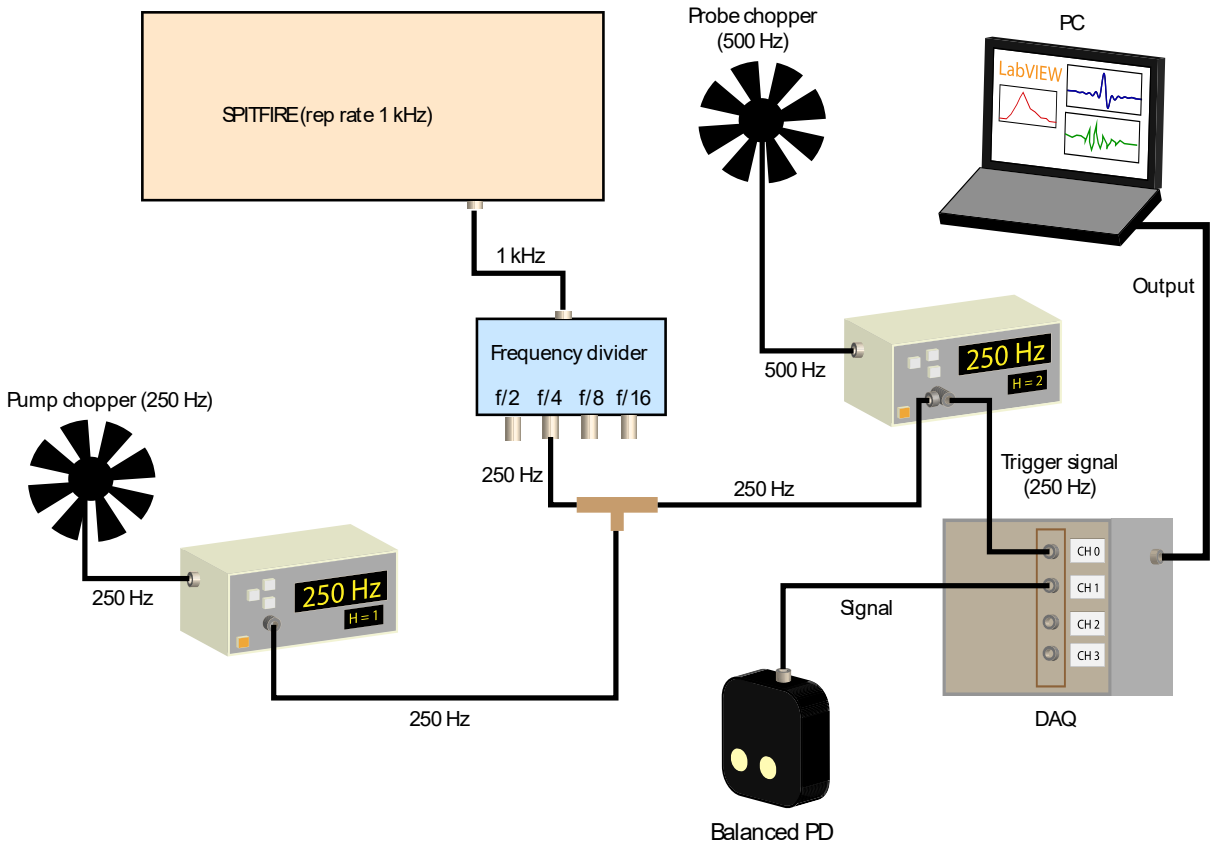

Figure 3.20: Pump-probe setup connection for DAQ.

3.5 Kindt-Schmuttenmaer correction

In this section, we will discuss the scanning scheme. In the optical pump — broadband THz probe experiment in our lab, we do a 2-d scanning scheme. That is, we perform THz TDS spectroscopy at different pump-probe delays. There can be unwanted spectral features, if the relative delay between the pump and all the points in the probe pulse do not remain constant. Thus, it is a must to perform the THz TDS correctly so that there is no artifact.

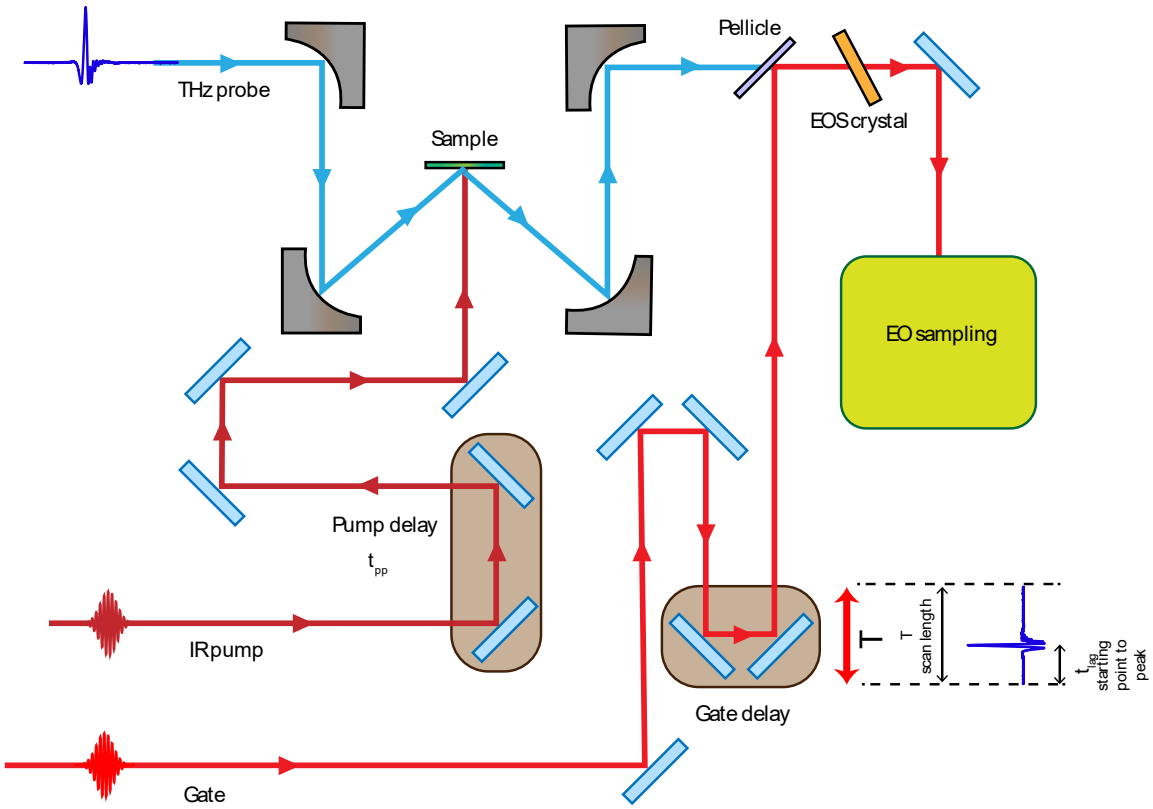

Figure 3.21: Simplified pump-probe setup with gate-probe delay with scan length T that gives a time-trace of THz. The pump delay is fixed.

3.5.1 Wrong scheme

Figure. 3.21 displays the cartoon of the pump-probe setup I built. The broadband THz (blue) reaches the sample in the cryostat, is reflected off it and reaches the EO sampling crystal. An optical gate pulse overlaps with the probe at the EO sampling crystal and the instantaneous change to its refractive index is proportional to the instantaneous electric field of the THz. To read out the full temporal response of the THz waveform, the gate is delayed with a motorized delay stage and by controlling the gate-probe delay time T, one can capture the time trace of the THz pulse. Here the THz TDS length is equal to the amount of time the delay stage moved (T). The pump (red) is also delayed using a motorized delay stage and controlling the pump-probe delay t_{pp}

allows for the study of photoexcited relaxation dynamics of the material. To obtain the photoexcited spectrum, the ideal approach is to tune the delay time t_{pp} using the pump-probe delay stage, then perform THz TDS by controlling the gate-probe delay T.

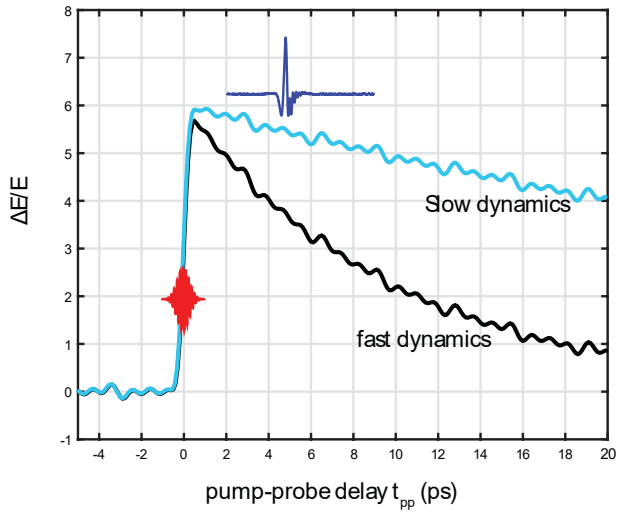

Figure 3.22: Slow and fast pump-probe dynamics. The red pulse at t_{pp} =0 is the pump pulse that initiates the dynamcis.

Figure 3.22 depicts the transient pump-probe signal for slow (light blue) and fast dynamics (black). The blue pulse indicates the THz pulse while the red pulse at $t_{pp} = 0$ ps denotes the pump that initiates the dynamics. The delay time t_{pp} is defined as the time delay between the pump and probe peaks. It is noted that the slow dynamics exhibit flat relaxation trend, and the relaxation time is longer than the temporal scan length of probe pulse. Hence, every single point in the probe pulse feels the photoexcitation equally. To be precise, with respect to each point in the probe pulse, the effect of the pump pulse is the same, as if each point in the probe were at the same pump-probe delay.

However, for the fast dynamics, we see a rapid relaxation and the signal exponentially drops fast. The relaxation time is also in the order of the probe pulse duration. Therefore, different points in the probe feels the pump effect differently as if they were at different time delays with respect to the pump.

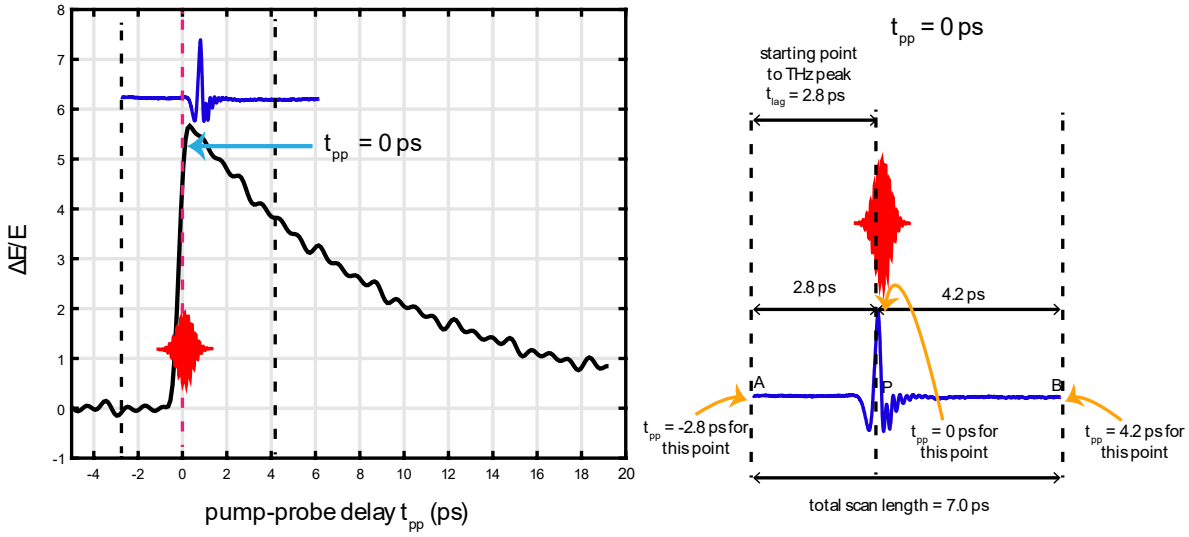

Figure 3.23: Case of $t_{pp} = 0$ ps for a THz pulse with scan length $T = 7$ ps and the relative pump-probe delay with respect to different data points in the THz probe pulse.

For example, consider the case in Fig. 3.23. The probe scan duration is $T = 7$ ps. And the peak of the THz occurs 2.8 ps after the first scanning point A. We define this time as t_{lag}. In a nutshell, the leftmost (A) point in the THz probe scan and the peak of the THz (P) are 2.8 ps apart, and the THz peak point P and the end point of the scan (B) are $7 - 2.8 = 4.2$ ps apart. For $t_{pp} = 0$ ps, the peak of the THz and the pump pulse must overlap. However, according to the figure, with respect to the starting point A of the THz, the pump-probe delay is -2.8 ps, as if point A reached

the sample 2.8 ps before the pump. And with respect to the end point (B), the delay is 4.2 ps, indicating that point B reaches the sample 4.2 ps after the pump.

For a 2-d scanning scheme, the effect of the pump on all the data points in the probe pulse should be the same, i.e., for $t_{pp} = 0$ ps, the delay should be 0 ps with respect to all the points in the probe. On the contrary, from Fig. 3.23 it is evident that different points in the probe pulse reach the sample at different time delays with respect to the pump. This will create artifacts and the photoinduced spectrum obtained spectrum obtained in this way is erroneous.

3.5.2 Corrected scheme

The main issue in the previous scheme is that to yield photoexcited spectrum at delay t_{pp}, we stayed at a fixed pump-probe delay t_{pp}, then performed THz TDS by controlling the gate-probe delay T. For this reason, the different THz probe points see the pump differently, thereby, leading to artifacts in the spectrum. To resolve this, we performed the Kindt-Schmuttenmaer simultaneous scanning scheme [100] where alongside the gate-probe delay scan T, the pump is also scanned simultaneously in a certain temporal direction such that the pump-probe delay with respect to all the probe points remains constant.

First, we define the time difference between the starting point (leftmost) of the THz scan and the peak THz as t_{lag}. The whole THz probe pulse scan duration is T. For dynamics at a certain t_{pp}, first the pump delay is moved to the relative time delay $t_{rel} = t_{pp} + t_{lag}$. Then, both the gate-probe delay scan (THz TDS) and the pump will start scanning simultaneously. The THz TDS scan duration is T. Also, the pump-probe delay will scan from $t_{rel} = t_{pp} + t_{lag}$ to $t_{rel} = t_{pp} + t_{lag} - T$. Therefore, the pump scanning duration is also T (Fig. 3.24).

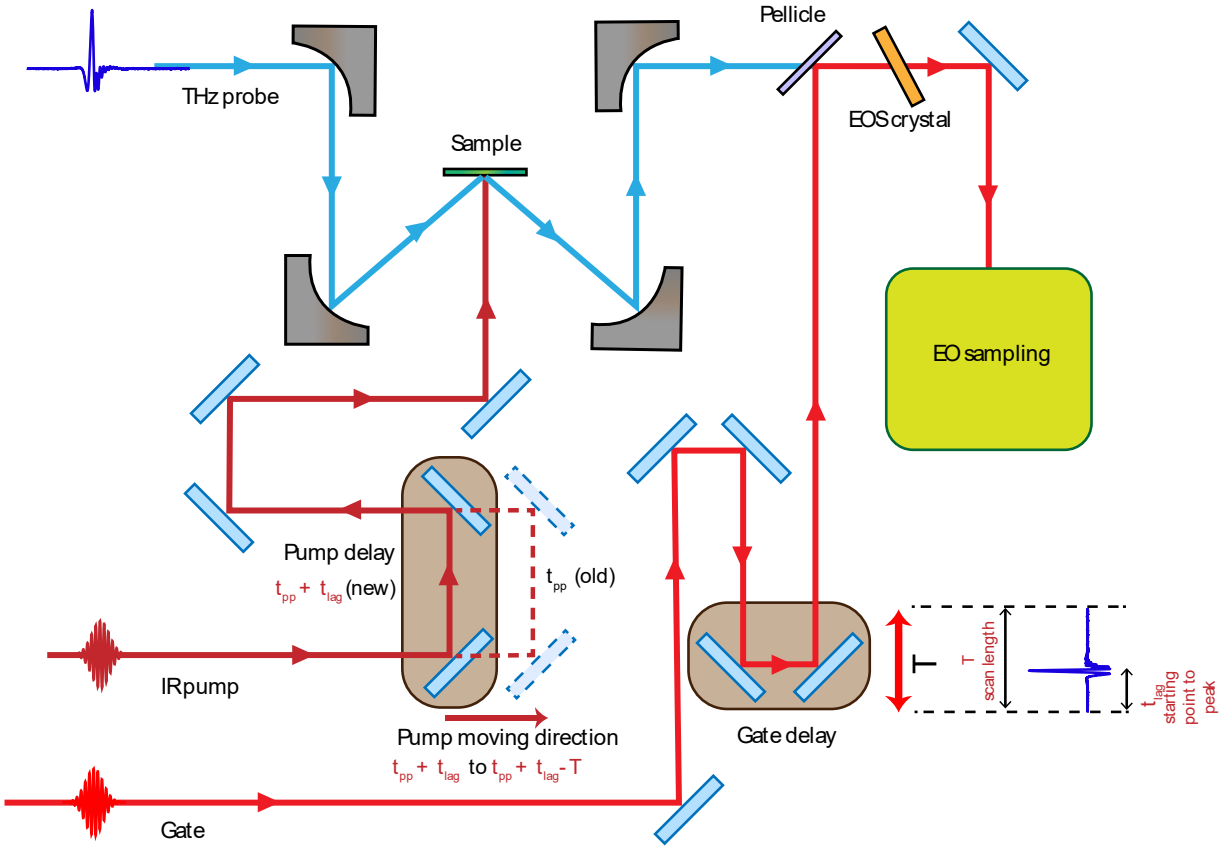

Figure 3.24: Simplified pump-probe setup with gate-probe delay with scan length T that gives a time-trace of THz. The pump delay is moved to $t_{rel} = t_{pp} + t_{lag}$ and scanned from $t_{rel} = t_{pp} + t_{lag}$ to $t_{rel} = t_{pp} + t_{lag} - T$, simultaneously with the THz TDS.

This is explained in Fig. 3.25. We choose $T = 7$ ps, $t_{lag} = 2.8$ ps. For $t_{pp} = 0$ ps, before scanning, the pump is moved to $t_{rel} = t_{pp} + t_{lag} = 0 + 2.8 = 2.8$ ps. We note that it looks as if the pump reached the sample 2.8 ps prior to the probe. However, we also note that with respect to to leftmost point (A) in the THz scan, the time delay is 0 ps, meaning that point A sees the pump at $t_{rel} = 2.8$ ps the same way the THz peak P sees the pump at $t_{pp} = 0$ ps (previous scheme).

When the scans start simultaneously, the pump takes the same time to scan from $t_{rel} = 2.8$ ps to $t_{pp} = t_{pp} + t_{lag} - T = 0 + 2.8 - 7 = -4.2$ ps as the probe to traverse the scan length $T =$

7 ps to complete a THz time trace. It must be made sure that both the pump and gate scanning stepsize and number of steps are exactly the same.

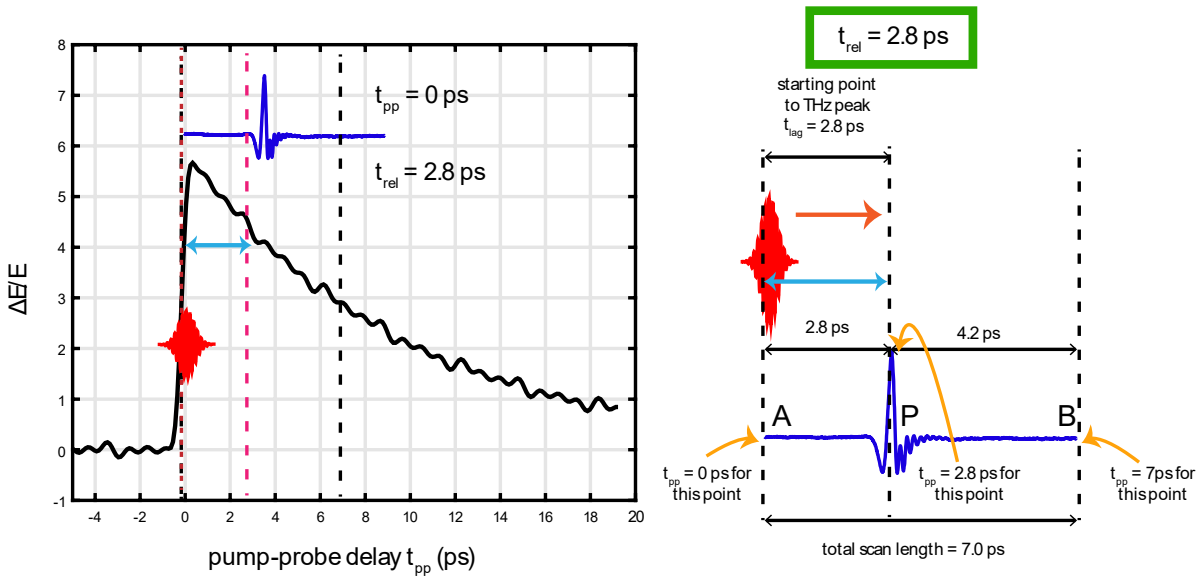

Figure 3.25: Case for $t_{pp} = 0$ ps. THz TDS scan length $T = 7$ ps and $t_{lag} = 2.8$ ps. For $t_{rel} = 2.8$ ps, the leftmost point (A) sees the pump as if it were at 0 ps delay from the pump.

Figure. 3.26 depicts the case for the running scan when $t_{rel} = 1.8$ ps. In this case, pump-probe delay is 0 ps with respect to the point C, 1 ps after the staring point A. The THz TDS runs simultaneously and is recorded in the DAQ. Similarly, Fig. 3.27 portrays the case when $t_{rel} = 0$. This means that the relative time delay between the pump and the THz peak P is 0 ps. From our discussion, we have noticed that for the case $t_{pp} = t_{rel}$, the point P is recorded. The reason is that t_{rel} is the relative delay between the pump and probe THz peak P. Earlier, we have seen in Fig. 3.25 that for $t_{rel} = 2.8$ ps, the pump looked like it arrived 2.8 ps earlier than the probe peak P and hence, the delay between point P and the pump was 2.8 ps. However, for point A in the scan, the delay was 0 ps. So, when $t_{rel} = t_{pp} = 0$ ps, the peak point P in the THz is recorded. Further, for $t_{rel} = -2$ ps, the point D, 4.8 ps apart from point A, sees the pump at 0 ps delay (Fig. 3.28).

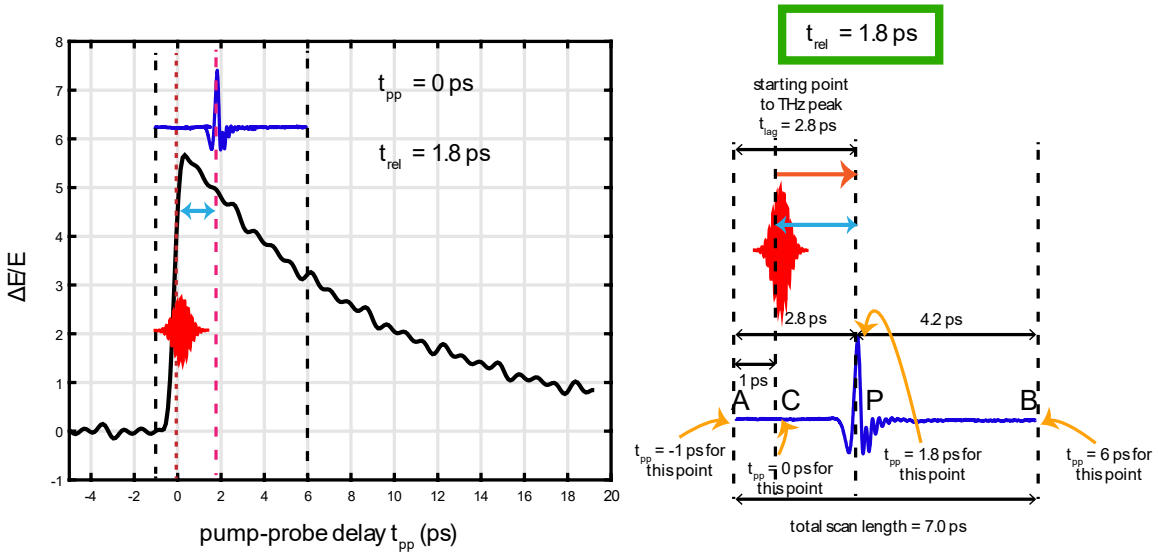

Figure 3.26: Case for $t_{pp} = 0$ ps. THz TDS scan length $T = 7$ ps and $t_{lag} = 2.8$ ps. For $t_{rel} = 1.8$ ps, the point C (in line with the pump, shown with dotted line). 1 ps after the starting point A sees the pump as if it were at 0 ps delay from the pump.

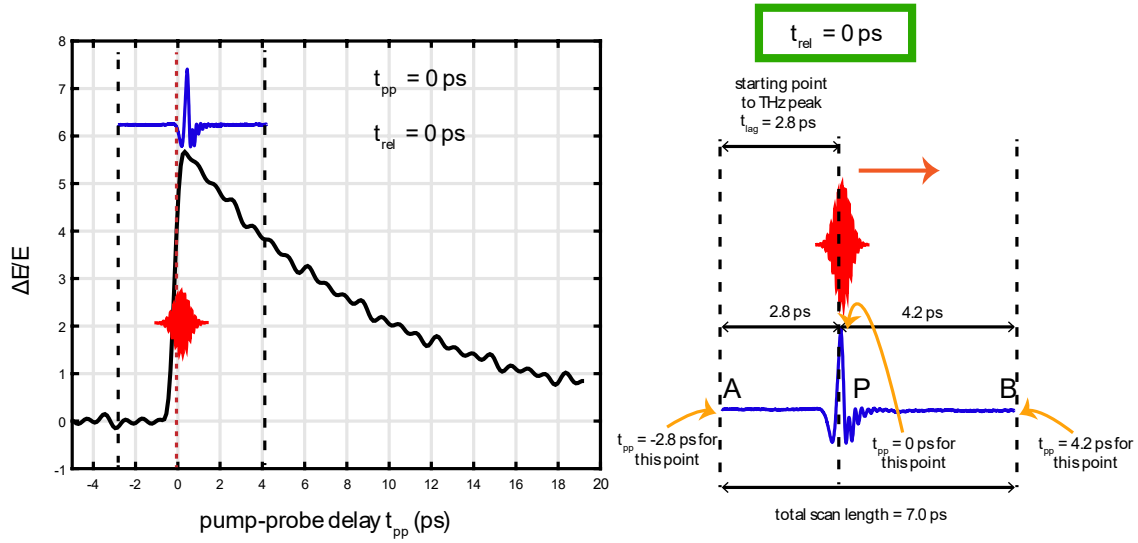

Figure 3.27: Case for $t_{pp} = 0$ ps. THz TDS scan length $T = 7$ ps and $t_{lag} = 2.8$ ps. For $t_{rel} = 0$ ps, the peak THz point P (in line with the pump, shown with dotted line), 2.8 ps after the point A, sees the pump as if it were at 0 ps delay from the pump.

Lastly, for $t_{rel} = -4.2$ ps, the rightmost point B in the THz TDS sees the pump at 0 ps delay. In this way, by simultaneously scanning both gate and pump, we are able to perform the THz TDS in the present of a pump beam which enables us to yield artifact-free photoinduced THz spectrum.

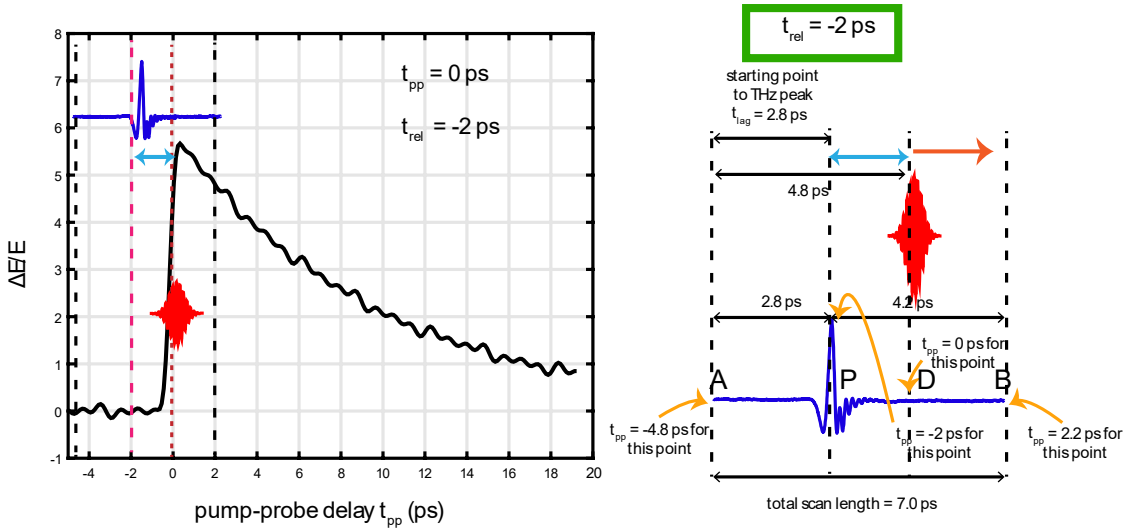

Figure 3.28: Case for $t_{pp} = 0$ ps. THz TDS scan length $T = 7$ ps and $t_{lag} = 2.8$ ps. For $t_{rel} = -2$ ps, the point D (in line with the pump, shown with dotted line), 4.8 ps after point A, sees the pump as if it were at 0 ps delay from the pump.

This method is valid for all time delays. For example, to gain photoinduced spectrum at $t_{pp} = 3$ ps with THz scan length $T = 7$ ps and $t_{lag} = 2.8$ ps, the pump is first moved to $t_{rel} = t_{pp} + t_{lag} = 3 + 2.8 = 5.8$ ps, then is scanned from $t_{rel} = 5.8$ ps to $t_{rel} = t_{pp} + t_{lag} - T = 3 + 2.8 - 7 = -1.2$ ps, simultaneously with the THz TDS.

Thus, by applying KS correction, we are able to perform convolution artifact-free THz spectroscopy in the presence of a photoexcitation pulse. In the next two chapters, I will show our optical pump – broadband THz probe results on TNS, in which all the data were taken using the KS correction scheme.

Chapter 4 Parametric Amplification & Exciton Condensate Signatures in Ta_2NiSe_5

4.1 Methods

In Chapter 2, we thoroughly described the physics of excitonic insulators (EI) and especially concentrated on Ta_2NiSe_5 (TNS) as a potential EI hosting an excitonic condensate. In the last chapter, we discussed the power of THz spectroscopy as a unique tool to unravel electronic response of the material encoded in the optical spectrum. In this chapter, we will employ an optical pump – broadband THz probe setup to investigate the optical signature of an exciton condensate manifesting as photoinduced reflectivity enhancement in TNS single crystals.

4.1.1 Pump-probe setup

The intrinsic timescale of numerous correlated phenomena matches the THz timescale, making it possible to probe them by means of state-of-the-art time-domain THz spectroscopic experiments. For our near-infrared optical pump – broadband THz probe experiment, we used a regenerative amplified Ti:sapphire laser system with pulse energy of 3 mJ, pulse duration of 35 fs, 1 kHz repetition rate and 800 nm central wavelength as the main light source. The light source is split into three ways: one beam for the pump pulse and two beams for the generation and detection of the THz pulse. Horizontally polarized 2.4 μm pump pulses were generated after 1mJ 800 nm laser pulse was injected into a commercial TOPAS-C optical parametric amplifier (OPA). The beam diameter was 3 mm FWHM. The pulse width out of the OPA, 2 mirrors before the sample was measured to be 45 fs. 2.4 μm (0.5 eV) pump was chosen for 2 reasons: (1) this was the lowest pump energy in our pump-probe setup, and (2) it is the closest energy to the insulating gap of TNS measured by ARPES and FTIR measurements (0.16 — 0.18 eV) [40, 41, 48].

4.1.2 THz generation & detection

For the broadband THz generation, we applied the 4-wave generation technique described in the previous chapter to generate broadband THz beams that cover a very broad spectrum of 0.5 ~ 22 THz. The incident angle for the THz probe on the sample is $30°$ and the beam diameter is ~ 1 mm. To detect the THz beam, we employed EO sampling. For this purpose, we used a 300 μm-thick $\langle 110 \rangle$ GaP detection crystal that enabled spectral measurements from 0.5 – 7.5 THz with electric field strength of ~80 $\mathrm{kV/cm}$.

We used a 1 MHz bandwidth Newport 2307 balanced photodetector to detect the signal. For the data acquisition, a NI PXIe-5122 Data Acquisition (DAQ) system with 100 MHz maximum sampling rate and 100 MHz bandwidth was used. The DAQ was triggered by the output from an optical chopper used to modulate the pump pulse (for details, see ref. [99]).

The TNS and gold reference samples were mounted inside a Janis ST-300 cryostat with a 36 mm-diameter, 600 μm-thick diamond window custom-made by Diamond Materials GmbH®. Integrating the diamond window to the cryostat gave us access to the broad THz spectrum at low temperatures owing to the broadband transmission properties of diamond.

4.2 Results

Since the pump and probe are horizontally and vertically polarized respectively, we oriented the sample in a way that the c-axis is along the horizontal direction, while the a-axis is oriented vertically. This setup enables us to photoexcite the sample along the c-axis and observe the dynamics along the a-axis (details shown in Fig. 4.1). Conversely, we can also do the experiment with pump polarization along the c-axis and probe polarization along the a-axis by

rotating the sample by 90°. Using a specialized quarter wave plate for 0.5 eV pump, it is also possible to perform measurements with pump and probe polarized in parallel direction.

4.2.1 Equilibrium response

To obtain equilibrium reflectivity of the sample, we measured $E_{gold}(t)$ and $E_{sample}(t)$. Here $E_{gold}(t)$ and $E_{sample}(t)$ are the reflection of the incident probe field from the gold reference and the TNS sample respectively, with t being the electro-optic gate time. Fast Fourier transforming (FFT) the signals yield the frequency-domain $E_{gold}(\omega)$ and $E_{sample}(\omega)$. The frequency-dependent reflectivity R is given as: $R = |r|^2 = |E_{sample}(\omega) / E_{gold}(\omega)|^2$.

Fig. 4.1a, b display the temperature-dependent equilibrium a-axis reflectivity and optical conductivity of TNS, respectively. From the figures, it is clear that there are multiple IR-active phonons in TNS along the chain. The locations of the phonons are consistent with previous infrared measurements [57, 65].

It was also observed that at lower temperatures, the conductivity displays sharper peaks, and with increasing temperature, the sample exhibits larger optical conductivity values. As we approach the room temperature, the conductivity starts developing flat features, similar to that in ref [57], in harmony with the equilibrium reflectivity data.

4.2.3 Directionality of the condensate response

Figure 4.2 displays a schematic of the pump and probe polarization with respect to the TNS crystal structure. The blue arrow depicts the probe polarization while the red arrow stands for pump polarization. As we know from our discussion in Chapter 2, TNS have alternating Ta and Ni chains along the *a*-axis with the exciton formation occurring along *c*-axis as a result of a charge transfer between adjacent Ta and Ni chains. As such we can pump both along (a-axis) or across the chain

(*c*-axis) and same protocol goes with the probe polarization as well. For an anisotropic material like TNS, material properties depend on the direction and hence, it is imperative to study the material as a function of pump and probe polarization.

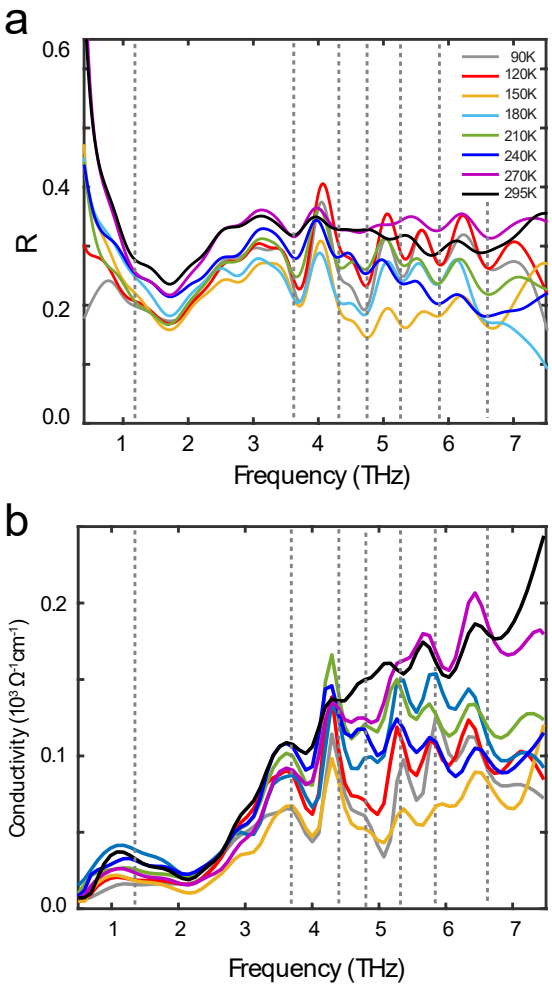

Figure 4.1: a, Equilibrium reflectivity and **b**, optical conductivity along the *a*-axis as a function of temperature. Phonon locations are denoted by gray dashed lines.

We performed time-resolved reflection-based broadband THz spectroscopy on TNS single crystals with lateral dimensions of 1 mm × 0.6 mm along the a and c axes, respectively, and a thickness of ~80 μm (see Appendix A for deltails) and measured the dynamics following above-

gap photoexcitation with 0.5 eV infrared pump pulses. Fig. 4.2b plots the photoinduced change in the peak probe electric field ΔE/E as a function of pump-probe delay time t_{pp}, for probe polarized along the chain (a-axis) and pump across the chain (c-axis). To do this, first we detected the probe THz time-domain scan (TDS) off the sample and found its peak. Then we fixed the gate time at the peak of the THz TDS, then controlled the delay between pump and probe using a motorized delay stage. Thus, we obtain the time trace of the relaxation dynamics upon photoexcitation.

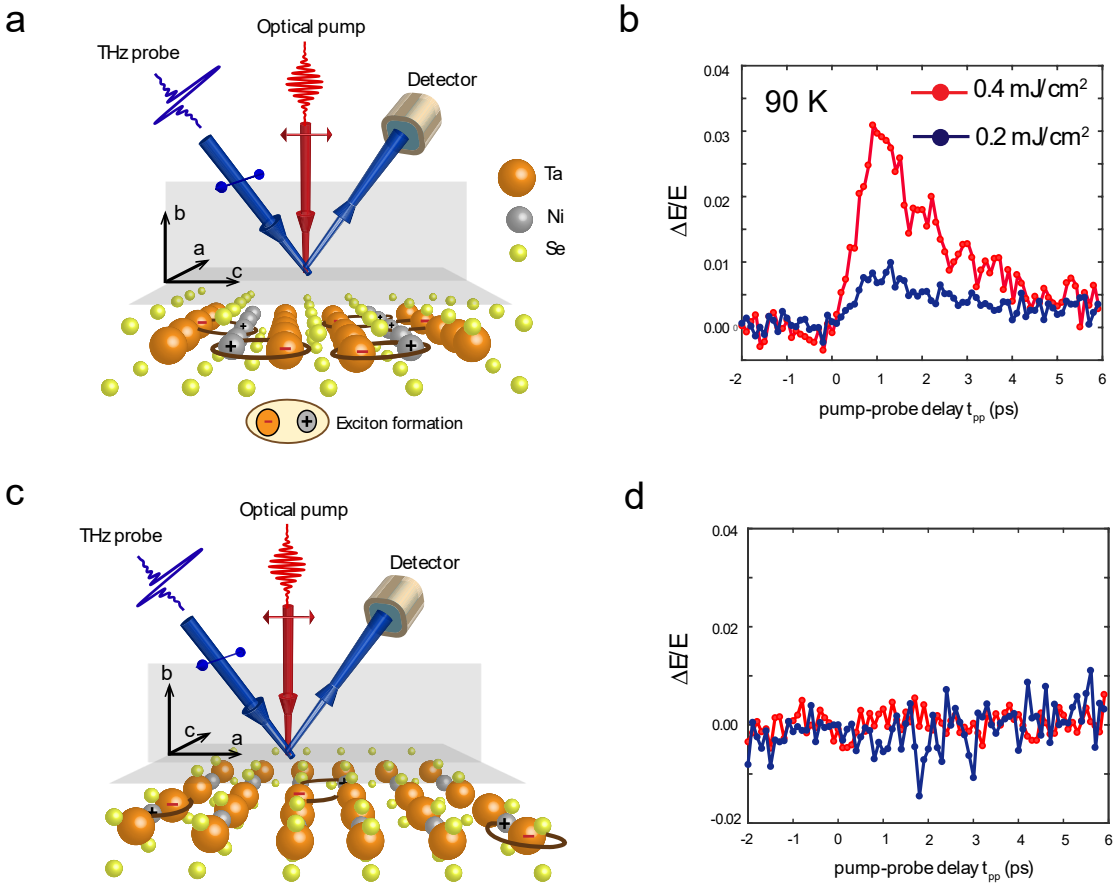

Figure 4.2: Pump and probe polarization scheme in TNS. **a**, Probe polarization (blue arrow) along the chain (a-axis) while pump polarization (red arrow) along (a-axis) or across (c-axis) the chain. **b**, Photoinduced change in peak probe electric field $\Delta E/E$ as a function of pump-probe delay time t_{pp}. **c**, Probe polarization across the chain (c-axis) while pump polarization (red arrow) along (a-axis) or across (c-axis) the chain. **d**, No pump-probe signal was observed.

It is evident from Fig. 4.2b that when probe is polarized along the *a*-axis, there is a nonzero pump-probe signal that indicates a fast photoexcited dynamics lasting ~ 2 ps. We performed fluence dependent measurements and for both high (0.4 $\mathrm{mJ/cm^2}$, red) and low (0.2 $\mathrm{mJ/cm^2}$, blue) fluences, a short-lived dynamics was observed. When we changed the pump polarization along *a*-axis while keeping the probe polarization constant (along *a*-axis), same dynamics was observed.

On the contrary, as clear in Fig. 4.2d, no pump-probe signal was recorded when the probe was polarized along the *c*-axis, irrespective of the pump polarization. Our results suggest that for an arbitrary pump polarization, the photoinduced response is always along the atomic chain manifested in the strong pump-probe signal when probed along the chain (*a*-axis).

Previous FTIR and NIR studies [57-59, 61] indicate a stronger condensate response parallel to the atomic chains (along the *a*-axis), irrespective of pump polarization. We observe a strong pump-probe response along the atomic chain. However, no response was observed across the chain. In concert with the previous report, it is clear that our THz probe is sensitive to the exciton condensate and the pump-probe signal is the direct spectral manifestation of the condensate when it is perturbed out of equilibrium by means of photoexcitation.

4.2.3 Photoinduced reflectivity enhancement

We measured the pump-induced transient change $\Delta E(t, t_{pp})$ in the reflected electric field of the probe pulse as a function of pump-probe delay time t_{pp} over the THz temporal window *t*. The signal $\Delta E(t, t_{pp})$ can be expressed as, $\Delta E(t, t_{pp}) = E_{sample,pumped}(t, t_{pp}) - E_{sample,unpumped}(t, t_{pp})$. From this, the total complex reflection coefficient, $r(\omega, t_{pp}) = r_0(\omega)[1 + \frac{\Delta E(\omega, t_{pp})}{E_{sample,unpumped}(\omega, t_{pp})}]$ is determined [73], where $r_0(\omega)$ is the equilibrium reflection coefficient previously obtained from equilibrium measurement. To measure the transient THz

signal without any artifacts, the standard Kindt and Schmuttenmaer scanning scheme was used [100, 101]. Using this formalism, we also compute the photoinduced change in reflectivity $\Delta R(\omega)$. This enables us to determine the reflectivity enhancement $(R + \Delta R)/R$ as well as the pump-induced percent change in reflectivity $\Delta R/R$.

Figures 4.3 – 4.10 depict the pump-induced change in probe electric field $\Delta E(t)$, its spectrum $\Delta E(\omega)$ and reflectivity enhancement $(R + \Delta R)/R$ at different pump-probe delays t_{pp}, as a function of fluence and temperature. The blue shaded plots represent the low fluence data while the red shaded plots depict the high fluence data. The first thing noticed is that the signal is largest at $t_{pp} = 1$ ps which also corresponds to the peak in the transient pump-probe signal as seen in Fig. 4.2b. Also, the signal drops around $t_{pp} = 2$ ps, consistent with characteristic lifetime of the fast relaxation dynamics. Here, $\Delta E(t)$ is the pump-induced signal as a function of the gate time t. We performed FFT to obtain the differential electric field $\Delta E(\omega)$ in the frequency domain. After comparing the $\Delta E(\omega)$ plot with reflectivity enhancement plot $(R + \Delta R)/R$, it was noticed that they follow similar trend, indicating that reflectivity enhancement plot $(R + \Delta R)/R$ originates from $\Delta E(\omega)$.

Figure 4.11 show the corresponding pump-induced relative reflectivity enhancement $(R + \Delta R)/R$ at four different temperatures, 1 ps after photoexcitation. A broadband fluence dependent signal is evident with a magnitude that decreases with increasing temperature, nearly vanishing at 270K. Importantly, the reflectivity enhancement peaks in the vicinity of the phonon resonances. For example, at 90K (Fig. 4.11a), an increase of approximately 25% is evident at 4.7 THz (corresponding to a B_{3u} phonon) that, as described below, plays a prominent role in the dynamics through preferential coupling to the band structure in the LT monoclinic phase. There is also a 9% increase centered at 1.8 THz (orange arrows) which does not overlap with any phonons.

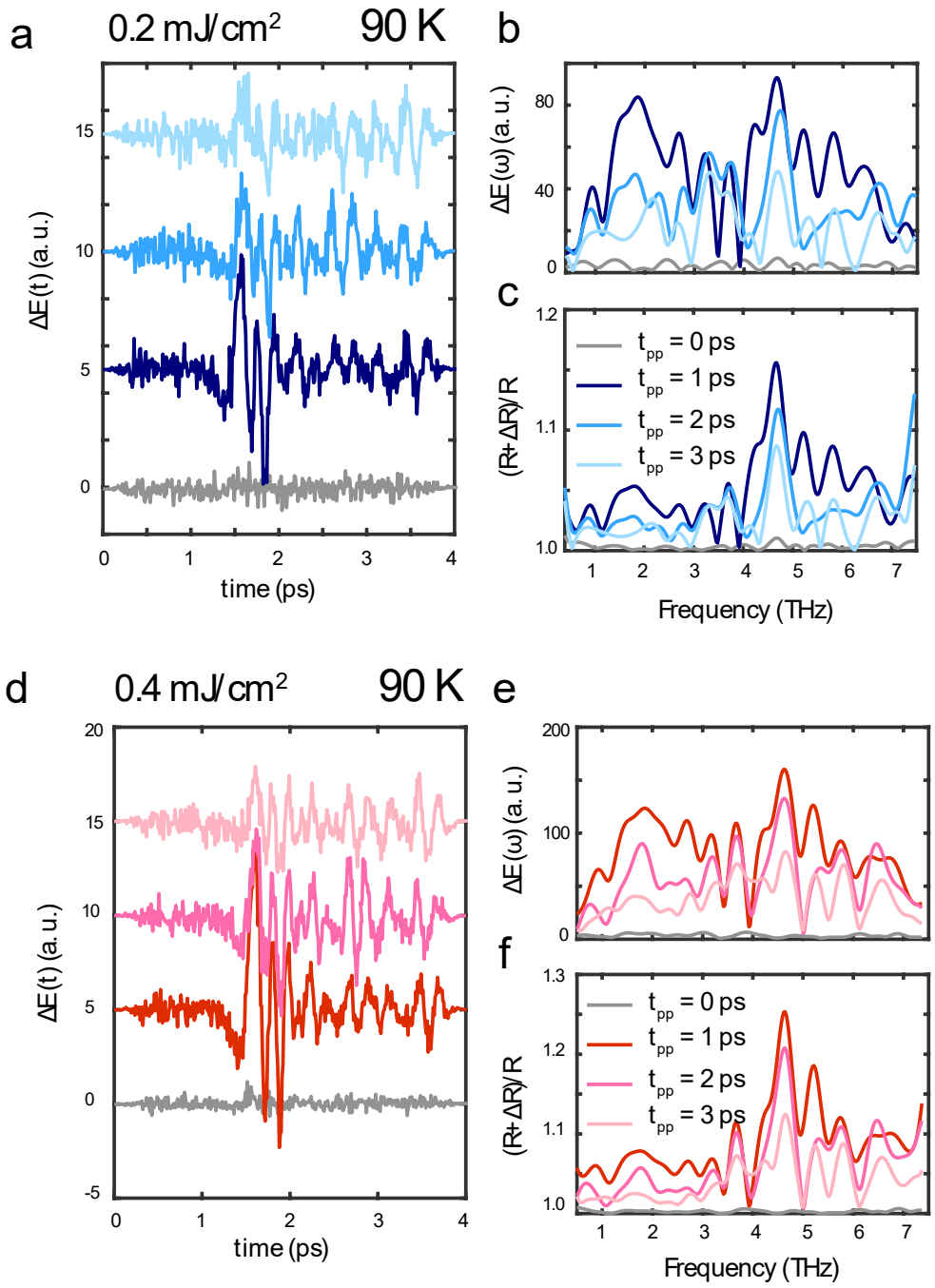

Figure 4.3: Pump-probe data at 90 K. **a**, Photoinduced change in reflected probe electric field, **b**, corresponding spectrum of the change, **c**, reflectivity enhancement for 0.2 mJ. cm^2 fluence. **d**, Photoinduced change in reflected probe electric field, **e**, corresponding spectrum of the change, **f**, reflectivity enhancement for 0.4 mJ. cm^2 fluence at different pump-probe delays.

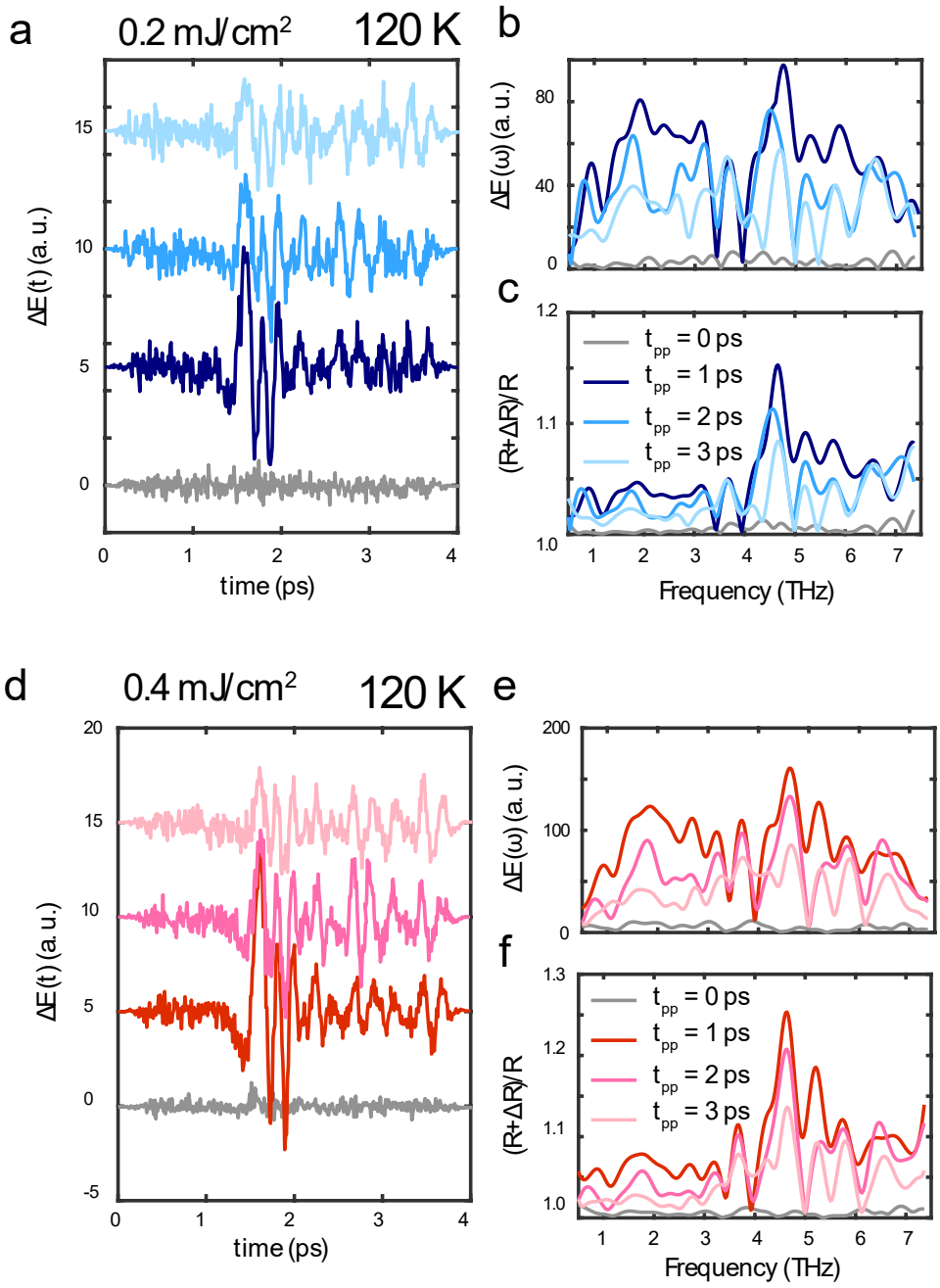

Figure 4.4: Pump-probe data at 120 K. **a**, Photoinduced change in reflected probe electric field, **b**, corresponding spectrum of the change, **c**, reflectivity enhancement for 0.2 mJ. cm^2 fluence. **d**, Photoinduced change in reflected probe electric field, **e**, corresponding spectrum of the change, **f**, reflectivity enhancement for 0.4 mJ. cm^2 fluence at different pump-probe delays.

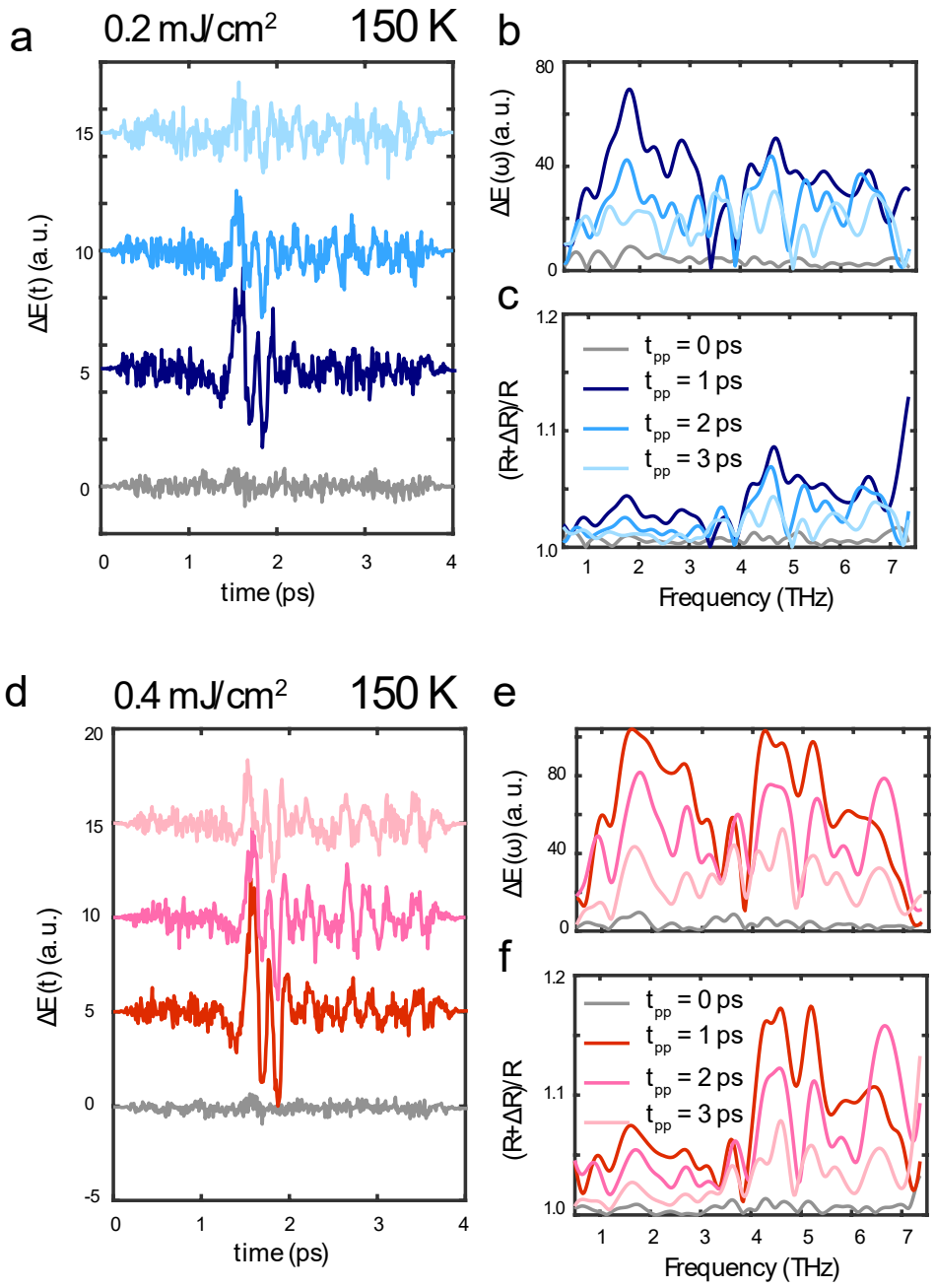

Figure 4.5: Pump-probe data at 150 K. **a**, Photoinduced change in reflected probe electric field, **b**, corresponding spectrum of the change, **c**, reflectivity enhancement for 0.2 mJ. cm^2 fluence. **d**, Photoinduced change in reflected probe electric field, **e**, corresponding spectrum of the change, **f**, reflectivity enhancement for 0.4 mJ. cm^2 fluence at different pump-probe delays.

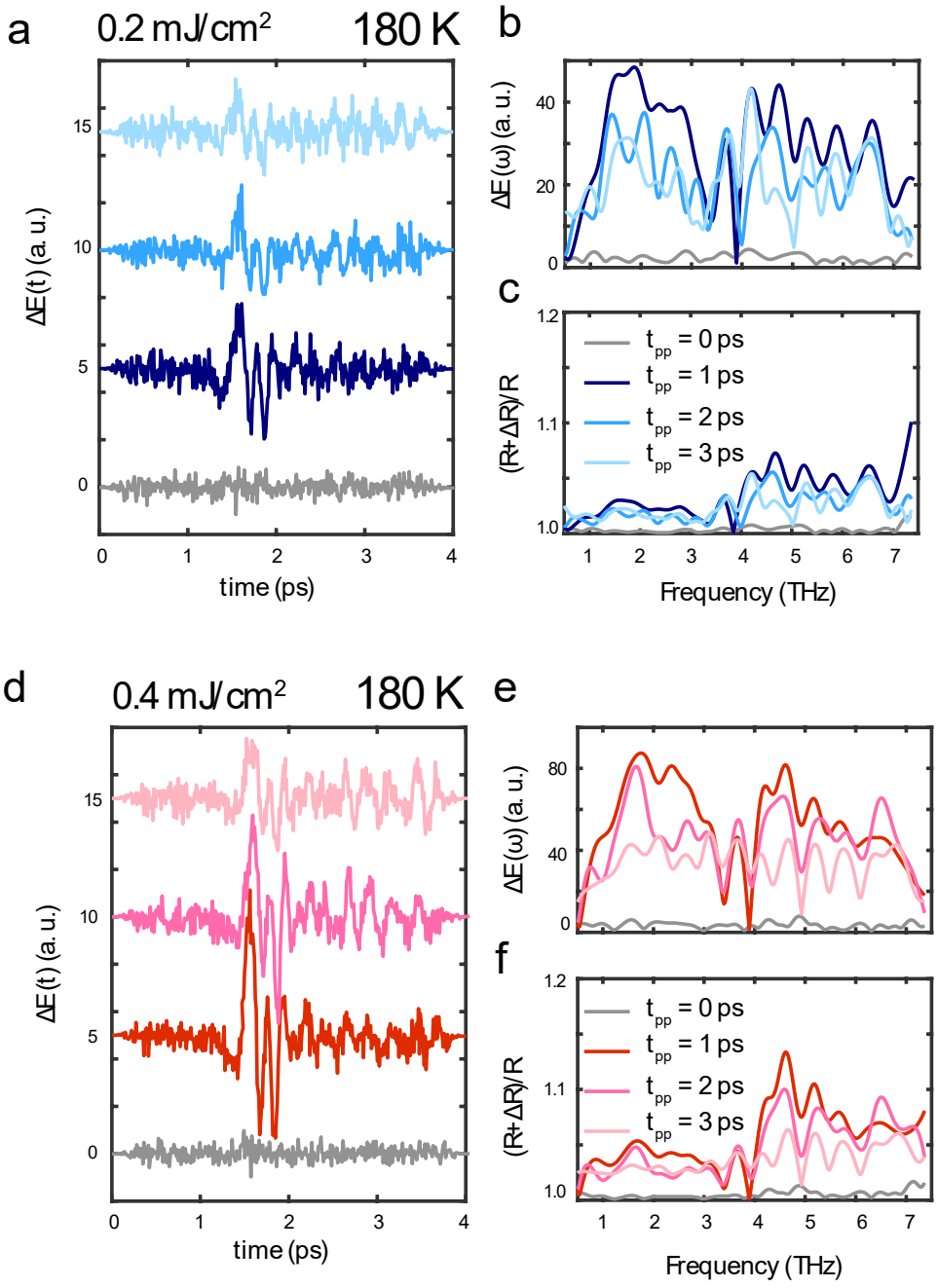

Figure 4.6: Pump-probe data at 180 K. **a**, Photoinduced change in reflected probe electric field, **b**, corresponding spectrum of the change, **c**, reflectivity enhancement for 0.2 mJ. cm^2 fluence. **d**, Photoinduced change in reflected probe electric field, **e**, corresponding spectrum of the change, **f**, reflectivity enhancement for 0.4 mJ. cm^2 fluence at different pump-probe delays.

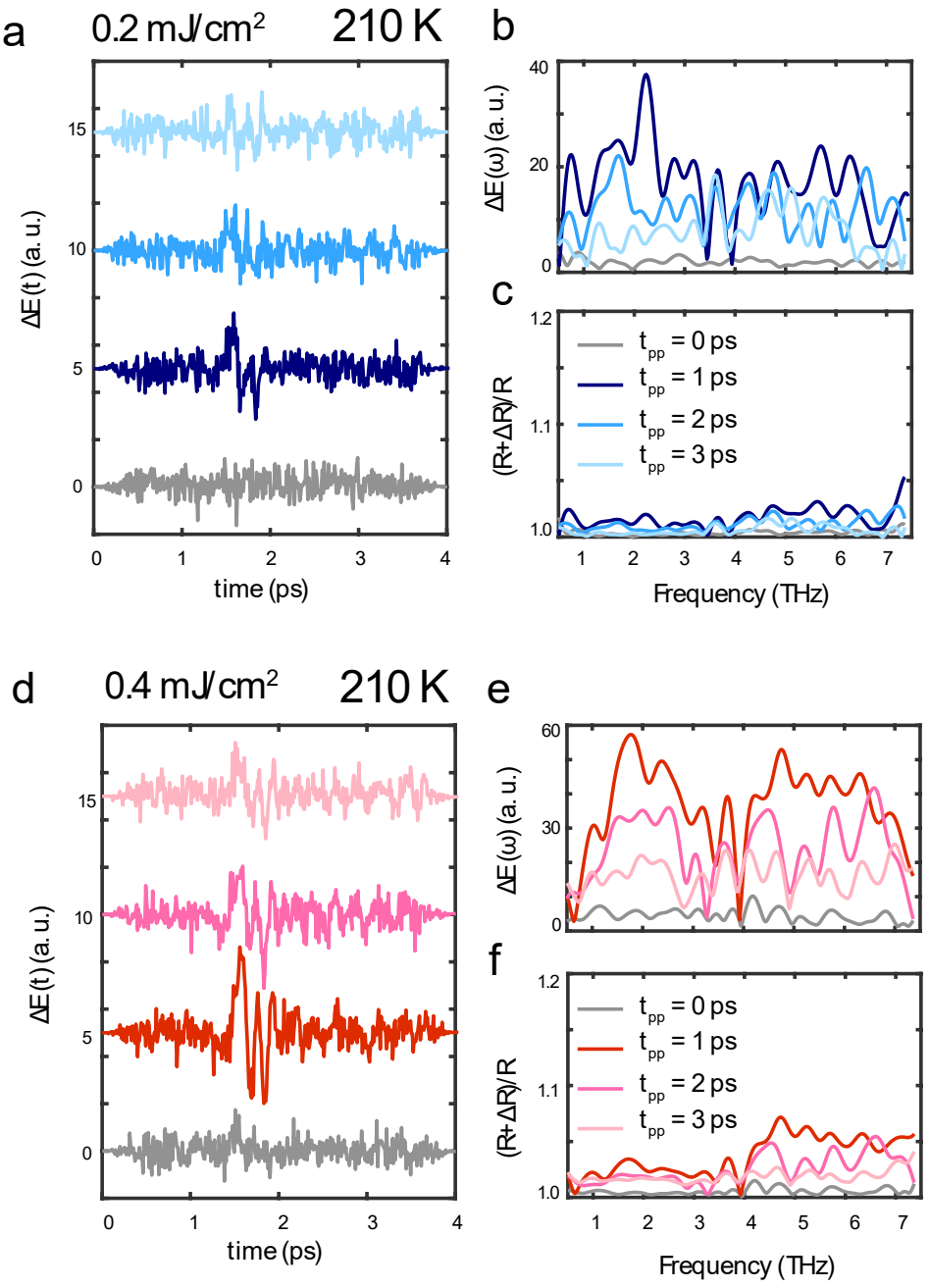

Figure 4.7: Pump-probe data at 210 K. **a**, Photoinduced change in reflected probe electric field, **b**, corresponding spectrum of the change, **c**, reflectivity enhancement for 0.2 mJ. cm^2 fluence. **d**, Photoinduced change in reflected probe electric field, **e**, corresponding spectrum of the change, **f**, reflectivity enhancement for 0.4 mJ. cm^2 fluence at different pump-probe delays.

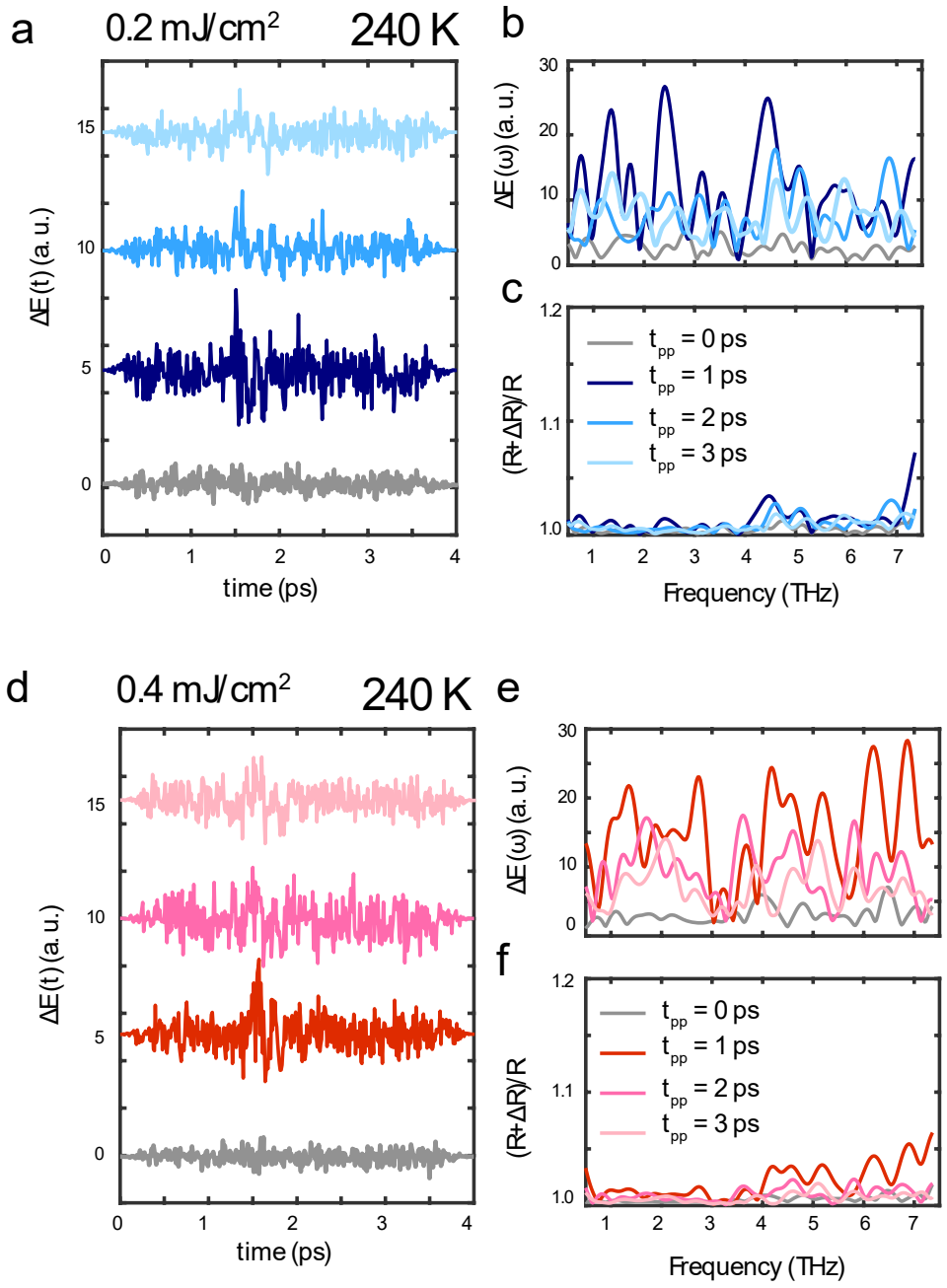

Figure 4.8: Pump-probe data at 240 K. **a**, Photoinduced change in reflected probe electric field, **b**, corresponding spectrum of the change, **c**, reflectivity enhancement for 0.2 mJ. cm^2 fluence. **d**, Photoinduced change in reflected probe electric field, **e**, corresponding spectrum of the change, **f**, reflectivity enhancement for 0.4 mJ. cm^2 fluence at different pump-probe delays.

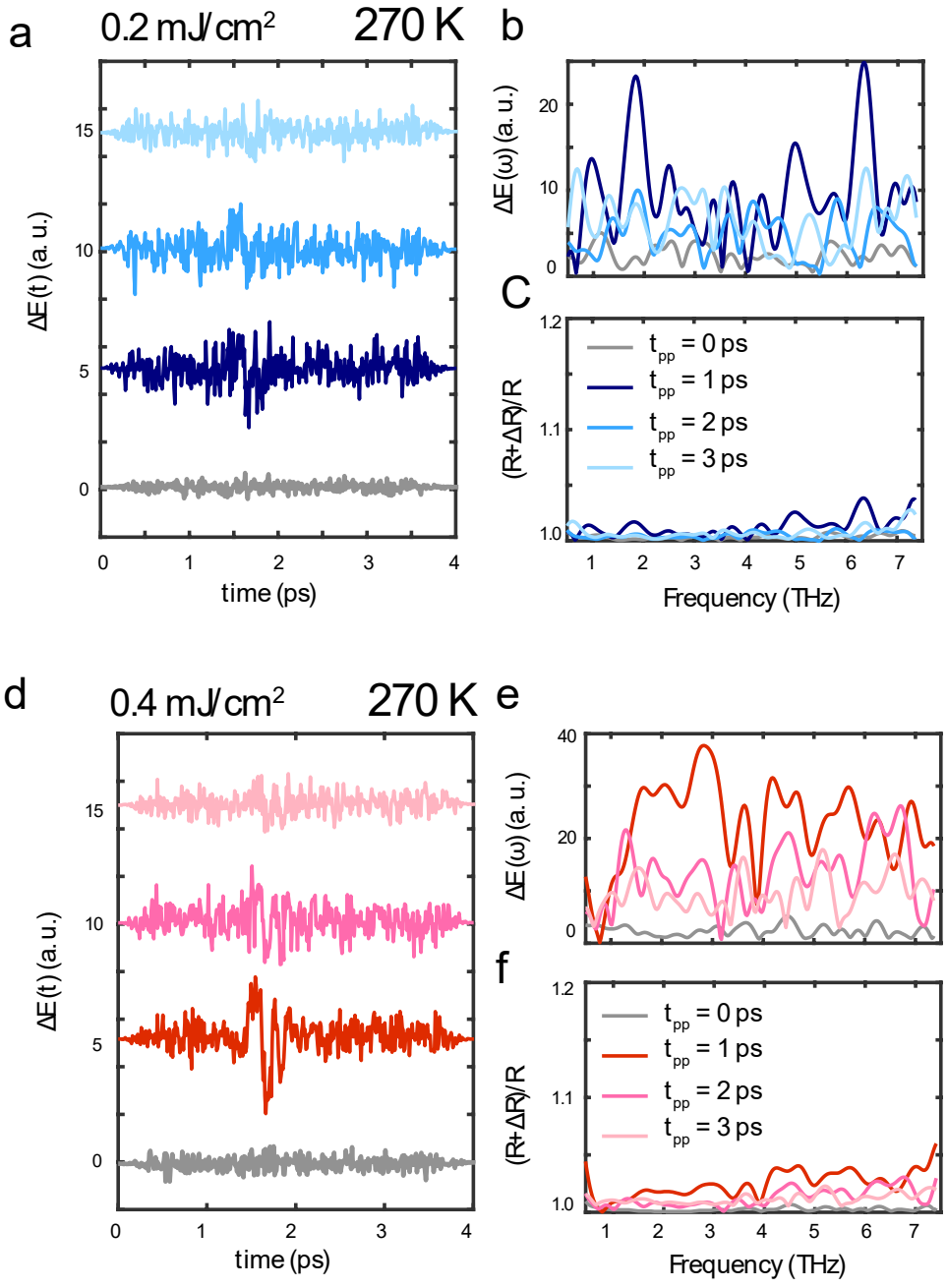

Figure 4.9: Pump-probe data at 270 K. **a**, Photoinduced change in reflected probe electric field, **b**, corresponding spectrum of the change, **c**, reflectivity enhancement for 0.2 mJ. cm^2 fluence. **d**, Photoinduced change in reflected probe electric field, **e**, corresponding spectrum of the change, **f**, reflectivity enhancement for 0.4 mJ. cm^2 fluence at different pump-probe delays.

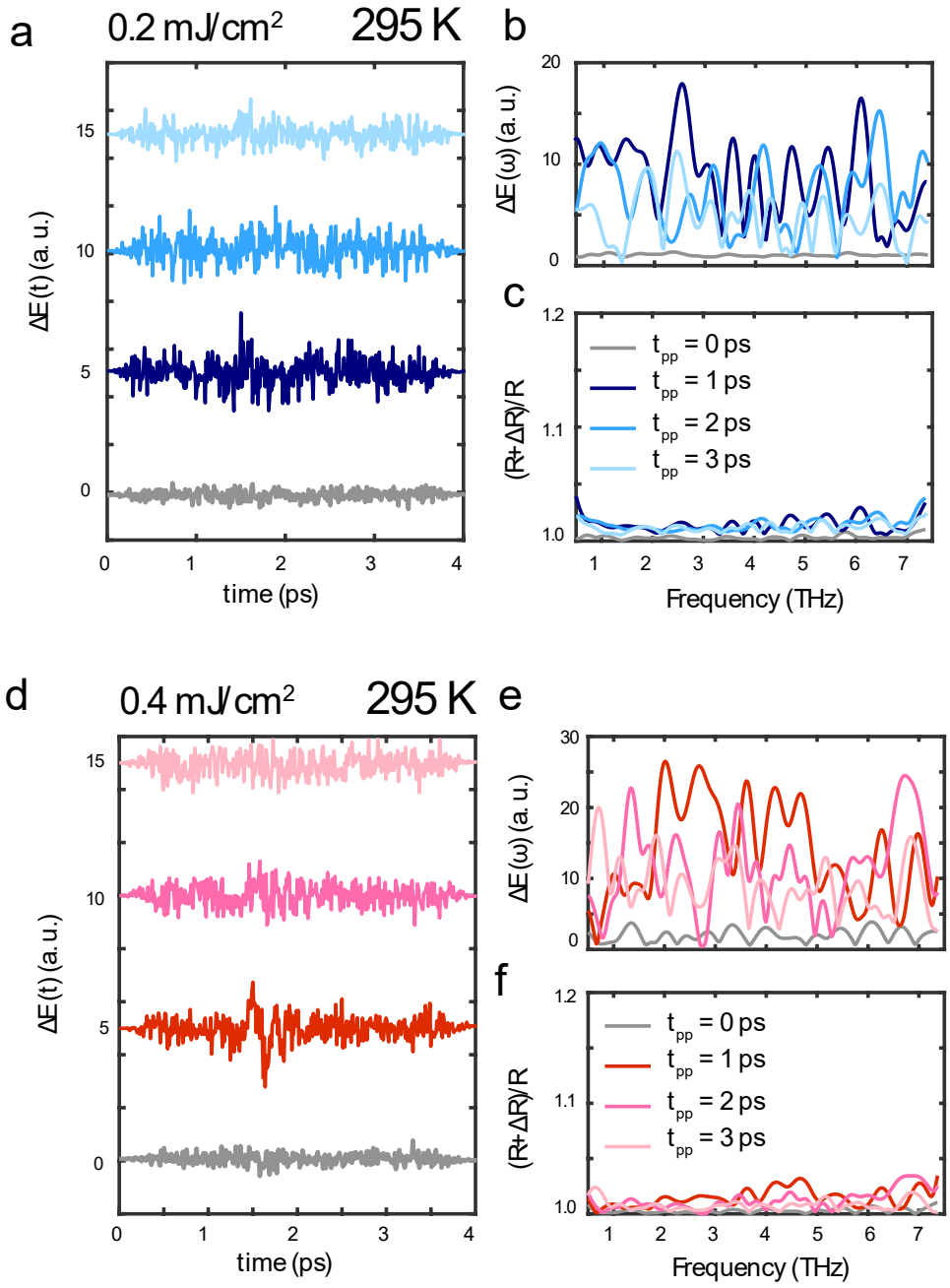

Figure 4.10: Pump-probe data at 295 K. **a**, Photoinduced change in reflected probe electric field, **b**, corresponding spectrum of the change, **c**, reflectivity enhancement for 0.2 mJ. cm^2 fluence. **d**, Photoinduced change in reflected probe electric field, **e**, corresponding spectrum of the change, **f**, reflectivity enhancement for 0.4 mJ. cm^2 fluence at different pump-probe delays.

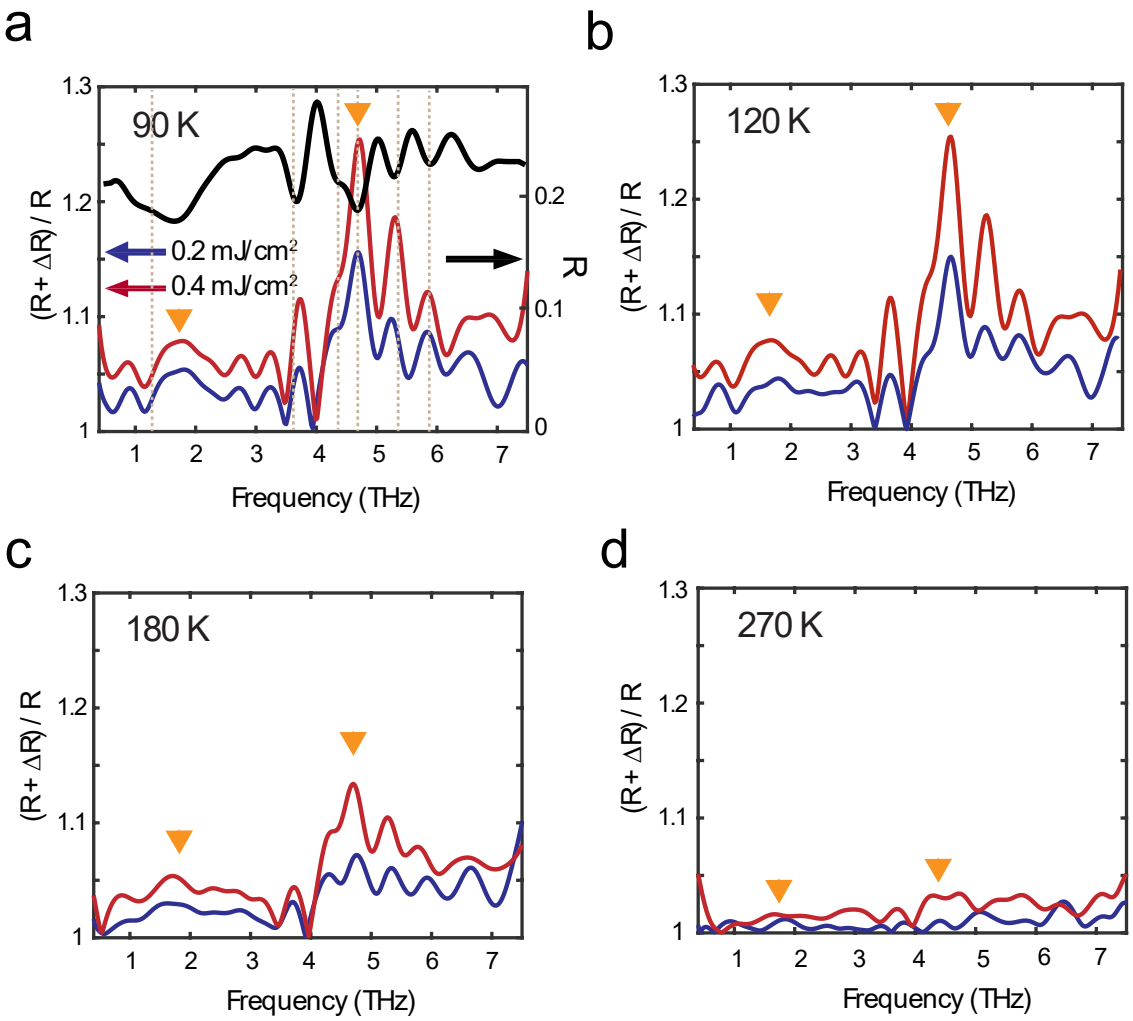

Figure 4.11: Temperature dependent reflectivity enhancement with probe polarization along the chain. **a**, Photoinduced enhancement of reflectivity $(R + \Delta R)/R$ at 90 K as a function of fluence, 1 ps after photoexcitation (left panel). Solid blue curves are for a pump fluence of 0.2 $\mathrm{mJ/cm^2}$ while red curves display 0.4 $\mathrm{mJ/cm^2}$ results. Right panel shows equilibrium reflectivity at 90 K (black curve) with phonon locations in the spectrum denoted by dashed vertical gray lines. **b-d**, $(R + \Delta R)/R$ data for 120 K, 180 K and 270 K, respectively. Orange inverted triangles serve as a guide to the eye to demonstrate the peaks in the reflectivity enhancement.

It is clear from Fig. 4.11a—d that the reflectivity enhancement is prominent at the IR-active phonon locations. In the next section, we will demonstrate that this photoinduced reflectivity

enhancement denotes the exciton condensate response and thus, can be an effective method to monitor exciton condensate dynamics in EIs.

4.2.4 Hallmarks of a BEC dynamics

Figures 4.12a and 4.12b plots the temperature dependence of the peak pump-induced reflectivity change $\Delta R/R$ at frequencies 1.8 THz and 4.7 THz, revealing a clear roll-off with increasing temperature. Focusing on the 4.7 THz data, the temperature dependence of $\Delta R/R$ is fit using the fitting formula,

$$\frac{\Delta R}{R}(T) = \frac{\frac{A}{\Delta_E}}{1 + B \exp\left(-\frac{\Delta_E}{k_B T}\right)}. \tag{4.1}$$

Here, A and B are parameters and Δ_E is a temperature-independent energy scale [43, 44, 60]. The fits – shown in Fig. 4.12b as dashed lines – yield $\Delta_E = 113 \pm 7$ meV ($\Delta_E = 120 \pm 13$ meV) for a fluence of $0.2\ \mathrm{mJ/cm^2}$ ($0.4\ \mathrm{mJ/cm^2}$), in reasonable agreement with the gap ($\sim$160 meV) from optical conductivity and ARPES studies [41, 58]. The reason behind using a temperature independent gap is that, according to the theoretical studies [41, 42], if the phase transition resembles that of a BEC, the gap will remain unchanged below and above T_C.

Moreover, specific heat analysis reveals that the pump-induced temperature rise is small (<5 K for $0.4\ \mathrm{mJ/cm^2}$), ruling out a thermal origin of the signal (Appendix B Fig. 1a – b). The absolute reflectivity increase ΔR can be obtained by multiplying $\Delta R/R$ by the equilibrium reflectivity as shown in Fig. 4.13a. ΔR is proportional to the increase in the number of reflected THz photons. The integral of ΔR over the spectral range 0.5 – 7.5 THz (shaded areas in Fig. 4.13a) is defined as,

$$\Delta\eta = \frac{1}{2\pi}\int_{0.5\ \mathrm{THz}}^{7.5\ \mathrm{THz}} \Delta R(\omega)\, d\omega, \tag{4.2}$$

Here, the quantity $\Delta\eta$ is termed as the integrated photoinduced change in reflectivity and can be seen as a photoinduced spectral weight change over the whole spectrum. Fig. 4.13b plots $\Delta\eta$ as a function of temperature and exhibits similar temperature behavior as $\Delta R/R$ at 1 ps delay. Fitting $\Delta\eta(T)$ with the same equation we used for $\Delta R/R(T)$ in (4.1), we obtain, $\Delta_E = 115 \pm 14$ meV, consistent with the gap value computed from (4.1).

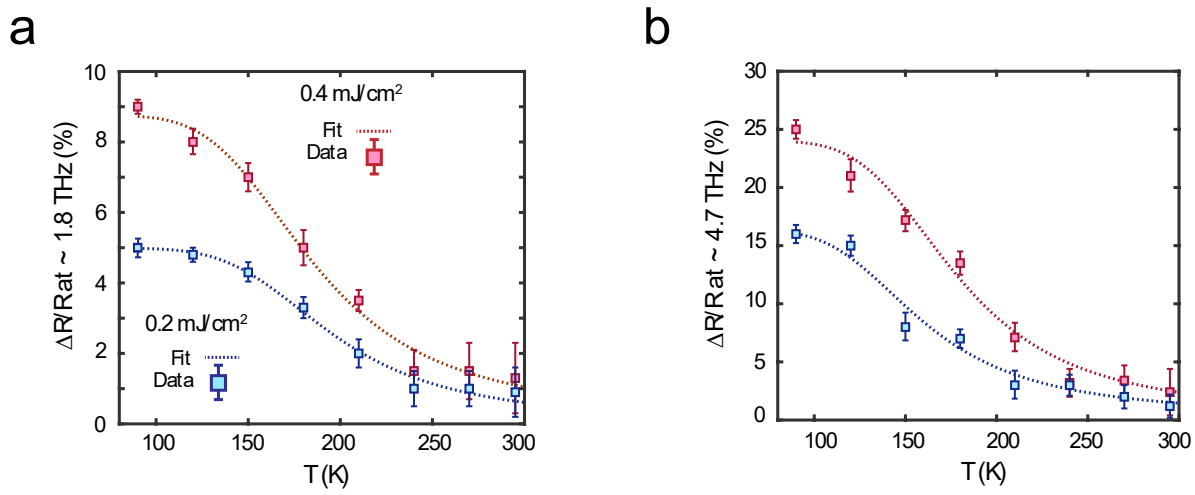

Figure 4.12: a, b, Temperature dependence of % change in reflectivity $\Delta R/R$ at ~1.8 THz and ~4.7 THz for both $0.2\ \mathrm{mJ/cm^2}$ (solid blue squares) and $0.4\ \mathrm{mJ/cm^2}$ (solid red squares) and the corresponding fits (dashed lines). Error bars represent standard deviations in fit values.

Collectively, the data in Fig. 4.1 and Fig. 4.13 suggest photoinduced perturbation of a BEC-like condensate response which results in broadband electronic dynamics encoded in the enhanced THz reflectivity, occurring well below the structural transition temperature. The spectra also reveal dynamic condensate-phonon coupling as indicated by peaks in the enhanced reflectivity spectrum at select infrared-active phonon frequencies. Furthermore, that the $\Delta R/R$ temperature behavior resembles that of an underdoped cuprate with a pseudogap where preformed pairs exist above T_C

but condensation takes place only below T_C [43]. The gap represents the pair binding energy and is temperature-independent, a key ingredient for a BEC-like phase transition. Similarly, in terms of exciton picture in TNS, the notion of preformed excitons and BEC-like phase transition is consistent with previous near-infrared and ARPES studies [39-42, 47, 52, 61].

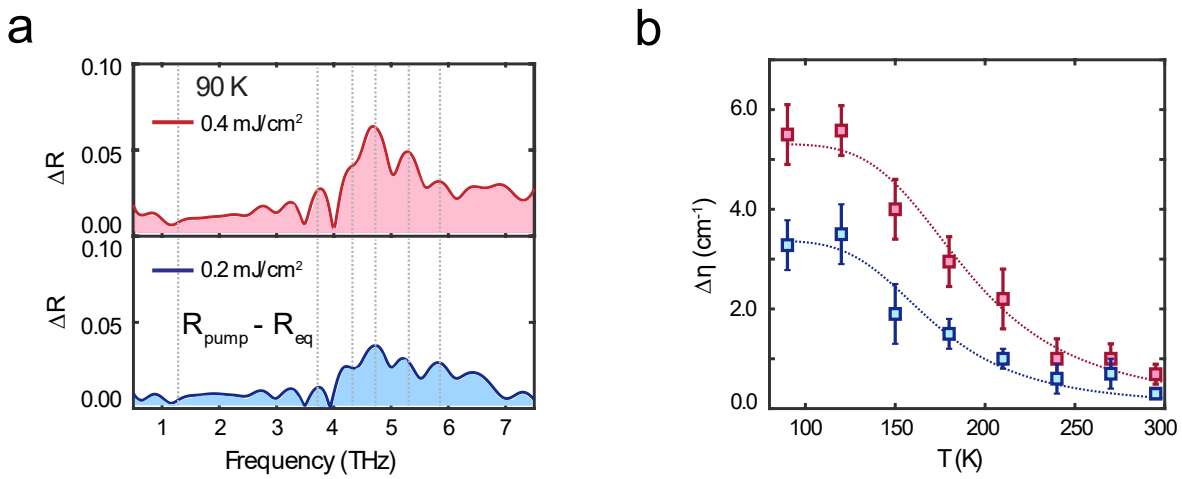

Figure 4.13: a, Photoinduced change in reflectivity ΔR for excitation fluence of 0.4 $\mathrm{mJ/cm^2}$ (top panel) and 0.2 $\mathrm{mJ/cm^2}$ (bottom panel). The shaded regions represent the integrated change in the reflectivity. Phonon locations are indicated by vertical gray dashed lines as a guide to the eye. **b**, Temperature dependence of photoinduced change in integrated reflectivity $\Delta\eta(T)$ for each fluence. Dashed lines are fits as described in the text.

Our experiment unravels the role of electron-phonon coupling in the form of a parametric reflectivity enhancement. We observed a prominent increase in the reflectivity at select IR phonon frequencies. Furthermore, this reflectivity increase shows a BEC-like temperature dependence. Hence, we can extract information about both the nature of the exciton condensate and its coupling to the phonons. When we calculated the integrated reflectivity change due to photoexcitation, it also exhibited a BEC-like trend, further verifying a condensate origin of the parametric emission spectrum.

4.2.5 Temporal dynamics

To obtain equilibrium The data showing the temporal response of the photoinduced condensate perturbation are presented in Fig. 4.14. Fig. 4.14a – b display 1-d pump-probe scans of the pump-induced change in the peak electric field of the THz pulse as a function of pump-probe delay time t_{pp} for different temperatures and fluences. The recovery dynamics exhibit a short-lived response of $\sim$2 ps and were fitted with a single-exponential decay.

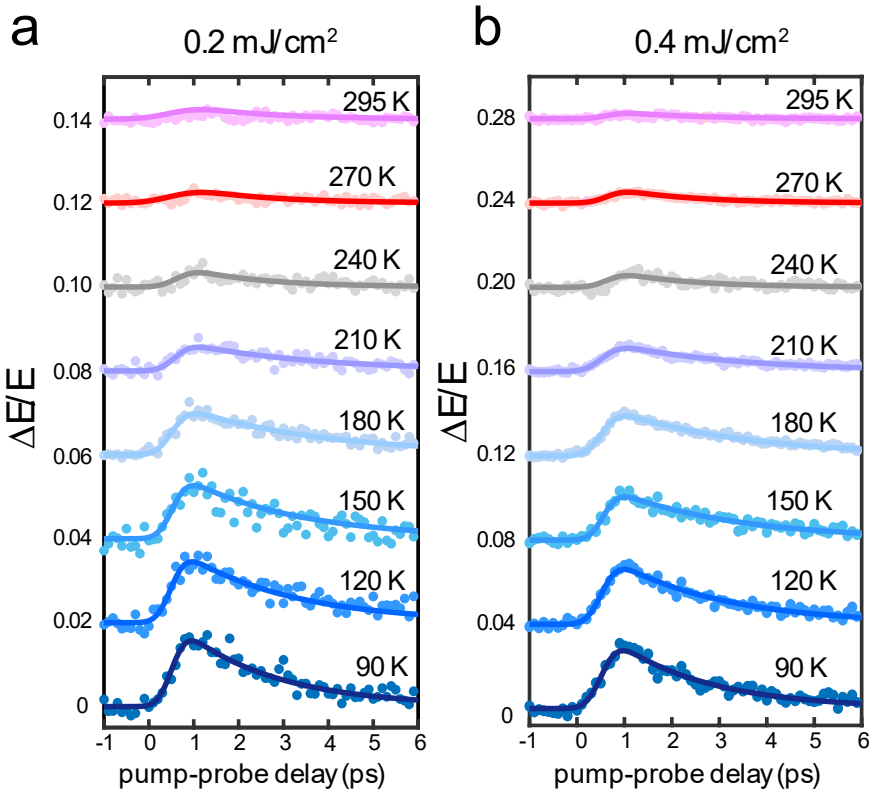

Figure 4.14: **a**, **b**, Photoinduced changes in peak THz probe electric field (solid circles) as a function of pump-probe delay time for 0.2 $\mathrm{mJ/cm^2}$ (**a**) and 0.4 $\mathrm{mJ/cm^2}$ fluence (**b**). Solid lines indicate a single-exponential decay fit.

The temperature dependence of the recovery time τ from the fits for 0.2 $\mathrm{mJ/cm^2}$ and 0.4 $\mathrm{mJ/cm^2}$ fluences are plotted in Fig. 4.15a and 4.15b. With decreasing temperature τ increases,

akin to dynamics associated with a gap as observed in superconductors and related materials [43, 60]. The dashed lines in Fig. 4.15a and b are fits to $\tau(T)$ utilizing a phenomenological temperature independent BEC gap model [43, 44],

$$\tau(T) = \frac{1}{A + B\sqrt{\Delta_E T}\exp\left(-\frac{\Delta_E}{k_B T}\right)}. \tag{4.3}$$

Here, A and B are fitting parameters. Fitting the relaxation time data using (4.3) we yield, $\Delta_E = 110 \pm 5$ meV, consistent with Δ_E as obtained from the $\Delta R/R$ data. This can be analogous with Rothword-Taylor (RT) model which is used to interpret gap opening. Deviation from the model at higher temperatures can be attributed to opening of additional decay channels due to phonon scattering or BCS-like partial closing of the gap [47, 60].

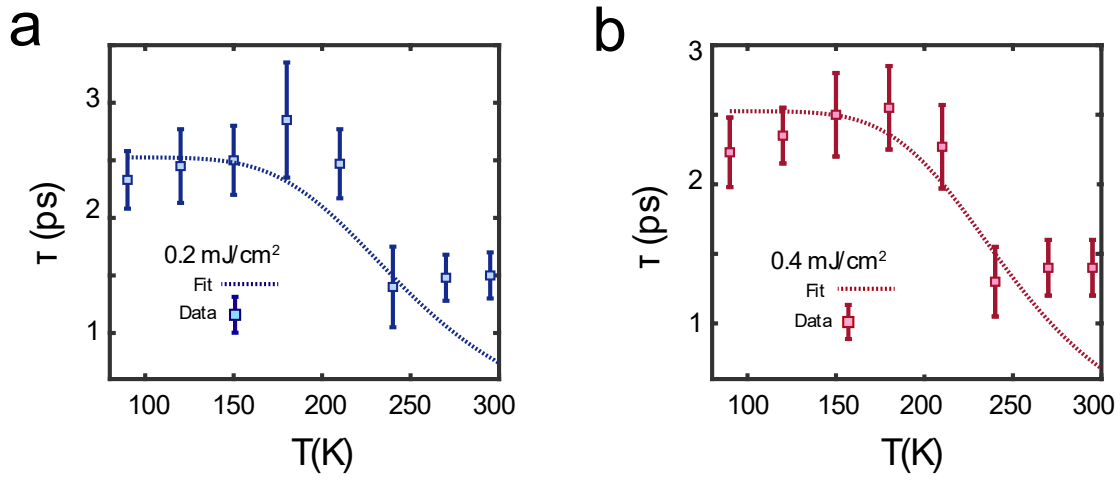

Figure 4.15: a, **b**, Temperature dependence of decay time as a function of fluence. Error bars represent the 95% confidence region from the single-exponential fits.

We know focus on relating the photoinduced reflectivity enhancement $\Delta R/R$ and integrated photoinduced change in reflectivity $\Delta\eta$ with the fast dynamics of the transient pump-probe signal as seen in Fig. 4.14.

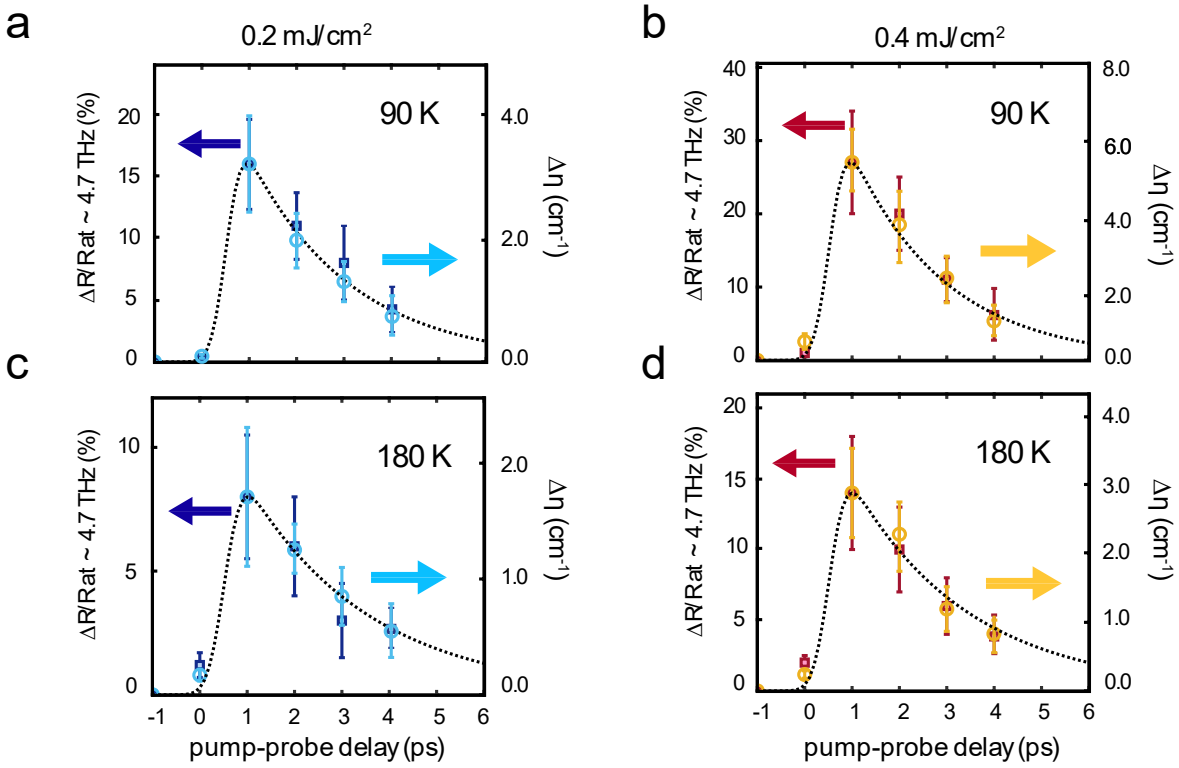

Figure 4.16: a, **b**, Temporal evolution of $\Delta R/R(T)$ (left panel, solid squares) and $\Delta\eta(T)$ (right panel, open circles) at different pump-probe delays, as a function of fluence for 90 K and **c**, **d**, 180 K. Error bars represent maximum uncertainties from the fits.

The dynamics obtained from the spectral response (i.e., full two-dimensional scans) are consistent with the 1-d scans. Fig. 4.16a and 4.16b display $\Delta R/R(T)$ and $\Delta\eta(T)$ at different pump-probe delays for two different temperatures (90 K and 180 K) at 0.2 $\mathrm{mJ/cm^2}$ fluence, while Fig. 4.16c and 4.16d plot the 0.4 $\mathrm{mJ/cm^2}$ fluence results. All data have been rescaled and plotted on the same figure with the left and right panels representing $\Delta R/R(T)$ (at 4.7 THz, solid squares)

and $\Delta\eta(T)$ (open circles), respectively. The dashed black lines correspond to the single-exponential decay fits at respective temperatures and fluences obtained from Fig. 4.15.

We observe that both $\Delta R/R(T)$ and $\Delta\eta(T)$ closely match the fits. Overall, the fast dynamics of $\Delta R/R(T)$ and $\Delta\eta(T)$ further confirms the electronic origin of the reflectivity enhancement.

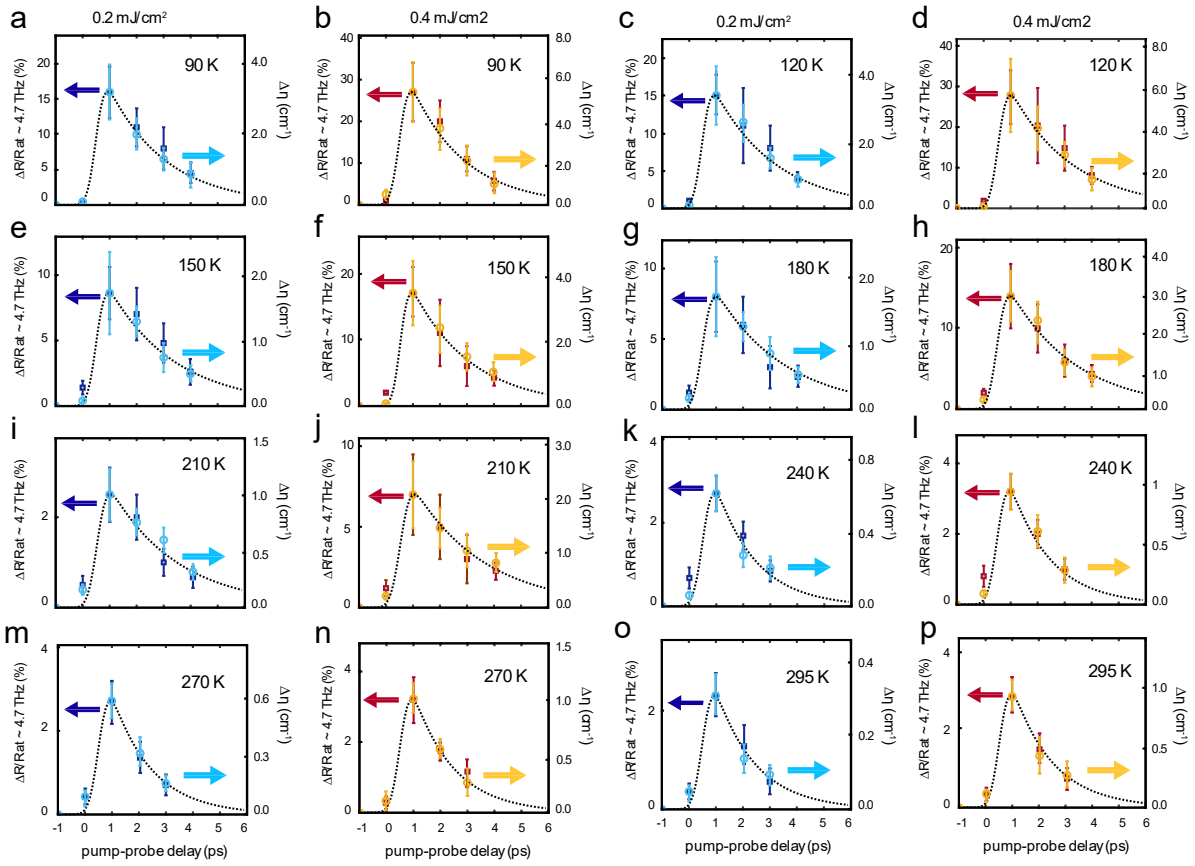

Figure 4.17: Dynamics of reflectivity enhancement $\Delta R/R$ at 4.7 THz (left panel, closed squares) and integrated pump-induced change in reflectivity spectral weight $\Delta\eta$ (right panel, open circles) as a function of temperature and fluence. Both sets of data were plotted on the same scale for comparison. The dotted lines represent single-exponential decay function utilized to determine the relaxation time τ. Error bars represent maximum uncertainties determined from the fits.

Figure 4.17 displays the temperature and fluence-dependent dynamics of the reflectivity enhancement $\Delta R/R$ (left panel, closed squares) and photoinduced change in spectral weight $\Delta\eta$ (right panel, open circles) at different t_{pp}. All the data were plotted on the same scale in order to facilitate a detailed comparison of the dynamics. The black dashed lines denote single exponential fits using the function,

$$f(t_{pp}) = a\left(\mathrm{erf}\left(b(t_{pp}+c)\right)+1\right)e^{-\frac{t_{pp}+c}{\tau}}. \quad (4.4)$$

Where, a, b and c are fitting parameters while τ denotes the relaxation time. As evident from the Fig. 4.17, $\Delta R/R$ and $\Delta\eta$ exhibit similar dynamics which verifies our observation that the reflectivity enhancement is attributed to an electronic origin arising from the photoexcitation in TNS. It was also noted that the dynamics of both $\Delta R/R$ and $\Delta\eta$ closely match the dynamics shown in Fig. 4.14a, b.

In the previous section, we showed that $\Delta R/R(T)$ and $\Delta\eta(T)$ both exhibit the properties of a BEC-like exciton condensate as manifested in the photoinduced peaks at the select IR phonon frequencies, implying condensate-lattice coupling. In this section, we have shown a good correspondence between the condensate response dynamics and the photoinduced relaxation dynamics. In conjunction with these two scenarios, our results reveal that the pump-induced reflectivity enhancement is a reporter of the exciton condensate dynamics and the transient photoinduced dynamics denote the perturbation of the condensate (pair breaking) to nonequilibrium phase and its subsequent relaxation (pair formation) back to the equilibrium.

4.2.6 Entangled order parameters

As we have discussed in Chapter 2 earlier, the topic of existence of an EI state and the origin of the phase transition TNS has drawn controversy since parasitic coupling from the lattice makes

it difficult to detect the EI state. Thus, numerous experiments have been performed to clarify the structural or electronic dominance of phase transition, albeit with contradictory results and interpretations [39-42, 45-63, 70, 71]. As such, it is necessary to explain the roles of lattice and electronic (excitonic) order parameters by disentangling them. In our experiment, we have demonstrated that the time-resolved THz spectroscopy reports unambiguous condensate signatures while simultaneously clarifying the dynamical repercussions of electron-phonon coupling in TNS. In this picture, the condensate is coupled to the IR phonons (4.7 THz B_{3u} phonon). When we perturb the condensate out of equilibrium by photoexcitation, photoinduced peaks appear in the enhanced reflectivity spectrum thanks to the condensate-lattice coupling. From the interesting BEC-like temperature dependence of the reflectivity enhancement, it can be noted that although the reflectivity enhancement occurs at 4.7 THz IR-active phonon frequency, it shows a BEC-like temperature dependence which is a signature of a BEC-like exciton condensate is coupled to the 4.7 THz phonon.

Another interesting observation is that, despite the possibility of a contribution from a structural order parameter intertwined with the excitonic order parameter, the observed temperature dependence of the enhanced reflectivity occurs well below the structural $T_C = 326$ K. Hence, while the LT monoclinic phase promotes electron-phonon coupling, the LT physics is dominated by the exciton condensate.

The experimental evidence demonstrates that the temperature roll-off plot has a significant drop around 240 K. It shows that the nonlinear phonon process has a different transition temperature than the equilibrium phase transition, indicating that the electron-phonon interaction is sensitive primarily to the electronic state. This is consistent with previous Raman measurement reporting a separate electronic transition temperature of $T_C^{el} = 237$ K when electron-phonon are

coupled. The T_C is further increased to 326 K in the presence of a B_{2g} strain [48]. There is another Raman study showing a Curie-Weiss temperature of $T_w = 240$ K which would be the transition temperature of TNS if no lattice order parameter was involved [51]. This conclusion merits further exploration as it could open new possibilities in interrogating complex systems like TNS. However, the temperature dependence of this process strongly suggests that time-resolved THz spectroscopy can disentangle the electronic and lattice contributions and traces the electronic contribution that resembles a BEC-like trend.

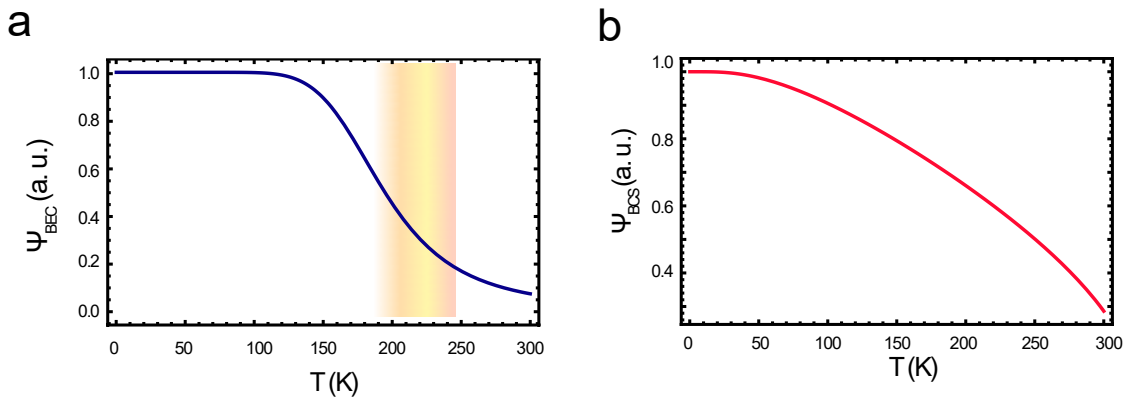

Figure 4.18: a, Temperature dependence of a BEC-like order parameter with a BEC gap of 130 meV. The yellow patch marks the region around 230 K which exhibits a slow drop similar to our results. **b**, A BCS-like lattice order parameter with $T_C = 326$ K.

To quantify the entangled order parameters, we use a toy model that show the interplay between the structural and excitonic order parameter. Assuming that the excitonic order parameter Ψ_{ex} is from a BEC-like exciton condensate, it can be expressed as,

$$\Psi_{ex} = \Psi_{BEC} = \frac{\frac{A}{\Delta_E}}{1 + B \exp\left(-\frac{\Delta_E}{k_B T}\right)}, \tag{4.5}$$

where Δ_E is the temperature independent BEC gap which denotes the exciton binding energy, and A, B are constants (similar to (4.1)). Plugging in $\Delta_E = 130$ meV, $A = 1400$ and $B = 1500$, we plot the normalized BEC like order parameter in Fig. 4.18a (blue line). The bending feature around 240 K is marked by the yellow region. In addition, we assume that the normalized lattice order parameter Ψ_L has a BCS-like temperature dependence and thus can be written as,

$$\Psi_L = \Psi_{BCS} = \frac{\Delta(0)}{160}\sqrt{1 - \frac{T}{T_C}}. \tag{4.6}$$

Here, $T_C = 326$ K and $\Delta(0) = 160$ meV. This is computed and plotted in Fig. 4.18, showing a second-order phase transition near 326 K (red line).

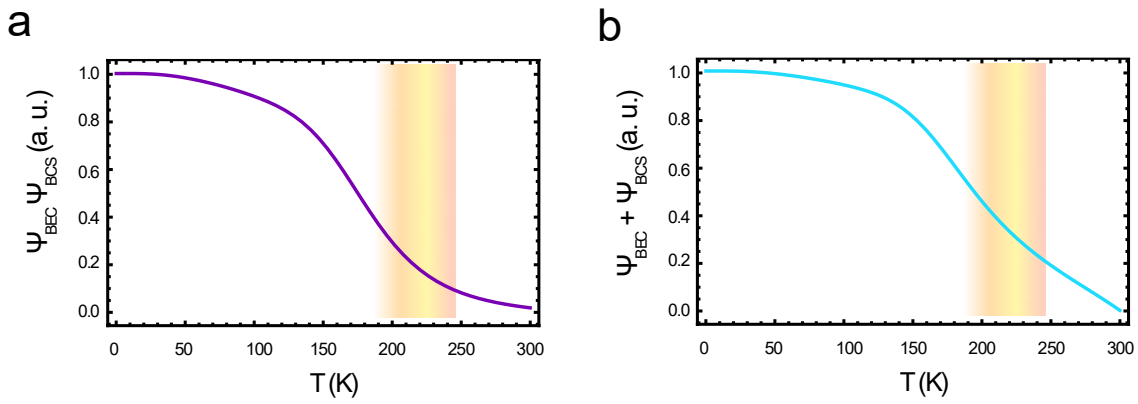

Figure 4.19: a, Temperature dependence of a entangled order parameter which is the product of BEC-like order parameter with a BEC gap of 130 meV and a BCS-like lattice order parameter with $T_C = 326$ K. The yellow patch marks the region around 230 K which exhibits a slow drop similar to our results. **b**, Sum of the two order parameters.

Now we discuss the case of an entangled order parameter as a combination of a BEC-like excitonic order Ψ_{BEC}, and a BCS-like lattice order parameter Ψ_{BCS}. For simplicity, we assume that there can be two possible combination: (1) The entangled order parameter $\Psi_{entangled}$ can be a product of Ψ_{BEC} and Ψ_{BCS}, i.e., $\Psi_{entangled} = \Psi_{BEC}\,\Psi_{BCS}$, as seen in Fig. 4.19a (purple curve), (2)

a linear combination of Ψ_{BEC} and Ψ_{BCS}, that is, $\Psi_{entangled} = a\,\Psi_{BEC} + b\,\Psi_{BCS}$. Fig. 4.19b plots the entangled order parameter when $a = b$. For simplicity, the entangled order parameter is normalized. In other words, $\Psi_{entangled} = \Psi_{BEC} + \Psi_{BCS}$ has equal contributions from structural and excitonic order parameters. It is evident from the figure that, for both combinations, a bending feature around 240 K is visible which is also evident in the BEC-like order parameter behavior as seen in Fig. 4.18a.

When, $b \gg a$, $\Psi_{entangled} \approx b\,\Psi_{BCS}$ (in the toy model, Ψ_{BEC} and Ψ_{BCS} are normalized and are assumed to be of the same order) and the order parameter would resemble that of a BCS order parameter with a transition temperature at 326 K (similar to Fig. 4.18b) with no feature around 240 K. Likewise, for $a \gg b$, $\Psi_{entangled} \approx a\,\Psi_{BEC}$ and the normalized entangled order parameter will look like BEC order parameter (Fig. 4.18a). Nonetheless, for the special case of $a = b$, we observed that the normalized entangled order parameter shows the bending feature around the 240 K regime. It implies that even for a BEC-BCS entanglement, the BEC-like order parameter will still be distinguishable and will exhibit hallmarks of a temperature independent BEC-like gap.

As such, in TNS, the entangled order parameter's temperature behavior is dominated by the BEC-like order parameter. This implies that if a BEC-like exciton condensate is present in a system with a structural order parameter, it will dominate the physics at low temperatures. In line with this, our results also confirm the sensitivity of the THz probe to the exciton condensate dynamics as observed in the BEC-like temperature behavior of the reflectivity enhancement as well as the photoinduced integrated reflectivity spectral weight change.

Although the lattice and electronic order parameters are entangled in TNS, a BEC-like temperature behavior was observed in our experiments. This leads to our conclusion that pushing the material out of equilibrium results in a nonlinear response which is sensitive to symmetry and

brings a new temperature scale as seen in our data. This enables us to monitor the condensate by reading out its coupling to the IR-active phonon. Concisely, our THz probe records the condensate response that was encoded in the complex phononic system in TNS in the form of parametric reflectivity enhancement.

4.3 Acknowledgement

This chapter, in part, is currently under review for publication of the material. Sheikh Rubaiat Ul Haque, Marios H. Michael, Junbo Zhu, Yuan Zhang, Lukas Windgätter, Simone Latini, Joshua P. Wakefield, Gu-Feng Zhang, Jingdi Zhang, Angel Rubio, Joseph G. Checkelsky, Eugene Demler, and Richard D. Averitt. The dissertation author was the primary researcher and author of this material.

Chapter 5 Fresnel-Floquet Formalism & Phonon Squeezing

5.1 Fresnel-Floquet mechanism & material dynamics

In this section we provide details of the phenomenological Fresnel-Floquet analysis which provides an alternate route to interpret optical responses of photoexcited materials. In conventional "snapshot" picture, the photoexcited dynamics of a material is imagined as snapshots of "time slices". Each snapshot represents an instantaneous state after photoexcitation. In this method, temporal evolution of spectroscopic feature is explained using the conventional equilibrium treatment, and measured optical parameters serve as spectral fingerprints of the instantaneous states as revealed by the snapshots.

In contrast, Fresnel-Floquet theory allows us to compute optical reflectivity of the materials with oscillating collective modes of the materials. After photoexcitation, the material parameters oscillate and modulate the complex refractive index which can be plugged into the Maxwell equation to obtain dynamic material parameters.

5.1.2 Fresnel-Floquet theory

To compute the material reflectivity at the probe pulse frequency, a better understanding of the character of light propagation inside the material is needed. It requires solving Maxwell equations with the frequency-dependent refractive $\tilde{n}(\omega)$ to find the wavevector of light k inside the medium. This satisfies the equation,

$$\left(\frac{\tilde{n}(\omega)^2\omega^2}{c^2} - k^2\right)E(\omega) = 0. \tag{5.1}$$

Here $E(\omega)$ is the electric field of the probe. Boundary conditions at the interface of the material for electric and magnetic fields lead to the usual Fresnel equations which relates $\tilde{n}(\omega)$ to the complex reflection coefficient $r(\omega)$. For normal incidence, it has the simple form,

$$\tilde{n}(\omega) = \frac{1 - r(\omega)}{1 + r(\omega)}. \tag{5.2}$$

A similar approach can be used to in the presence of an oscillating field at frequency ω_d. We model the effects of the oscillating field on the photons phenomenologically through an oscillating permittivity:

$$\delta\varepsilon(t) = 2A_d \cos(\omega_d t)\,. \tag{5.3}$$

This gives rise to a parametric drive with frequency ω_d and a subsequent mixing of signal (ω_s) and idler (ω_{id}) frequency components, satisfying the relation $\omega_s + \omega_{id} = \omega_d$ (For more details, see ref. [102]). Hence, light eigenmodes inside the material should be understood as the Floquet states that take the form,

$$E(t) = e^{ikx}\left(E_s e^{-i\omega_s t} + E_{id} e^{i\omega_{id} t} + c.c.\right), \tag{5.4}$$

where the wavevector k was found from the solving the Maxwell equations. Using (5.1), (5.3) and (5.4) the new equations in the presence of the parametric drive term are,

$$\left(\frac{\tilde{n}(\omega_s)^2\omega_s^2}{c^2} - k^2\right)E_s(\omega) + A_d E_{id} = 0, \tag{5.5a}$$

$$\left(\frac{\tilde{n}(\omega_{id})^2\omega_{id}^2}{c^2} - k^2\right)E_{id}(\omega) + A_d E_s = 0. \tag{5.5b}$$

Because of the coupling between signal and idler components, every frequency will have two transmission channels associated with different wavevectors, and two eigenmodes inside the material for an incoming field E_0:

$$E_j = t_j E_0 e^{ik_j x}\left(e^{-i\omega_s t} + \alpha_j e^{i\omega_{id} t}\right), \tag{5.6}$$

where $j = 1, 2$, α_j is the relative amplitude given by the eigenvector with k_j, while t_j is the transmission coefficient of the j-th channel. The reflectivity is computed by solving the Fresnel-

Floquet equations which involve matching electric and magnetic fields parallel to the sample surface for both signal and idler frequencies. Inside the sample the total electric field becomes,

$$E_{sample} = \sum_{j=1}^{2} t_j E_0 e^{ik_j y}\left(e^{-i\omega_s t} + \alpha_j e^{i\omega_{id} t}\right), \tag{5.7}$$

and the electric field in the air becomes,

$$E_{air} = E_0\left(e^{\frac{i\omega_s y}{c} - i\omega_s t} + r_s e^{-\frac{i\omega_s y}{c} - i\omega_s t} + r_{id} e^{\frac{i\omega_{id} y}{c} + i\omega_{id} t}\right). \tag{5.8}$$

Here r_s and r_{id} denote the complex reflection coefficient at signal and idler frequencies, respectively. Using Maxwell's equations, the magnetic field and matching boundary condition are determined at $y = 0$ (sample-air interface). This yields the equations for the driven system:

$$1 + r_s = t_1 + t_2, \tag{5.9a}$$

$$1 - r_s = \frac{k_1 t_1}{\omega_s} + \frac{k_2 t_2}{\omega_s}, \tag{5.9b}$$

$$r_{id} = t_1 \alpha_1 + t_2 \alpha_2, \tag{5.9c}$$

$$r_{id} = \frac{k_1 t_1 \alpha_1}{\omega_{id}} + \frac{k_2 t_2 \alpha_2}{\omega_{id}}. \tag{5.9d}$$

From these equations, it is possible to determine the complex reflection coefficients at signal and idler frequencies.

5.1.2 Experimental observations & Fresnel-Floquet formalism

Insight into the experimentally observed reflectivity dynamics can be obtained from a minimal phenomenological model based on Fresnel-Floquet theory [103]. Briefly, the sample permittivity ε acquires an oscillatory component upon photoexcitation given as $\delta\varepsilon(t) \propto \cos(\omega_d t)$, where ω_d is the driving frequency (importantly, ω_d is distinct from the pump photon energy). Plugging the dynamic permittivity (i.e., $\varepsilon = \varepsilon_{eq} + \delta\varepsilon(t)$, where ε_{eq} is the equilibrium permittivity)

into the dispersion relation determined from Maxwell's equations and applying the appropriate boundary conditions (see Eqns. 5.1 – 5.9) enables calculation of $\Delta R/R$.

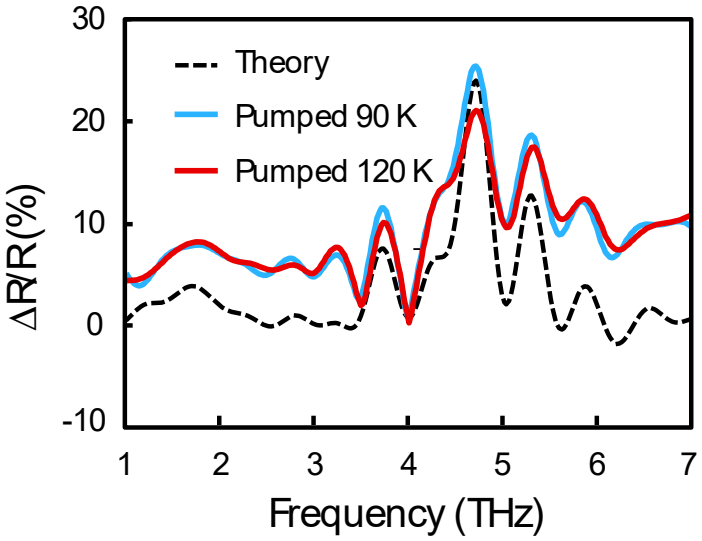

Figure 5.1: a, Theoretical analysis (black dashed line) using Fresnel-Floquet analysis using $\omega_d = 9.4$ THz and experimental data (red and blue) showing good agreement.

To fit the experimental $\Delta R/R$ data, ε_{eq} is obtained from the experimentally measured reflectivity and taking ω_d= 9.4 THz. This is twice the frequency of the 4.7 THz (ω) B_u phonon and is fully justified using an effective Hamiltonian description and DFT calculations in the following sections. The fit of $\Delta R/R$ is shown in Fig. 5.1 and is in good agreement with experiment, highlighting that the dominant contribution to ω_d is the 4.7 THz phonon. The deviation from experiment likely arises from neglecting other IR phonons that participate (to a lesser degree) in the dynamics.

Our analysis reveals that the dynamically evolving material properties act as a parametric drive at $\omega_d = 2\omega$ (depicted in Fig. 5.2). Specifically, an incident THz probe photon at frequency ω_s interacts with the dynamic interface to generate reflected photons at the signal (ω_s) and idler

frequencies ($\omega_{id} = \omega_d - \omega_s$). Thus, $\Delta R/R$ is effectively the stimulated parametric emission spectrum. Importantly, our results show that Fresnel-Floquet analysis provides an approach to describe coherent nonlinear effects, in contrast to analysis of the dynamics as "frozen snapshots" of the optical conductivity at each pump-probe delay.

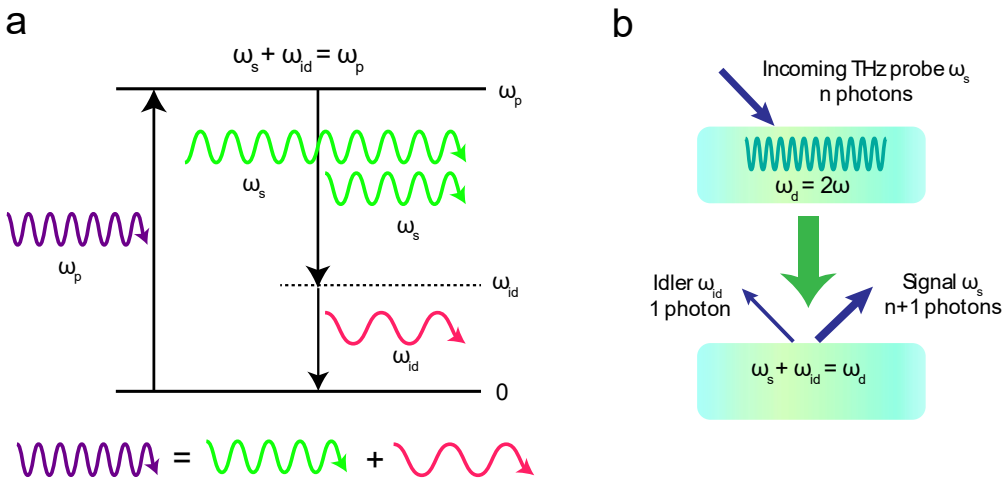

Figure 5.2: a, Principle of an OPA where in the presence of a pump beam (ω_p), an incoming signal photon (ω_s) creates a weaker idler beam (ω_{id}). **b**, Incoming THz photon ω_s interacting with 2ω drive and creating signal (ω_s) and idler (ω_{id}) photons, resulting in enhanced reflected signal at ω_s.

5.2 Phonon Squeezing

In the previous chapter, we presented our results on the optical pump – broadband THz studies on TNS, a putative EI. A photoinduced reflectivity enhancement at THz frequencies is observed that showed a BEC-like temperature dependence, suggesting a novel method to trace the spectral fingerprints of the exciton condensate. Simultaneously, dynamic condensate-lattice coupling was also observed revealed by pronounced peak at select IR phonon locations. In this chapter, we will demonstrate that this nonlinear optical process of photoinduced reflectivity is a parametric process and originates from squeezing oscillations of IR phonons upon condensate

perturbation and can have broader impact in leading to novel THz photon sources using EI as the gain medium.

5.2.1 Squeezing from quantum mechanical perspective

Before we explain our results on the hallmarks of exciton condensate signatures in terms of phonon squeezing, we first illustrate phonon squeezing in this section. Consider a quantum particle in a parabolic potential. In the ground state, it has finite $\langle X^2 \rangle_0$. Then the Hamiltonian can be written as,

$$H = \frac{p^2}{2m} + \frac{m\omega^2}{2} X^2. \tag{5.10}$$

We can estimate $\langle X^2 \rangle_0$ using the Heisenberg uncertainty principle:

$$\langle p^2 \rangle = \frac{1}{\langle X^2 \rangle}, \tag{5.11}$$

which enables us to calculate the ground state energy as a function of $\langle X^2 \rangle_0$. Plugging (5.11) into (5.10) we have,

$$E(\langle X^2 \rangle) = \frac{1}{2m \langle X^2 \rangle} + \frac{m\omega^2}{2} \langle X^2 \rangle, \tag{5.12}$$

the energy needs to be minimized with respect to $\langle X^2 \rangle$ in order to find the ground state energy as well as $\langle X^2 \rangle_0$.

$$\frac{\partial E}{\partial \langle X^2 \rangle} = 0 = -\frac{1}{2m \langle X^2 \rangle_0^2} + \frac{m\omega^2}{2}$$

$$\langle X^2 \rangle_0 = \frac{1}{m\omega}.$$

Using (5.2) we obtain, $\langle p^2 \rangle_0 = m\omega$ and hence, $E_0 = \omega$. We can now map the ground state wave function in the phase space which takes up the form depicted in Fig. 5.3:

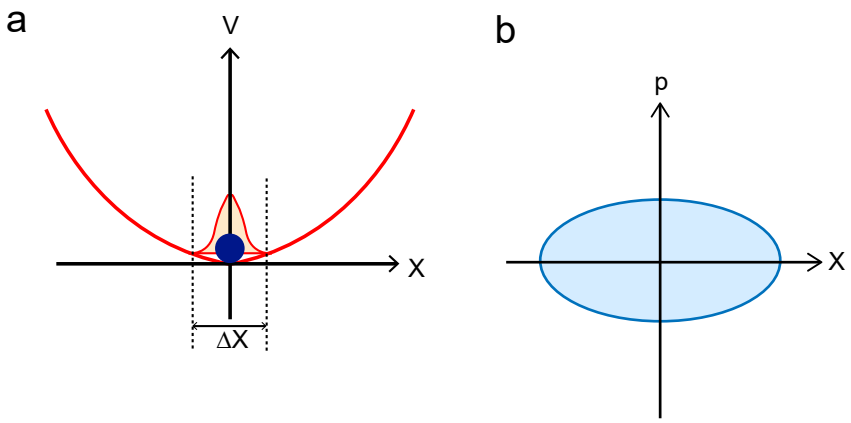

Figure 5.3: a, A particle in a simple harmonic potential, the region enclosed by the dotted lines denotes the uncertainty in position, **b**, the phase space representation of the initial state.

Now, let us consider a situation when at $t = 0$, the parabolic potential suddenly changes from $\frac{m\omega^2}{2}X^2$ to $\frac{m\Omega^2}{2}X^2$. Fig. 5.2 shows a pictorial representation of the transient process where the parabolic potential goes through an abrupt change.

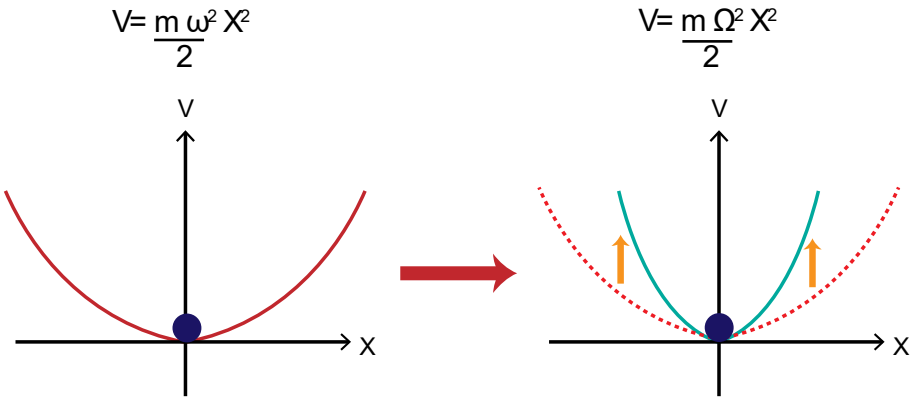

Figure 5.4: The left parabola represents the harmonic potential $\frac{m\omega^2}{2}X^2$. A sudden change of the harmonic potential from the initial state to a new equilibrium (teal) at $t = 0$.

For the classical particle in equilibrium, this change would not matter. However, for the quantum particle, this new equilibrium corresponds to a new state with $\langle X^2 \rangle_N$ and $\langle p^2 \rangle_N$. Note that, at $t = 0$, we have $\langle X^2 \rangle_0 \neq \langle X^2 \rangle_N$. Again, minimizing the total energy with respect to $\langle X^2 \rangle_N$ yields $\langle X^2 \rangle_N = \frac{1}{m\Omega}$. When $\Omega > \omega$, it is observed that $\langle X^2 \rangle_N < \langle X^2 \rangle_0$. Utilizing (5.11), it can be seen that $\langle p^2 \rangle_N > \langle p^2 \rangle_0$. In the new equilibrium, the wavefunction is too "spread out" in momentum p, and too "squeezed" in position X (see Fig. 5.5).

A mismatch between the initial state and the new equilibrium launches evolution of the wave function shown in Fig. 5.4 (phase space representation). Note that during this evolution, $\langle X \rangle = 0$ and $\langle p \rangle = 0$. However, $\langle X^2 \rangle$ and $\langle p^2 \rangle$ oscillate periodically in time with frequency 2Ω. This process is called phonon squeezing.

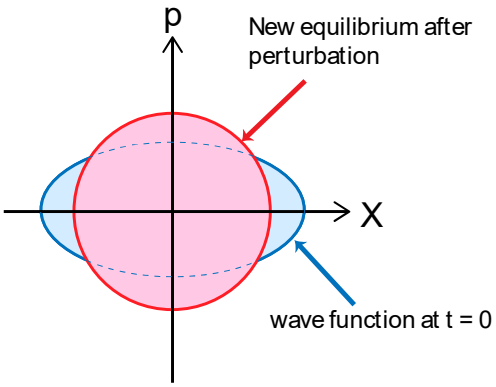

Figure 5.5: After a sudden change in potential at $t = 0$, new equilibrium state (red) depicting "spread out" state in position and "squeezed" state in momentum.

For a more quantitative explanation, a rigorous mathematical formulation is necessary. According to Heisenberg's uncertainty principle, the ion position and momentum in a crystal cannot be determined precisely even in the ground state:

$$\Delta X \, \Delta p \geq \frac{\hbar}{2}. \tag{5.13}$$

The manifestation of the uncertainty in the ground state of the material can be described as fluctuations of both position and momentum coordinates,

$$\langle X^2 \rangle \, \langle p^2 \rangle \geq \frac{\hbar^2}{4}. \tag{5.14}$$

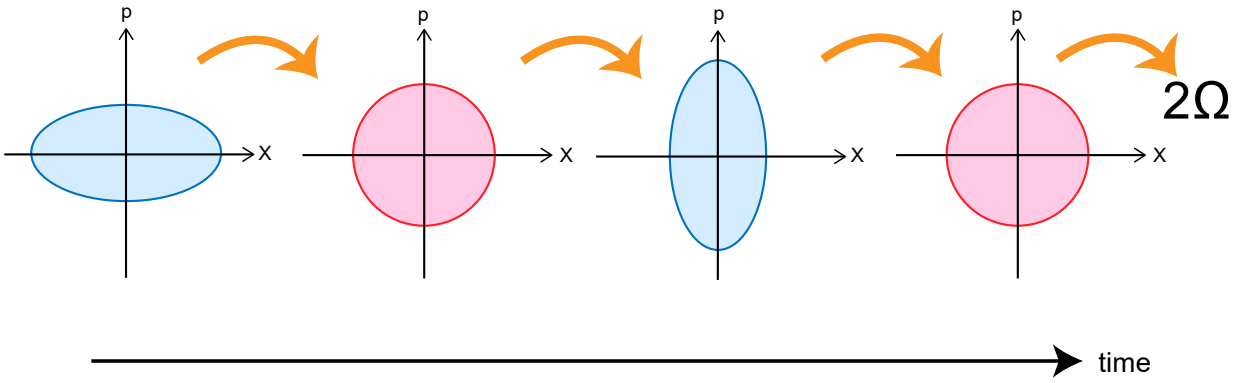

Figure 5.6: Evolution of the wavefunction of the quantum particle (phase space representation), showing a 2Ω oscillation.

Equation (5.14) shows that even the product of fluctuations in position and momentum are constant, one can reduce fluctuation in X at the expense of increasing fluctuation in p. This is the basic principle of squeezing. Squeezing is usually expressed in terms of creation and annihilation operators, a and $a^\dagger$ as shown below,

$$X = \frac{a + a^\dagger}{\sqrt{2}}, \tag{5.15a}$$

$$p = -i \, \frac{a - a^\dagger}{\sqrt{2}}. \tag{5.15b}$$

As a result, fluctuations are given by the expressions,

$$\langle X^2 \rangle = \frac{\langle a^\dagger a \rangle + \langle a a^\dagger \rangle}{2} + \frac{\langle a^\dagger a^\dagger \rangle + \langle a a \rangle}{2}, \tag{5.16a}$$

$$\langle p^2 \rangle = \frac{\langle a^\dagger a \rangle + \langle a a^\dagger \rangle}{2} - \frac{\langle a^\dagger a^\dagger \rangle + \langle a a \rangle}{2}. \tag{5.16b}$$

Since the first term, $\frac{\langle a^\dagger a \rangle + \langle a a^\dagger \rangle}{2}$, is common on to both $\langle X^2 \rangle$ and $\langle p^2 \rangle$, in order to reduce fluctuations in X while increasing them in p, anomalous expectation values of the type $\langle aa \rangle$ and $\langle a^\dagger a^\dagger \rangle$ need to be created. A state with such anomalous expectation values can be described as a condensate of entangled phonon pairs. To summarize, "squeezed state" and condensate of entangled phonon pairs refer to the same concept: reducing the uncertainty in the ion position by increasing the uncertainty in the ion momentum and vice versa.

The ground state of phonons in Ta_2NiSe_5 is not squeezed. Upon photoexcitation, the IR phonons are squeezed due to the presence of photoelectrons and the squeezing takes place in the form of an oscillation. For a phonon with frequency ω, the fluctuation terms become,

$$\langle X^2 \rangle = \langle X^2 \rangle_0 + A \cos(2\omega t)\,, \tag{5.17a}$$

$$\langle p^2 \rangle = \langle p^2 \rangle_0 - A \cos(2\omega t). \tag{5.17b}$$

From (5.17a) and (5.17b), it is found that both $\langle X^2 \rangle$ and $\langle p^2 \rangle$ have an oscillatory component $A\cos(2\omega t)$, which oscillates at twice the IR phonon frequency ω (see Fig. 5.7). This is the resonance condition for squeezing. The terminology "oscillation of squeezed phonons" means periodically alternating between reducing fluctuation in the ion position by increasing fluctuations in the momentum and increasing fluctuation in the ion position by reducing fluctuations in the momentum.

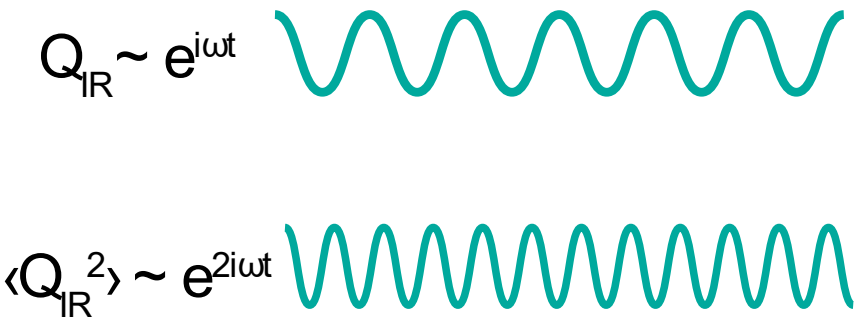

Figure 5.7: Schematic of a phonon (top) and corresponding phonon squeezing (bottom) oscillation at twice the phonon frequency.

5.2.3 Fresnel-Floquet theory

In this optical pumping at 0.5 eV excites electron-hole pairs and is off-resonant with respect to the phonons. From symmetry arguments, the photo-excited electron occupation couples to IR active modes through a phonon squeezing Hamiltonian:

$$H = \sum_k g_k \, Q_{IR}^2 \, c_k^\dagger c_k \, . \tag{5.18}$$

In (5.18), g_k is the electron-phonon coupling strength and Q_{IR} is the IR phonon coordinate. It can be shown how such a term can naturally arise through a dipole-dipole interaction between IR active phonon dipole moments linearly coupled to electron dipole transitions. Squeezing of IR active phonons by photo-excited electrons through this type of interaction has been explored in previous studies in the context of photo-induced superconductivity [104]. We use ab-initio DFT calculations outlined in the next section to calculate g_k and find a very strongly coupled IR phonon at 4.7 THz.

5.2.4 Phonon squeezing

In this section a detailed account of the IR-phonon squeezing process and the coherent oscillation at twice the phonon frequency is presented. Phonon squeezing provides a route to generate phonons at frequency ω with higher energy (i.e., > ω) pump photons. In this case, the expectation value of the phonon coordinate is zero (i.e., $\langle Q_{IR} \rangle = 0$). However, phonon fluctuations can be excited through a Raman process, $\langle Q_{IR}^2(t) \rangle = \langle Q_{IR}^2 \rangle_0 + A\, cos(2\omega t)$. To clarify this, the effective Hamiltonian for a phonon system can be written as,

$$H_{ph} = \frac{\Pi^2}{2M} + \frac{M\left(\omega_0^2 + f(t)\right)Q_{IR}^2}{2} + ZEQ_{IR}, \tag{5.19}$$

where Π is the momentum of the phonon coordinate Q_{IR}, ω_0 is the bare phonon frequency (in this case, it is 4.7 THz), M is the phonon mass, Z is the IR activity of the phonon, E is the electric field, and the effective parametric drive $f(t)$ is given by the photoexcited electron population coupled to the phonon,

$$f(t) = \sum_k \frac{g_k}{M} n_k(t)\,. \tag{5.20}$$

Here, g_k is the electron-phonon coupling (as above) and $n_k(t)$ is the photoexcited electron occupation. The electron occupation dynamics was modeled as a fast photoexcitation process that thermalizes back to equilibrium on a characteristic timescale and the parametric drive $f(t)$ is written as $f(t) = f_0\theta(t)\, \mathrm{e}^{-\gamma \mathrm{t}}$. If the characteristic thermalization time is of the order of ~2 ps, then $f(t)$ can be taken as a theta function. In contrast, for timescales much smaller than 100 fs, the period of phonon oscillations, $f(t)$ is a delta function. In both cases, fast electron dynamics provide an impulsive Raman drive with a broad frequency spectrum which linearly excites phonon fluctuations $\langle Q_{IR}^2(t) \rangle$. The equations of motions of the phonon field fluctuations are:

$$\partial_t\langle Q_{IR}^2\rangle = \frac{\langle Q_{IR}\Pi + \Pi Q_{IR}\rangle}{M}, \tag{5.21a}$$

$$\partial_t\langle Q_{IR}\Pi + \Pi Q_{IR}\rangle = -2M\big(\omega_0^2 + f(t)\big)\langle Q_{IR}^2\rangle + 2\frac{\langle\Pi^2\rangle}{M} - 2Z\langle E Q_{IR}\rangle, \tag{5.21b}$$

$$\partial_t\langle\Pi^2\rangle = -M\big(\omega_0^2 + f(t)\big)\langle Q_{IR}\Pi + \Pi Q_{IR}\rangle - Z\langle E\Pi + \Pi E\rangle, \tag{5.21c}$$

At $k = 0$, we substitute $E = \frac{ZQ_{IR}}{\varepsilon\varepsilon_0}$, and rewrite the equations (5.21b) and (5.21c) as,

$$\partial_t\langle Q_{IR}\Pi + \Pi Q_{IR}\rangle = -2M\big(\omega^2 + f(t)\big)\langle Q_{IR}^2\rangle + 2\frac{\langle\Pi^2\rangle}{M}, \tag{5.21d}$$

$$\partial_t\langle\Pi^2\rangle = -M\big(\omega^2 + f(t)\big)\langle Q_{IR}\Pi + \Pi Q_{IR}\rangle, \tag{5.21e}$$

where $\omega^2 = \omega_0^2 + \frac{Z^2}{\varepsilon\varepsilon_0 M}$ is the renormalized phonon frequency at $k = 0$. Expanding the phonon fluctuations gives $\langle Q_{IR}^2\rangle = \langle Q_{IR}^2\rangle_0 + \langle Q_{IR}^2\rangle_1$. Here $\langle Q_{IR}^2\rangle_0$ is the thermal fluctuation and $\langle Q_{IR}^2\rangle_1 \propto f(t)$. To linear order in $f(t)$, the equations of motion are $\frac{\langle\Pi^2\rangle_1}{M} = M\omega^2\langle \mathrm{Q}_{\mathrm{IR}}^2\rangle_1 + Mf(t)\langle Q_{IR}^2\rangle_0 + \mathcal{O}(f^2)$. Combining equations (5.21a), (5.21d) and (5.21e) yields:

$$(\partial_t^2 + 4\omega^2)\langle Q_{IR}^2\rangle_1 = -4f(t)\langle Q_{IR}^2\rangle_0. \tag{5.22}$$

Equation (5.22) provides insight into the IR phonon driving and the relevant phonon fluctuation frequency. It shows that parametric resonance of the phonon coordinate at twice the phonon frequency 2ω appears as a regular resonance for the phonon fluctuations $\langle Q_{IR}^2\rangle$ [105]. It is also significant that the resonance of the phonon fluctuations acts as a filter for the broadband electron dynamics leading to coherent oscillations. These oscillations are responsible for parametrically amplifying the TNS reflectivity at select IR phonon frequencies. It can also be noticed that the left side of (14) resembles the simple harmonic oscillation equation of phonon fluctuation $\langle Q_{IR}^2\rangle_1$ where the frequency of the oscillation (2ω) is twice the phonon frequency ω. This mathematical formulation demonstrates the source of the 2ω driving frequency in the

parametric amplification process and further justifies the excellent agreement between theory and experiment as depicted in Fig. 5.1.

While Fresnel-Floquet theory provides a good fit to the data, further analysis is required to justify $\omega_d = 9.4$ THz since IR-active phonons are not directly excited by the pump. Electron-phonon coupling provides a mechanism whereby photoexcitation with above-gap 0.5 eV pulses polarized along the *a*-axis can couple to the IR modes. This is captured by an effective electron-phonon Hamiltonian,

$$H_{e-ph,eff} = \sum_k g_k \, Q_{IR}^2 \, (n_{ck} - n_{dk}), \tag{5.23}$$

where Q_{IR} is the phonon coordinate, $(n_{ck} - n_{dk})$ represents the photoexcited electron occupation and g_k is the effective electron-phonon coupling as stated in (5.20).

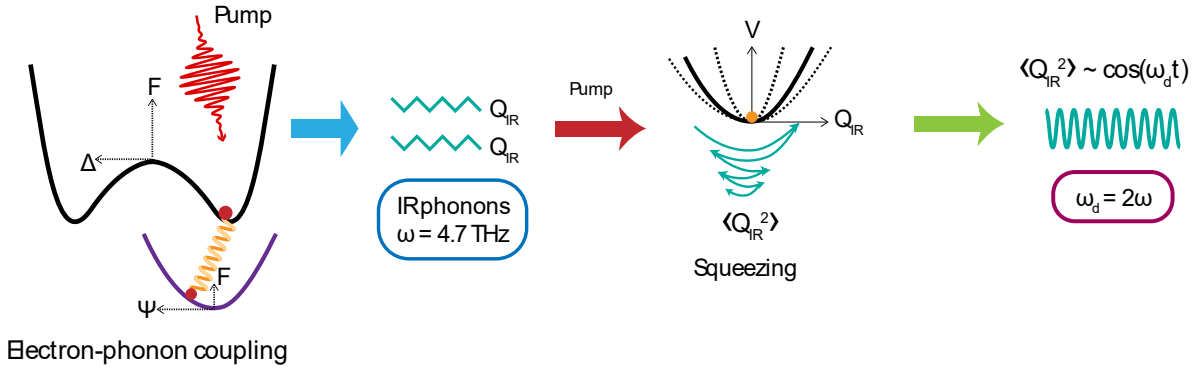

Figure 5.8: Photoinduced modulation of electron-phonon coupling for dominant 4.7 THz phonon. Squeezed phonons oscillating at frequency 2ω, act as the drive for parametric photon generation.

Since IR phonons are not directly excited by the off-resonant pump, the expectation value of the phonon mode is zero (i.e., $\langle Q_{IR} \rangle = 0$). However, above-gap photoexcitation (see Eqns. 5.18

– 5.22 in Methods) leads to squeezed phonons that coherently oscillate at twice the phonon frequency 2ω, $\langle Q_{IR}^2(t)\rangle = \langle Q_{IR}^2\rangle_0 + A\,cos(2\omega t)$, as shown in Fig. 5.8. Although, this 2ω overtone does not have a dipole due to its symmetry and thus cannot emit THz radiation, it can create stimulated emission. In short, the 2ω phonon squeezing oscillation serves as the driving frequency ω_d, creating a photon pair with opposite momenta whose frequencies satisfy the parametric resonance relation,

$$\omega_s(k) + \omega_{id}(-k) = \omega_d = 2\omega. \tag{5.24}$$

To sum up, above-gap photoexcitation initiates phonon dynamics that result in enhanced THz reflectivity.

To show that this phenomenon is related to squeezing from a quantum mechanical perspective, we now expand $\langle Q_{IR}^2\rangle$ in terms of creation and annihilation operators. Using the definition $Q_{IR} = \frac{a+a^\dagger}{\sqrt{2M\omega}}$, we find the expression,

$$\langle Q_{IR}^2\rangle = \frac{\langle a^\dagger(t)a^\dagger(t)\rangle + \langle a(t)a(t)\rangle + \langle a^\dagger(t)a(t)\rangle + \langle a(t)a^\dagger(t)\rangle}{2M\omega}. \tag{5.25}$$

Here, expectation values of $a(t)a^\dagger(t)$ and $a^\dagger(t)a(t)$ do not oscillate rapidly while the anomalous pairs $a^\dagger(t)a^\dagger(t)$ and $a(t)a(t)$ oscillate at twice the phonon frequency 2ω. As a result, a state with phonon fluctuation that oscillate at twice the phonon frequency implies the existence of a condensate of phonon pairs $\langle a^\dagger(t)a^\dagger(t)\rangle \neq 0$. This creation of anomalous phonon pairs is associated to the squeezing process.

Thus, our temperature dependent reflectivity enhancement data, together with this mathematical analysis, and phenomenological modeling establishes the phonon squeezing as the dominant effect, suggestive of a parametric process.

5.3 DFT calculations

In the previous section, we showed that phonon squeezing at twice the IR phonon frequency serves as the driving frequency for the parametric amplification process. In principle, any of the IR phonons can couple to the electrons to enable parametric enhancement of the reflectivity. To investigate this, DFT calculations were performed in the frozen phonon limit where the band structure is calculated for lattice displacements corresponding to various phonon eigenmodes.

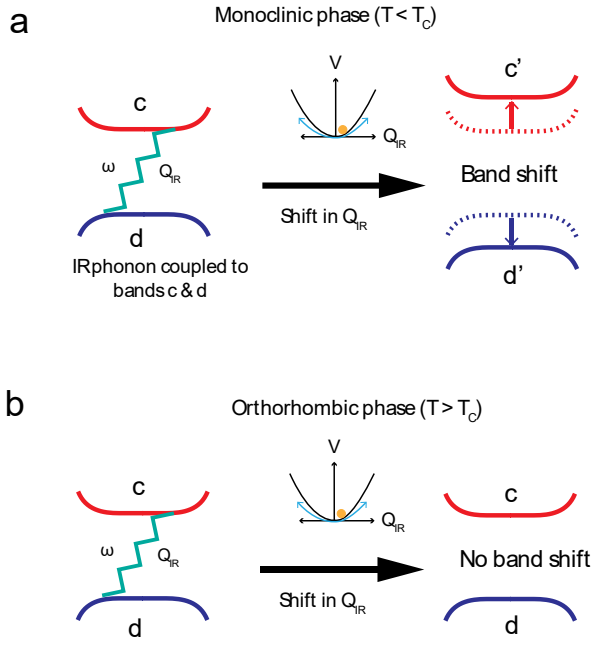

Figure 5.9: a, Schematic summary of DFT calculations for 4.7 THz phonon revealing strong electron-phonon coupling resulting in a band shift in the monoclinic phase. **e**, In the high-temperature orthorhombic phase, no significant band shift arises from electron phonon coupling.

The DFT results are pictorially shown in Fig. 5.9 in the vicinity of Γ point. The calculations reveal that for the 4.7 THz B_u phonon, electron-phonon coupling in the low-temperature

monoclinic phase is the strongest (Fig. 5.10) with small displacements of the phonon coordinate Q_{IR} leading to a band shift as in Fig. 5.9b and Fig. 5.11a. The other phonons in the vicinity of 4.7 THz do not couple nearly as strongly. Moreover, the calculations reveal no significant phonon-induced band shift in the high-temperature orthorhombic phase (Fig. 5.9b, Fig. 5.11b). Thus, DFT calculations provide a microscopic basis for the experimentally observed THz stimulated emission spectrum in Fig. 4.12, 4.13 and 5.1 described using phonon squeezing and Fresnel-Floquet theory. Furthermore, DFT reveals that the electron-phonon coupling is very sensitive to the phase transition in TNS.

The details of the DFT calculations are as follows: The phonon spectrum at the Γ point was computed using the Density Functional Perturbation Theory routines of the VASP code [106-109] employing the vdW-opt88 functional [110, 111] on a $48 \times 4 \times 6$ mesh. The Born effective charges were calculated on a similar k-mesh while the IR-activity was derived using phonopy [112] and the phonon spectroscopy code by described in ref. [113]. The electronic band structure plots have been obtained using a $24 \times 4 \times 6$ k-mesh and a 320 eV cutoff using the standard PBE functional.

For the monoclinic geometry there are 21 symmetry allowed IR-active modes, 11 B_u and 10 A_u modes. Among these, only four modes are in the frequency range near 4.5 THz, listed in Table 5.1. Upon displacing the phonon coordinates Q_{IR} in the positive or negative direction about the equilibrium positions, we recalculated the electronic band structure. From the calculation, it is evident that only mode 26 (frequency ~4.7 THz) shows a strong modulation of the conduction bands upon a small displacement of the phonon coordinate, suggesting a strong coupling of this mode to the electronic degrees of freedom (Fig. 5.10).

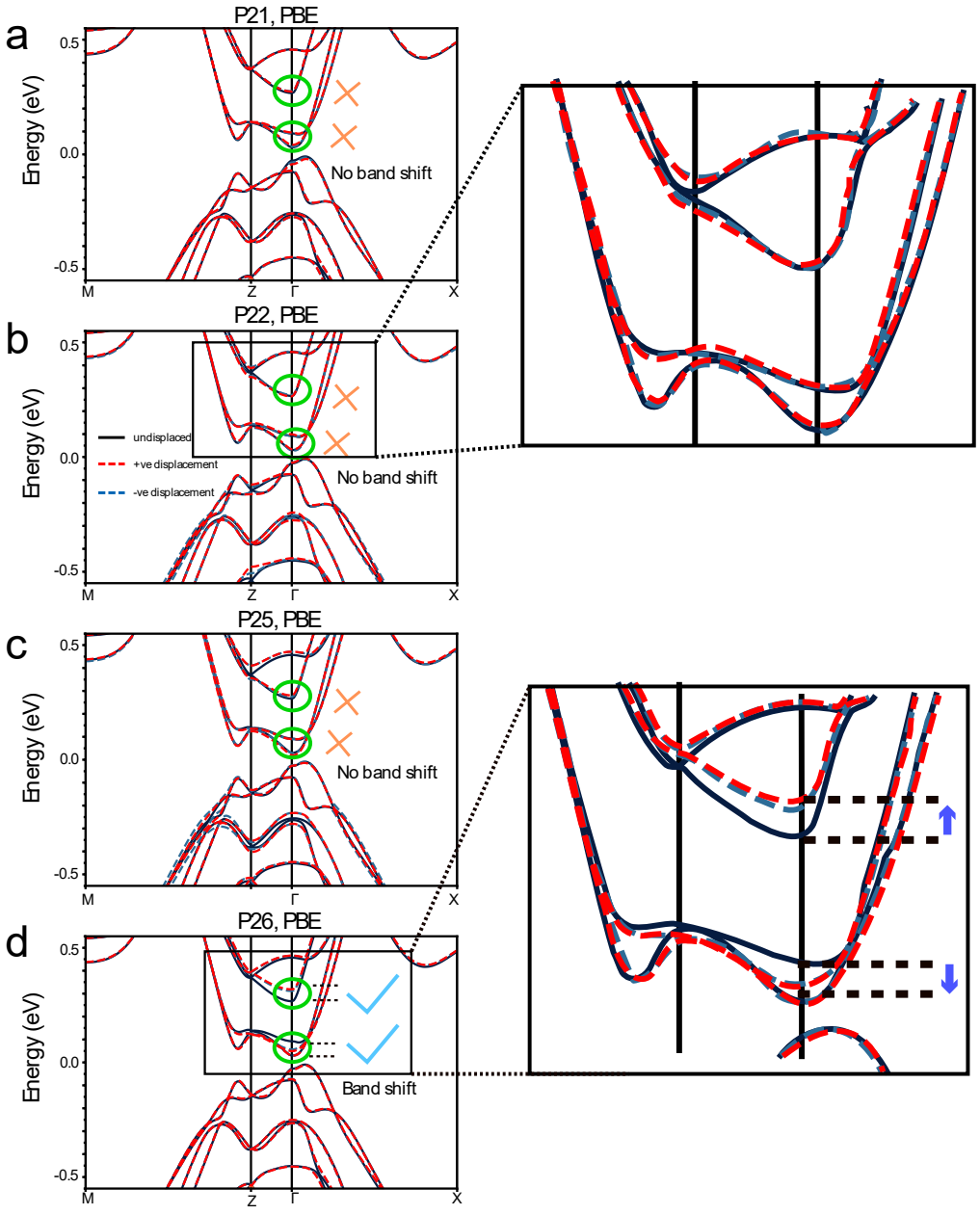

Figure 5.10: Recalculated band structures in the monoclinic phase after displacement of the IR-phonon coordinate along the positive (red dashed line) and negative (dark blue dashed line) directions with respect to the equilibrium structure (black solid line) for **a**, mode 21, **b**, mode 22, **c**, mode 25 and **d**, mode 26 using the PBE functional. Green ellipses represent the shift in bands. Phonon mode 26 shows the largest renormalization and thus the strongest coupling to the band structure upon displacement along its eigenmode. Insets show the zoomed in profiles of the renormalized band structures. Blue arrows signify the direction of the energy shift.

The other phonons do not display significant coupling to the band structure. As a result, no shift in the band structure was observed for the phonon displacements along their eigenmodes. Since we observe the reflectivity enhancement at ~4.7 THz where there is a B_{3u} phonon, the DFT calculation supports our experimental data as well as the theoretical formalism of parametric amplification. Fig. 5.11 displays the evolution of the electron-phonon coupling for the 4.7 THz mode for monoclinic (Fig. 5.11a) and orthorhombic (Fig. 5.11b) phases. It is shown from the *ab initio* calculation that the electron-phonon coupling for the 4.7 THz phonon is strong in the monoclinic phase. This results in a large band renormalization. On the contrary, the band shift almost disappears in the orthorhombic phase. This underscores the relation of the IR-active mode with the order parameter of TNS which is also evident in our experimental observations.

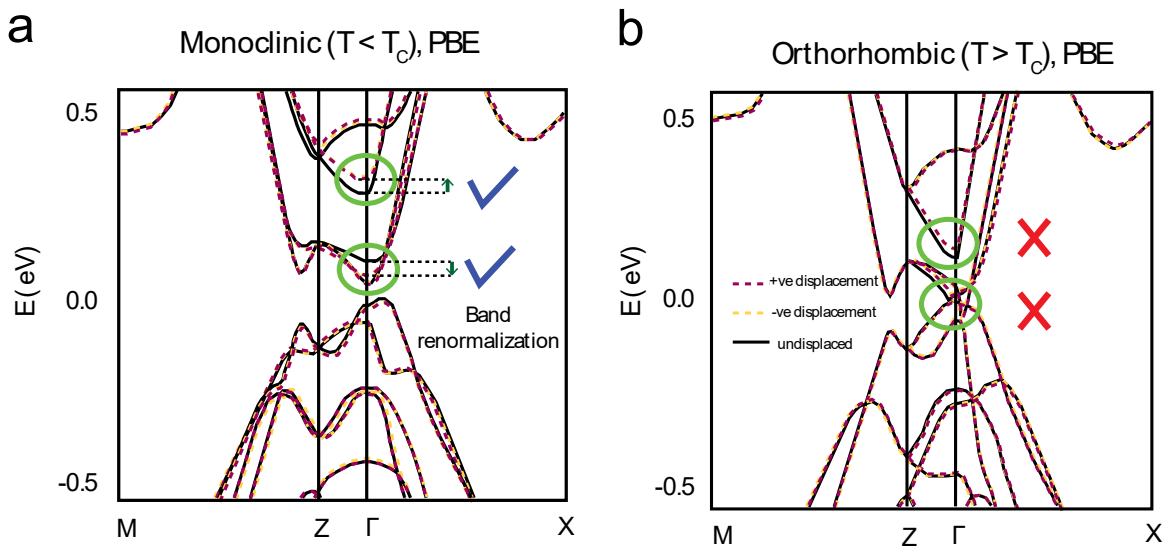

Figure 5.11: Evolution of the 4.69 THz mode. The temperature-dependence of the electron-phonon coupling for 4.69 THz B_u mode and (mode 26) in the **a**, monoclinic and **b**, orthorhombic phases using the PBE functional. For the monoclinic phase, the electron-phonon coupling is strong and thus the shift in the bands owing to the displacement of the phonon coordinate along its eigenmode is large. Contrary to this, the band shift almost disappears for the orthorhombic phase. This demonstrates that the electron-phonon coupling is mediated by the low-temperature order parameter.

Table 5.1: IR-active phonon modes near 4.5 THz. Here there are four phonons with frequency close to 4.5 THz, frequency regime of our interest. Only the 4.69 THz B_u mode is observed to be strongly coupled to the band structure.

Phonon	Symmetry	Frequency (THz)
21	B_u	4.24
22	A_u	4.31
25	A_u	4.63
26	B_u	4.69

This framework, in conjunction with the temperature dependence of the parametric reflectivity enhancement (Fig. 4.12, 4.13), reveals that the phonons are strongly coupled with the exciton condensate. In particular, the experimental temperature dependent results are consistent with $g_k \propto \Delta_{TNS}^2$. That is, the electron-phonon coupling g_k is proportional to the square of the order parameter Δ_{TNS} as embodied in the interaction induced gap. This may involve a contribution from a structural order parameter intertwined with the excitonic order parameter [38, 41, 68], though we note that the observed temperature dependence of the enhanced reflectivity occurs well below T_c. Thus, while the monoclinic phase promotes strong electron-phonon coupling, we expect the dominant contribution to originate from the exciton condensate.

5.4 Possibility of THz emission from exciton condensate

We considered the possibility of THz emission from the exciton condensate. Experimentally, the THz probe was blocked to see if the detector picked up any THz signal emitted from the sample due to photoexcitation. However, no THz emission was observed. TNS is a centrosymmetric crystal with inversion symmetry, resulting in the exciton condensate to have

inversion symmetry as well. As a result, radiation is not expected by optical rectification method, as seen in ZnTe or $LiNbO_3$, without a current or magnetic field bias.

Figure 5.12 pictorially elucidates the excitation process. When pumped with an intense IR pulse, electron-phonon coupling triggers the squeezing of the IR-active phonons and results in the overtone (squeezing oscillation) at twice the phonon frequency. This overtone cannot emit radiation owing to the fact that it does not have any dipole (Fig. 5.12a).

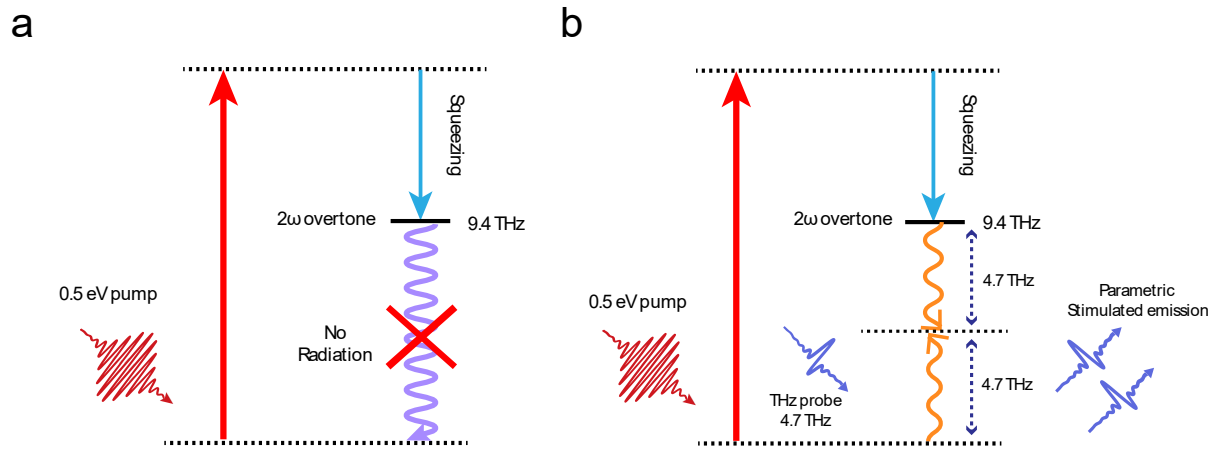

Figure 5.12: a, Schematic of the squeezing process. The 9.4 THz 2ω overtone is Raman active and thus cannot emit THz. **b**, On the contrary, it can emit stimulated radiation with the photon provided by the THz probe.

Instead, we propose the stimulated THz emission scenario (Fig. 5.12b), where the probe THz is amplified by the oscillating material parameters (phonon squeezing effect in our case) upon pumping. Although the 2ω squeezing overtone has no dipole and hence, cannot emit THz, it can emit stimulated radiation. This can be explained by parametric amplification. First, the optical pump initiates the material dynamics at frequency 2ω $(= \omega_d)$ oscillation which is twice the IR phonon frequency ω. Then the probe THz pulse reaches the sample. Since it is a broadband pulse,

it consists of every frequency component from 0 to 7.5 THz (including ω that coincides with the IR phonon frequency). As the referee suggested, we have now included a brief explanation on the possibility of THz emission in the main text.

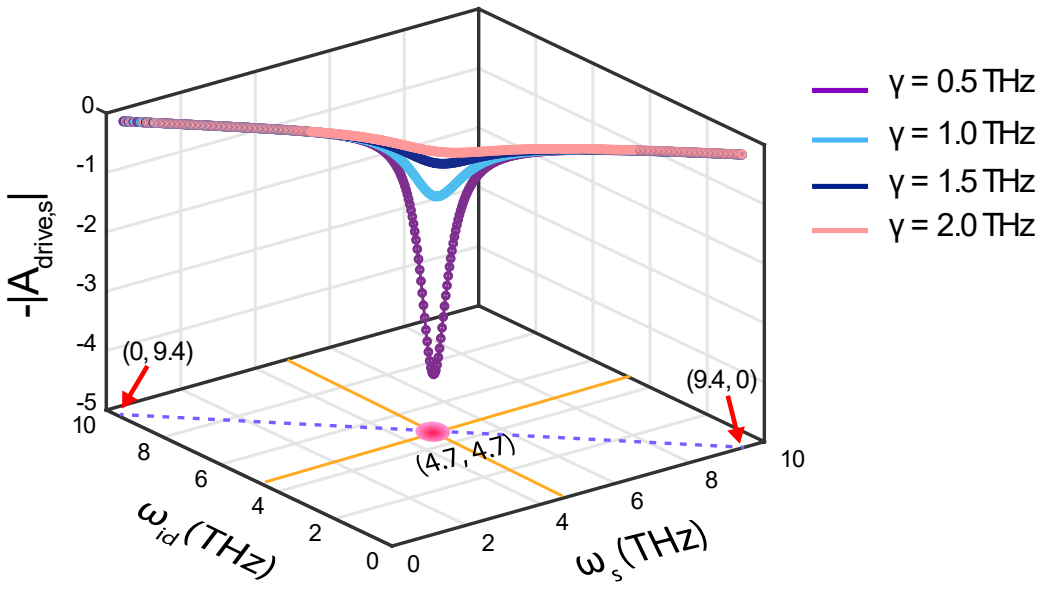

Figure 5.13: Amplitude of the drive (inverted) for the signal for different scattering rates showing a peak for (ω_s, ω_{id}) = (4.7 THz, 4.7 THz).

When the signal pulse frequency ω_s pulse interacts with the interface that is oscillating at ω_d frequency and satisfies the parametric resonance condition, it emits a pair of photons at ω_s and $\omega_{id} = \omega_d - \omega_s$, respectively. As we can see, from this stimulated emission process we get an extra photon at ω_s frequency, which results in the amplification of the signal captured by the detector.

In the case when $\omega_s = \omega_d/2$ (parametric degenerate down conversion), the maximum amplification is achieved. This is shown in Fig. 5.13 where we simulated the driving amplitude of the signal in the presence of the 2ω squeezing oscillation. As seen in the figure, after the pump introduces the squeezed phonon oscillation of 9.4 THz (twice the frequency of the 4.7 THz IR

phonon), we solved the Maxwell's equation and plotted the negative amplitude of the parametric drive for the signal beam $-|A_{drive,s}|$ (THz probe pulse in our experiment) as a function of different scattering rates and it was observed that it peaks at $\omega_s = \omega_{id} = \frac{\omega_d}{2} = \omega = 4.7$ THz (red dot).

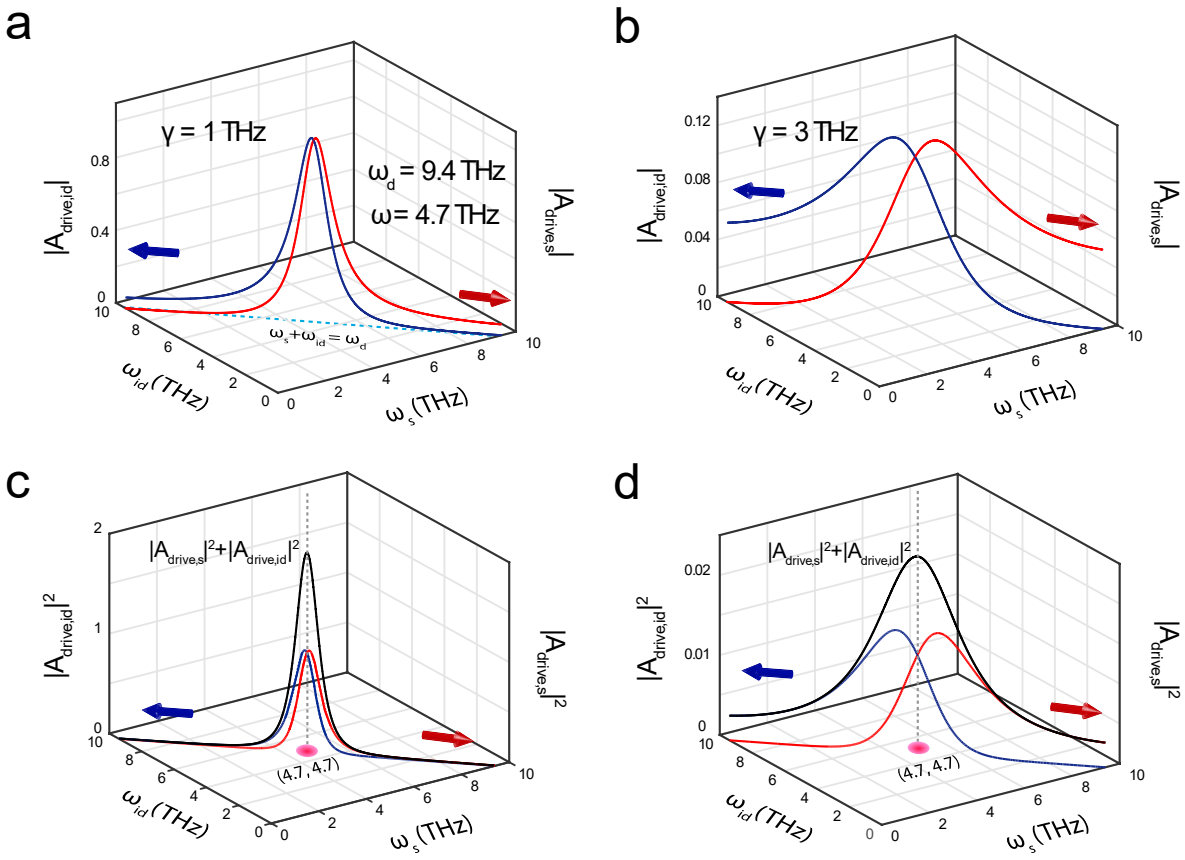

Figure 5.14: a, Driving amplitudes for signal (red, right vertical panel) and idler (blue, left vertical panel) beams for $\gamma = 1$ THz and **b**, $\gamma = 3$ THz. Higher scattering rate exhibits broadening feature. **c**, Sum (black) of the square of signal (red) and idler (blue) amplitudes for $\gamma = 1$ THz and **d**, $\gamma = 3$ THz.

Next, in Fig. 5.14, we plot the driven amplitudes for signal $|A_{drive,s}|$ (red), idler $|A_{drive,id}|$ (blue) for $\gamma = 1$ THz (a) and 3 THz (b) as a function of signal and idler frequencies which satisfy the resonant condition $\omega_s(k) + \omega_{id}(-k) = \omega_d = 2\omega = 9.4$ THz. Here ω is the IR phonon

frequency. The black curves at (c) and (d) denote $|A_{drive,s}|^2 + |A_{drive,s}|^2$ for the corresponding scattering rates which reach the peak values when $\omega_s = \omega_{id} = 4.7$ THz, matching the IR phonon frequency that is squeezed upon pumping. Another interesting observation is that, both signal and idler driven amplitudes have a long tail feature around 4.7 THz which shows broadening for larger scattering rates, consistent with our experimental observation of a broad stimulated emission spectrum $\Delta R/R$.

5.5 Possibility of thermal phonon shift as an alternate explanation

There are two experimental signatures that favor a parametric amplification scenario: (1) as a function of frequency, the photoinduced change in the reflectivity is positive owing to energy extracted from the oscillating drive inside the material into the reflected beam [103, 105], and (2) it is centered around 4.7 THz in a symmetric way. This indicates that parametric amplification arising from Raman-type modulation at 9.4 THz is the most natural mechanism that fits the data. To further verify, we considered other plausible scenarios that might support the experimental observation. As a result, we took into account the possibility of thermal phonon shift as a competing mechanism.

Fig. 5.15a shows equilibrium reflectivity at 90 K (black curve) as well as the reflectivity red shifted by 0.1 THz (red dashed curve), assuming that thermal effects red shifts the reflectivity. If thermal phonon shift was responsible for the reflectivity enhancement, the difference between equilibrium reflectivity and thermally red shifted reflectivity should ideally match ΔR, the pump-induced change in reflectivity. As seen in Fig. 5.15b, there is an unambiguous difference in trend between the photoinduced reflectivity change (red curve) and the reflectivity change due to red shift of phonons (orange curve). It was noted that, thermal shift of phonons results in both negative

and positive changes in reflectivity. Whereas according to Fresnel-Floquet parametric amplification theory, an overall positive change in reflectivity is expected.

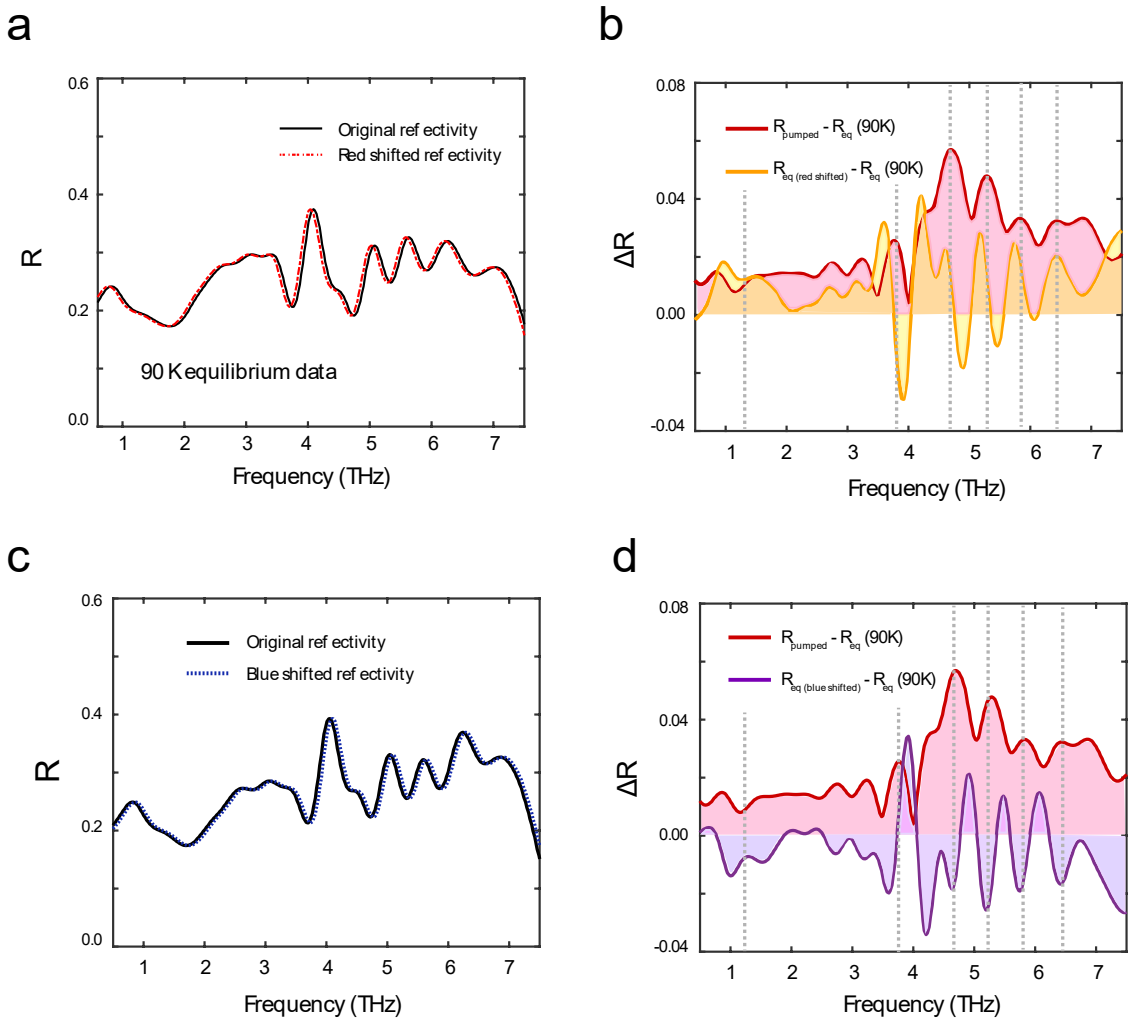

Figure 5.15: **a**, Equilibrium reflectivity at 90 K (black line) and reflectivity red shifted by 0.1 THz (red dashed line). **b**, Photoinduced reflectivity change $R_{pumped} - R_{eq}$ (red curve) along with reflectivity change due to red shift of phonons (orange curve) showing very different trends. We used 0.4 mJ/cm^2 pump fluence. **c**, Equilibrium reflectivity at 90 K (black line) and reflectivity blue shifted by 0.1 THz (blue dashed line). **d**, Photoinduced reflectivity change $R_{pumped} - R_{eq}$ (red curve) along with reflectivity change due to blue shift of phonons (orange curve). The shaded regions under the curves are guide to the eye.

In addition, blue shift of phonons was also considered (Fig. 5.15c), and as depicted in Fig. 5.15d, negative and positive changes in reflectivity were observed similar to the red shifted case. It is evident that there is no similar pattern between photoinduced reflectivity enhancement (red curve) and reflectivity change due to blue shifted phonons (purple curve). This is contradictory to our experimental observation of a universally positive value ΔR as a function of frequency. However, this phenomenon is well captured by the parametric amplification formalism which proves to be the most natural explanation for the data.

5.6 Acknowledgement

Chapter 5, in part, is currently under review for publication of the material. Marios H. Michael, Sheikh Rubaiat Ul Haque, Lukas Windgätter, Simone Latini, Yuan Zhang, Angel Rubio, Richard D. Averitt, Eugene Demler, and Richard D. Averitt. The dissertation author was the primary researcher and author of this material. The remaining part is a reprint of work published in *Physical Review B* **105**, 174301 (2022). In both cases, the thesis author is the coauthor of this material.

Chapter 6 Summary and Broader Impacts

6.1 Condensate, phonon squeezing, & parametric amplification

From Chapters 4 and 5, we have presented our findings on TNS, and our results demonstrate unambiguous optical signatures of exciton condensate manifested in parametric amplification at IR-active phonon frequencies assisted by photoinduced phonon squeezing. These results, combined with previous reports about formation of an exciton condensate at monoclinic phase [40-42, 46-48, 52, 56, 58, 59, 61, 62, 64], demonstrate that nonlinear THz parametric stimulated emission serves as a sensitive reporter of condensate dynamics and the coupling to dynamically fluctuating degrees of freedom.

In recap, we observe photoinduced enhancement of the THz reflectivity with a temperature dependence that is indicative of a photoexcited BEC-like condensate response below T_C. Preferential enhancement of the reflectivity was also observed at select infrared-active phonons, revealing dynamic condensate-lattice interactions. The magnitude of the reflectivity enhancement $\Delta R/R$ at 4.7 THz displays an order parameter-like temperature behavior that can be fitted with a phenomenological temperature independent BEC gap model.

In support of the previous paragraph, our theoretical analysis demonstrates that the dominant electron-phonon coupling is with the 4.7 THz B_{3u} phonon. DFT calculations confirm that for the 4.7 THz phonon, the electron-phonon coupling is strongest in the low-temperature monoclinic phase and there is no significant coupling at the high-temperature orthorhombic phase.

Utilizing a minimal phenomenological model based on Fresnel-Floquet theory, and an effective electron-phonon Hamiltonian, we show that above-gap (0.5 eV) photoexcitation leads to

squeezed phonons that oscillate at twice the phonon frequency 2ω. This 2ω oscillation in the material serves as a parametric drive ω_d. The THz probe pulse with frequency ω_s interacts with the dynamic material interface and generates reflected photon pairs at the signal (ω_s) and idler ($\omega_{id} = \omega_d - \omega_s$) frequencies. This shows that $\Delta R/R$ arises from stimulated parametric emission.

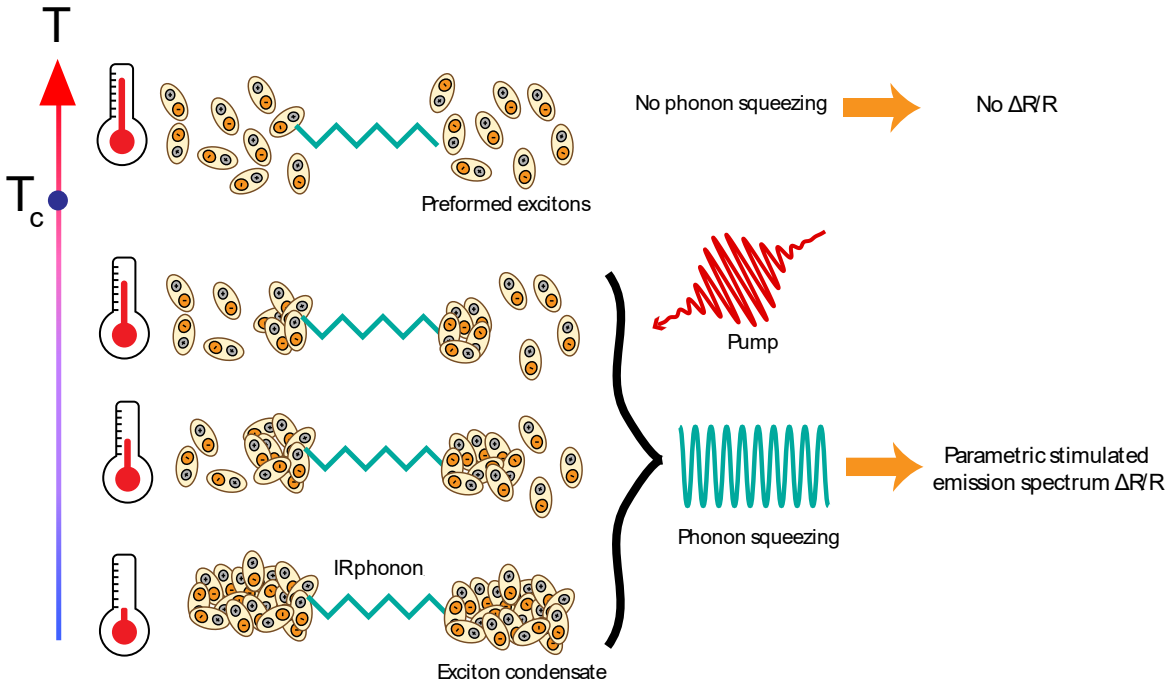

Figure 6.1: The parametric amplification process in summary. The preformed excitons condense below T_C and strong condensate-lattice coupling exists which plays a major role in the phonon squeezing process upon photoexcitation. The squeezing oscillation serves as the driving frequency, subsequently amplifying the probe THz field.

Figure 6.1 captures the parametric amplification process and establishes the relation between the exciton condensate and the parametric amplification via phonon squeezing. Our results demonstrate the signatures of a BEC-like exciton condensate, congruent with preformed excitons pictures above T_C. In this scenario, preformed excitons exist much above T_C. However,

they only form the condensate below T_C and thus, below T_C, the condensate-phonon coupling is strong. Upon photoexcitation, the electron-phonon (condensate-phonon) coupling is modulated and leads to phonon squeezing at twice the phonon frequency. This squeezing oscillation serves as the parametric drive ω_d which parametrically amplifies the incoming THz probe, bringing in the reflectivity enhancement spectrum $\Delta R/R$.

Above T_C, the condensates are broken into preformed excitons, and the condensate-lattice coupling exists no more. As a result, no phonon squeezing oscillation is observed. This confirms that the condensate and its coupling to the IR phonons provides the ground for the phonons to be squeezed and oscillate, as represented in the BEC-like temperature dependence. In other words, if the phonon squeezing oscillation and the parametric amplification originated from excitonic correlation only and no condensate, no such temperature dependence would be observed. In essence, the exciton condensate serves as the gain medium for the parametric amplification process.

6.2 Insight into the EI phase of TNS

We have experimentally demonstrated that our nonequilibrium data unveils the interplay between electronic and lattice order parameters and tracks the exciton condensate response otherwise invisible in the equilibrium regime. There are broader implications of this in disentangling intertwined order parameters, accessing novel phases, and more specifically, in studying excitonic insulators.

Apart from the nature of the bound pairs, there are a few subtle differences between a superconducting and an exciton condensate. A superconductor shows gap opening, drop in resistance and kink in specific heat across the phase transition. Likewise, an excitonic insulator

would show an insulating gap, discontinuity in resistance and specific heat. However, superconductors exhibit Meissner effect which not only is a gold standard for superconductivity, but also gives a clear idea about the condensate formation according to the Anderson-Higgs mechanism.

On the contrary, there is no such "smoking gun" feature for an excitonic insulator. Moreover, the lattice interaction with excitonic correlation hinders the identification of the exciton condensate in equilibrium measurement. Although ARPES or optical conductivity measurements can report the gap attributes and measuring resistivity can shed light on the charge transport properties, they cannot reveal the condensate hallmarks that is optically silent due to parasitic coupling to other degrees of freedom. As such, we drove the material out of equilibrium using an optical pulse and tracked its dynamics using a THz probe which is sensitive to electronic correlation.

Our experiment unravels the role of electron-phonon coupling in the form of a parametric reflectivity enhancement. We observed a prominent increase in the reflectivity at select IR phonon frequencies. Furthermore, this reflectivity increase shows a BEC-like temperature dependence. Hence, we can extract information about both the nature of the exciton condensate and its coupling to the phonons. When we calculated the integrated reflectivity change due to photoexcitation, it also exhibited a BEC-like trend, further confirming a condensate origin of the parametric emission spectrum.

Together with the theoretical calculations, we identified the phonon (4.7 THz) that is most strongly coupled to the excitonic correlations as well as sensitive to the phase transition. We observe a condensate-driven parametric reflectivity amplification process which can well be explained with a minimal phenomenological theory and DFT. As such, we propose it as a novel

scheme to trace spectral fingerprints of exciton condensate in excitonic insulators with strong phononic coupling such as TNS. This new phenomenon introduces a new possibility of harnessing the nonlinear optical properties of the exciton condensate in TNS.

The THz probe is amplified by the 9.4 THz squeezed phonon oscillation of the 4.7 THz mode which is directly coupled to the condensate. This is a very special case where a light field is amplified by a phonon field as opposed to a conventional optical parametric amplifier, paving the way towards new phonon-based THz lasers. In light of this, we think our results have the potential to influence thinking in the field of TNS excitonic insulator and, more broadly, highlight that parametric dynamics is a useful tool to unravel complex dynamics in quantum materials.

6.3 Fresnel-Floquet theory & the future of nonlinear optics

Along these lines, a key feature of our results is that Fresnel-Floquet theory offers a framework to describe coherent nonlinear effects for fast dynamics in quantum materials. This is different from conventional “snapshot” picture where the change in optical conductivity is extracted from the photoinduced reflectivity change at each pump-probe delay. This is an important example of THz nonlinear optics in quantum materials, an emerging concept that will be of importance far beyond TNS, providing a powerful framework and approach to interrogate numerous materials.

Fresnel-Floquet theory provides a systematic approach to phenomenologically analyze coherent dynamics in quantum materials. It also offers a new framework to extract novel optical properties for nonlinear optical processes, opening a new avenue of research in the field of nonlinear optics on quantum materials.

Our results also show the first spectral fingerprints of an exciton condensate in terms of an IR phonon response. Notably, phonon squeezing provides a route to drive the condensate without direct excitation of the Higgs mode. In addition, the momentum dependence of electron-phonon coupling parameter g_k motivates future experiments to measure the reflectivity enhancement as a function of pump photon energy. Our experimental technique and the application of Fresnel-Floquet theory are applicable to a host of other quantum materials to gain new insights into subtle interactions that modify the condensate response from textbook expectations.

Moreover, condensate-driven THz parametric amplification may lead to novel photon sources and optoelectronic devices using EIs. Further, our results suggest intriguing potential for novel single-photon THz quantum optics, paving the way towards EI-based THz lasers that can drive innovation in quantum information and sensing technology.

Appendix A Sample Preparation & Characterization

Single crystals of Ta_2NiSe_5 (TNS) were grown by a vapor transport method with iodine as the transport agent. Stoichiometric amounts of Ta, Ni, and Se powders were first pre-reacted at 900 ℃ before the vapor transport process, which was performed across a temperature gradient spanning 850 ℃ to 900 ℃ (see Appendix A Fig. 1).

The resultant crystals had lateral dimensions of 1 mm × 0.6 mm along the a and c axes, respectively, with a thickness of ~80 μm. The structure and single-phase purity of the resulting crystals was confirmed by powder X-ray diffraction. Appendix A Fig. 2 displays the temperature-dependent resistivity of TNS. A sudden drop in resistivity is observed at 326 K (indicated by the blue triangle), indicating a phase transition.

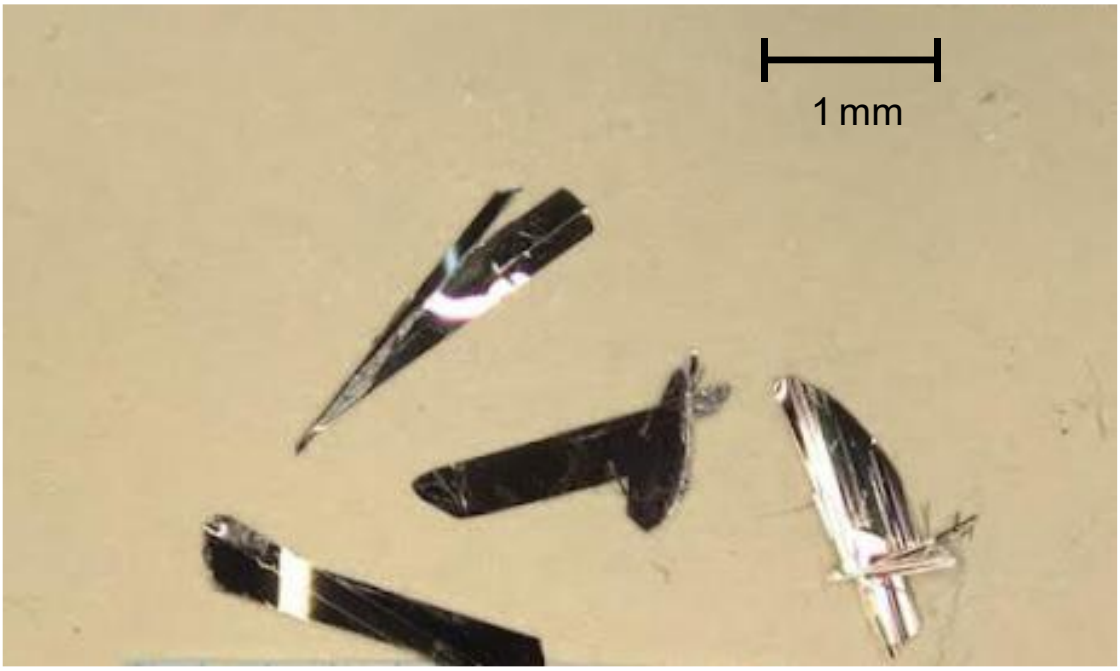

Appendix A Figure 1: TNS single crystal samples. The scale is a guide to the eye for size comparison.

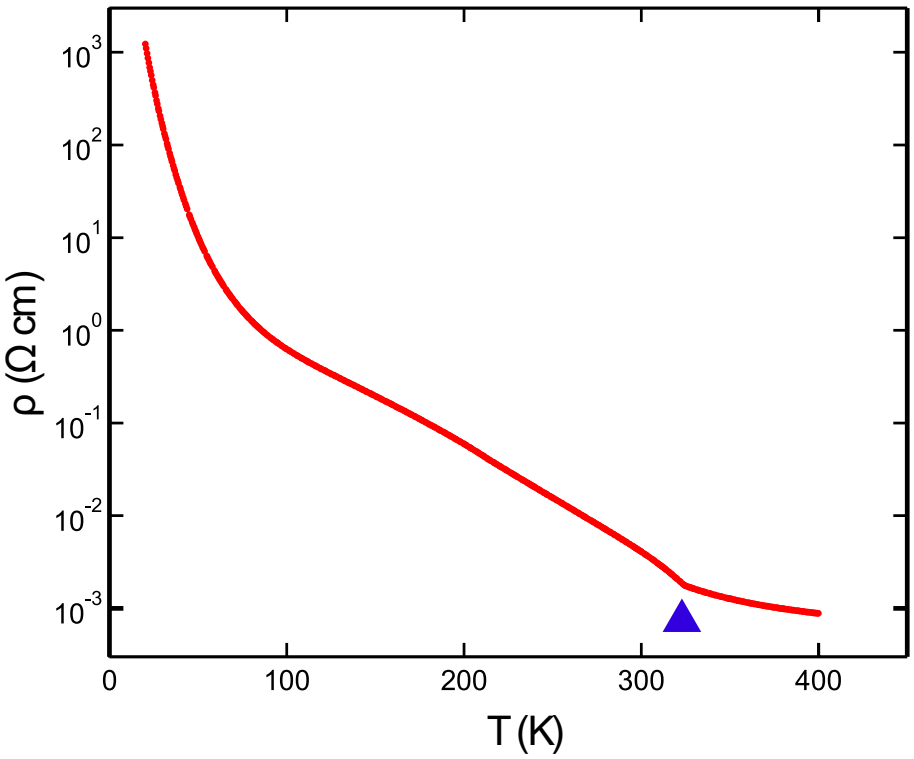

Appendix A Figure 2: Resistivity of Ta_2NiSe_5 single crystal plotted against the temperature. The blue triangle emphasizes an anomaly at $T = 326$ K, corresponding to the temperature of the phase transition.

Appendix B Specific Heat Analysis

We estimate the lattice temperature after photoexcitation. For a given pump fluence, we estimate the absorbed energy over the pumped volume and calculate the effective temperature after electron-phonon thermalization using the relation,

$$Q_{pump} = \int_{T_i}^{T_f} N\, C(T) dT\,, \tag{B1}$$

where Q_{pump} is the total absorbed energy, N is the number of moles in the excited volume, $C(T)$ is the temperature-dependent lattice specific heat of TNS, and T_i and T_f are the initial and final temperature after electron phonon thermalization, respectively. Q_{pump} is derived from the relation,

$$Q_{pump} = F\, A\, (1 - R). \tag{B2}$$

Here F is the pump fluence, A is the area of the pump beam on the sample with a diameter ~3 mm (pump beam FWHM diameter), and R is the reflectivity at 2.4 μm (0.5 eV) which is ~0.45 [71]. N can be written as $N = V_{excited}/V_{molar}$, where photoexcited volume $V_{excited}$ is estimated as a cylindrical disk with a diameter of ~3 mm and height equal to the penetration depth d, and molar volume V_{molar} was calculated as 106 $\mathrm{cm}^3/\mathrm{mol}$. We used the temperature dependent specific heat $C(T)$ data from Ref. [40] and fitted it using Debye model (Appendix B Fig. 1).

The final temperature was calculated numerically and plotted as a function of fluence. Extended Data Fig. 5b displays temperature raise ΔT as a function of fluence for different initial temperatures T_i. We note that, upon photoexcitation the temperature change is very small; even for the highest fluence in our experiment (0.4 $\mathrm{mJ/cm}^2$), the temperature rise is only ~5 K for an initial temperature of 90 K and ~3 K for an initial temperature of 300 K. This eliminates the

possibility of any significant thermal heating effect and further confirms that our experimental findings are largely due to electronic (excitonic) correlations. Since the insulator-semiconductor phase transition temperature for TNS is 326 K, the specific heat analysis also shows that the sample remains in excitonic insulator phase (below T_c) after photoexcitation.

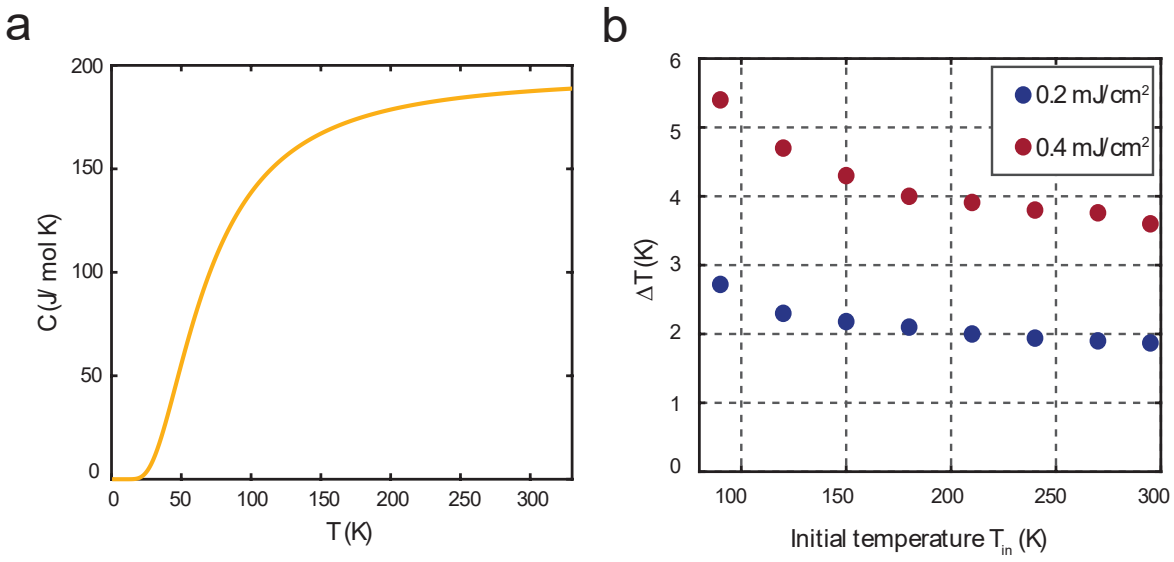

Appendix B Figure 1: a, Specific heat of TNS obtained from ref. [40], then modeled with a Debye fitting. **b**, fluence-dependent temperature increase ΔT for different initial temperatures T_i. It is observed from the plot that the photoinduced temperature rise is minimal, ruling out a thermal origin.

Appendix C Thermal Effect Analysis

In pump-probe experiments, thermal heating due to the excitation pulse can happen which will raise the temperature of the material. This can affect the actual signal. As a result, one needs to take into account the thermal and nonthermal contributions in order to analyze experimental data.

We added the plot of pump-induced time-resolved signal $\Delta E(t)$ which is the photoinduced change in the probe electric field, its corresponding FFT and photoinduced reflectivity enhancements for both $0.2\ \mathrm{mJ/cm^2}$ and $0.4\ \mathrm{mJ/cm^2}$ fluences at 90 K in Appendix C Fig. 1. In the figure, (a) and (d) are the signals, (b) and (e) are the Fourier transforms while (c) and (f) are the photoinduced reflectivity enhancements for both fluence. As seen in the figure, the FFT and the reflectivity enhancement curves follow a very similar trend (see (b) and (c) for $0.2\ \mathrm{mJ/cm^2}$, and (e) and (f) for $0.4\ \mathrm{mJ/cm^2}$ fluence. In this way, we can see a one-on-one correspondence between raw data and our observation of reflectivity enhancements select IR-active phonon frequencies.

Now we will show that this signal is predominantly of electronic origin. First, we performed the specific heat analysis as described in the Methods to calculate the photoinduced temperature rise. From Appendix B Fig. 1, it can be seen that the temperature rise is minimal for both fluences, ruling out a large thermal effect or any thermal phase transition.

We also note that for both pump fluences, the $(R + \Delta R)/R$ curves exhibit identical trends (except the magnitudes) with prominent peaks at the phonon frequencies. If the signal was of predominantly thermal origin and involved a mere phonon shift, $(R + \Delta R)/R$ plots would show different patterns as a function of pump fluence. We also did not observe any difference in the line shape for both high and low fluences. Furthermore, the reflectivity enhancement at 4.7 THz

exhibits a temperature dependence that can be analyzed with a BEC model, implying a mostly electronic origin.

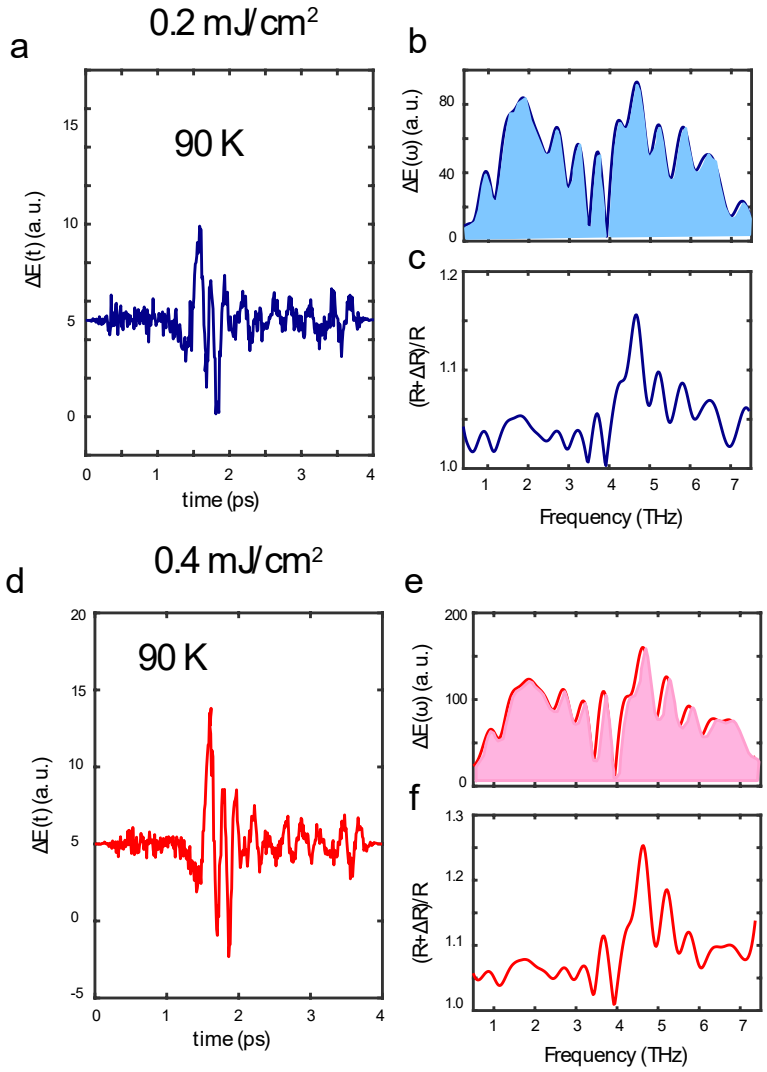

Appendix C Figure 1: a, Photoinduced change in reflected probe electric field, **b,** corresponding spectrum of the change. **c,** Reflectivity enhancement for 0.2 mJ. cm^2 fluence. **d**, Photoinduced change in reflected probe electric field, **e**, corresponding spectrum of the change, **f**, reflectivity enhancement for 0.4 mJ. cm^2 fluence at $t_{pp} = 1$ ps.

Now, to further support our findings and compute the thermal contribution, we will perform a thorough analysis of temperature dependent reflectivity spectrum. Let's assume that at

temperature T_0, optical pumping transiently raises the sample temperature by ΔT. Then the final temperature of the system becomes, $T_0 + \Delta T = T_1$. If heating and thermal phonon shifts are largely responsible for the signals, the pump-induced reflectivity enhancement spectrum at T_0 will match the ratio of equilibrium reflectivity at T_1 and T_0. This relation can be expressed as,

$$\frac{R_{pumped}(T_0)}{R_{eq}(T_0)} = \frac{R_{eq}(T_1)}{R_{eq}(T_0)}, \tag{C1}$$

where $R_{pumped}(T_0) = R_{eq}(T_0) + \Delta R\ (T_0)$. To test this scenario, we performed pump-probe measurements at 90 K and 100 K as shown in Appendix C Fig. 2. We measured the equilibrium and nonequilibrium (pumped) reflectivity at 90 K to compute the photoinduced reflectivity enhancement spectrum (solid red line). Then we compared the results with the 100 K equilibrium reflectivity data (purple dashed line).

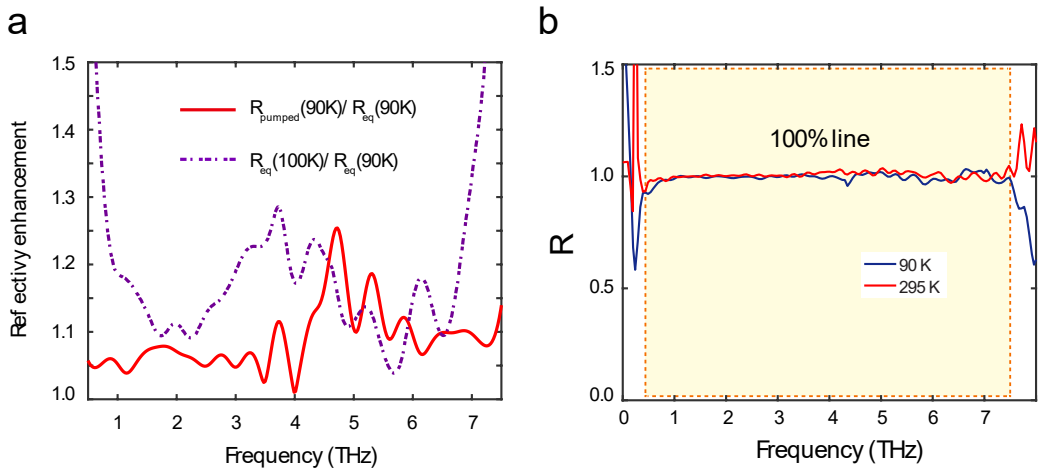

Appendix C Figure 2: a, Reflectivity enhancement $(R + \Delta R)/R$ at 90 K (red) compared with reflectivity changed due to thermal effect (purple dashed line), showing a different trend. **b**, 100% line for a gold reference with reflectivity attaining the value of unity in the frequency regime of 0.5 – 7.5 THz, defining the reliable region.

For the thermal origin of the signal, the curves are expected to overlap with each other. On the contrary, no similar trend is observed from the figure. The reason that the ratio between equilibrium reflectivity data at 100 K and 90 K is more than 1 is that the material goes through an insulator-semiconductor phase transition at 326 K. As such, as the temperature increases, the reflectivity gets larger and hence, $\frac{R_{eq}(100\ K)}{R_{eq}(90\ K)} > 1$. However, there is no significant peaks at the IR phonon frequencies, which is contrary to the photoinduced enhancement plot represented by the solid red curve. We are adding the 100%-line plot to demonstrate the reliable spectral region and the repeatability of our measurements.

It is evident from the figure that thermal effect may be responsible for some reflectivity enhancement but is unable to explain the prominent enhancement at select IR phonon frequencies (especially the 4.7 THz B_{3u} phonon). However, our proposed mechanism of squeezed phonon oscillations at 9.4 THz which is twice the frequency of the 4.7 THz IR phonon strongly coupled to the exciton condensate can reproduce the data very well as seen in Fig. 5.1, pointing out that our signal is largely due to electronic effect.

References

[1] Basov, D. N., Averitt, R. D., van der Marel, D., Dressel, M. & Haule, K., Electrodynamics of correlated electron materials. *Reviews of Modern Physics* **83**, 471-542 (2011).

[2] Nambu, Y., Quasiparicle and Gauge invariance in the theory of superconductivity. *Physical Review* **117**, 648-663 (1960).

[3] Anderson, P. W., Coherent excited states in the theory of superconductivity. *Physical Review* **110**, 827-835 (1958)

[4] Grüner, G., Zawadowski, A. & Chaikin, P. M., Nonlinear conductivity and noise due to charge density wave depinning in $NbSe_3$. *Physical Review Letters* **46**, 511-515 (1981).

[5] Grüner, G., The dynamics of charge density waves. *Reviews of modern* Physics **60**, 1129-1181 (1988).

[6] Watanebe, H & Murayama H., Unified description fo Nambu-Goldstone boson without Lorentz invariance. *Physical Review Letters* **108**, 251602 (2012).

[7] Chang, J., Blackburn, E., Holmes, A. T., Christensen, N. B., Larsen, J., Mesot, J. Liang, R., Bonn, D. A., Hardy, W. N., Watenphul, A., Zimmermann, M. v., Forgan, E. M. & Hayden, S. M., Direct observation of competition between superconductivity and charge density wave order in $YBa_2Cu_3O_{6.67}$. *Nature Physics* **8**, 871-876 (2012).

[8] Song, S., Yu., T. L., Lou, X., Xie, B. P., Xu, H. C., Wen, C. H. P., Yao, Q., Zhang, S. Y., Zhu, X. T., Guo, J. D., Peng, R. & Feng, D. L., Evidence of cooperative effect on the enhanced superconducting transition temperature at the $FeSe/SrTiO_3$ interface. *Nature Communications* **10**, 758 (2019).

[9] Kotliar, G., Savrasov, S. Y., Haule, K., Oudovenko, V. S., Parcollet, O. & Marianetti, C. A., Electronic structure calculations with dynamical mean-field theory. *Reviews of Modern Physics* **78**, 865-951 (2006).

[10] Averitt, R. D. & Taylor, A. J., Ultrafast optical and far-infrared quasiparticle dynamics in correlated electron materials. *Journal of Physics: Condened. Matter* **14**, R1357 (2002).

[11] Basov, D. N., Averitt, R. D. & Hsieh, D., Towards properties on demand in quantum materials. *Nature Materials* **16**, 1077-1088 (2017).

[12] Imada, M, Fujimori, A. & Tokura, Y., Metal-insulator transitions. *Reviews of Modern Physics* **70**, 1039 (1998).

[13] Kaindl, R. A., Eickemeyer, Woerner, M. & Elsaesser, T., Broadband phase-matched difference frequency mixing of femtosecond pulses in gaSe: Experiment and theory. *Applied Physics Letters* **75**, 1060 (1999).

[14] Kaindl, R. A., Smith, D. C., Joschko, M., Hasselbeck, M. P., Woerner, M. & Elsaesser, T., Femtosecond infrared pulses tunable from 9 to 18 μm at an 88 MHz repetition rate. *Optics Letters* **23**, 861 (1998).

[15] Reimann, K., Smith, R. P., Weiner, A. M., Elsaesser, T. & Woerner, M., Direct field-resolved detection of terahertz transients with amplitudes of megavolts per centimeter. *Optics Letters* **28**, 471 (2003).

[16] Wu, Q., Zhang, X.-C., Free-space electro-optic sampling of terahertz beams. *Applied Physics Letters* **67**, 3523 (1995).

[17] Basov, D. N. & Timusk, T., Electrodynamics of high-T_c superconductors. *Reviews of Modern Physics* **77**, 1721 (2005).

[18] Zhang, J. & Averitt, R. D., Dynamics and control in complex transition metal oxides. *Annual Reviews of Materials* Research **44**, 19-43 (2014).

[19] Stojchevska, L., Vaskivskyi, Mertelj, T., Kusar, P., Svetin, D., Brazovskii, S. & Mihailovic, D., Ultrafast switching to a stable hidden quantum state in an electronic crystal. *Science* **344**, 177-180 (2014).

[20] Demser, J., Averitt, R. D., Taylor, A. J., Kabanov, V. V.m Kang, W. N., Kim, H. J., Choi, E. M. & Lee, S. I, Pair-breaking and superconducting state recovery dynamics in MgB_2. *Physical Review Letters* **91**, 267002 (2002).

[21] Zhang, J., Tan, X., Liu, M.-K., Teitelbaum, S. W., Post, K. W., Jin, F., Nelson, K. A., Basov, D. N., Wu, W. & Averitt, R. D., Cooperative photoinduced metastable phase control in strained manganite films. *Nature Materials* **15**, 956-960 (2016).

[22] Fausti, D., Tobey, R. I., Dean, N., Kaiser, S., Dienst, A., Hoffman, M. C., Pyon, S., Takayama, T., Takagi, H. & Cavalleri, A., Light-induced superconductivity in a stripe-ordered cuprate. *Science* **331**, 189-191 (2011).

[23] Mitrano, M., Cantaluppi, A., Nicoletti, D., Kaiser, S., Perucchi, A., Lupi, S., Di Pietro, P., Pontiroli, D., Riccò, M., Clark, S. R., Jaksch, D. & Cavalleri, A., Possible light-induced superconductivity in K_3C_{60} at high temperature. *Nature* **530**, 461-464 (2016).

[24] Fox, M., *Optical Properties of Solids*. Oxford University Press, 2010.

[25] Wang, F., Dukovic, G. Brus, L. E & Heinz T. F., The optical resonances in carbon nanotubes arises from excitons. *Science* **308**, 838-841 (2005).

[26] Chernikov, A., Berkelbach, T. C., Hill, H. M., Rigosi, A., Li, Y. Aslan, O. B., Reichman, D. R., Hybertsen, M. S. & Heinz, T. F., Exciton Binding Energy and Nonhydrogenic Rydberg Series in MonolayerWS2. *Physical Review Letters*. **113**, 076802 (2014).

[27] Frenkel, J.,On the Transformation of light into Heat in Solids. *Physical Review*. **37**, 17 (1931).

[28] Wannier, G.,The Structure of electronic excitation levels in insulating crystals. *Physical Review* **52**, 191 (1937).

[29] Jérome, D., Rice, T. & Kohn, W., Excitonic insulators. *Physical Review* **158**, 462 (1967).

[30] Kohn, W. & Sherrington, D., Two kinds of bosons and Bose condensates. *Reviews of Modern Physics* **41**, 1 (1970).

[31] Kohn, W., Excitonic phases. *Physical Review Letters* **19**, 439 (1967).

[32] Halperin, B. I. Rice, T. M., Possible anomalies at a semiconductor-semimetal transition. *Reviews of Modern Physics* **40**, 755 (1968).

[33] Eisenstein, J. P., Exciton condensation in bilayer quantum Hall systems. *Annu. Rev. Condened. Matter Physics* **5**, 159-181 (2014).

[34] Amo, A., Lefrère, J., Pigeon, S., Adrados, C., Ciuti, C., Carusotto, I., Houdré, R., Giacobino, E. & Bramati, A., Superfluidity of polaritons in semiconductor microcavities. *Nature Physics* **5**, 805-810 (2009).

[35] Kogar, A., Rak, M. S., Vig, S., Husain, A. A., Flicker, F., Joe, Y. I., Venema, L., MacDougall, G. J., Chiang, T. C., Fradkin, E., Wenzel, J. v. & Abbamonte, P., Signatures of exciton condensation in a transition metal dichalcogenide. *Science* **358**, 1314-1317 (2017).

[36] Song, Y., Jia, C., Xiong, H., Wang, B., Jiang, H., Huang, K., Hwang, J., Li, Z., Hwang, C., Liu, Z., Shen, D., Sobota, J. A., Kirchmann, P., Xue, J., Devereaux, T. P., Mo, S.K., Shen, Z.X. & Tang, S., Evidences for the exciton gas phase and its condensation in monolayer 1T-$ZrTe_2$. *Preprint at* https://arxiv.org/abs/2201.11592 (2022).

[37] Tamakasu, K., Nakamura, Y. & Uchida, S., Charge dynamics across the CuO_2 planes in $La_{2-x}Sr_xCuO_4$. *Physical Review Letters* **69**, 1455-1458 (1992).

[38] Golež, D., Sun, Z., Murakami, Y., Georges, A. & Millis, A. J., Nonlinear spectroscopy of collective modes in an excitonic insulator. *Phys. Rev. Lett.* **125**, 257601 (2020).

[39] Wakisaka, Y., Sudayama, T., Takubo, K., Mizokawa, T., Arita, M., Namatame, H., Taniguchi, M., Katayama, N., Nohara, M. & Takagi, H., Excitonic insulator state in Ta_2NiSe_5 probed by photoemission spectroscopy. *Physical Review Letters* **103**, 026402 (2009).

[40] Lu, Y.F., Kono, H., Larkin, T. I., Rost, A., Takayama, T., Boris, A.V., Keimer, B. & Takagi, H., Zero-gap semiconductor to excitonic insulator transition in Ta_2NiSe_5. *Nature Communications* **8**, 14408 (2017).

[41] Seki, K., Wakisaka, Y., Kaneko, T., Toriyama, T., Konishi, T., Sudayama, T., Saini, N. L., Arita, M., Namatame, H., Taniguchi, M., Katayama, N., Nohara, M., Takagi, H., Mizokawa, T. & Ohta, Y., Excitonic Bose-Einstein Condensation in Ta_2NiSe_5 above room temperature. *Physical Review B* **90**, 155116 (2014).

[42] Sugimoto, K., Nishimoto, S., Kaneko, T. & Ohta, Y., Strong coupling nature of the excitonic insulator state in Ta_2NiSe_5. *Physical Review Letters* **120**, 247602 (2018).

[43] Kabanov. V. V., Demser, J., Podonik, B. & Mihailovic, D., Quasiparticle relaxation dynamics in superconductors with different gap structures: theory and experiments on $YBa_2Cu_3O_{7-\delta}$. *Physical Review B* **59**, 1497 (1999).

[44] Kabanov. V. V., Demser, J. & Mihailovic, D., Kinetics of a superconductor excited with a femtosecond optical pulse. *Physical Review Letters* **95**, 147002 (2005).

[45] Kaneko, T., Toriyama, T., Konishi, T. & Ohta, Y., Orthorhombic-to-monoclinic phase transition induced by the Bose-Einstein condensate of excitons. *Physical Review B* **87**, 035121 (2013).

[46] Fukutani, K., Stania, R., Kwon, C. I., Kim, J. S., Kong, K. J., Kim, J. & Yeom, H. W., Detecting photoelectrons from spontaneously formed excitons. *Nature Physics* **17**, 1024-1030 (2021).

[47] Chen, L., Han, T. T., Cai, C., Wang, Z. G., Wang, Y. D., Xin, Z. M. & Zhang, Y., Doping-controlled transition from excitonic insulator to semimetal in Ta_2NiSe_5. *Physical Review B* **102**, 161116(R) (2020).

[48] Volkov, P. A., Ye, M., Lohani, H., Feldman, I., Kanigel, A. & Blumberg, G., Critical charge fluctuations and quantum coherent state in excitonic insulator Ta_2NiSe_5. *npj Quantum Materials* **6**, 52 (2021).

[49] Ye, M., Volkov, P. A., Lohani, H., Feldman, I., Kim, M., Kanigel, A. & Blumberg, G., Lattice dynamics of the excitonic insulator $Ta_2Ni(Se_{1-x}S_x)_5$. *Physical Review B* **104**, (045102 (2021).

[50] Nakano, A., Hasegawa, T., Tamura, S., Katayama, N., Tsutsui, S. & Sawa, H., Antiferroelectric distortion with anomalous phonon softening in the excitonic insulator Ta_2NiSe_5. *Physical Review B* **98**, 045139 (2018).

[51] Kim, K., Kim, H., Kim, J., Kwon, C., Kim, J. S. & Kim, B. J., Direct observation of excitonic instability in Ta_2NiSe_5. *Nature Communications* **12**, 1969 (2021).

[52] Pal, S., Grover, S., Harnagea, L., Telang, P., Singh, A., Muthu, D. V. S., Waghmare, U. V. & Sood, A.K., Destabilizing excitonic insulator phase by pressure tuning of exciton phonon coupling. *Physical Review Research* **2**, 043182 (2020).

[53] Saha, T., Golež, D., Ninno, G.D., Mravlje, J., Murakami, Y., Ressel, B., Stupar, M. & Ribič, P. R., Photoinduced phase transition and associated timescales in the excitonic insulator Ta_2NiSe_5. *Physical Review B* **103**, 144304 (2021).

[54] Mor, S., Herzog, M., Noack, J., Katayama, N., Nohara, M., Takagi, H., Trunschke, A., Mizokawa, T., Monney, C. & Stähler, J., Inhibition of the photoinduced structural phase transition in the excitonic insulator Ta_2NiSe_5. *Physical Review B* **97**, 115154 (2018).

[55] Mor, S., Herzog, M., Golež, D., Werner, P., Eckstein, M., Katayama, N., Nohara, M., Takagi, H., Mizokawa, T., Monney, C. & Stähler, J., Ultrafast electronic band gap control in an excitonic insulator. *Physical Review Letters* **119**, 086401 (2017).

[56] Lee, J., Kang, C.J., Eom, M. J., Kim, J. S., Min, B. I. & Yeom, H. W., Strong interband interaction in the excitonic insulator phase of Ta_2NiSe_5. *Physical Review B* **99**, 075408 (2019).

[57] Larkin, T. I., Dawson, R. D., Höppner, M., Takayama, T., Mathis, Y. L., Takagi, H., Keimer, B. & Boris, A. V., Infrared phonon spectra of quasi-one-dimensional Ta_2NiSe_5 and Ta_2NiS_5. *Physical Review B* **98**, 125113 (2018).

[58] Larkin, T. I., Yaresko, A. N., Pröpper, D., Kikoin, K. A., Lu, Y.F., Takayama, T., Mathis, Y. L., Rost, A. W., Takagi, H., Keimer, B. & Boris, A. V., Giant exciton Fano resonance in quasi-one-dimensional Ta_2NiSe_5. *Physical Review B* **95**, 195144 (2017).

[59] Werdehausen, D., Takayama, T., Höppner, M., Albrecht, G., Rost, A.W., Lu, Y.F., Manske, D., Takagi, H. & Kaiser, S., Coherent order parameter oscillations in the ground state of the excitonic insulator Ta_2NiSe_5. *Science Advances* **4**, eaap8652 (2018).

[60] Werdehausen, D., Takayama, T., Albrecht, G., Lu, Y.F., Takagi, H. & Kaiser, S., Photo-excited dynamics in the excitonic insulator Ta_2NiSe_5. *Journal of Physics.: Condensed Matter* **30**, 305602 (2018).

[61] Bretscher, H. M., Andrich, P., Telang, P., Singh, A., Harnagea, L., Sood, A. K. & Rao, A., Ultrafast melting and recovery of collective order in the excitonic insulator Ta_2NiSe_5. *Nature Communications* **12**, 1699 (2021).

[62] Mazza, G., Rösner, M., Windgätter, L., Latini, S., Hübener, H., Millis, A. J., Rubio, A. & Georges, A., Nature of symmetry breaking at the excitonic insulator transition: Ta_2NiSe_5. *Physical Review Letters* **124**, 197601 (2020).

[63] Watson, M. D., Marković, I., Morales, E. A., Le Fèvre, P., Merz, M., Haghighirad, A. A. & King, P. D. C., Band hybridization at the semimetal-semiconductor transition of Ta_2NiSe_5 by mirror-symmetry breaking. *Physical Review Research* **2**, 013236 (2020).

[64] Bretscher, H. M., Andrich, P., Murakami, Y., Golež, D., Remez, B., Telang, P., Sing, A., Harnagea, L., Cooper, N. R., Millis, A. J., Werner, P., Sood & A. K., Rao, A., Imaging the coherent propagation of collective modes in the excitonic insulator Ta_2NiSe_5 at room temperature. *Science Advances* **7**, eabd6147 (2021).

[65] Tang, T., Wang, H., Duan, S., Yang, Y., Huang, C., Guo, Y., Qian, D. & Zhang, W., Non-Coulomb strong electron-hole binding in Ta_2NiSe_5 revealed by time- and angle-resolved photoemission spectroscopy. *Physical Review B* **101**, 235148 (2020).

[66] Golež, D., Dufresne, S. K. Y., Kim, M. J., Boschini, F., Chu, H., Murakami, Y., Levy, G., Mills, A. K., Zhdanovich, S., Isobe, M., Takagi, H., Kaiser, S., Werner, P., Jones, D. J., Georges, A., Damascelli, A. & Millis, A. J., Unveiling the underlying interactions in Ta_2NiSe_5 from photo-induced lifetime change. *Physical Review B* **106**, L121106 (2022).

[67] Kim, M.J., Schultz, A., Takayama, T., Isobe, M., Takagi, H. & Kaiser, S., Phononic soft mode behavior and a strong electronic background across the structural phase transition in the excitonic insulator Ta_2NiSe_5. *Physical Review Research* **2**, 042039(R) (2020).

[68] Subedi, A., Orthorhombic-to-monoclinic transition in Ta_2NiSe_5 due to a zone-center optical phonon instability. *Physical Review Materials* **4**, 083601 (2020).

[69] Windgätter, L., Rösner, M., Mazza, G., Hübner, H., Georges, A., Millis, A. J., Latini, S. & Rubio, A., Common microscopic origin of the phase transition in Ta_2NiS_5 and the excitonic insulator candidate Ta_2NiSe_5. *npj Computational Materials* **7**, 210 (2021).

[70] Baldini, E., Zong, A., Choi, D., Lee, C., Michael, M. H., Windgätter, L., Mazin, I. I., Latini, S., Azoury, D., Lv, B., Kogar, A., Wang, Y. Lu, Y., Takayama, T., Takagi, H., Millis, A. J., Rubio, A., Demler, E. & Gedik, N., The spontaneous symmetry breaking in Ta_2NiSe_5 is structural in nature. *Preprint at* https://arxiv.org/abs/2007.02909 (2020).

[71] Seo, Y.S., Eom, M. J., Kim, J. S., Kang, C.J., Min, B.I. & Hwang, J., Temperature-dependent excitonic superfluid plasma frequency evolution in an excitonic insulator. *Scientific Reports* **8**, 11961 (2018).

[72] Kida, N. & Tonouchi, M., Spectroscopic evidence of a charge-density-wave condensate in a charge-ordered manganite: Observation of a collective excitation mode in $Pr_{0.7}Ca_{0.3}MnO_3$ by using THz time-domain spectroscopy. *Physical Review B* **66**, 24401 (2002).

[73] Fujioka, J., Takahashi, Y., Kida, N., Shimano, R. & Tokura, Y., Optical investigation of the collective dynamics of charge-orbital density waves in layered manganites. *Physical Review B* **82**, 140409 (R) (2010).

[74] Kaindl, R. A., Carnahan, M. A., Hägele, Lövenich & Chemla, D. S., Ultrafast terahertz probes of transient conducting and insulating phases in an electron-hole gas. *Nature* **423**, 734 (2003).

[75] Hilton, D. J., Prasankumar, R. P., Fourmaux, S., Cavalleri, A., Brassard, D., El Khakani, a. A., Kieffer, J. C., Taylor, A. J. & Averitt, R. D., Enhanced photosusceptibility near T_C for the light-induced insulator-to-metal phase transition in vanadium dioxide. *Physical Review Letters* **100**, 019906 (2008).

[76] Kampfrath, T., Sell, A., Klatt, G., Pashkin, A., Mährlein, S., Dekorsy, T., Wolf, M., Fiebig, M., Leitenstorfer, A. & Huber, R., Coherent terahertz control of antiferromagnetic spin waves. *Nature Photonics* **5**, 31 (2011).

[77] Rajasekaran, S., Okamoto, J., Mathey, L., Fechner, M., Thampy, V., Gu, G. D. & Cavalleri, A., Probing optically silent superfluid stripes in cuprates. *Science* **359**, 575-579 (2018).

[78] Matsunaga, R., Tsuji, N., Fujita, H., Sugioka, A., Makise, K., Uzawa, Y., Terai, H., Wang, Z., Aoki, H. & Shimano, R., Light-induced collective pseudospin precession resonating with Higgs mode in a superconductor. *Science* **345,** 1145-1149 (2013).

[79] Wu, Q. & Zhang, X.-C., Free-space electro-optic sampling of terahertz beams. *Applied Physics Letters* **67**, 3523 (1995).

[80] Wu, Q. & Zhang, X.-C., Ultrafast electro-optic field sensors. *Applied Physics Letters* **68**, 1604 (1996).

[81] Wu, Q. & Zhang, X.-C., 7 THz broadband GaP electro-optic sensors. *Applied Physics Letters* **70**, 1784 (1996).

[82] Hirori, H., Doi., A, Blanchard & Tanaka, K., Single-cycle terahertz pulses with amplitudes exceeding 1 MV/cm generated by optical rectification in $LiNbO_3$. *Applied Physics Letters* **98**, 091106 (2011).

[83] Hebling, J., Yeh, K.-L., Hoffman, M. C., Bartal, B. & Nelson, K. A., Generation of high-power terahertz pulses by tilted-pulse-front excitation and their application possibilities. *Journal of the Optical Society of America B* **25**, B6 (2008).

[84] Cook, D. J. & Hochstrasser, R. M., Intense terahertz pulses by four-wave rectification in air. *Optics Letters* **25**, 1210 (2000).

[85] Kress, M, Löffler, T., Eden, S., Thomson, M. & Roskos, H. G., Terahertz-pulse generation by photoionization of air with laser pulses composed of both fundamental and second-harmonic waves. *Optics Letters* **29**, 1120 (2004).

[86] Liu, J. & Zhang, X.-C., Terahertz-radiation-enhanced emission of fluorescence from gas plasma. *Physical Review Letters* **103**, 235002 (2009).

[87] Liu., J. Dai, J., Chin, L. & Zhang, X.-C, Broadband terahertz wave remote sensing using coherent manipulation of fluorescence from asymmetrically ionized gas. *Nature Photonics* **4**, 627 (2010).

[88] Wen. H & Lindenberg, A. M., Coherent Terahertz polarization control through manipulation of electron trajectories. *Physical Review Letters* **103**, 119903 (2009).

[89] Zhang, Z.-Z, Chen, Y., Cui, S., He, F., Chen, M., Zhang, Z.-Z, Yu, J., Chen, L., Sheng, Z., & Zhang, J., Manipulation of polarizations for broadband terahertz waves emitted from laser plasma filaments. *Nature Photonics* **12**, 554 (2018).

[90] Dai, J., Karpowicz, N., & Zhang, X.-C., Coherent polarization control of terahertz waves generated from two-color laser-induced gas plasma. *Physical Review Letters* **103**, 023001 (2009).

[91] Dai, J. & Zhang, X.-C., Terahertz wave generation from gas plasma using a phase compensator with attosecond phase-control accuracy. *Applied Physics Letters* **94**, 023001 (2009).

[92] Dai, J., Xie, X. & Zhang, X.-C., Detection of broadband terahertz waves with a laser-induced plasma in gases. *Physical Review Letters* **97**, 103903 (2006).

[93] Karpowicz, N., Dai, J., Lu, X., Chen, Y., Yamaguchi, M., Zhao, H., Zhang, X.-C., Zhang, L., Zhang, C., Price-Gallagher, M., Fletcher, C., Mamer, O., Lesimple, A. & Johnson, K., Coherent heterodyne time-domain spectrometry covering the entire “terahertz gap”. *Applied Physics Letters* **92**, 159901 (2008).

[94] Xie, X., Dai, J. & Zhang, X.-C., Coherent control of THz wave generation in ambient air. *Physical Review Letters* **96,** 075005 (2006).

[95] Kim, K.-Y., Glownia, J. H., Taylor, A. J., & Rodriguez, G., Terahertz emission from ultrafast ionizing air in symmetry-broken laser fields. *Optics Express* **15**, 4577 (2007).

[96] Kostin, V. A., Laryushin, I. D., Silaev, A. A. & Vvedenskii, N. V., Ionization-induced multiwave mixing: terahertz generation with two-color laser pulses of various frequency ratios. *Physical Review Letters* **117**, 035003 (2016).

[97] Zhang, L.-L., Wang, W.-M., Wu, T., Zhang, R., Zhang, S.-J., Zhang, C.-L., Zhang, Y., Sheng, Z.-M. & Zhang, X.-C., Observation of terahertz radiation via the two-color laser scheme with uncommon frequency ratios. *Physical Review Letters* **119**, 235001 (2017).

[98] Wang, W.-M., Sheng, Z.-M., Li, Y.-T., Zhang, Y., & Zhang, J. Terahertz emission driven by two-color laser pulses at various frequency ratios. *Physical Review A* **96,** 023844 (2017).

[99] Werley, C. A., Teo, S. M. & Nelson, K. A., Pulsed laser noise analysis and pump-probe signal detection with a data acquisition car, *Review of Scientific Instruments* **82**, 123108 (2011).

[100] Kindt, J. T. & Schmuttenmaer, C. A., Theory of determination of the low-frequency time-dependent response function in liquids using time-resolved terahertz pulse spectroscopy. *Journal of Chemical Physics* **110**, 8589-8596 (1999).

[101] Coslovich, G., Kemper, A. F., Behl, S., Huber, B., Bechtel, H. A., Sasagawa, T. Martin, M. C., Lanzara, A. & Kaindl, R. A., Ultrafat dynamics of a vibrational symmetry breaking in a charge-ordered nickelate. *Science Advances* **3**, e1600735 (2017).

[102] Michael, M. H., Först, M., Nicoletti, D., Haque, S. R. U., Zhang, Y., Cavalleri, A., Averitt, R. D., Podolsky, D. & Demler, E., Generalized Fresnel-Floquet equations for driven quantum materials. *Physical Review B* **105**, 174301 (2022).

[103] Kennes, D. M., Wilner, E. Y., Reichman, D. R. & Millis, A. J., Transient superconductivity from electronic squeezing of optically pumped phonons. *Nature Physics* **13**, 479-483 (2017).

[104] Garrett, G. A., Rojo, A. G., Sood, A. K., Whitaker, J. F. & Merlin, R., Vacuum squeezing of solids: Macroscopic quantum states driven by light pulses. *Science* **275**, 1638-1640 (1997).

[105] Buzzi, M., Jotzu, G. Cavalleri, A., Cirac, J. I., Demler, E. A., Halperin, B. I., Lukin, M. D., Shi, T., Wang, Y. & Podolsky, D., Higgs-mediated optical amplification in a nonequilibrium superconductor. *Physical Review X* **11**, 011055 (2021).

[106] Kresse, G. & Furthmüller, J., Efficient iterative schemes for *ab inito* total-energy calculations using a plane-wave basis set. *Physical Review B* **54**, 11169-11186 (1996).

[107] Kresse, G. & Furthmüller, J., Efficiency of *ab inito* total-energy calculations for metals and semiconductors using a plane-wave basis set. *Computational Materials Science* **6 (1***),* 15-50 (1996).

[108] Kresse, G. & Hafner, J., *Ab initio* molecular dynamics for liquid metals. *Physical Review B* **47**, 558-561 (1993).

[109] Kresse, G. & Hafner, J., Norm-conserving and ultrasoft pseudopotentials for first-row and transition elements. *Journal of Physics: Condensed Matter* **6**, 8245-8257 (1994).

[110] Kilmeš. J., Bowler, D. R. & Michaelides, A., Van der waals density functionals applied to solids. *Physical Review B.* **83**, 195131 (2011).

[111] Kilmeš. J., Bowler, D. R. & Michaelides, A., Chemical accuracy for the van der Waals density functional. *Journal of Physics: Condensed Matter* **22**, 022201 (2009).

[112] Skelton, J. M., Burton, L. A., Jackson, A. J., Oba, F., Parker, S. C. & Walsh, A., Lattice dynamics of the tin sulphides SnS_2, SnS and Sn_2S_3: vibrational spectra and thermal transport. *Physical Chemistry Chemical Physics* **19**, 12452-12465 (2017).

[113] Togo, A. & Tanaka, I., First principles phonon calculations in materials science. *Scripta Materialia* **108**, 1-5 (2015).